CRANFIELD UNIVERSITY

NGUNJOH LAWRENCE NDAMKA

MICROSTRUCTURAL DAMAGE OF THERMAL BARRIER COATINGS DUE TO CMAS ATTACK

SCHOOL OF APPLIED SCIENCES
SURFACE ENGINEERING AND NANOTECHNOLOGY INSTITUTE (SENTI)

Full Time Ph.D Student
Academic Year: 2010 - 2013

Supervisor: Prof. J. R. Nicholls
Dr. R. Wellman
Dr. M. Craig

October 2013

CRANFIELD UNIVERSITY

SCHOOL OF APPLIED SCIENCES
SURFACE ENGINEERING AND NANOTECHNOLOGY INSTITUTE (SENTI)

Ph.D

Academic Year 2010 - 2013

NGUNJOH LAWRENCE NDAMKA

MICROSTRUCTURAL DAMAGE OF THERMAL BARRIER COATINGS DUE TO CMAS ATTACK

Supervisor: Prof. J. R. Nicholls
Dr. R. Wellman
Dr. M. Craig

October 2013

This thesis is submitted in full fulfilment of the requirements for the degree of PhD.
(NB. This section can be removed if the award of the degree is based solely on examination of the thesis)

ABSTRACT

Over recent years, due to a constant desire for higher efficiency engines and hence increased turbine entry temperatures and a proportional reduction in CO_2 emissions, there is a need to understand how molten slags (CMAS: Calcia magnesia alumina-silicate), including volcanic ash, affect engine life. Thermal barrier coatings (TBC) are employed together with cooling technology to protect engine hardware from the high temperature seen within the turbine and combustion zones. At current operating temperatures, CMAS can adhere to the TBC surface resulting in premature degradation of the coating. The columnar, high porosity microstructure of electron beam physical vapour deposited (EB-PVD) TBCs make them particularly susceptible to CMAS/molten deposit attack. CMAS attack of PYSZ is reported in literature to be characterised by penetration of the melt along the columnar structure, chemically attacking the TBC whereupon yttria is leached from PYSZ and into the melt, creating an yttria depleted interaction zone.

A new approach for classifying and reporting CMAS attack on TBCs is introduced in this thesis and a degradation map is created to acknowledge that the mechanism and severity of CMAS damage is related to variation in the CMAS compositions. CMAS degradation of EB-PVD has been extensively studied by previous authors, all reporting similar degradation mechanism with varying degree of severity. In this study, this category of CMAS degradation mechanism is termed “classic” CMAS attack.

The primary aim of this study has been to investigate the damage caused by volcanic ash and CMAS to materials used within an aerospace gas turbine engine. The thesis investigates two aspects. It is recognised that, debris ingested by the engine will cause erosion damage to components in the cooler section of the engine (compressor), thus the first part examines this

issue. A series of erosion tests with Eyjafjallajokull volcanic ash and similar sized MIL spec silica sand have been undertaken with two compressor-typical materials (Ti-6Al-4V and Inconel 718). The results were consistent with volcanic ash behaving like fine silica sand both at room and at compressor operating temperatures. The measured erosion rates are consistent with a ductile erosion mechanism with peak rates of material loss at lower impact angle. The results would appear to fit classical ductile erosion models where the material loss depends on particle velocity and follows a power with an exponent close to 2.4.

The second aspect investigates chemical/molten deposits infiltration in the hotter section of the engine (turbine), especially damage to TBCs. A novel technique of assessing the mechanism and severity of damage is introduced, by adopting the concept of Basicity Index (B.I.) which has been used in the past in industries such as welding; to determine the quality of a weld metal, and in mining; to examine the quality of the slag bi-product which is suggestive of the purity of the metal. Here, Basicity Index has been shown to be a good indicator of the mechanism and severity of damage caused by molten deposits to TBCs and may be used to categorise different modes of attack.

Three categories of CMAS compositions are identified based on soil composition across the world; Low Basicity Index (B.I.) refers to B.I. < 1.8, Mid-range B. I. (Near Neutral deposits): B.I. = 1.8 – 2.2, and High B.I.: B.I. = 2.2 or above. Gadolinium zirconate ($Gd_2Zr_2O_7$) is widely accepted in literature to mitigate the effect of Low B.I. CMAS damage. The results show that, whilst Gadolinium zirconate (GZO) mitigates Low B.I. attack, it provides limited resistance to Near Neutral CMAS attack after an exposure as little as 4h at 1430 °C, while the sample showed complete failure after 8h. The attack rate of GZO was increased when High B.I. CMAS was used, with complete failure of coating integrity after 4h exposure at 1430 °C. This goes to show that, whilst GZO can provide CMAS protection in regions of the world

with Low B.I. CMAS composition, it remains susceptible if operated in other regions in the world containing Near Neutral or High B.I. compositions. It is believed that with the higher temperatures likely to result in next generation aero-engines and with sand chemistry varying around the world, basicity driven TBC degradation will become more prevalent.

ACKNOWLEDGEMENT

First and foremost I would like to thank my principal supervisor, Prof. John Nicholls for his support and general guidance throughout the life of this Ph.D. not to mention his advice and unsurpassed knowledge of thermal barrier coatings. This thesis would never have been possible without the vision of my second supervisor, Richard Wellman for presenting me with the opportunity to study for a Ph.D. His good advice, support and friendship have been invaluable to me on an academic, professional and personal level, for which I remained extremely grateful. I want to thank both John Nicholls and Richard Wellman for all their contributions of time, ideas and funding to make my Ph.D. experience productive and stimulating. I would also like to acknowledge Mark Craig for agreeing to take over from Richard two years into my Ph.D. It has been an honour to be his first Ph.D. student.

I would like to acknowledge members of my review panel, Dr. Mick Whelan, Dr. Adriana Encinas-Oropesa and Prof. Jim Harris for their helpful guidance and suggestions in general. Thanks are owed to the members of John Nicholls' group, National High Temperature and Surface Engineering Centre, for their kindness, friendship and support and for their immense contribution to my personal and professional time at Cranfield University. I want to thank Tony Gray for producing the coatings used in this study, Rolls Royce for supplying the samples of Eyjafjallajokull volcanic ash and for support from the EU NEWAC programme. I would also like to acknowledge Tim Pryor for his commitment in ensuring all equipment and practices were safe and also for his quick response in whenever action was needed. I thank Christine Chalk for her keen eyes for Health and Safety practices for which our

department was exemplary. I would also like to acknowledge Tracey Roberts and Andrew Dyer for their technical support. I would also like to thank Simon Gray, Tim Rose and Sandra Craig for their knowledge based advice and insightful discussions about the research.

For this research, SEM, EBSD, FIB and XRD analyses were essential. I am most grateful to Dr. Xianwei Liu for his support and the expert analytical knowledge he shared with me. The amount of time that he invested in my project and continued doing so after I left to start work I am particularly indebted to him.

My time at Cranfield University was made enjoyable in large part due to the friends and group that became a part of my life. I thank my friends and colleagues, past and present students at Cranfield; Zhixu Xing, Andrew Kelly, Vladimir Krastev, Charles Crouzat, Marina Stamenova and Sandra Tegha for providing me support and friendship. I also thank Arthur Hawkins whom I have had the opportunity to collaborate with and for resolving my questions on erosion related experiments. My time at Cranfield was also enriched by the Afro-Caribbean Society (ASC) which I was once the vice-president for some social distractions that I needed.

Lastly, but by no means least, I would like to thank my family for all their love and encouragement. My hard-working parents sacrificed their lives for my sister and I and provided unconditional love and care. For my Barnsley College tutors for enhancing my love for science and supported in all my pursuits, Judith Brown, Meg Stoke, Camille Stanley I thank them wholeheartedly. To Mr and Mrs Morgan, well my life would never have been possible without your unconditional love through good and bad times. I

shall forever remain indebted to them for the faith they showed in me and my intellect.

Thank you.

Table of Contents

TABLE OF CONTENTS

Table of Contents

Table of Contents

Table of Contents

Table of Contents

List of Figures

LIST OF FIGURES

List of Figures

List of Figures

List of Figures

List of Figures

List of Figures

List of Figures

List of Figures

List of Figures

List of Figures

List of Figures

List of Tables

LIST OF TABLES

List of Tables

List of Equations

LIST OF EQUATIONS

List of Abbreviations, Symbols and Nomenclature

ABBREVIATIONS, SYMBOLS AND NOMENCLATURE

List of Abbreviations

Abbreviations	Full Meaning
APS	Air Plasma Spray
At%	Atomic percent
B.I.	Basicity Index
CAS	Calcium Alumino-Silicate
CMAS	Calcia Magnesia Alumina-Silicate
CTE	Coefficient of Thermal Expansion
CVD	Chemical Vapour Deposition
DSC	Differential Scanning Calorimetry
DVD	Directed Vapour Deposition
EB-PVD	Electron Beam Physical Vapour Deposition
EBSD	Electron Backscatter Diffraction
EDAX	Energy Dispersive X-Ray Analysis
EMPA	Electron Microprobe Analysis
ESEM	Environmental Scanning Electron Microscopy
FCC	Face-Centered Cubic
FEG	Field Emission Gun
FIB	Focused Ion Beam
FOD	Foreign Object Damage
HBI	High Basicity Index
HP	High Pressure
HPT	High Pressure Turbine
HT	High Temperature
HVOF	High Velocity Oxy-Fuel
IP	Intermediate Pressure

List of Abbreviations, Symbols and Nomenclature

LBI	Low Basicity Index
LP	Low Pressure
LPPS	Low Pressure Plasma Spray
MBI	Mid-range Basicity Index
MSZ	Magnesia Stabilised Zirconia
PS	Plasma Spray
PYSZ	Partially Yttria Stabilised Zirconia
SD	Sessile Drop
SEM	Scanning Electron Microscopy
SFC	Specific Fuel Capacity
TBC	Thermal Barrier Coating
TET	Turbine Entry Temperature
TGO	Thermally Grown Oxide
VA	Volcanic Ash
VPS	Vacuum Plasma Spray
XRD	X-Ray Diffraction
YSZ	Yttria Stabilised Zirconia

List of Abbreviations, Symbols and Nomenclature

List of Symbols

Symbol	Meaning
Q	Heat Transfer
Σ	Summation
ΔT	Temperature differential
η	Viscosity
t	Time
ρ	density
k	Thermal conductivity
A	Area
T_1	Compressor exit temperature
T_2	Turbine entry temperature
η_p	Propulsive efficiency
T	Temperature
R	Gas constant
H	Hardness
Δx	Coating thickness
E	Erosion rate
V	Volume of material removed
c	Fraction of particles which cut in idealised manner
M	Mass
p	Plastic flow stress
f(α)	Function of impact angle
v	Particle velocity
n	Velocity exponent
V_p	Volume of particle
V_i	Volume of material removed per impact
ρ_p	Particle density
r_p	Particle radius
K_c	Fracture toughness

List of Abbreviations, Symbols and Nomenclature

Nomenclature

The following nomenclature was adapted throughout this thesis to keep in line with the generally accepted naming system within the industry. The nomenclature has two constituents; the body and the subscript. The body represents the oxides of the chemical elements present, i.e. C for calcium oxide (CaO), M for magnesium oxide (MgO), A for aluminium oxide (Al_2O_3) and S for silicon oxide (SiO_2). The subscript represents the amount of the individual oxides in the overall chemistry, in mole%, for example $C_{35}M_{10}A_5S_{50}$ indicates a composition consisting of 35 mole% of CaO, 10 mole% MgO, 5 mole% Al_2O_3 and 50 mole% SiO_2.

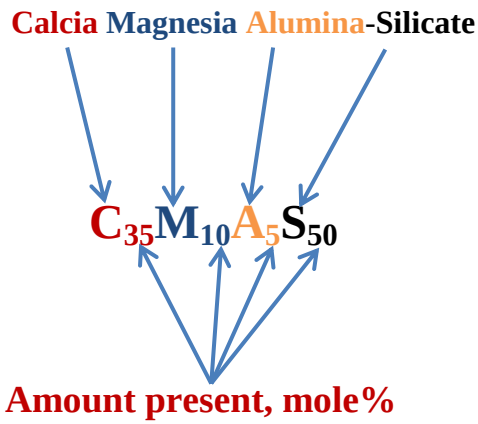

Partially yttria stabilised zirconia (PYSZ) referred in this thesis infer to a ceramic composition containing 6-8 wt% yttria doped zirconia.

1 Introduction

Gas turbine engines operate in a very aggressive environment characterised by high temperatures, mechanical and thermal induced loads and the presence of oxidising and corroding substances. The design of a gas turbine engine must meet certain essential operational criteria in order to withstand these service conditions, whilst providing high efficiency and high reliability [1]. Thermal barrier coatings (TBCs) are used to protect aero and industrial gas turbine engine from thermally induced damage. Thermal barrier coatings (TBCs) consist of a low thermal conductivity material systems which are used to provide a thermal insulation to components operating in the hot section of turbine engine (blades, vanes, seals and combustion panels). A secondary function of TBCs is restricting the access of deposits and contaminants to the substrate materials (Figure 1). This improves the durability and energy efficiency of these engines.

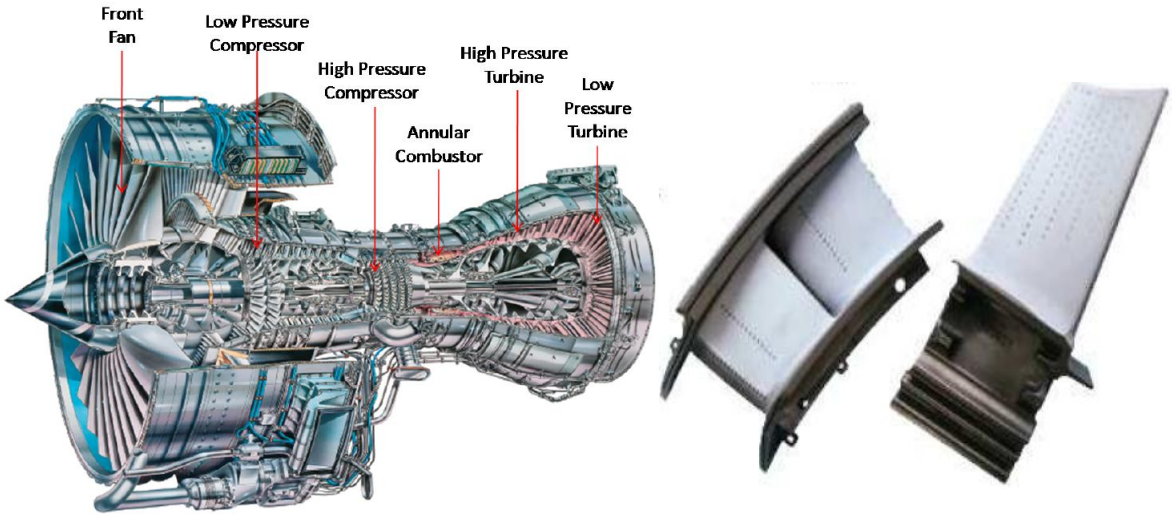

(a) (b) (c)

Figure 1: (a) Sections of the Rolls Royce Trent 500 gas turbine engine [2]. Vanes (b - plasma sprayed) and blades (c - electron beam physical vapour deposited) are components in the turbine section requiring a TBC [3]

The turbine entry temperature is directly related to the thrust generated by the engine, thus increasing the operating temperature will increase the work output and improve thermal efficiency of the engine thus lowering greenhouse gas emission. A temperature increase of 55.5°C leads to approximately 10% increase in work output, yielding an overall increase of 1-1.5% in efficiency [4] which is reflected in a significant savings in fuel consumption and hence emission of greenhouse gases.

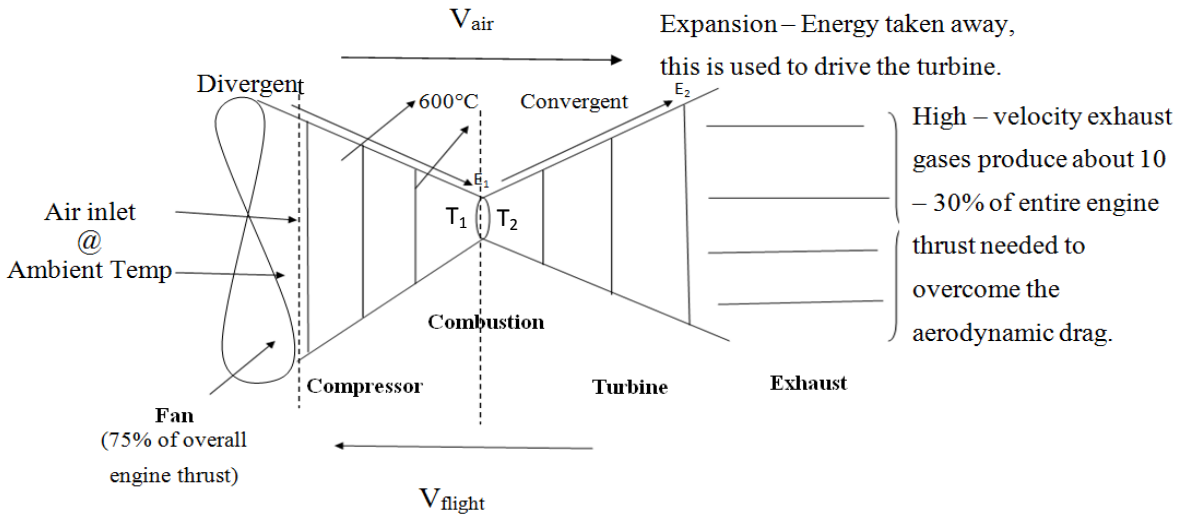

Figure 2: Schematic diagram showing sections of a gas turbine engine.

$E_1 @ T_1, E_2 @ T_2$. $T_2 > T_1$,

Where E_1 is the energy at compressor section with temperature T_1 (compressor exit temperature) and E_2 is the energy in the turbine section with temperature T_2 (turbine entry temperature).

Figure 2 illustrates a schematic diagram of a turbine engine and the principles of operation can be summarised as;

- An aircraft engine (e.g. Trent 800) ingests over one tonne of air per second.
- Inlet air from the fan is compressed, fuel is added and the mixture is ignited. This puts more energy into the system. The increase in energy, E also results in an increase in temperature, T. Temperature is directly proportional to thermal efficiency.

- 75% of the engine thrust is produced by the fan compressing the bypass air and expanding it through the exhaust nozzle (adiabatic compression) [5].
- Energy is also directly proportional to thrust output (mass of air sucked into the engine multiplied by its change in speed).
- Therefore, temperature is directly proportional to power output.
- It can be concluded that, at higher operating temperatures, the engine's fuel burning efficiency increases and this increases the power output and performance efficiency (Figure 3). The propulsive efficiency, η_p can be expressed in terms of the air inlet velocity and the exhaust velocity, as given below;

$$\eta_p = \frac{2 \times V_{inlet}}{V_{inlet} + V_{exit}}, where$$

Figure 3: Jet engine propulsive efficiency

- Also, burning at higher temperature means less fuel is required to produce the necessary power, hence more air miles per gallon.
- High temperature → Thermal efficiency + Low emission.

Efficiency, $D = \frac{T_2 - T_1}{T_2}$ where T_2 is the turbine entry temperature (TET) and T_1 is the compressor exit temperature. Thus an increase in T_2 results in an overall increase in the efficiency of the engine [6].

The efficiency of aero-engines can be reduced by as much as 7% to 10% due to the intake of sand/volcanic ash by the engine. This thesis aims to review the effect of airborne particles on

aero-engine material performance. Solid particle erosion is prevalent in the compressor section while at elevated temperature (turbine section), these ingested particulates may deposit onto hot components and melt, leading to molten (chemical) attack of thermal barrier coating systems on turbine blades. A Basicity concept is introduced to classify the effect of the variation in sand/volcanic ash chemistry around the world. In both cases (erosion and chemical attack), the performance of materials can be improved through better surface engineering and coatings development.

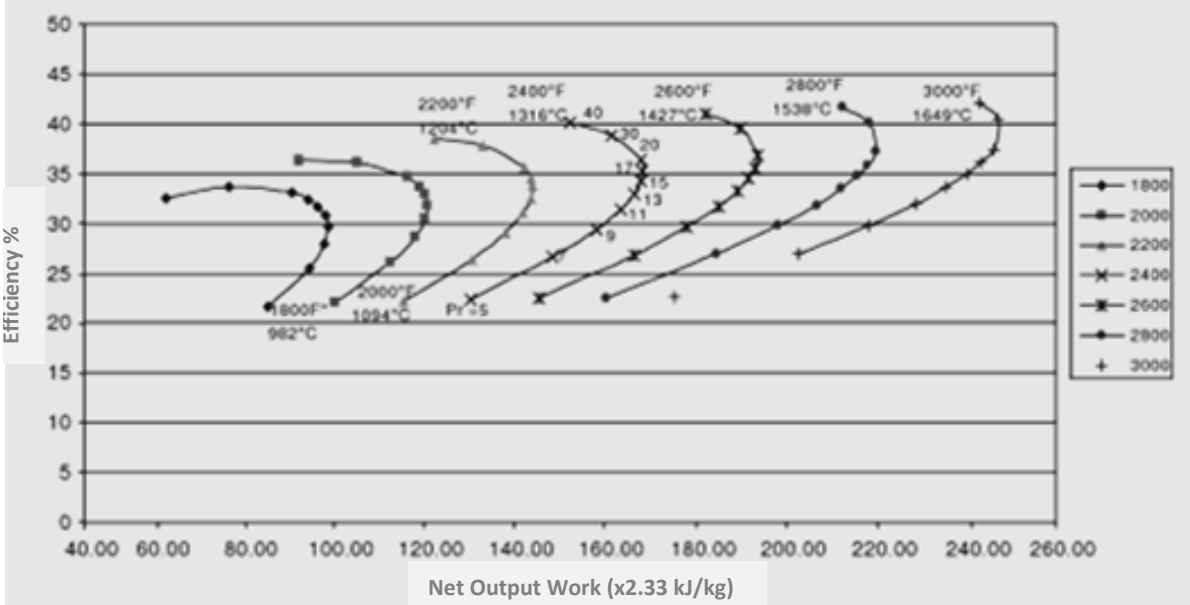

Figure 4: Performance map of a simple cycle gas turbine engine [1]

Figure 4 shows the efficiency against the work output of a gas turbine engine. There are many factors that affect both the performance and the efficiency of a turbine engine, including the mass flow rate of air through the engine and the engine operating temperature (turbine entry temperature). The air flow should be clean and unrestricted to prevent engine problems such as erosion, corrosion and other deposit induced damage.

A principal focus of this research is to investigate the effect that molten slags (volcanic ash and calcium-magnesium alumino-silicate – CMAS) has on thermal barrier coating systems in

the turbine section of a gas turbine engine, with respect to time, temperature and deposition flux. A secondary focus was to assess compressor damage, hence the erosion rate of the engine compressor components by volcanic ash was also investigated.

1.1 Aims

1) The primary focus of this research was to investigate volcanic ash (akin to CMAS) damage to the components in the compressor and turbine sections.
    - In the compressor section:
        - To investigate the erosion behaviour of engine ingested CMAS and/or VA on compressor components:
            - Erosion of two typical compressor alloys; Ti64 and In718
    - In the turbine section:
        - To investigate the effect CMAS composition has on the degradation mechanisms of EB-PVD TBCs.
            - Suggest how Basicity Index affects the severity of molten deposits attack.
            - Propose CMAS resistance TBCs
        - Erosion behaviour of CMAS modified EB-PVD TBCs
2) This study aims to establish the effects that molten deposits have on the performance of a thermal barrier coating system. This study aims to test the effect of slag's Basicity as a factor controlling the severity of molten slag attack, in terms of depth of penetration and general coating degradation. With this in mind and with the consideration of the overall scope of this study, some critical research questions were formulated;
    1. What is the predominant damage caused by volcanic ash to turbine and compressor components?
    2. How can a TBC system that is resistant to this type of attack be designed?

In recent years, a significant volume of research has been undertaken in this area, especially looking into the effect of CMAS attack on TBCs [7-12]. Fewer papers have been published

on the role of volcanic ash. And in both cases, very little research has been carried out looking at the minimum level required to initiate damage over a range of temperatures and times [13]. This project aims to extend the initial work started in 2009 [13], the first to investigate minimum level require for CMAS infiltration and so determine threshold levels for both volcanic ash and CMAS.

1.2 Hypotheses

1. Compressor Section

    - In the compressor section, variations in temperature, impact velocity and particular size will affect the rate and may affect the mechanism of erosion of compressor materials. Two representative materials are investigated, a titanium alloy, Ti64 (Ti- 6Al- 4V) and a nickel based alloy, IN718 (55Ni, 21Cr).

2. Turbine Section

i. Changing the amount of CMAS deposited will affect the rate of CMAS attack.

    - Independent variable – Mass of CMAS deposit
    - Controlled (constant) variables – Time at Temperature and slag's Basicity
    - Dependent variable – Severity of attack (Depth of penetration, morphology of attack).

ii. Time at temperature (Severity of exposure) will affect the rate of CMAS attack.

    - Independent variables – Time (hours) and Temperature (°C)

- Controlled (constant) variables – Basicity Index and Mass deposited
- Dependent variable – severity of attack (Depth of penetration, morphology of attack)

iii. The severity of CMAS damage is dependent on Slag Basicity.

- Independent variable – Basicity Index
- Controlled (constant) variables – Mass deposited and Time at Temperature
- Dependent variable – severity of attack (Depth of penetration, morphology of attack)

2 Literature Review

2.1 Materials Used in Compressors and Turbines

Materials selection for the turbine section of an engine limits the maximum temperature a gas turbine engine can operate at, in terms of strength versus temperature capability, as demonstrated in Figure 5. The gas temperatures in turbine engines vary between 1200 °C and 2000 °C and very few engineering materials can successfully operate at temperatures within this range without some degradation. Single crystal nickel based superalloys (such as CMSX -4 and CMSX -6) used in turbine blades are capable of operating at the highest peak temperature with operation up to 1163 °C. Materials operating under these conditions can fail in several ways, including creep, fatigue, corrosion, oxidation and erosion [5].

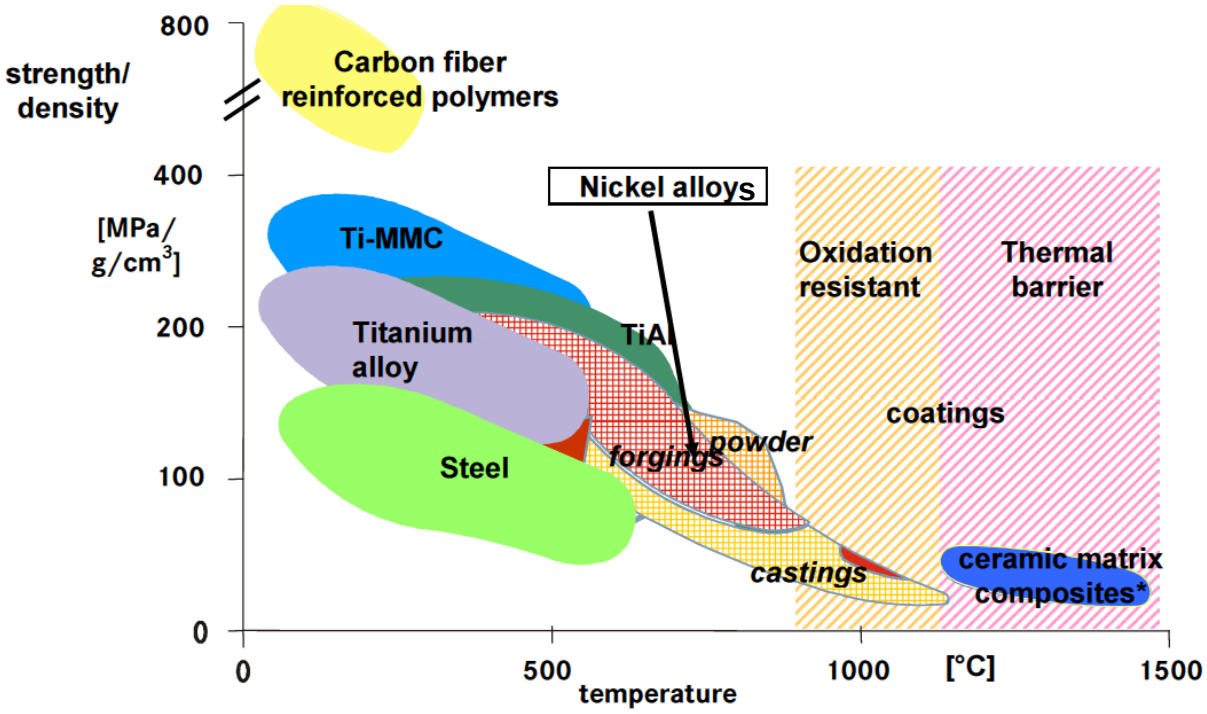

Figure 5: Temperature capabilities of classes of materials [14].

The compressor is made up of the fan and alternating stages of rotating blades and static vanes (Figure 6). The primary function of the compressor section (also known as the cold section, relative to the combustor, turbine and exhaust) is to supply enough air to satisfy the requirements of the combustor. The compressor is also responsible for increasing the static pressure of the mass of air and then discharges it to the combustion burners in an efficient manner. The next generation of materials used in the compressor section of commercial aircraft engines are required to improve efficiency and increase durability at lower costs through a combination of heat resistance, high strength and low weight. Aluminium alloys are used at the front of the compressor housing. At intermediate temperatures, titanium alloys are used whereas at the highest temperatures, steel alloys are used because of the working temperatures increase.

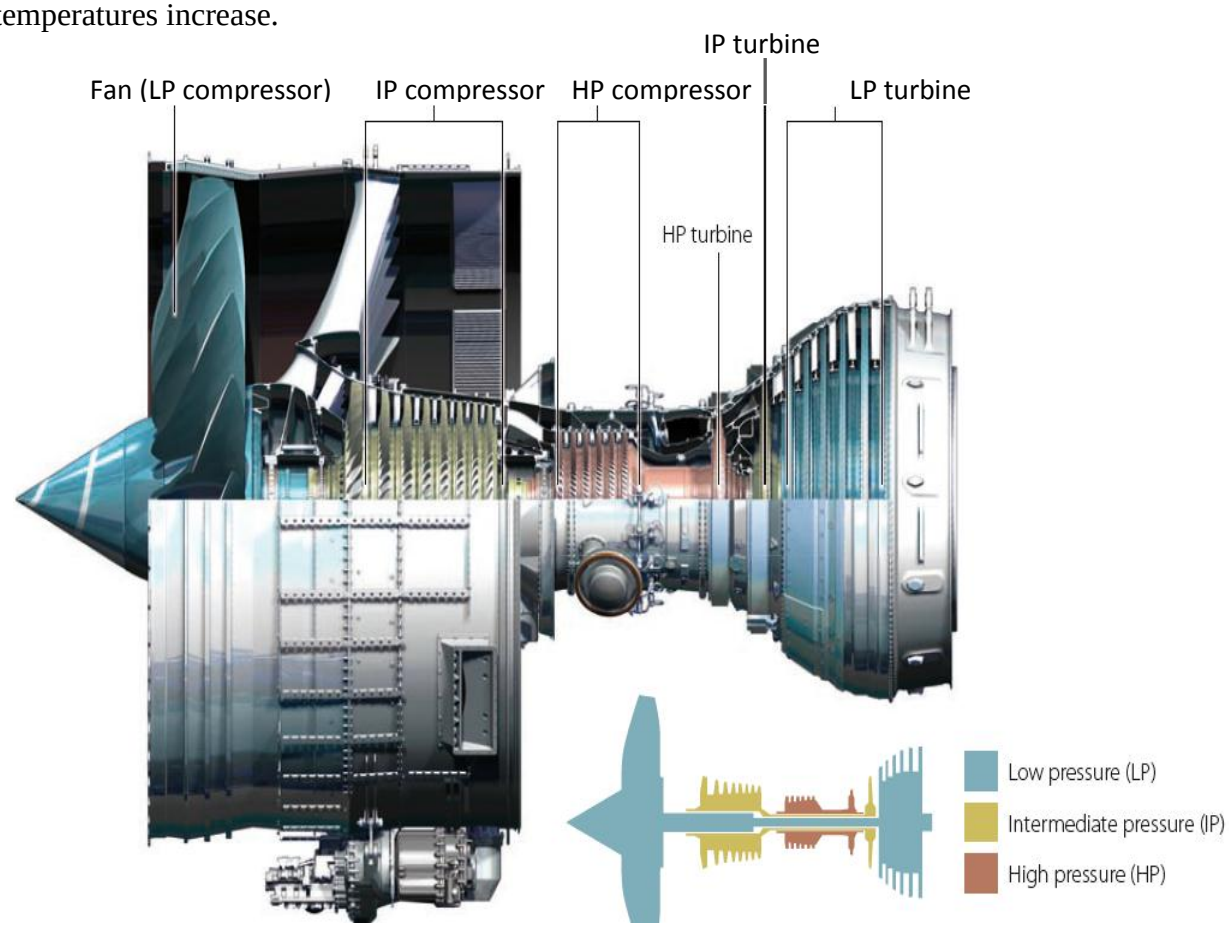

Figure 6: Three-shaft configuration of a Rolls-Royce Trent engine illustrating the different stages of the compressor. Courtesy of Rolls-Royce [2]

The LP compressor blades, or fan blades, are those blades that you can see. At the front of the engine, the low-pressure (LP) compressor blades (also called fan blades) must be strong enough to withstand any impact in the event of a bird strike. Engine bird strikes can cause immense damage to the engine, in some cases leading to complete engine failure if the compressor blades break and get sucked into the engine. The maximum rotational speed of a LP compressor blade is limited by stress considerations; therefore a fan blade material is expected to provide structural stiffness and strength at the operating temperature, good resistance to fatigue, to creep at higher temperatures and containment should a blade fails as well as provide high specific properties for lighter rotating parts and effective damping for noise reduction. For these reasons the blades are made from titanium alloy, for example Ti64 or higher creep strength, high temperature titanium alloys. The composition of Ti64 is shown in Table 1.

Table 1: Ti 6Al-4V Chemical and Mechanical Data

wt%	**Al**	**V**	**C**	**N**	**O**	**H**	**Fe**	**Y**	**Others**	**Ti**
MIN	5.5	3.5	_	_	_	_	_	_	_	_
MAX	6.75	4.5	0.08	0.5	0.2	0.0125	0.3	0.005	0.1	Balance

Alloy	**Melting point ℃**	**Density g/cm³**	**Tensile strength, min N/mm²**	**Yield strength RP0.2N/mm²**	**Elongation at 5 %**	**Hardness Rockwell C**
Solution treatment	1634 - 1664	4.42	828	759	10 - 18	36

High-pressure (HP) compressor (also known as second stage compressor) is where the second stage of air compression occurs. As the air compresses and moves rearward, the air temperature is raised by about 290 °C [15]. Nickel superalloys, for instance Inconel 718

(composition listed in Table 2, Figure 7) are mostly employed in the final stages of the HP compressors due to their high temperature strength and better oxidation/corrosion resistance, whereas titanium alloys (e.g. Ti64) are used at the front of the compressor; low-pressure and intermediate-pressure (IP) compressor (Figure 7).

Table 2: Inconel 718 Chemical and Mechanical Data

wt%	Cr	Ni	Mo	Nb	Ti	Al	C	Mn	Si	Co	Fe
MIN	17.0	50	2.8	4.75	0.7	0.2	_	_	_	_	_
MAX	21.0	55	3.3	5.5	1.15	0.8	0.08	0.35	0.35	1	Balance

Alloy	Melting point ℃	Density g/cm³	Tensile strength Rm N/mm²	Yield strength RP0.2N/mm²	Elongation at 5 %	Brinell hardness HB
Solution treatment	1260-1340	8.2	965	550	30	≤363

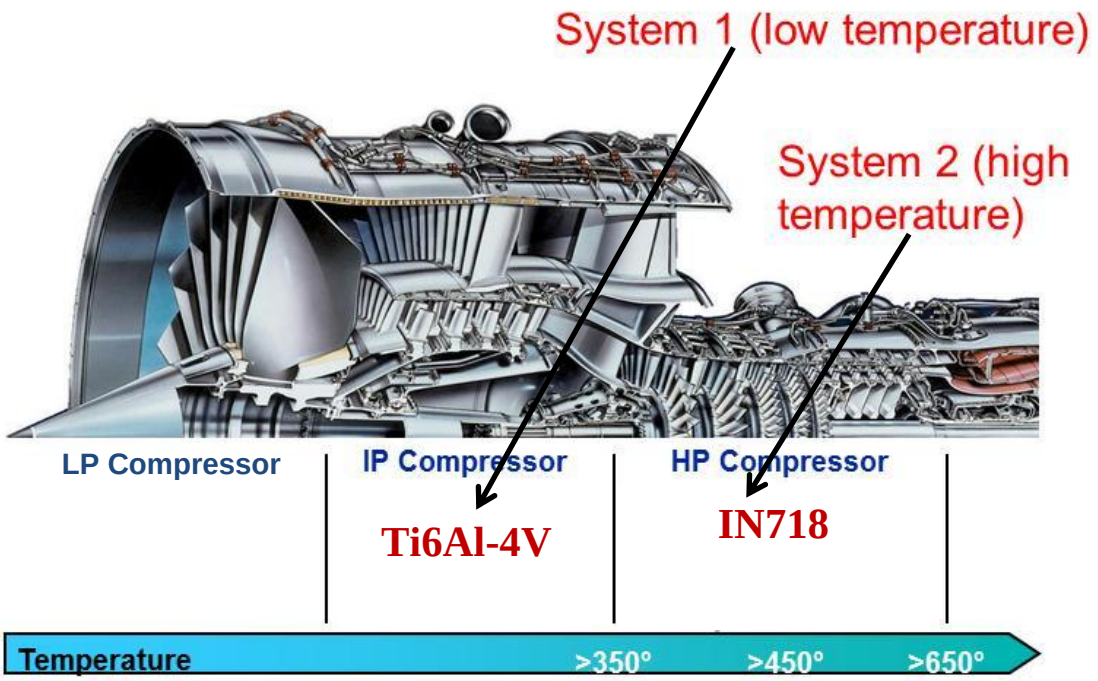

Figure 7: Summary of Compressor Section of a Trent Engine. Courtesy of Rolls-Royce

The material of choice in the turbine section of a gas turbine engine is the family of Nickel superalloys. In turbine blade applications, single crystal nickel based alloys are used in the hottest sections with coating technology to minimise the material's life limiting factors, by protecting the base metal (substrate) from high temperature attack and preventing excessive microstructural degradation, as shown in Figure 8 [16]. Figure 8 illustrates the various components of a thermal barrier coating system, which are used to make maximum use of the properties of the applied materials operating in the elevated temperature environment and to improve the life of the component [17].

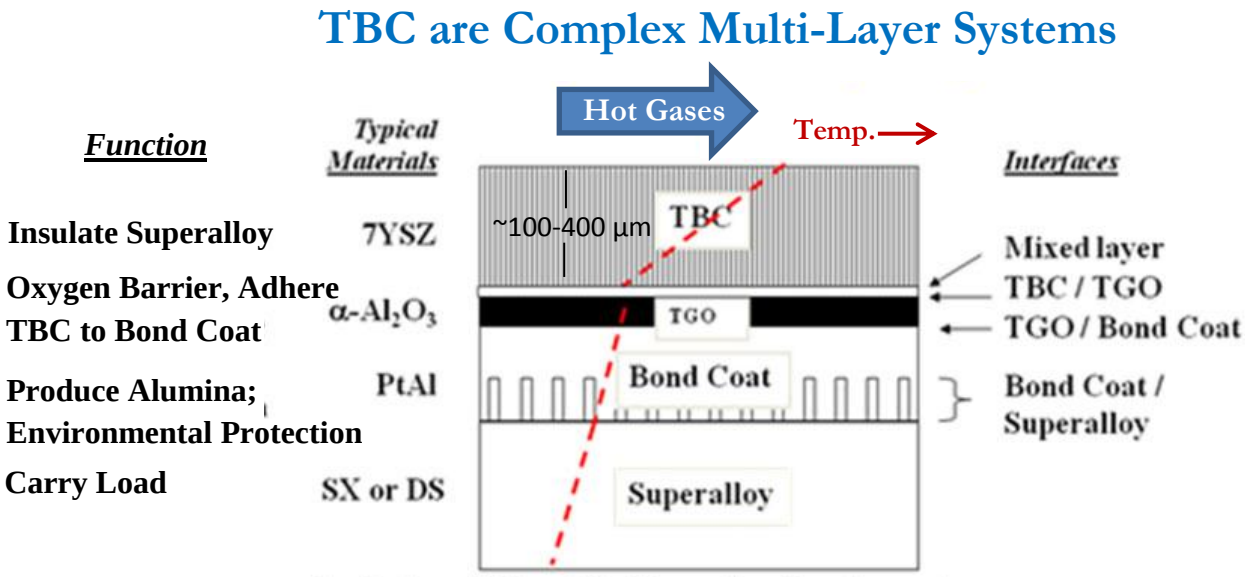

Figure 8: A schematic illustration of a TBC system [18].

Thermal barrier coatings (TBC) are an important part of recent developments to achieve a greater turbine inlet temperatures and the production of more environmentally friendly aero-engines. Thermal barrier coating will reduce the metal temperature by up to 150^{o}C as illustrated in Figure 9 [16].

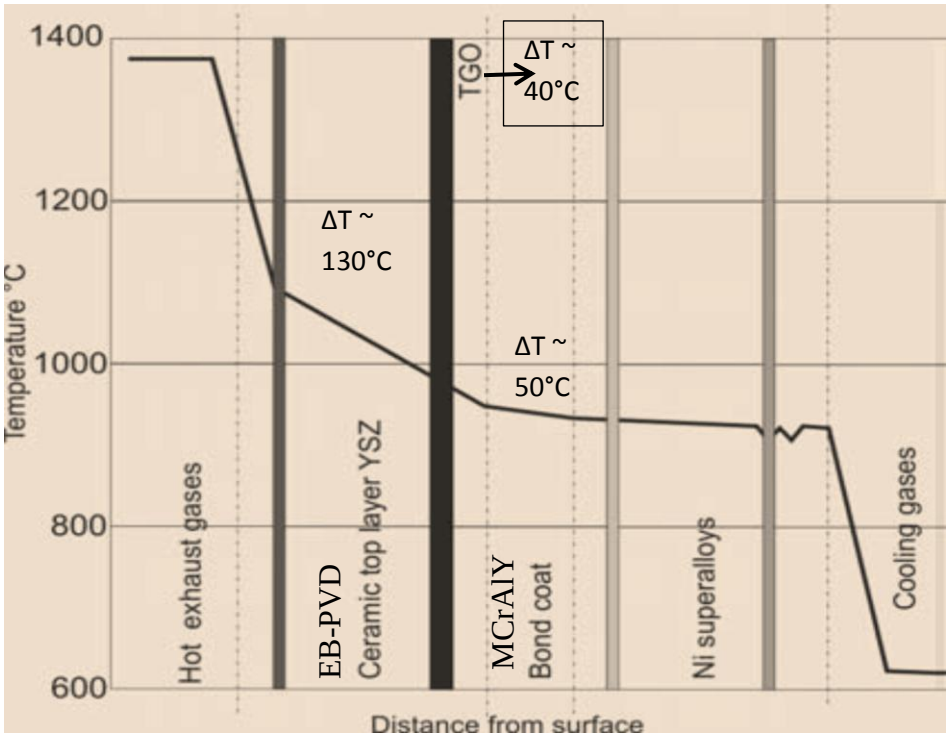

Figure 9: Distribution of temperature on surface of a TBC component [16].

2.2 Coating Systems within High Pressure Turbines – Thermal Barrier Coatings (TBCs)

2.2.1 Fundamentals of TBCs

Thermal barrier coatings promote overall turbine engine efficiency by extending component lifetimes. TBCs are important in aircraft application because of their ability to withstand higher temperatures, thereby allowing an increase in gas turbine engine operating temperatures and reduce cooling requirements, which subsequently helps in achieving engine performance goals [19]. Initial research into thermal barrier coating began back in the 1960s and in the mid 1970s, the first successful test was conducted in the turbine industry. By the 1980s, this was viable and TBCs were in operation in some commercial aircraft gas turbine engines [20].

TBC system	Year of introduction	Bond coat	Ceramic coat	Design of layers
Early combustion TBC	1963	Flame-sprayed Ni-Al	APS 22MSZ	Ceramic/bond coat
	1973	APS Ni-Cr/Al	APS 22MSZ	Ceramic/cemet bond coat
	1974	APS CoCrAlY	APS 22MSZ	Graded
	1980	APS NiCoCrAlY	APS 22MSZ	Ceramic/bond coat
Gen I	1984	APS NiCoCrAlY	APS 7YSZ	Ceramic/bond coat
Gen II	1982	LPPS NiCoCrAlY	APS 7YSZ	Ceramic/bond coat
Gen III	1987	LPPS NiCoCrAlY	EB-PVD 7YSZ	Ceramic/bond coat

Figure 10: Early developmental history of TBCs with magnesia stabilised zirconia (MSZ) in the early days to current yttria stabilised zirconia (YSZ) system [20].

2.3 Components of TBC System:

TBC systems consist of a metallic substrate (generally a Ni or Co-based superalloy), a bond coat - MCrAlY (where M = Ni, Co or both, with thickness in the range of 75-125μm, [17]), PtNiAl or Pt diffused bond coat, which is primarily designed as a local Al reservoir, facilitating the formation of a protective α-Al_2O_3 surface oxide, which promotes bonding between the substrate + bond coat and the top coat and also provides protection against non-protective, breakaway oxidation and hot-corrosion [21]. A ceramic top coat, typically yttria stabilised zirconia (zirconia stabilised with 7-8wt.% Y_2O_3) which acts as a thermal insulator and is deposited on top of a thin (< 10 μm, more typically 1 μm for EB-PVD) thermally grown oxide (TGO), of α-Al_2O_3. The TGO is formed as a result of thermal oxidation of the bond coat [22], at the ceramic/bond coat interface [23]. The TGO also facilitates the adhesion of the ceramic to the bond coat.

In summary, a TBC system consists of four parts (Figure 11):

1. A metallic substrate, providing structural strength. For example the single crystal alloys CMSX-4.

2. A bond coat, providing oxidation/corrosion resistance and also promotes bonding between the substrate and the ceramic top coat. Examples; diffused aluminides (β-NiAl, Pt-NiAl), diffused platinum γ+γ' structures or MCrAlY overlay coatings (NiCrAlY, NiCoCrAlY).
3. A thermally grown (α-Al_2O_3) oxide, formed between the ceramic top coat and the bond coat due to high temperature oxidation of the bond coat during manufacture and later service.
4. An outer ceramic top coat providing the thermal insulation typically consisting of 8% partially yttria stabilized zirconia (PYSZ). Most recently, new ceramic compositions have been adopted aiming at lowering further the thermal conductivity [24].

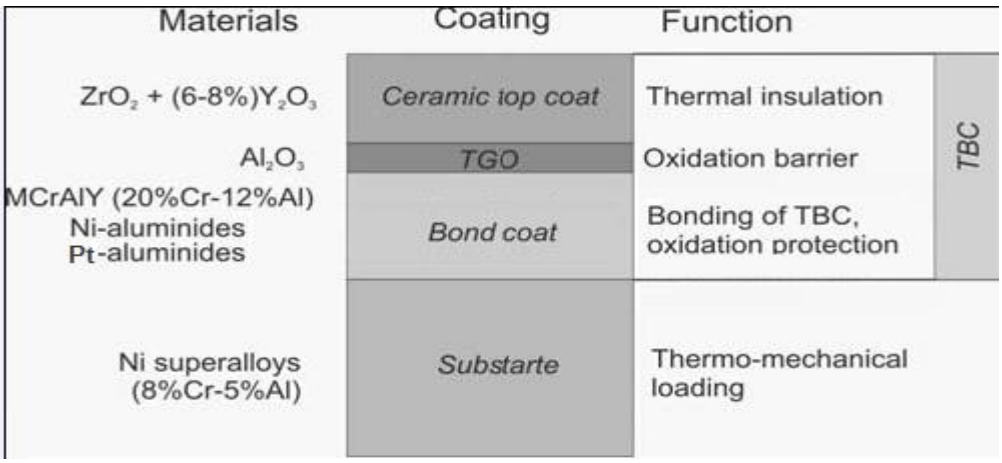

Figure 11: Thermal barrier coating layers and function of individual sub-layers [17].

2.3.1 The Superalloy Substrate:

The TBC is generally deposited onto a temperature capable alloy, commonly a Ni or Co based superalloys. Critical characteristics for a substrate material are: creep resistance, corrosion resilience, high temperature strength, ductility and oxidation resilience. There will be a trade-off between oxidation and corrosion resistance and strength for the selected substrate material, for example, CMSX- 4. However, for the material to be suitable in the manufacturing of a superalloy substrate, castability is an important factor [25].

In order to maximise performance and efficiency of an aero engine, substrate components need to operate in an environment where the gas temperature often exceeds the operational limits of the substrate material. TBC protected superalloy substrates are constantly cooled to safer operating temperature levels by passing relatively cool air (600 - 700^{o}C) through internal cooling passages in order to maintain component integrity at high operating temperatures [26].

Since 1950, Nickel-based superalloys have substantially been developed for use in the hot section of gas turbine engines. Currently, no alternative, commercially available, metallic materials can compete with the high temperature characteristics of Ni superalloys, which offer the desirable properties of high-temperature strength and structural stability, creep resistance, resistance to fatigue and oxidation as well as high stiffness. The beneficial mechanical properties are due to the presence of very stable γ' ordered FCC precipitate (Ni_3Al, Ti) providing a high temperature strengthening mechanism, due to coherent precipitation in the γ'-Ni matrix [27]. Ni-based superalloys generally contain Co, Fe, Cr, Mo and W in solid solution in the γ-(Ni) matrix.

Hence, Nickel-base superalloys strengthening can be defined by two main mechanisms; solid solution strengthening and precipitation hardening. Superalloys develop high temperature strength through solid solution strengthening. Cr and refractory elements, such as W, Mo, Ta are important solid solution hardeners. However, the most important strengthening mechanism is precipitation hardening, through the formation of secondary phase precipitates such as γ' (as formed in CMSX-4) and carbides. The essential precipitation hardeners in nickel based superalloys are Al and/or Ti, with a total concentration typically <10at.%. The result of which is a formation of a two-phase equilibrium microstructure, consisting of γ and γ'. As mentioned above, the γ and γ'-precipitate fraction/size is largely responsible for the

high temperature strength and their incredible resistance to creep deformation. The amount of γ' is a function of the chemical composition and temperature, as can be seen in the Ni-Al-Ti ternary phase in Figure 12 [28]. Cr and Al within the alloy provide oxidation and/or corrosion resistance due to the formation of a protective oxide layer.

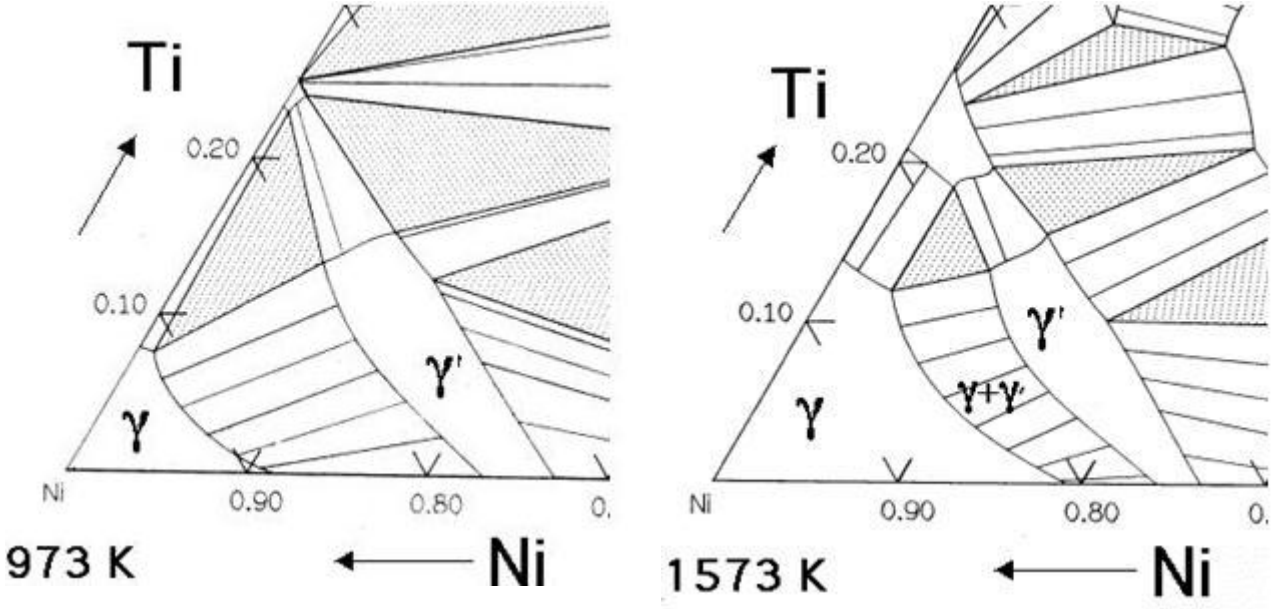

Figure 12: The Ni-Al-Ti ternary phase diagrams show the γ and γ' phase field [28].

2.3.2 Bond Coat and the formation of the TGO

2.3.2.1 Bond Coat

With the recent development of single crystal superalloys used in the manufacture of turbine blades, there has been an increase in the percentages of refractory elements used to enhance high temperature mechanical properties, at the expense of corrosion resistance elements such as aluminium and chromium [29]. This has led to the development of coatings that were primarily designed to protect the components from high temperature oxidation. For the case of TBC systems, those coatings also act as a bond coat to facilitate the adhesion of the ceramic component to the substrate. The primary function of the bond coat is to provide a

medium for the growth of a slow growing, stable oxide layer [30]. Table 3 is an illustration of the most commonly used types of bond coats, mainly aluminides (NiAl and Ni_2Al_3), Pt-aluminide and MCrAlY.

Table 3: Different types of bond coat

Deposition method	**Bond Coat**	**Topology of surface**
EB-PVD (Two phase or single phase)	NiCoCrAlY, NiAl, NiAlPt	Smooth
APS (Overlay, two phase)	NiCrAlY	Rough
Diffusion (Single phase)	Aluminides (NiAl, Ni_2Al_3 and PtNiAl)	Smooth
Electroplating (Two phase or single phase)	NiCrAlYTa, PtNiAl, Pt-diffused	Smooth

Since the ceramic top coat has a high oxygen diffusion rate (oxygen permeability), the bond coat material acts as a source of Al or Cr to form a slow growing TGO, which provides an oxygen diffusion barrier to prevent oxygen from reaching the metallic substrate [31]. The addition of Al or Cr will protect the metallic substrate against high temperature oxidation, by capturing the available oxygen and forming alumina and chromia respectively. Other desirable properties for the bond coat material are; chemical homogeneity, formation of α-Al_2O_3, and if that is not possible then the formation of chromia scale plus adequate creep/yield properties [32]. Ideally, the bond coat material should have a coefficient of thermal expansion between those of the top coat material and the substrate, in order to alleviate the effect of thermal expansion coefficient mismatch [25].

2.3.2.2 Thermally Grown Oxide (TGO)

The thermally grown oxide is formed between the bond coat and the top coat interface due to high temperature oxidation of the bond coat during manufacture and continues to grow in

thickness during exposure at elevated temperatures in service. The growth rate of the TGO and its adherence to the MCrAlY bond coat, platinum aluminide bond coat or platinum-diffused bond coat are crucial determining factors for the durability of a thermal barrier coating [33]. The performance of the TBC system depends on the functionality of the TGO layer. The best TGO layers are of low thickness, are uniform, have a pore free morphology, with low oxygen permeability and good adherence to the bond coat [32]. Rapid and uneven growth of the TGO leads to localised stress concentrations which can nucleate cracks and initiate failure dynamics [21]. The TGO acts as an oxidation barrier to retard the process of oxidation of the bond coat and is most effective in this respect if created mainly of α-Al_2O_3 oxide [25].

2.3.3 Ceramic Top Coat

Yttria stabilised zirconia (partially yttria stabilised zirconia, PYSZ, ZrO_2 7–8 wt.% Y_2O_3; usual thickness within a range of 125-250μm) is commonly used as the top coat for turbine blades because of its low thermal conductivity and high coefficient of thermal expansion [34], as can be seen from Figure 13, which reduces the thermal expansion mismatch between the top coat and the superalloy substrate. The ceramic top coat creates the largest temperature gradient, with a temperature reduction in the region of 150^o C [16]. The most important characteristics for a top coat material are low thermal conductivity (to achieve a higher thermal gradient), high melting point (to minimise structural changes through sintering and inter-diffusion), strain tolerance and high coefficient of thermal expansion, CTE [34]. Ideally, materials for the TBC top coat are desired to have a coefficient of thermal expansion close to that of the substrate. The nickel alloys used for gas turbine blades have a CTE from 14.0 to 16.0 x 10^{-6} K^{-1}. YSZ has a CTE of 9.0 x 10^{-6} K^{-1} [16]. The graph in Figure 13 shows thermal conductivity and coefficient of thermal expansion of various materials. As illustrated in

Figure 13, zirconia and nickel alloys have CTE fairly close to each other but with thermal conductivities that differ by an order of magnitude, ideal for a thermal barrier coating system.

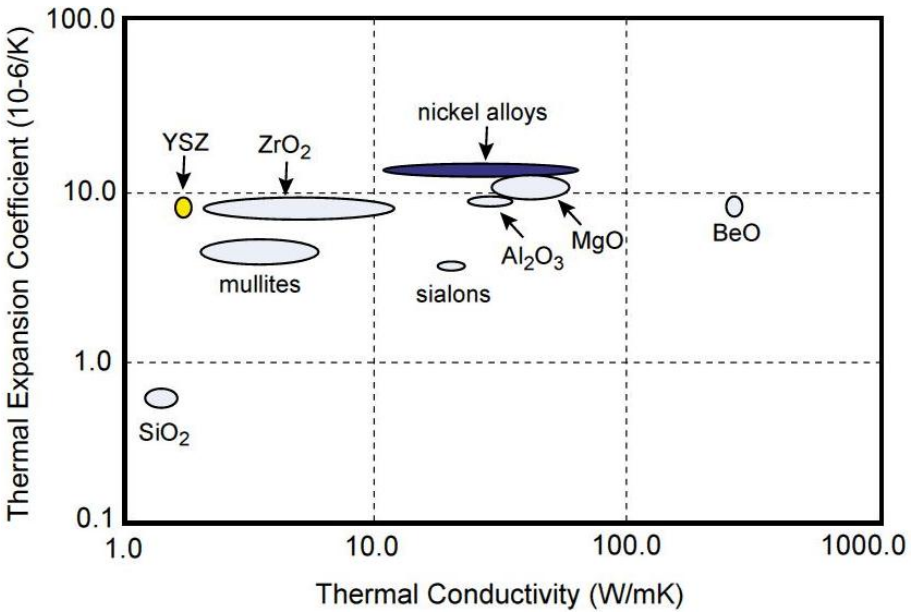

Figure 13: Plot of Thermal Conductivity vs. Thermal Expansion Coefficient [16].

2.4 Phase Diagram and Phase Stability

Phase stability is also an important characteristic for a TBC top coat. Zirconia exists as three allotropes that are stable at different temperatures. Pure zirconia will undergo a 3-5% volume change and phase transform upon cooling from the tetragonal (t) phase to a monoclinic (m) phase. At temperature below 1170 °C (the transformation temperature), zirconia is stable in its monoclinic phase (m); above 1170 °C but below 2370 °C as the tetragonal phase (t) and is stable in its cubic phase form above 2370 °C. The Y_2O_3 partially stabilised (6-8wt.%) solid solution will prevent the detrimental effect of the transformation to the low-temperature monoclinic structure of ZrO_2, with its associated volume change, by stabilising the high-temperature tetragonal crystal structure at all temperature of interest (known as t') [35]. Should this tetragonal to monoclinic transformation occur, it would result in a change in

volume and introduces as high as a 10% increase in shear stress which can cause the coating to fail by spallation.

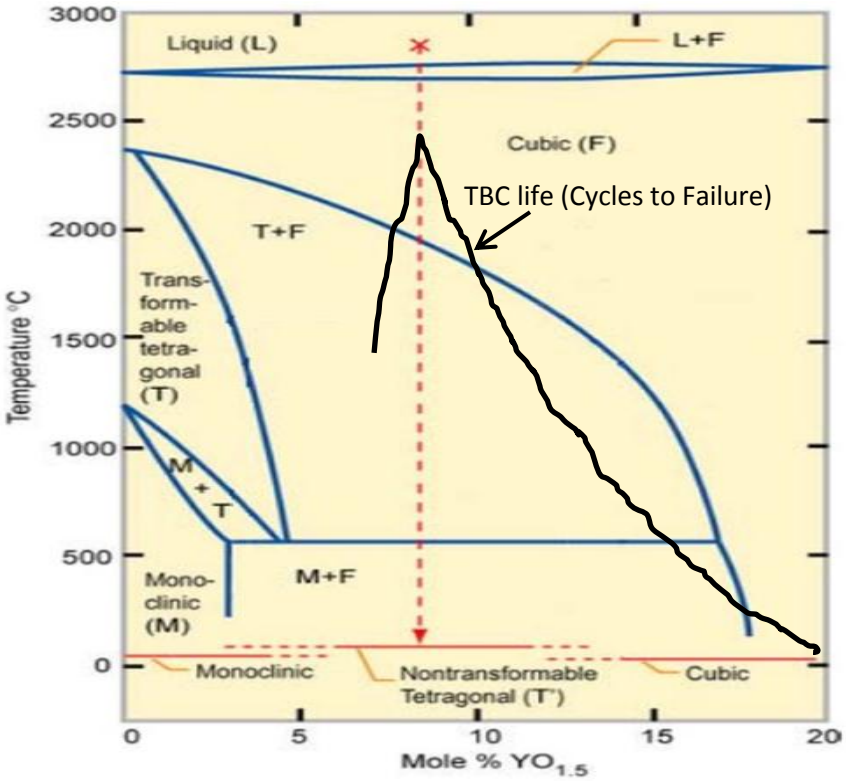

Figure 14: Yttria - Zirconia phase diagram. TBC spallation life in a furnace thermal cycle test as a function of Y_2O_3 content is superimposed. [36]

Figure 14 shows an equilibrium phase diagram of an YSZ TBC system. The TBC microstructure will affect how the top layer of the TBC performs. As noted earlier, the yttria composition of the TBC has a stabilising effect upon the ZrO_2.This is reflected in the YSZ equilibrium phase diagram above, and properties such as the coefficient of thermal expansion and the thermal conductivity will be affected by the yttria content. From Figure 14, it can be concluded that;

- Cooling to room temperature under equilibrium conditions, partially stabilised Zirconia (i.e. composition of 3 to 18 mol% $YO_{1.5}$) results in monoclinic + cubic (M + F) phase transformation, while
- Cooling a fully stabilised zirconia (i.e. compositions >18 mol% $YO_{1.5}$) results in only the cubic (F) phase, at room temperature, and
- For compositions of 6 to 12 mol% of the total stabiliser additions to ZrO_2 (irrespective of the type of stabiliser), TBC life has a maximum value. Figure 14 indicates that this region is predominantly where the formation of the metastable tetragonal (t') phase occurs upon cooling.
- The metastable tetragonal ZrO_2 (t') phase helps prevent the disruptive transformation to equilibrium phases of monoclinic and cubic ZrO_2 during thermal cycling [37].

TBC literature supports the view that, superior performance of YSZ TBC for advanced gas turbine applications is achieved at a Y_2O_3 content of between 6 and 8%wt. corresponding to 7.6 to 8.7mol% $YO_{1.5}$ [38], part of this data is shown in Figure 15.

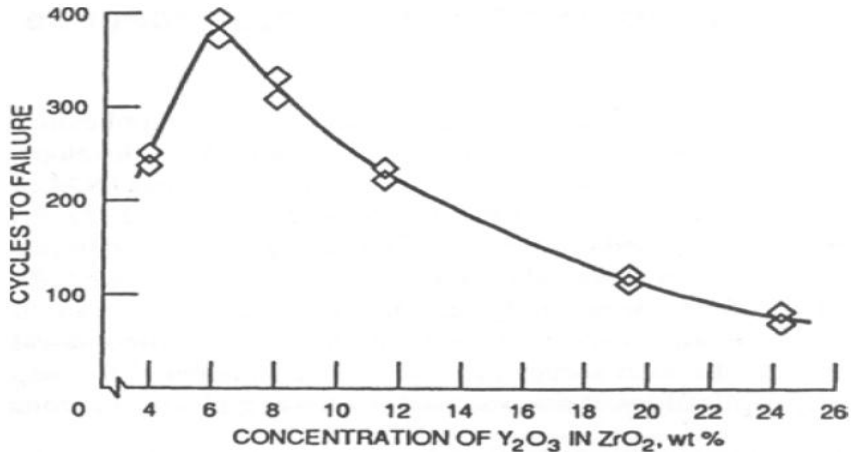

Figure 15: Effect of Y_2O_3 content on the performance of ZrO_2 - base plasma spray thermal barrier coatings. The graph shows that the optimum cycles to failure of YSZ TBC occur at composition of 6-8%wt. Y_2O_3 [38].

Table 4: Summary of some important characteristics necessary for a TBC top coat material [39]

Property	Requirement	Rational
Melting point	High	Operating environment at high temperature
Thermal Conductivity	Low	*ΔT is inversely proportional to k
Thermal expansion coeff.	High	Close to that of the substrate
Phase	Stable	Phase change is structurally detrimental
Oxidation resistance	High	Operation environment is highly oxidizing
Corrosion Resistance	Good	Operation environment may be corrosive
Strain tolerance	High	Operation environment imposes large strain ranges

* The total temperature reduction (ΔT) is inversely proportional to the thermal conductivity (k) of the material, and given by [40];

$$\Delta T = \left(\frac{1}{kA}\right)\left(\frac{dQ}{dt}\right)\Delta x \qquad \text{Equation 1}$$

Where k is thermal conductivity, ΔT is the temperature reduction, Δx is the coating thickness and dQ/dt is a heat flux through cross section A. In order to achieve the greatest ΔT, k has to be low and the thickness of the coating should be increased. However, weight is a limiting factor and increasing the coating thickness will increase the overall weight of the component.

2.5 TBC Pore Morphology and Deposition Techniques

The thermal and mechanical properties of a TBC system are related to the morphology of the porosity which is present within the ceramic layer of the TBC. Differences in pore morphology depend upon the method of deposition (which includes plasma spraying, electron beam physical vapour deposition and more recently plasma spray physical vapour deposition). The bond coat is typically deposited by means of either vacuum plasma spray

(VPS), air plasma spraying (APS), high-velocity oxy-fuel (HVOF), or chemical vapour deposition (CVD) processes [41] but can also be formed by electroplating processes [42], whereas the two most important methods used for TBC top-coat deposition are APS deposition and electron-beam physical-vapour deposition (EB-PVD), [43]. These two methods have different characteristics and microstructures, which are further discussed below.

2.5.1 Electron Beam Physical Vapour Deposition (EB-PVD) Process

EB-PVD is a physical vapour deposition process performed under vacuum conditions, in which the ceramic source to be deposited, is heated to a high temperature, resulting in a high material vapour pressure using a high energy (focused) electron beam, to create the vapour cloud. The vapour cloud consists of atoms, molecules, ions, and clusters of atoms vapourised from a source ingot. The substrate to be coated is rotated in the vapour, which deposits on the substrate to form the coating (Figure 16).

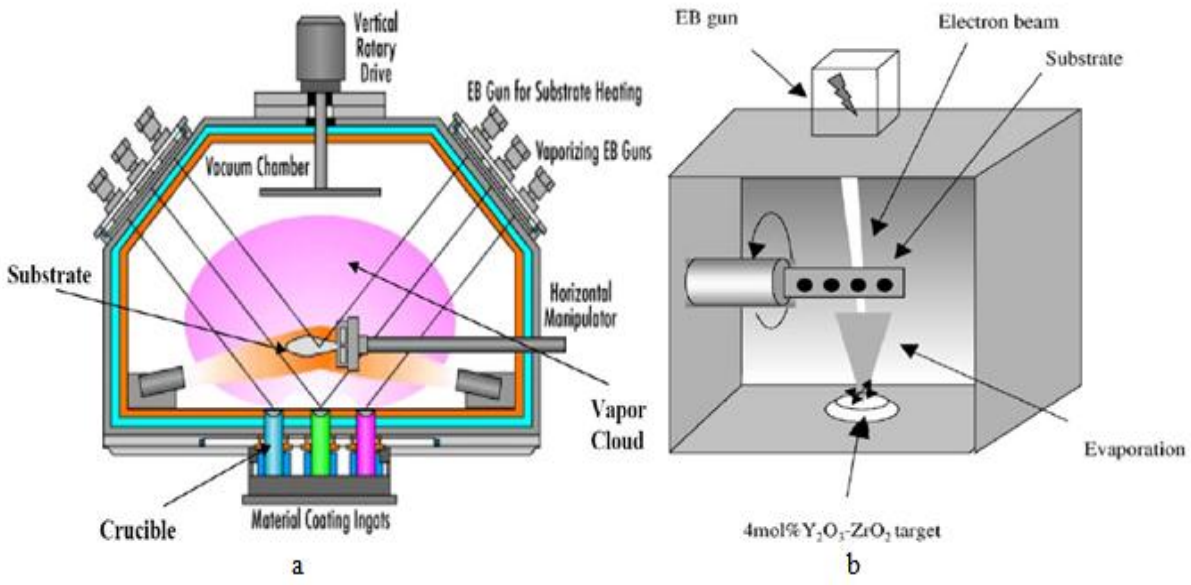

Figure 16: Schematic of the EB-PVD coating chamber [44], [45]

2.5.1.1 Advantages of EB-PVD process

The EB-PVD process offers extensive advantages for controlling variations in the structure and morphology of the deposited materials. The EB-PVD process offers many desirable characteristics: it has a relatively high deposition rate (between 4-10 µm/min with an evaporation rate of approximately 10-15Kg/hour) but is somewhat slower than the APS process. EB-PVD processes also produce relatively dense coatings (73 - 77%, although not as dense as APS process, 85 – 90% dense), coatings with controlled composition and microstructure, low contamination and high thermal efficiency [44], [45]. The surface finish of the EB-PVD coatings is much smoother than for PS coatings, with typical roughness of 0.5-1 µm Ra. The columnar microstructure of the EB-PVD system (Figure 17) reduces the elastic modulus in the plane of the coating.

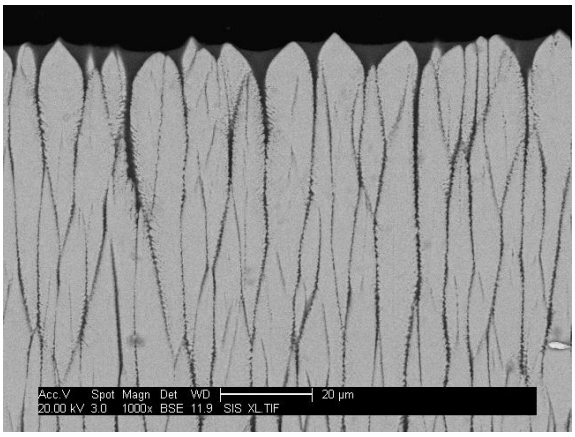

Figure 17: Micrograph of an electron beam physical vapour deposited TBC.

Coatings produced by the EB-PVD process usually have a good surface finish and a uniform microstructure. The microstructure and composition of the coating can be easily altered by manipulating the process parameters such as electron gun current power, powder particle size, ingot feed rate and ingot compositions. Coating thickness can also be altered, the typical

thickness of an EB-PVD coating is about 150 – 200 µm. Properties and performance of the coating is highly dependent upon the coating microstructure and thickness [25; 44].

2.5.2 Plasma Spray Process

The plasma spray coating process is a thermal deposition method in which the material to be deposited is heated to a semi molten state by an electrical heat source. This high temperature partially ionised gas stream propels the molten particles towards the substrate. Plasma spray process can be performed in an open atmosphere (air) or in a vacuum (or low pressure environment known as vacuum or low pressure plasma spray) [46]. Figure 18 illustrates this process, where a stream of inert gas (argon and/or nitrogen) carrying the coating material in powder form flows through a cylindrical nozzle into the plasma jet, here it is heated and propelled towards the surface of the substrate.

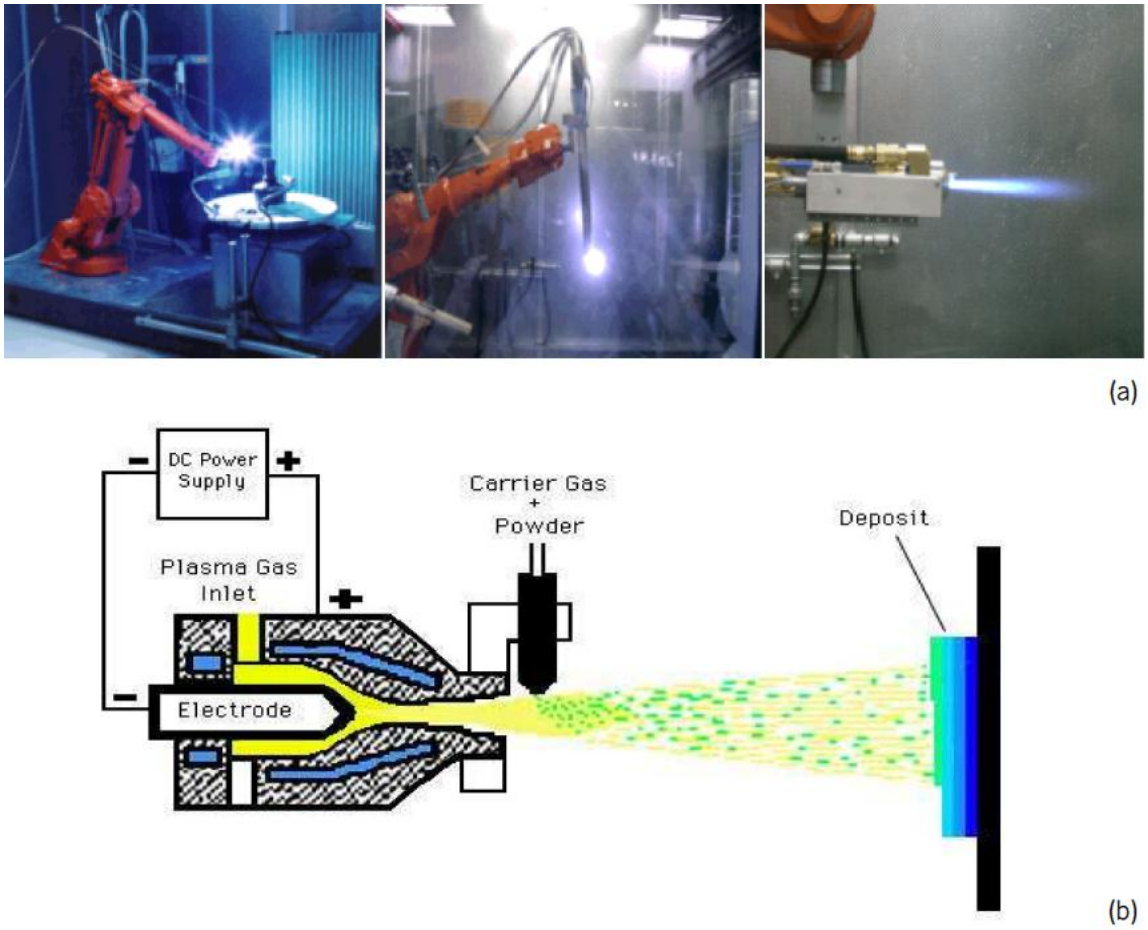

Figure 18: (a) Photographs of plasma-spraying equipment and deposition process, (b) schematic of the APS process [3]

APS coating characteristics are influenced by process parameters such as spraying velocity, powder size and position of the injected particulates in the plasma. Spraying velocity and the position of the injecting particles in the plasma are critical characteristics because they determine the physical state of the particles when they reach the surface of the substrate.

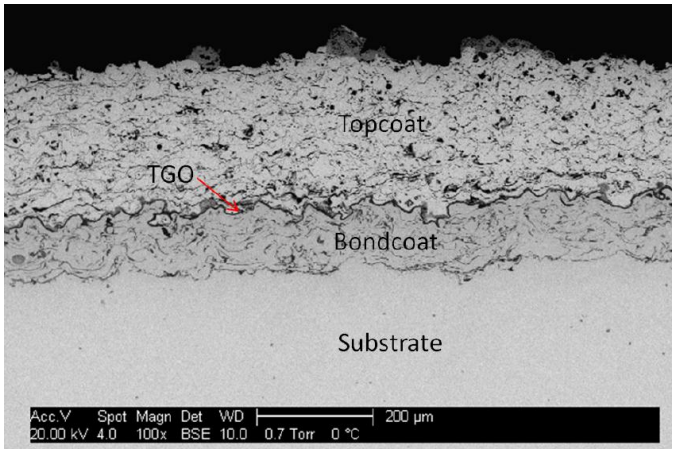

Figure 19: Topology of APS YSZ coating

The APS structure is laminar and consists of a rough (4-10 µm Ra) coating denser than EB-PVD structures (10-15% porosity [16]), coarse, disc-like microstructure with cracks parallel to the surface structure, as illustrated in Figure 19. Figure 20 schematically illustrates the difference in microstructure between plasma sprayed and EB-PVD coatings [17]. For comparison, the EB-PVD method gives rise to a columnar grain structure, which is much better under conditions of cyclic thermal gradient and will prevent the build-up of tensile stresses due to differences between the coefficient of thermal expansion of the TBC and the substrate [47].

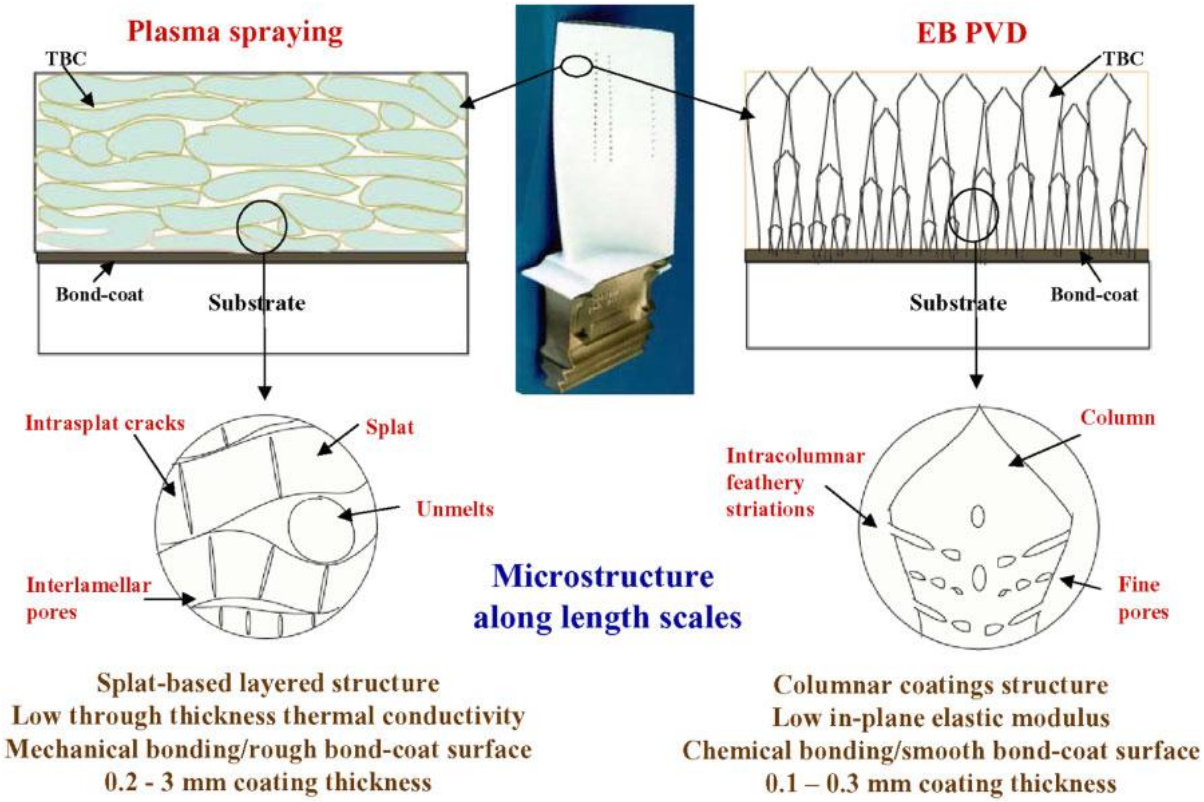

Figure 20: Pore structure morphology of EB-PVD and APS TBC [17] (adapted from [48]).

Optimisation of the TBC pore morphologies improves the overall TBC system performance, by reducing the thermal conductivity of the system while retaining a high in-plane strain tolerance. Lower thermal conductivity in the region of the TGO/bond coat interface reduces the coefficient of thermal expansion (CTE) mismatch strain in the TGO layer, retard the TGO growth rate and slow impurity diffusion within the bond coat. Subsequently, TBC materials with lower thermal conductivity might allow the design of TBC system with reduced thickness, thereby reducing the significant centrifugal load that the system imposes on the rotating turbine engine components.

The columnar microstructures of EB-PVD TBCs have finer distribution of intracolumnar and elongated intercolumnar pores. The intercolumnar pores predominantly become aligned perpendicular to the plane of the coating as its thickness increases [49][16]. The large, through thickness intercolumnar pores are less effective at reducing through thickness heat transfer of the coating, meanwhile the fine intracolumnar pores contribute a moderate reduction in the thermal conductivity as they are generally inclined to the heat flow. However, EB-PVD coatings have considerably higher thermal conductivity than their APS counterparts [49]. Figure 21 and Figure 22 indicate that TBC thermal conductivity is strongly affected by the morphology of the porosity in the coating, therefore the coating deposition route greatly alters thermal conductivity.

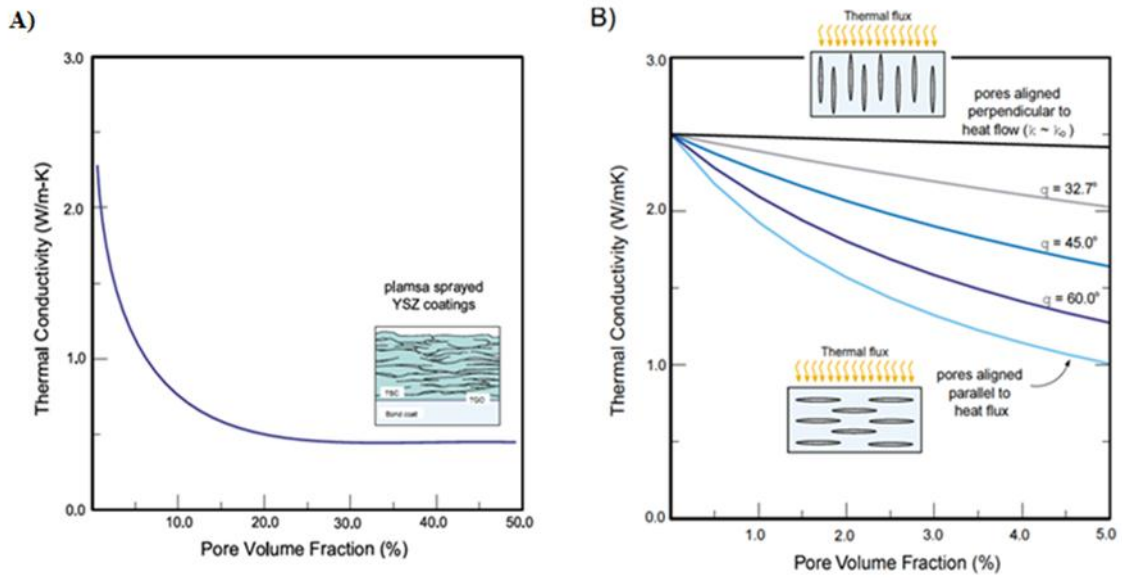

Figure 21: The effect of pore volume fraction and morphology on the thermal conductivity of a given material. In a) the experimentally determined thermal conductivity reduction is shown for plasma sprayed coatings having an increasing amount of porosity. In b) the calculated reduction in the thermal conductivity is shown for a material in which elongated cracks with different orientations to the heat flux have been introduced [50].

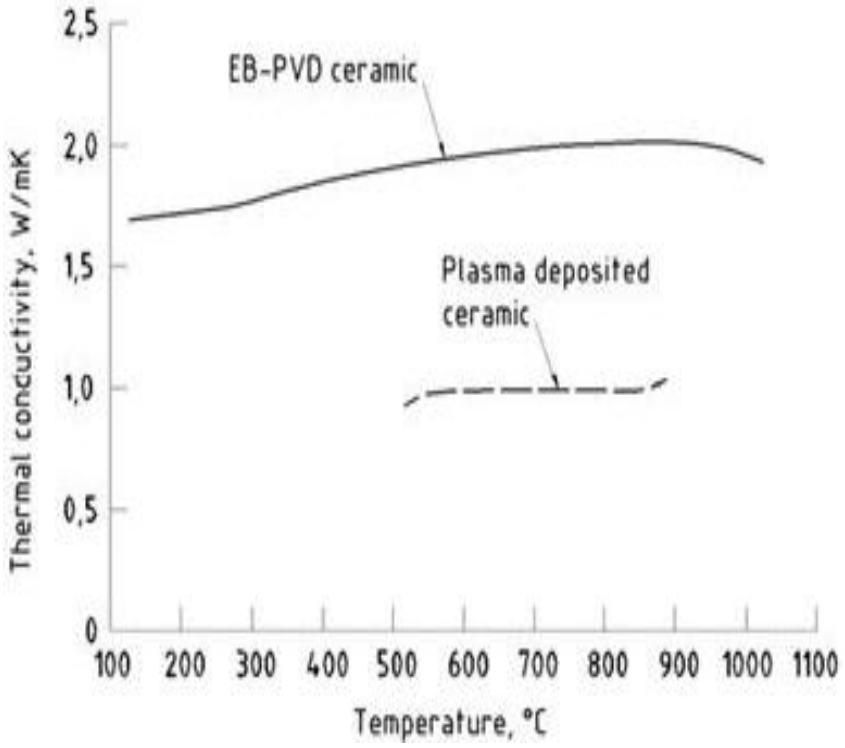

Figure 22: The effect of deposition technique on the thermal conductivity of EP-PVD and PS deposited TBC.

The choice of deposition technique is largely determined by the application of the coating, desired coating characteristics, cost, production rate, temperature limitation of the substrate, uniformity and consistency of the process, and its compatibility with subsequent processing steps. Chemical and physical conditions during the deposition process can strongly affect the resultant microstructure of the coating (i.e., single crystal, polycrystalline, amorphous, epitaxial, single or two-phase) [44].

Thermal barrier coating systems are used to improve the life of components operating under severe conditions including corrosion, oxidation and erosion. Whether applied by EB-PVD or APS methods, the process yields distinct characteristics that differ between the methods used (Table 5). For example, EB-PVD TBCs have higher thermal conductivity even though it's only ~75% dense and consisting of micro-pores and nano-pores. The thermal insulation

mechanism of APS TBCs is similar to that of multilayer TBCs, with the in-plain cracks and micro-cracks acting like insulation barriers thereby lowering the thermal conductivity [18].

Table 5: Properties of TBCs produced by plasma spray and EB-PVD processes [51]

Properties/Characteristics	**EB-PVD**	**Plasma Sprayed**
Thermal Conductivity (W/mK)	1.5-1.9	0.8-1.1
Surface Roughness (µm) Ra	1.0	10.0
Adhesive Strength (MPa)	400	20-40
Young's Modulus (GPa)	90	200
Erosion Rate (Normalised to PVD)	1	7
Microstructure	Columnar	Laminar

In order for a TBC system to be used in turbine applications, a combination of low thermal conductivity, spallation resistance, erosion resistance, phase stability and pore morphology stability characteristics are needed [16]. Low thermal conductivity and spallation resistance are the two most critical characteristics in terms of TBC systems application to aircraft engine performance. Thermal conductivity is partly dependent on the volume fraction and morphology of the porosity within the top coat and also on the gross topcoat microstructure, while spall resistance is a function of the mechanical and thermal expansion properties of all three layers [16].

2.6 Failure Mechanisms of Thermal Barrier Coatings

The atomic scale structure of ceramic materials determines its properties (such as hardness, brittleness, refractory nature, electrical insulator) and may lead to problems within the overall TBC structure due to this refractory behaviour necessary to achieve the requirements for a TBC system to reduce the temperature of the base metal and provide some resistant to corrosion attack (oxidation, hot corrosion) for the components on which it is applied. A thermal barrier coating system is required to have a low thermal conductivity and high chemical and thermodynamical stability at higher temperature. This is limiting in terms of the number of potential materials available; mainly limited to a section of oxide materials.

Ceramic bonds are covalent, ionic or mixed (both covalent and ionic). The covalent bonds involve sharing of electrons whereas the ionic character is given by the difference of electronegativity between the cations (+) and anions (-). The low thermal expansion coefficient of ceramics will introduce a mismatch of CTE between the ceramic coating and the metallic substrate [20]. This drives TBC failure which may occur at the bond coat and TGO interface, and sometimes at the TGO/ceramic interface, but normally the former.

Failure modes of thermal barrier coatings can be classified into two categories: Thermal cycle dependent failure governed by strain misfits also termed ‘intrinsic failure’ by Evans et al. [52], or ‘extrinsic failures’ which are dependent on external factors [52]. Extrinsic failures can be caused by a number of external factors such as dust particle ingestion, leading to erosion or in the hot gas paths to the formation of deposits that may melt and infiltrate the TBC [18]. Evans et al. [52] proposed a schematic of various degradation mechanisms as shown in Figure 23. The various mechanisms associated with thermal barrier coating failure are described in this section.

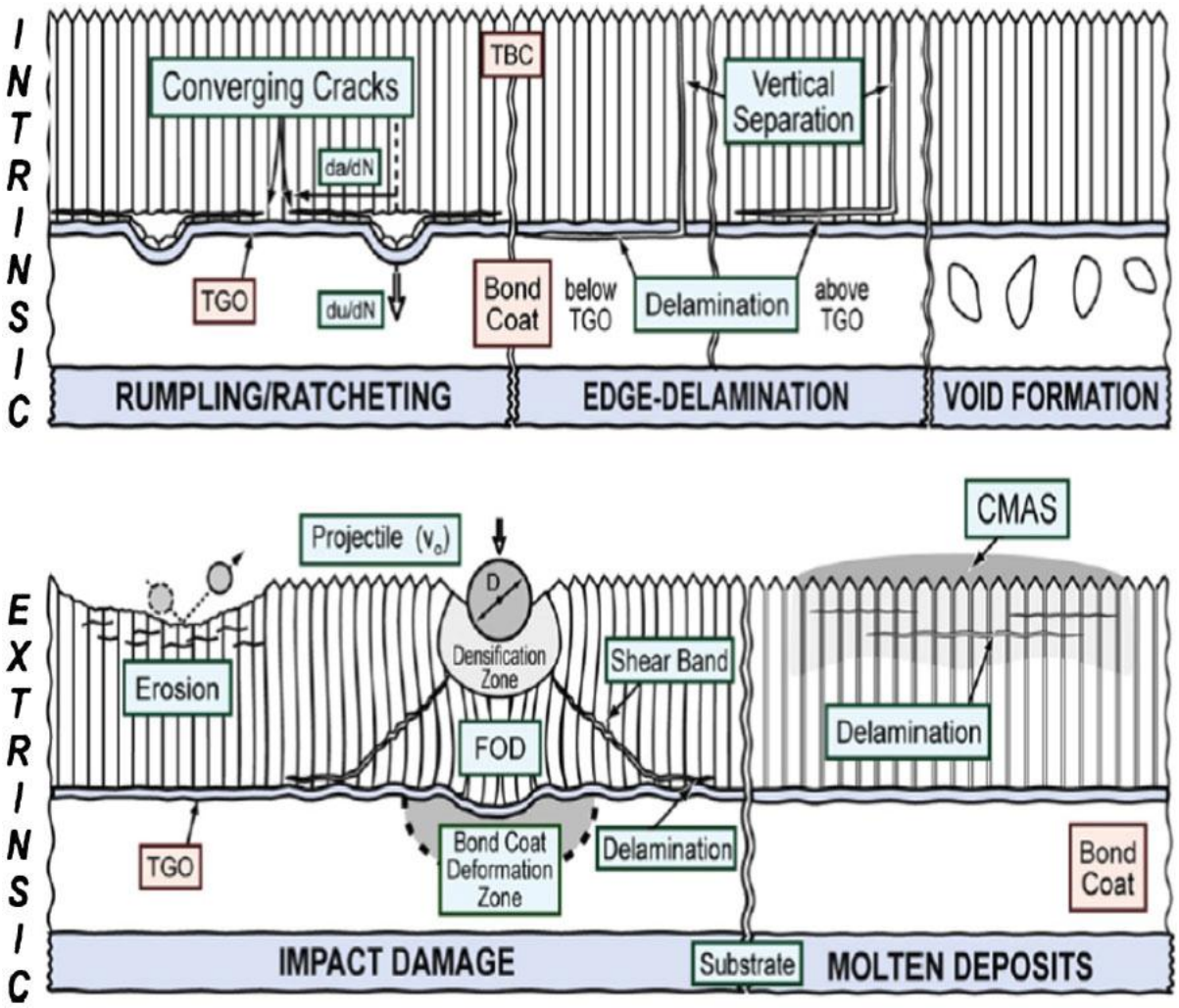

Figure 23: A schematic of the degradation model proposed by Evans et al. [52]

- Thermal fatigue and Temperature dependent cyclic failure
- Creep of bond coat
- Sintering and associated shrinkage
- Erosion damage and Foreign body impact
- Molten deposits (CMAS and volcanic ash) infiltration and phase transformation

2.6.1 Thermal Fatigue and Temperature Dependent Cyclic Failure

Engine thermal cycles (temperature, dwell time, rates of excursions, gradients and cycling frequency) play a significant part in TBC failures. Between the substrate and the top layer of

a TBC system is a metallic bond coat, MCrAlY or platinum aluminide (PtNiAl), for the purpose of providing oxidation resistance. Bond coat oxidation results in the formation and growth of the TGO that induces stresses and displacements at the TBC/TGO/bond coat interfaces eventually leading to TBC spallation [18]. Bond coat oxidation is one of the primary causes of TBC failure [53; 54]. The failure mechanisms of EB-PVD and APS thermal barrier coatings differ somewhat, with EB-PVD TBC occurring by spallation of the thermally grown oxide or in some cases by crack formation in the TGO whereas oxidation failure of an APS will normally occur within the TBC in the vicinity of the TGO, a factor which is linked to thermal mismatch between TBC and substrate [55]. TGO thickness grows over time during engine operation, resulting in a volume expansion and in-plane compressive 'growth' stresses. Upon cooling to ambient temperature, the system develops very high 'thermal' compressive residual stresses in the TGO, owing to a mismatch in the coefficient of thermal expansion with the substrate, reaching about 3–6 GPa [18].

During thermal cycling, the TGO seeks to relax stresses, by means of releasing strain energy (out of plane displacements), preferentially into the bond coat since above the brittle-to-ductile transition temperature, the bond coat is able to creep, behaving superplastically at higher temperatures [20]. Progressive roughening of the bond coat/TGO/top coat interfaces occurs during repeated thermal cycling due to the formation of undulations ('ratcheting', 'rumpling' or 'bucking') within the bond coat surface, as shown in Figure 24. Once the stored energies at the interfaces exceed a threshold value, cracks and spallation can occur. Initial surface imperfections, including rough bond coat surfaces, are considered to be contributory factors to the level of residual stresses and crack initiation.

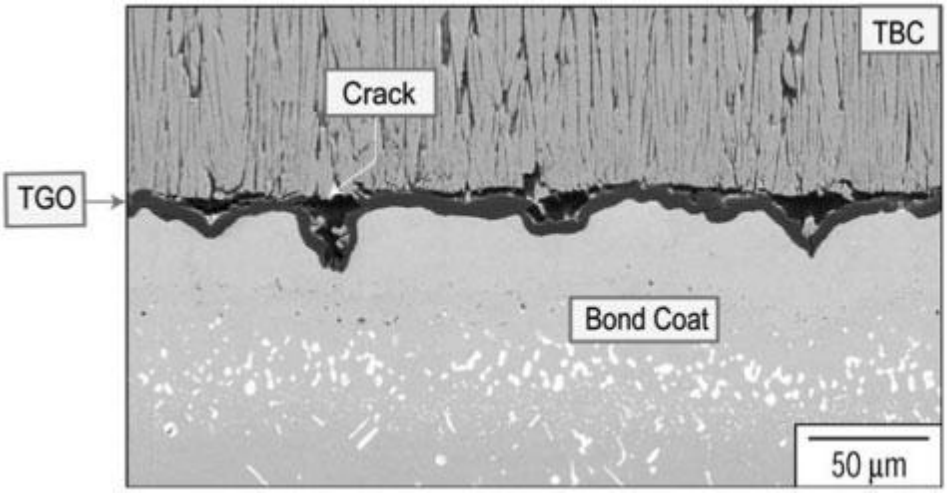

Figure 24: TGO undulations in a thermally cycled TBC (YSZ top coat and NiAlPt bond coat) [18]

Interdiffusion between the bond coat and the substrate along with growth of the TGO results in the depletion of Al in the bond coat. The Al depletion region may promote the formation of other oxides that accelerate localised oxidation by providing fast oxygen diffusion paths, such as Ni containing spinel. Loss of Al by interdiffusion between the bond coat and the substrate, and by bond coat oxidation also leads to phase transformations from β to γ' and/or a martensitic transformation (for a β NiAlPt bond coat) [18]. Several of the concurrent mechanisms of thermal fatigue and temperature dependent failure during engine service are schematically depicted in Figure 25 (adapted from Clarke and Levi [52]).

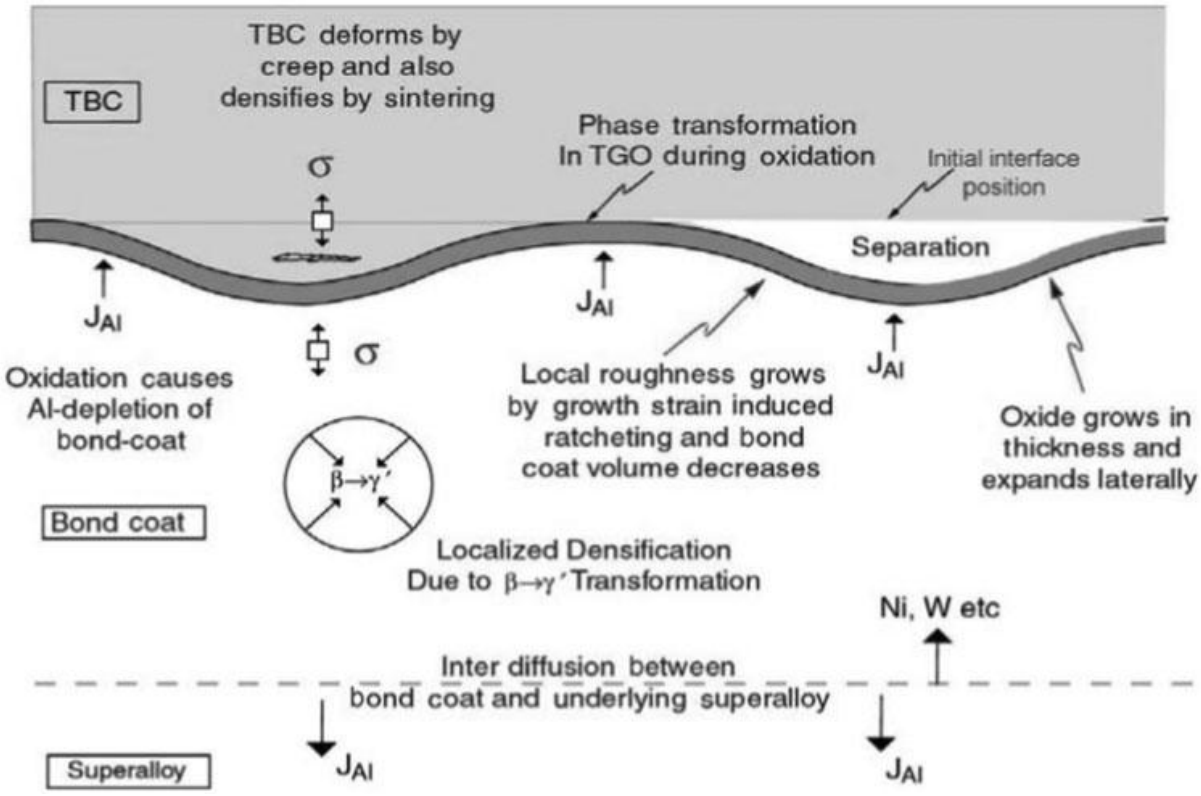

Figure 25: Schematic summary of several of the concurrent mechanisms occurring in the bond coat, TGO and TBC during use at high temperatures [56] (adapted from Clarke and Levi [52]).

During the early days of TBC application, TGO thickness of ~6 microns was considered in industry to be maximum allowable thickness to avoid TBC spallation. Thermally grown oxide thickness up to 17 microns has been observed before failure for the β-NiAl bond coat by Darolia et al. [57; 58] at GE Aviation. The concept of critical TGO thickness is definitely not a very useful guide since the critical TGO thickness strongly depends on bond coat composition, impurities, microstructure and thermal cycling history.

2.6.2 Conclusions Aimed at Optimising TGO Life

The above scenario suggests the following guidelines for longer TBC life:

i. Slow growing TGO: Unfortunately this attribute cannot be independently controlled. Thermally grown oxide formation and growth depends on the bond coat composition.

ii. Create and maintain a strong adhesion between the TGO and bond coat and TGO and top coat: It is universally agreed that impurities such as S diffuse to the TGO/bond coat interface and weaken it. Also, rapid conversion to α-Al_2O_3 and minimisation of other faster growing oxides (e.g. spinels) is essential.

iii. Minimise strain mismatch between the bond coat and the substrate.

iv. Higher yield strength and creep resistant bond coat to avoid rumpling.

v. Minimal surface imperfections, meaning flat and smooth surfaces.

vi. Bond coat compositions with slow growing TGO which can tolerate thicker TGOs.

2.6.3 Creep of Bond Coat

Creep is a time-dependent deformation under stresses much lower than the material's yield stress. Creep deformation is material sensitive and the temperature range over which it occurs differ in various materials. Creep tends to occur at a significant rate at temperatures in excess of 0.4 Tm [59]. Creep occurs under the principle that, when a material is loaded with a constant load, it will stretch elastically as well as gradual plastic deformation which consequently may lead to rupture. Thus, at high temperatures creep often governs the stability of materials.

Creep of the bond coat is a critical factor in the failure of TBCs and is usually active above 0.6 Tm in °K. Thermal activation of these deformation processes during typical service conditions of TBCs occur above 0.6 Tm (°K) of the bond coat materials commonly used. Two overlay bond coat materials used in current state-of-the-art TBCs are CoNiCrAlY and NiCrAlY alloys and their creep strain rates have been measured experimentally by Thompson et al [60; 61]. Thompson et al found that, the steady state creep rates is related to the stress by an empirical power law, with stress exponents of ~ 2.9 and ~ 4.5 respectively for the two coating systems. The relationship between creep rate and the residual stress states of the

aforementioned bond coats was predicted using a numerical model. At temperatures above 700 °C, stresses in the bond coat relax over time due to creep.

On cooling down to room temperature, especially at high cooling rates, stresses regenerate due to differential thermal contraction and stress levels in the bond coat might be enhanced. The reason for this being that at high cooling rates, typical of those experienced by TBCs under service conditions, a limited degree of creep relaxation can take place. The level of the enhanced stresses will depend on factors such as the relative values of expansivity, creep parameters and modulus of the bond coats. Depending on the amount of stress, it is likely to enhance the initiation of microcracks and debonding of the TBC hence leading to spallation [62].

2.6.4 Sintering and Associated Shrinkage

Another temperature dependent TBC failure mechanism is associated with the sintering and densification of the porous structure of the ceramic top coat, resulting in increased thermal conductivity and decreased stain tolerance. Sintering occurs when the ceramic top coat of a thermal barrier coating is at a sufficiently high temperature. Sintering increases the thermal conductivity of the system and also induces in-plane tensile stresses because of the constraint of the substrate, leading to shrinkage at the surface of the top coat and consequently causing the TBC to fail [18].

The columnar microstructure of the EB-PVD TBC disappears after sintering has occurred. This leads to an increase in Young's Modulus, resulting to the coating losing its strain tolerance and increases top-coat stresses [25]; [63]. Molten deposits that infiltrate the TBC also lead to increases in the in-plane Young's Modulus by 10 fold (from ~ 20 GPa to ~ 200 GPa) [18], because upon cooling, the molten deposit solidifies and stiffening of the TBC

structure occurs leading to spallation of the TBC. The variation in the stress distribution also changes the strain energy release rate and failure mechanisms. Phase destabilisation (metastable t' to monoclinic phase) is not currently a TBC life limiting factor since TBC operating temperatures are below the threshold of this transformation, though, it is becoming an issue for future aircraft engines and power generation turbines that run for extended periods of time (e.g. 20 000+ h) [18].

2.6.5 Molten Deposits Infiltration

Under certain turbine operating conditions (such as in coastal or Middle East regions), siliceous materials such as airborne dust, sand, fly ash, volcanic dust, concrete dust and fuel residue ingested into the engine accumulate on certain hotter surfaces, generally on the concave side of the blade, and melt when sufficiently hot (temperatures above 1240 °C, depending on the composition of the deposit). Partially yttria stabilised zirconia ceramics (e.g. YSZ) are currently the coating material of choice for four main areas within gas turbine engines: as a combustor tiles, HP turbine blades and nozzle guide vanes, as well as abradable seals for turbine blade tip-path clearance [64]. Molten deposits, such as CMAS, are known to affect the lifetime of components in a gas turbine engine. CMAS is the general name given to these deposits, as the predominant oxides are that of Calcia (**C**aO), Magnesia (**M**gO), Alumina (**A**l_2O_3) and Silica (**S**iO_2). However, the composition of CMAS (Calcia-Magnesia-Alumino-Silicates) varies from region to region across the world, be it run way debris, sand or volcanic eruption. Depending on the operating environment, oxides of other elements such as iron, nickel, titanium and chromium may also be present in smaller amounts.

Stott et al. [65] noted that sand chemistry throughout the Middle East varied leading to differences in melting temperature of any deposits formed. The composition and properties of molten deposits found in an aircraft engine can greatly affect the severity of damage caused

[65]; [13]. In the turbine section of a gas turbine engine, the TBC surface temperature may be above the melting temperature of CMAS. If so, the CMAS will melt and because CMAS has excellent wetting properties, it infiltrates the outer layer right down to where TBC temperature equals melting temperature of the CMAS [66]. Figure 26 provides a schematic of this mechanism, which then solidifies to form a glassy deposit, causing loss of porosity, loss of the columnar structure and a subsequent loss of strain tolerance of the TBC. Due to this slag infiltration and solidification, the coating becomes stiffer with a subsequent increase in thermal conductivity and a detrimental effect in its insulating capacity. This results in a thermal expansion mismatch between the CMAS and TBC, introducing cracks and compressive stresses into the system upon cooling to ambient temperature, which are obvious to see, resulting in spallation and loss of thermal protection to the superalloy and subsequent failure [67].

2.6.6 Previous Studies of CMAS Attack

Over recent years, due to the drive for higher efficiency engines and hence increased turbine entry temperatures, CMAS attack of TBCs has become an increasing concern [9; 11; 13; 34; 68] as engine hardware temperatures start to exceed 1300 °C [12; 12; 69]. CMAS related TBC failure of engine hardware was first observed in the early 1980's, especially in aircraft engines that were operating near volcanic ash clouds or from siliceous material ingested with the air intake (sand, dust, cement and runway debris). Further examination confirmed this failure to be linked with a glassy deposit, mostly containing CaO, MgO, Al_2O_3 and SiO_2 (CMAS). Borom et al. [70] studied the molten deposits obtained from an aircraft engine that have been operating in sand laden environment and found CaO, MgO, Al_2O_3 and SiO_2 to be the main oxides of these deposits, with appreciable amounts of impurities such as V, S, P, Ni and Fe oxides as well as components of the TBC [71]. The same oxide constituent of the

deposit was found from aircraft engines that have been operating in the USA, Middle East and Far East, although in different amounts. This is an indication that the chemistry of the deposits is very similar irrespective of geographical location or time of service.

The incipient melting point of "standard CMAS" used throughout this study was determined to be ~1235 °C. Other CMAS compositions from the open literature are listed in Table 6. Smialek et al. [72] analysed an aircraft engine with CMAS deposits, while Aygun et al. [73] analysed sand from Iraq. Although there are slight variations, the compositions are very similar and the onset of melting is well within the engine operating temperature range. In studies involving 7YSZ TBCs exposed to "standard CMAS", an interaction zone was observed, where the zirconia was depleted in yttria, instigating a phase transformation from tetragonal to monoclinic and was floating in the CMAS melt [74].

Table 6: Variation in CMAS compositions used by previous authors.

Elements (mol.%)	**Wellman et al. (2010)** [13]	**Aygun et al. (2007)** [73]	**Borom et al. (1996)** [70]	**Kramer et al. (2006)** [11]	**Smialek et al. (1994)** [72]	**Rai et al. (2010)** [12]	**Wolfgang Braue (2009)** [75]
CaO	35	38	32.1	33	20.9	32.7	33.6
MgO	10	5	10	9	9.5	9.4	9.9
Al_2O_3	7	4	6.9	6.5	7.5	6.8	10.1
SiO_2	48	50	46	45	49.8	46.2	22.4
TiO_2	-	-	-	-	1.8	-	-
Fe_2O_3	-	1	3.2	-	4.7	3.2	-
NiO	-	-	1.6	-	4.2	1.7	-
Na_2O	-	1	-	-	1.5	-	
K_2O	-	1	-	-	-	-	-

Research by Kramer et al. [11] reported that the speed at which CMAS infiltrates the TBC is quick and found full impregnation of the EB-PVD TBC within four hours at 1240 °C. This result showed that CMAS easily wets TBC at temperatures above the CMAS melting point ($T_m{}^{CMAS}$) and that the reaction was very quick. Therefore, at temperatures above and/or in

the CMAS melting range ($T_{tbc} \geq T_m^{CMAS}$), CMAS wetting and penetration can be expected in a short amount of time. Further work by Levi et al. [52] confirmed that CMAS wetting of TBC can start within seconds at 1300 °C. Whitman et al. [13] also observed severe damage in TBC with small amount of CMAS within 4 hours at 1300 °C.

The mechanism of CMAS degradation has been extensively studied by Levi et al. [10; 11; 22; 52; 56; 68; 71; 76; 77]. Firstly, molten CMAS is said to have an excellent wetting characteristic and a low viscosity, which enables rapid infiltration into the TBC inter-columnar gaps, cracks and porous structures, and upon cooling, the melt freezes and the CMAS infiltrated TBC becomes stiff, losing its strain tolerance. Delamination cracks can therefore develop in the coating leading to TBC spallation during in-service thermal cycling [66]. An illustration of this mechanism can be seen from Figure 26.

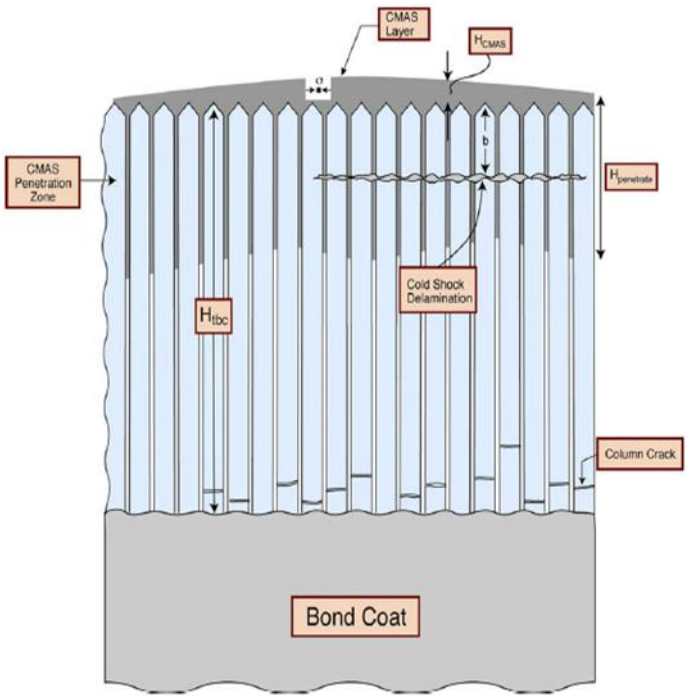

Figure 26: A representation of a CMAS layer that forms on the TBC and penetrates once it melts [66].

Secondly, a chemical interaction takes place between the molten CMAS and the PYSZ top coat ceramic, degrading the column tips and the porous morphology, especially in the upper part of the coating. The initially fine-scale micro and nano-porous structure and the feather-like porosity are replaced by larger globules filled with CMAS. Braue [78] reported the formation of a new phase in the interfacial reaction zone which was identified as a Ca-Zr-Fe silicate phase, while Stott [65] and later Krämer [12] – [11] suggested that PYSZ dissolves into the CMAS until the zirconia solubility limit is attained, in which case the excess zirconia is then re-precipitated as a fine grain structure depleted in yttria. Bacos et al. [79] reported two types of interaction between CMAS and TBC;

i. CMAS infiltration into the TBC microstructure
ii. Chemical attack of the TBC by a dissolution-re-precipitation mechanism, with excess zirconia re-precipitated as a new Zr-rich phase and some of CMAS chemical elements.

Both of these interactions are said to lead to the progressive degradation of the TBC top coat, via delamination cracks, due to reduction in the compliance of the TBC and loss of column integrity and porous morphology. EB-PVD TBC top coats contain porous layers, which makes it susceptible to CMAS and volcanic ash attack, with the molten materials infiltrating the pores and columnar grain boundaries, resulting in both chemical and microstructural degradation of the coating. For the standard CMAS composition, as defined by [13]; [73]; [80]; [11]; [72]; [12], there is a large coefficient of thermal expansion mismatch between the molten deposit, which is a glassy material, and the ceramic TBC, which can cause delamination and spalling of the TBC from the bond coat, as a result of compressive stresses [13].

The composition and properties of the deposits found in an aircraft engine can greatly affect the severity of damage [65]. Stott et al. [65] had noted that sand chemistry, throughout the Middle East, varied leading to differences in melting temperature of any deposits formed. Stott et al. [65] also observed that deposits with large calcium contents increased the rate of grain boundary and grain attack. Calcium oxide acts as a network modifier and should reduce the viscosity of the melt. Calcium has also been observed to be present in re-crystallised zirconia and may help stabilise cubic phase of zirconia.

As has been discussed above, much research has been undertaken in the area of the effect of CMAS attack on TBCs, however, none have studied the effect of changing the acidic and basic characters of the molten deposits on the performance of the TBC. Also, there are few researches that have investigated the critical issue of the minimum level required to initiate damage. This project will extend aspects of the initial work started in 2009 by Whitman et al. [13], the first to investigate minimum level require for CMAS infiltration, and will extend this to investigate the role of CMAS chemistry, in particular the role of acid – base reactions on CMAS damage.

2.6.7 Erosion Damage and Foreign Object Damage of TBCs

Extrinsic failures of thermal barrier coating have limited the full utilisation of TBCs. Extrinsic damage is primarily dependent on the microstructure and properties of the ceramic top coat, with the TBC/TGO and TGO/bond coat interfacial properties playing a significant role. For erosion and foreign object damage (FOD), factors such as impacting particle size, mass of impinging particle, velocity, temperature, rotational speed of the component, impact location and impingement angles relative to the specific locations on the component (leading or trailing edge) are important in differentiating between these two forms of damage (impact or erosion damage).

The leading edge of a turbine blade could experience a 90° impact whereas other locations are subjected to lower angles of impingement. In the thermal barrier coated combustor liners, particles are impacting the surface at about 20° or lower. Deakin et al. [81] demonstrated that EB-PVD TBCs are generally 7–10 times more erosion resistant than their APS counterpart, in the majority of the particle impingement conditions mentioned above [81]. This finding was similar to that observed from analysing field returned hardware. Figure 27 shows an average particle size distribution collected from a high pressure turbine blade which has been operating in a dust laden environment [9]. Particle size ranges from 10 µm (classified as small size fraction – sand, ash and dirt generally ingested with air) to 100 µm (debris from upstream engine components such as the combustor). Particles trajectory in the hot gas flow path can be mapped with different particles size, rendering impact and erosion damage particle size and location specific [18].

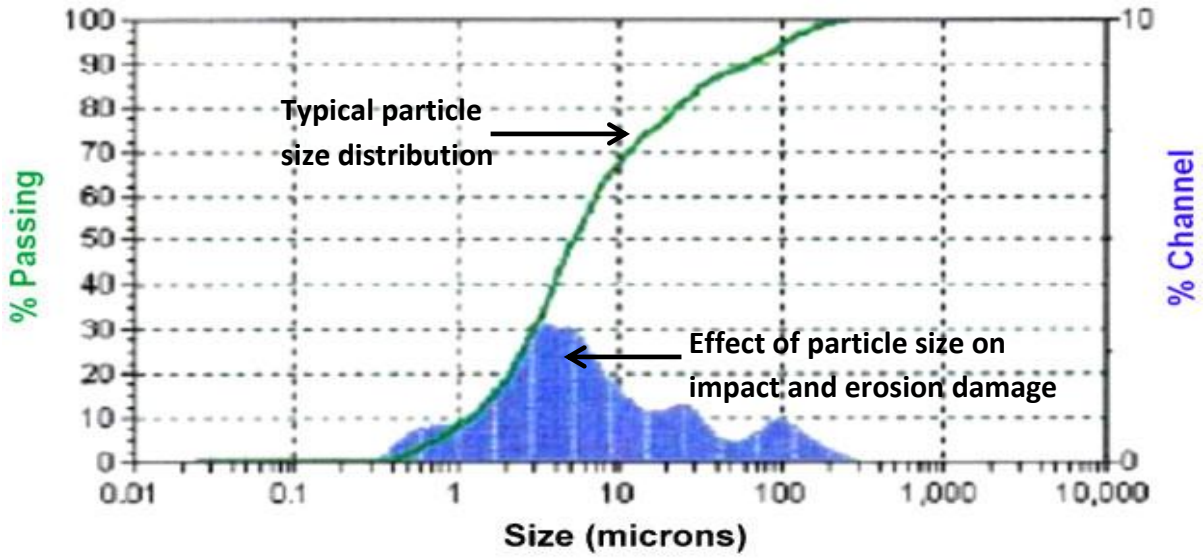

Figure 27: Typical particle size distribution in a in a dust collected from a HP turbine blade [18].

Examples of impact damage and erosion mechanisms for thermal barrier coated turbine blades are given in Figure 28. Areas of impact, noted by compressed and fractured TBC columnar structure, can be seen in Figure 28a, and in some areas show cracks propagating

from the impact origin to the bond coat/alumina interface, eventually leading to TBC spallation. Typical field examples of TBC erosion are characterised by gradual thinning of the TBC as shown in Figure 28b. TBC erosion generally occurs on the pressure side pocket, and on the suction side near the leading edge of the blade. By understanding the mechanistic behaviour of erosion, TBC erosion can be mapped and aid in the design of turbine blades, for example thicker TBC can be specified on areas of the blade locations susceptible to erosion on the basis of field experience.

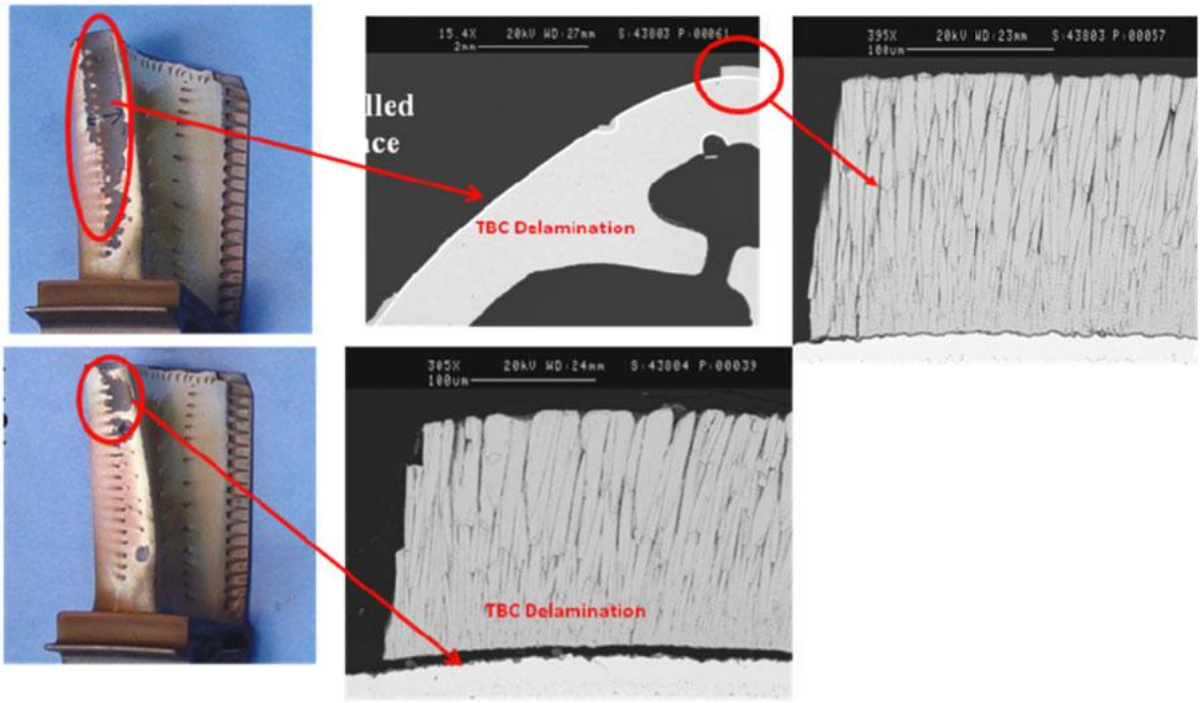

a

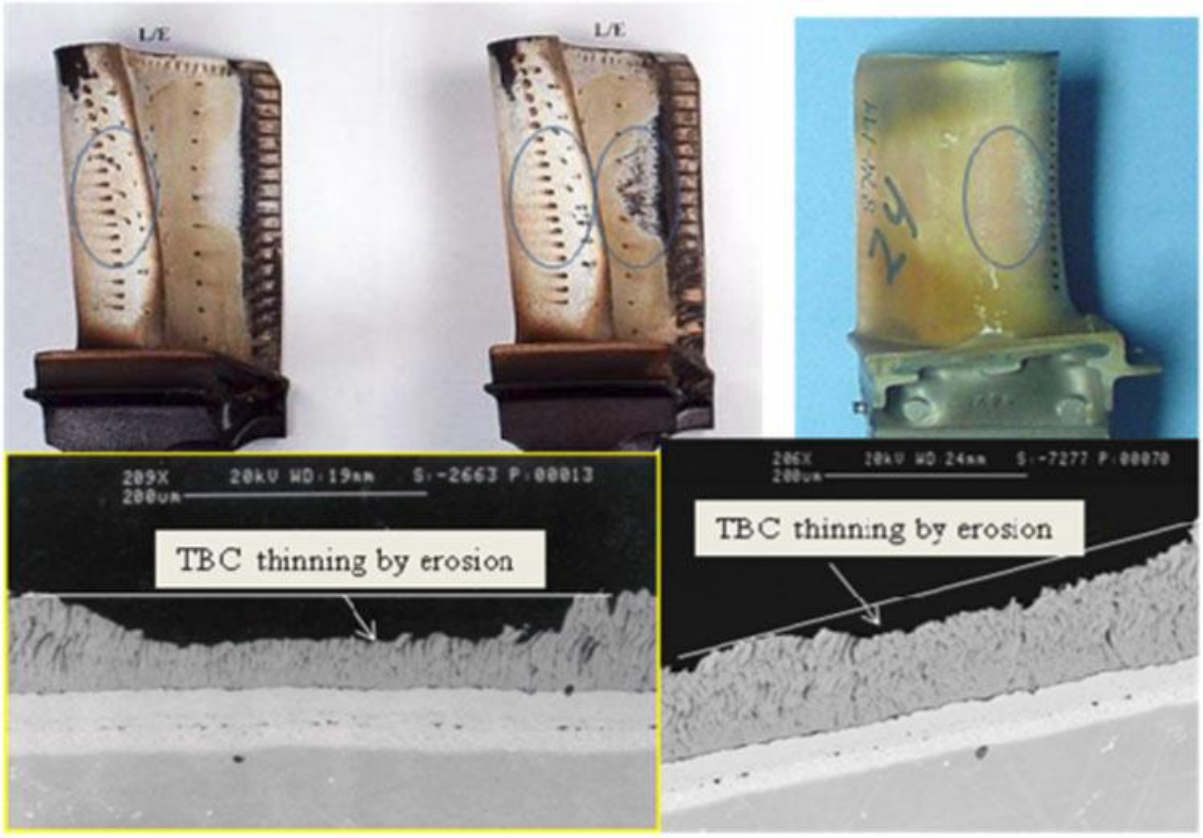

b

Figure 28: a) TBC delamination at leading edge of HPT blade by particle impact and b) TBC erosion locations and microstructural evolution [18].

Steenbakker et al. [82] first developed a mechanistic model using a dimensionless parameter, D/d, to link erosion damage based on TBC microstructure; column diameter (d) and contact footprint (D) of the impacting particle. In a joint collaboration between Columbia University, University of California, Santa Barbara, GE, Cambridge University, UK and Harvard University [83][84], the D/d model was further developed to illustrate mechanisms of stress wave propagation and a schematic of erosion damage initiation and threshold was produced (Figure 29). It can be inferred from Figure 29 that increasing the toughness should have the most pervasive influence on TBC erosion, through its role in elevating the critical threshold and, in some cases, decreasing the removal rate (Figure 29). However, the desired benefit

may not be fully realised through increased toughness since the TBC is quite ductile at temperatures >900 °C.

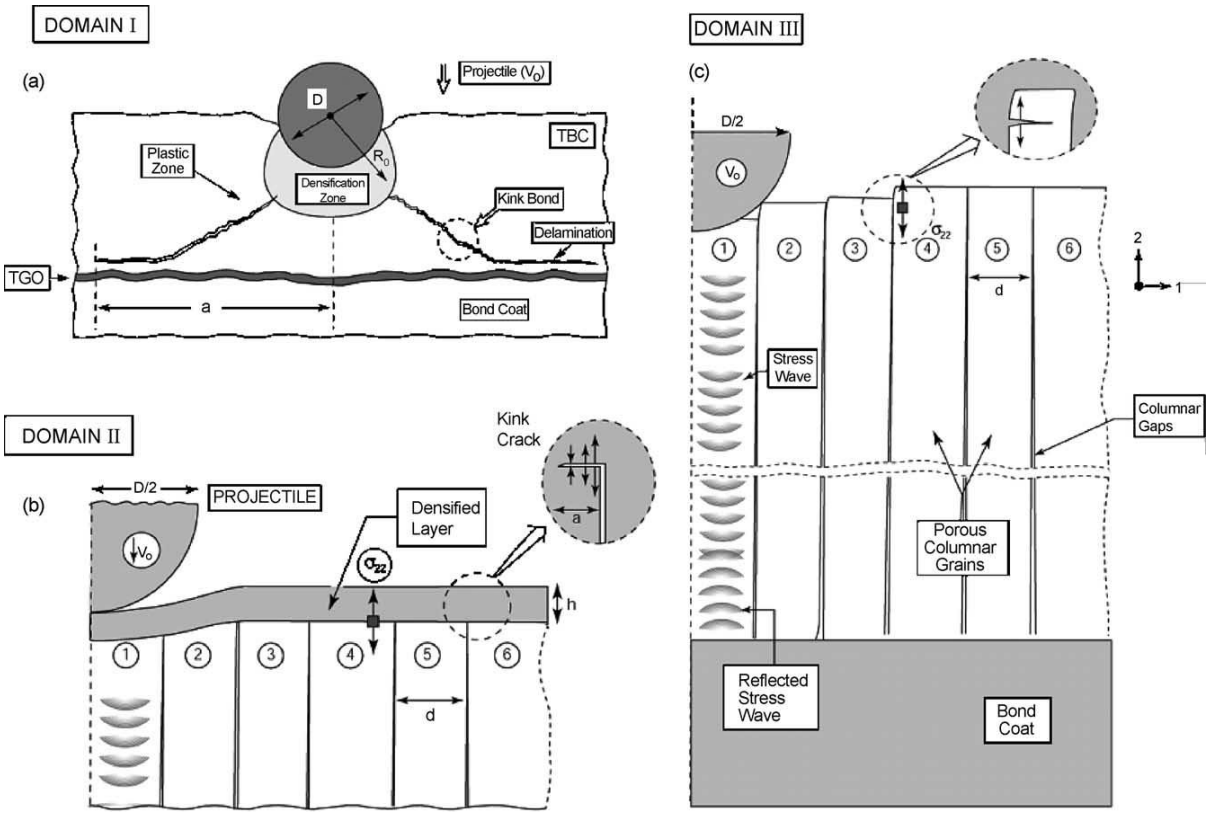

Figure 29: Particle erosion mechanism of crack initiation and propagation with low kinetic energy, mainly with small particles [83].

2.7 Materials for TBCs

Thermal barrier coatings, coupled with internal cooling, enable metallic materials to be used in the combustor and turbine sections of a gas turbine engine where the gas temperature exceeds the melting point of metals. Under such condition, the thermal conductivity of the ceramic material dictates the temperature drop across the TBC.

The primary function of TBCs is as a thermal barrier but because of the extremely aggressive environment in which they operate, they are required to meet severe performance constraints. For example, high melting point, to withstand stresses associated with thermal cycling, no

phase transformation between room temperature and the operation temperature, thermal expansion compatibility with the metallic substrate, chemical inertness, thermodynamic compatibility with the oxide formed by oxidation of the bond coat, good adherence to the metallic substrate, erosion resistance, high fracture toughness and resistance to deformation, low sintering rate of the porous microstructure [85].

However, thermal conductivity and thermal expansion coefficient are the most important design criterion that must be met before a material is classed as suitable for thermal barrier coating applications. The number of materials found to successfully satisfy all of these requirements to be used as a TBC is very limited. Typical properties of various materials for TBC applications are summarised in Table 7. The advantages and disadvantages of potential TBC materials are also discussed in this chapter.

Table 7: TBC materials and their properties [86]

	Zirconia	**Garnet Ceremics**	**Mullite**	**Rare earth zirconate**
Melting Temperature, K	2973	2243	2123	2573
Thermal Conductivity, $Wm^{-1}K^{-1}$	2.0	3.0	3.3	1.6
Modulus of Elasticity (TBC), GPa	21	Not available	30	175
CTE, (1 x 10^{-6}) K^{-1}	10	9.1	5.3	8.0 - 9.1
Poisson's Ratio	0.25	Not available	0.25	~ 0.28

Improvements of the current state-of-the art TBC material, YSZ can be achieved by:

- Post-deposition treatment of the coating with sealants or laser irradiation of the surface for better corrosion resistance,
- Gradient or multi-layered coatings with other materials,
- Thick TBC for a better thermal insulation coating [86].

2.7.1 Zirconia Based Materials

Yttria stabilised zirconia (ZrO_2 doped with 7-8wt.% Y_2O_3, YSZ) is the current material of choice for thermal barrier coating applications both in aero and industrial turbine engines. This oxide has several important characteristics for a successful TBC material, compared with other ceramics, notably high melting point, low thermal conductivity, high coefficient of thermal expansion and chemical inertness when in contact with alumina that grows on the bond coat [34; 87]. These YSZ coatings are most commonly deposited using electron beam physical vapour deposition (EB-PVD) or air plasma spray (APS) technique.

Figure 30 shows the microstructures of "as-deposited" APS, EB-PVD and directed vapour deposition, DVD coatings (a, b and c respectively). However, YSZ coatings deposited by EB-PVD method have excellent strain tolerance and better cyclic life than APS YSZ, due to its columnar microstructure. A major drawback of the YSZ coating is the limited operation temperature for high-temperature, long-term applications because zirconia exists as a polymorph and may, with time, undergo a phase transformation. At higher operating temperatures, there is a phase transformations from the metastable tetragonal (t') phase to tetragonal and cubic (t +c) and then to monoclinic (m), introducing cracks into the system due to a 5% volume change. The drive for process efficiency, control and flexibility, cost reduction, and composition and microstructural uniformity have led to the development of new processes such as DVD and suspension plasma spray from modifications to existing EB-PVD and APS processes [18].

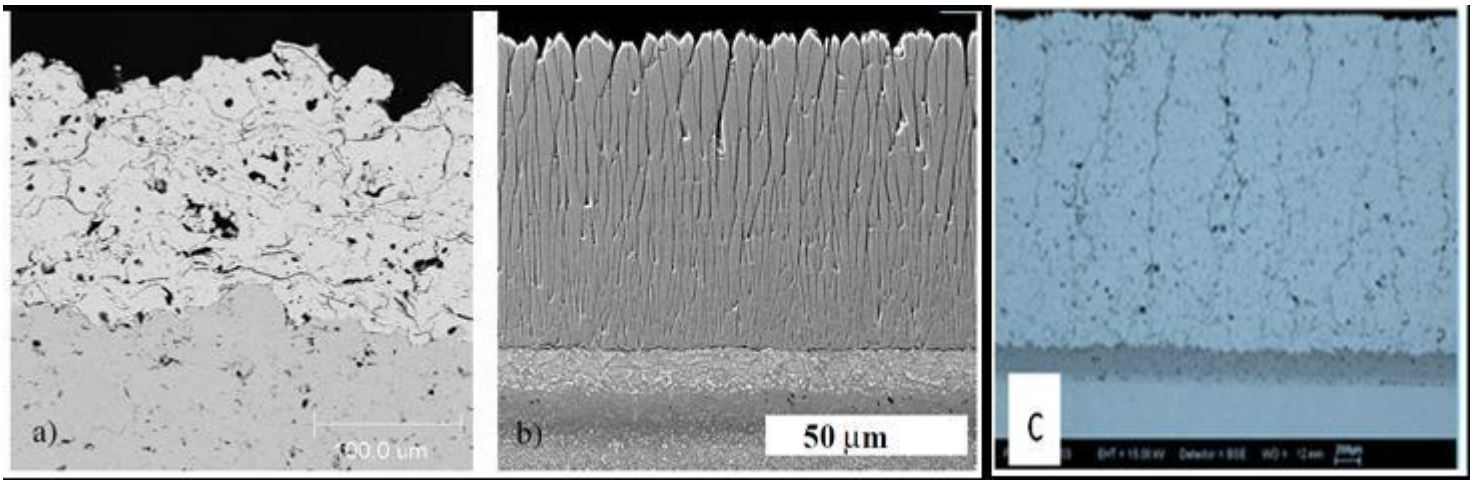

Figure 30: Microstructures of; a) APS, b) EB-PVD [87] and c) DVD [18] thermal barrier coating top coat

Rare earth zirconates with a cubic pyrochlore structure, $M_2^{3+}Zr_2^{4+}O_7$, (M = rare earth element), are being considered as alternate TBC materials because several of the zirconate pyrochlores have lower thermal conductivity than YSZ [88]. The crystal structure consists of the corner-shared Zr^{4+} site octahedral forming the back bone of the network and the M^{3+} ions fill the holes which are formed by 6 Zr^{4+} octahedral sites. Pyrochlores can largely tolerate vacancies at the M^{3+}, Zr^{4+}, and O^{2-} -sites without undergoing phase transformation. However, replacing the M^{3+} ion with larger ions can result in a stable pyrochlore structure up to 1500 °C, likewise replacement of the Zr^{4+} ion by a smaller ion can also be used to stabilise the pyrochlore structure. They can therefore be formed from a range of cations, since the M site can have a charge of 3+ or 2+, and Zr can be replaced by elements with valence of either 4+ or 5+. Previously studied rare earth pyrochlores include; $La_2Zr_2O_7$, $La_2Hf_2O_7$, $Pr_2Hf_2O_7$, $Ce_2Zr_2O_7$, and $Sm_2Ti_2O_7$.

Table 8: Thermal Conductivity of Potential TBC Materials Compared to Reference YSZ.

Material	YSZ	$La_2Zr_2O_7$	$Gd_2Zr_2O_7$	$Nd_2Zr_2O_7$	$Sm_2Zr_2O_7$
Thermal Conductivity (W/m-k)	2.2 (1273 K)	1.6 (1273 K)	1.6 (973 K)	1.6 (973 K)	1.5 (973 K)

2.7.2 Mullite

Mullite is an aluminosilicate compound with composition $3Al_2O_3.2SiO_2$, formed by the high temperature interaction of SiO_2 and Al_2O_3 containing compounds. Mullite has been considered for TBC applications because of its low density, high thermal stability, low oxygen diffusivity (which accounts for its stability in harsh chemical environments), low thermal conductivity and favourable strength and creep behaviour [89]. For applications, such as in diesel engines, where the operating temperatures are lower than those encountered in gas turbine engines, and where the thermal gradients across the coating are large, mullite is considered an excellent alternative to zirconia for the purpose of providing a thermal barrier coating. Engine tests performed with both materials showed that mullite coated components in diesel engines have a significantly longer life compared to zirconia coated parts. However, the thermal cyclic life of mullite coatings at temperatures above 1273K is much shorter than that of zirconia coatings. Mullite coatings crystallise at 1023-1273K, accompanied by a volume contraction, causing cracking and de-bonding.

2.7.3 Al_2O_3

Alumina is considered a possible thermal barrier coating material because of its chemical inertness and very high hardness. Kingswell et al. [90] studied the erosion behaviour of plasma sprayed alumina coatings compared with that of bulk material of ceramics and found that the erosion mechanism of alumina coatings differed from that of bulk sintered alumina. Bulk ceramic erosion generally occurs by a combination of fracture mechanisms [91], [92] with median and radial cracks developed during particle impaction at the ceramic surface [93]. Upon particles rebounding off the impact site, lateral cracks develop parallel to the surface which finally follow a curved path before propagating towards the surface, leading to chipping and loss of material [94].

Alumina is widely used as an alternative layer in graded and/or composite structures TBCs because of its capability of larger temperature drop from the coating surface to the substrate and also due to its superior thermal shock resistance compared to that of YSZ [95]. Moreover, alumina graded zirconia TBCs possess lower residual stress [96], higher hardness, lower porosity and improved adhesion [97].

In a multilayer zirconia system, alumina acts as a stabiliser for tetragonal zirconia phase by the following mechanisms [98]:

1. Grain-size control in nano-structure coatings, by virtue of its higher elastic modulus than zirconia, and
2. Solid solution formation

By alumina playing the stabilizer role, it allows the use of lower amounts of other stabilizers and thus may reduce their harmful effects, such as oxygen diffusion. This concept is important in the effort to produce molten slag (CMAS and VA) resistant thermal barrier coating. More on this is discussed in the chapter "Designing CMAS resistant coatings".

2.7.4 Rare Earth Elements

Rare earth oxides (La_2O_3, Yb_2O_3, CeO_2, Dy_2O_3, Pr_2O_3, Nb_2O_5 and Gd_2O_3) have shown great potential as candidate component oxides for rare earth lanthanide doped for thermal barrier coatings, due to their lower thermal diffusivity and higher thermal expansion coefficient, compared to that of the current state-of-the-art TBC material, partially Y_2O_3 stabilised ZrO_2. However, most of the rare earth oxides are polymorphic at elevated temperatures and this phase transformation will, to some extent, affect their ability to resist thermal shock [89].

2.8 Physiochemical Studies of VA and CMAS

Volcanic ash (VA) and synthetic CMAS both possessed very important physical (density, viscosity and melting points) and chemical (Basicity Index and oxidation potential) properties, all of which are strongly influenced by the chemical composition, structure of the slag and temperature [99]. Viscosity is an important parameter for high temperature systems. Experimentally, it is difficult to measure the viscosity of CMAS or volcanic ash since it requires specialist ultra-high temperature equipment. For this reason, CMAS viscosity has not been researched therefore it is not available in the open literature. Therefore, chemical compositions have been used to estimate viscosity as a function of temperature, based on Giordano's viscosity model [100]. The compositional dependency of viscosity as highlighted by Giordano's viscosity model is discussed in more detail in section 2.9.1. In this work, three different slag compositions have been studied with different Basicity Index. Also, trends in viscosity for different slag compositions have been identified, as a function of temperature. All the oxides in CMAS are also found in VA, although in different fractions, as illustrated in Table 9. Volcanic ash also has a significant fraction of iron oxides as well as alkali-metal oxides, both of which lower the melting point.

Table 9: Chemical composition of VA and Standard CMAS

Minerals	**Melting point (°C)**	**SiO_2**	**Al_2O_3**	**CaO**	**MgO**	**Fe_2O_3**	**Na_2O**	**K_2O**	**TiO_2**
Volcanic ash (wt.%)	1160	59.6	15.1	4.4	1.3	10.1	5.7	2.4	1.5
CMAS (mol.%)	1245	35.0	7.0	48.0	10.0	-	-	-	-

The volcanic ash analyses given in Table 9 are an average of 15 analyses taken randomly from an Eyjafjallajokull volcanic ash sample. These analyses agree well with the composition published by Sigfusson et al. [101] and it suggests this volcanic ash belongs to the

trachyandesite or latite family of igneous rocks characterised by an intermediate silica content [102]. The CMAS composition falls within the pseudo-wollastonite region in the CaO-SiO_2 - Al_2O_3 ternary phase diagram [103]. Pseudo-wollastonite has the stoichiometric formula $CaSiO_3$ and is a high-temperature crystalline phase.

2.9 Viscosity

The viscosity of the melt has a marked effect on the rate of penetration. At constant composition, the rates of mass transport and thermal transfer by diffusion are related inversely to the viscosity of the melt [104]. Viscosity is an internal property that describes a fluid's resistance to flow. The temperature and the chemical composition of the melt are instrumental in determining the viscosity of a slag system. The viscosity behaviour of high-silica slags is governed by the ratio of SiO_2 to modifiers, whereas for low-silica melts, the important factor in determining melt viscosity is the ratio of CaO to modifiers or alkali [105]. Volcanic ash and the CaO-MgO-Al_2O_3-SiO_2 slag system, of varying compositions, were considered in this study. It follows that, the viscosity of a molten slag is raised if the structural complexity is increased, due to increase in the concentration of network-forming ions in the ortho-silicate-silica composition range [104].

Melt viscosity can be calculated from an Arrhenius equation, which gives the temperature dependence of viscosity [106]:

$$\eta = \mathrm{A} \cdot \mathrm{e}^{\left(\frac{\mathrm{E}}{\mathrm{RT}}\right)} \qquad \text{Equation 2}$$

Where η = viscosity of slag, A = Pre – exponential term, E = Activation energy for viscous flow, R = Gas constant and T = Temperature, in Kelvin.

As mentioned above, slag viscosity is a function of the slag composition, temperature and the structure (oxygen partial pressure) of the system [99; 107]. Viscosity plays an important role

in the adhesion of ash particles, their vitrification and solidification process [108]. Slag viscosity will therefore have significant effects on both the depth of penetration and dissolution rate of TBCs, with the depth of penetration controlled by wettability (surface energy/tension) and viscosity of the melts [109].

2.9.1 Basicity Index and Melt Viscosity

The Basicity of molten deposits greatly affects the viscosity, as was proposed by Seok et al. [110]. Basicity – Viscosity model (Figure 31) predicts High B.I. melt to be less viscous than Low B.I., which was found to be the case in this study, with Low B.I. deposits forming a viscous glass at the surface of the sample (Figure 86) while High B.I. melt quickly formed a melt pool at the bottom of the coating.

The viscosity values for three different slag compositions were calculated based on the viscosity model proposed by Giordano et al. [100], at two separate temperatures (their melting points and melting points + 50 ºC). The relationship between viscosity and basicity is shown in Figure 31; the trend observed is a polynomial curve and the results would suggest that the higher the Basicity Index of the slag, the lower is its viscosity.

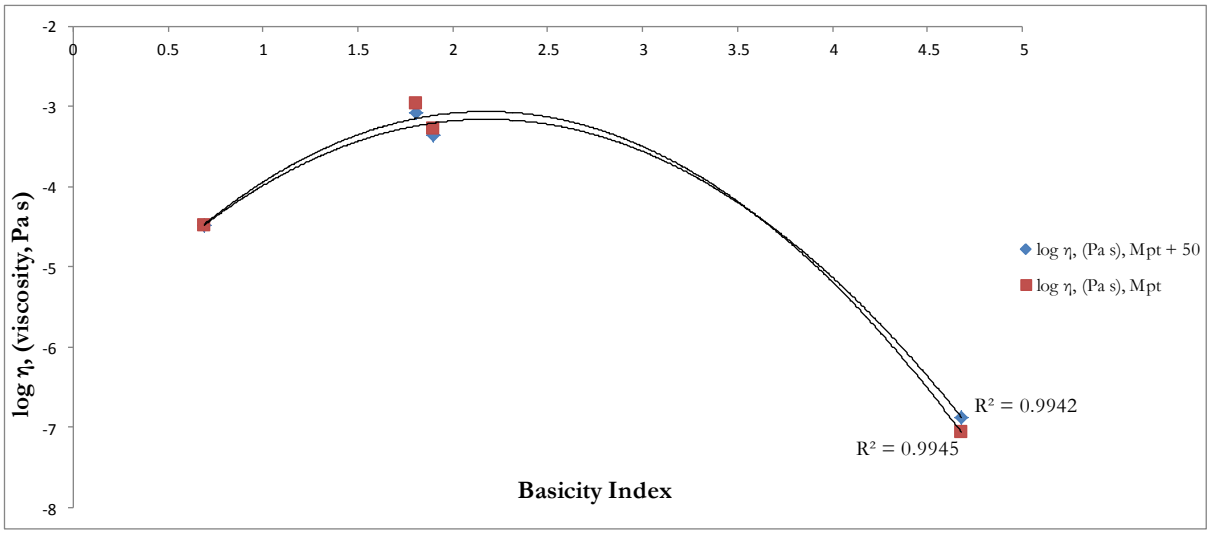

Figure 31: Effect of Basicity Index on viscosity as predicted by Giordano's thermodynamic model [100]

2.9.2 Effect of oxide content on the viscosity of volcanic ash and CMAS

It has generally been considered that a liquid slag contains molecular compounds. These are assumed to be dissociated into the component oxides (CaO, SiO_2, MgO and Al_2O_3) to an extent which varies with the composition. Pure silica and silica rich melts have a very high viscosity (~1 x 10^5 – 1 x 10^4 Pa s) at the melting point (1600 – 1725 °C). These melts are also characterised by a very weak tendency to crystallise; on rapid cooling a glass is formed which differs from a solid to the extent that the long-range atomic ordering of the crystalline state is absent [104]. Addition of basic oxides decreases the viscosity by breaking the hexagonal network of silica, as shown in the reactions below:

$$CaO \longrightarrow Ca^{2+} + O^{2-}$$

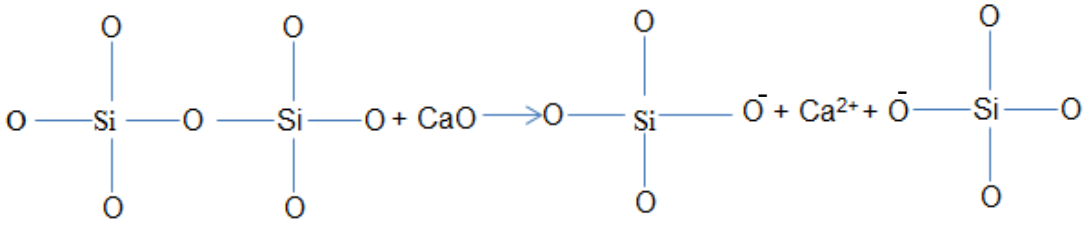

$$Na_2O \longrightarrow 2Na^{2+} + O^{2-}$$

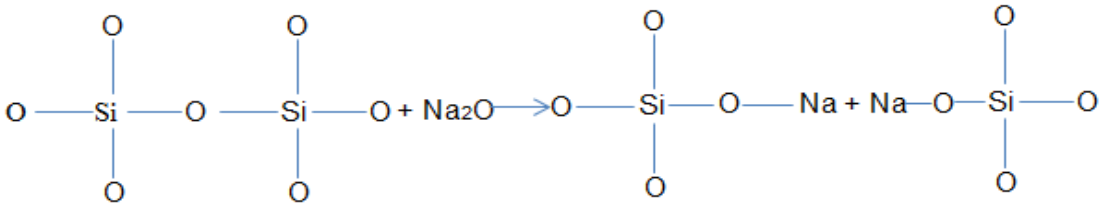

The structure of basic oxides (CaO and MgO) is a close-packed array of oxygen ions with the cations accommodated in the intervening interstices (Figure 32). Most of these oxides form

structures similar to that of sodium chloride [111], in which each cation is surrounded by and in very close proximity to six oxygen anions (co-ordination number of six). This is called an octahedral co-ordination [104].

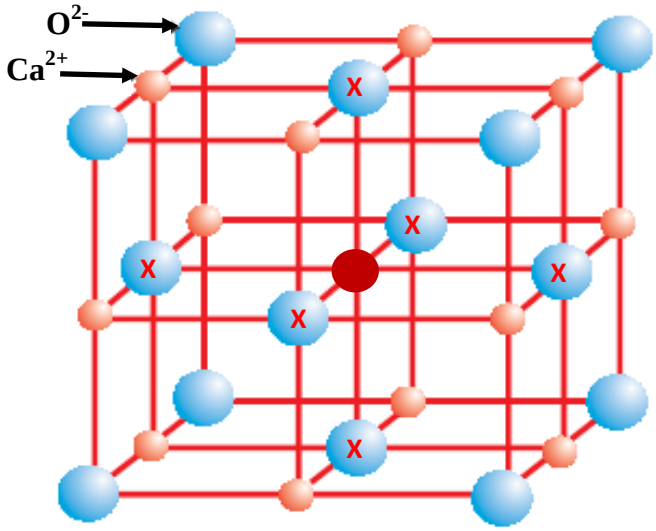

Figure 32: The structure of calcium oxide (redrawn based on [111]), illustrating the 6–fold coordination.

SiO_2, Al_2O_3, CaO, MgO, and Fe_2O_3 are the major oxide constituents in volcanic ash. Model CMAS is in loose chemical combination with CaO, MgO, Al_2O_3 and SiO_2. The amount of SiO_2 determines the acidity of the melt, whereas the CaO and MgO content in the melt affects the basicity. Al_2O_3 meanwhile is amphoteric and can act in both ways. Seok et al. [110] describe the CaO/SiO_2 ratio as the most important factor in determining slag basicity. This ratio was also used in his study as an indication of the slag viscosity. From this work one can draw the following observations:

- Viscosities increased with decreasing temperature, following an Arrhenius law.
- The melt Basicity has a more dominant effect on viscosity. Increasing Basicity lowers slag viscosity due to the break-up of the silicate oxides in the slag. These observations are in line with Liang et al.'s [112] investigation on the effect of Basicity on melting point

and viscosity of slag; who found that, with increasing slag Basicity, viscosity decreased sharply with a fall in the melting point.

- Increasing the amount of CaO decreases the melt viscosity by breaking the Si-O-Si linkage.

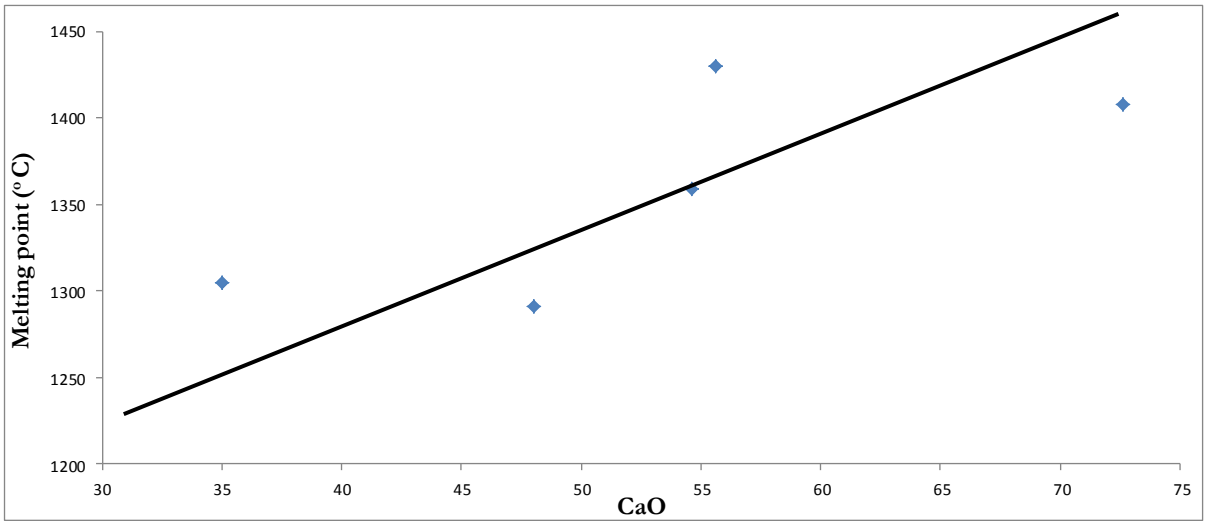

Figure 33: Effect of CaO on melting temperature (see Appendix B) as predicted by Giordano's thermodynamic model [100]

The effect of CaO addition on the melting temperatures of slag is shown in Figure 33. The graph illustrates an increasing trend, which indicates that CaO acts as a network modifier and increase the melting temperature with increased CaO in the slag composition. However in Figure 34, the relationship between CaO addition and the Basicity Index of the deposit is shown. It can be observed that increasing CaO content has an increasing effect on slag's Basicity index, whereas the effect of SiO_2 content is a mirror image to that of CaO (Figure 34) showing a decreasing pattern with increasing SiO_2 content.

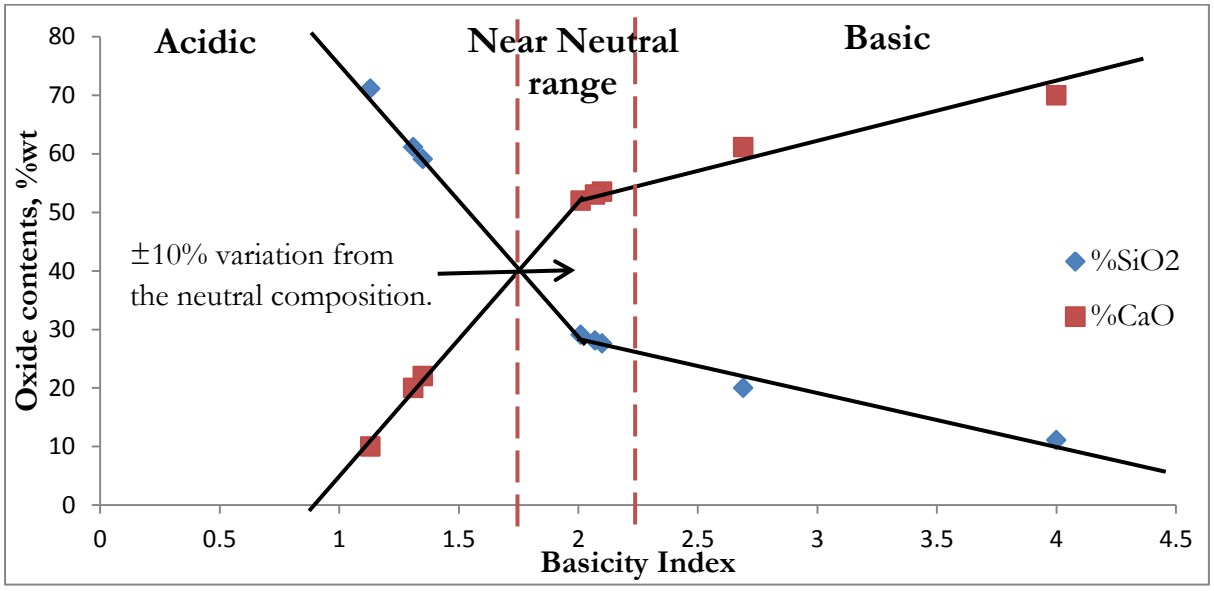

Figure 34: Effect of oxide content on slag's Basicity Index (see Appendix A)

- The viscosities depend on Al_2O_3 and Fe_2O_3 content more strongly than MgO content.
- Al_2O_3 and MgO lead to an increase in the slag's viscosity.
- Increasing Fe_2O_3 content lowers the melting temperature of the slag and also lowers the melt viscosity.
- In the system CaO-MgO-Al_2O_3-SiO_2, the viscosity increases rapidly with increasing SiO_2 content [104]. The effect of SiO_2 content on the melting point of five different slag compositions is shown in the graph in Figure 35. A decreasing trend is observed, clearly suggesting that, slag's melting point decreases with an increase in its SiO_2 content. Hence it can be concluded that, the observed pattern is in direct contrast to that observed for the effect of CaO content on the melting temperatures of slags.

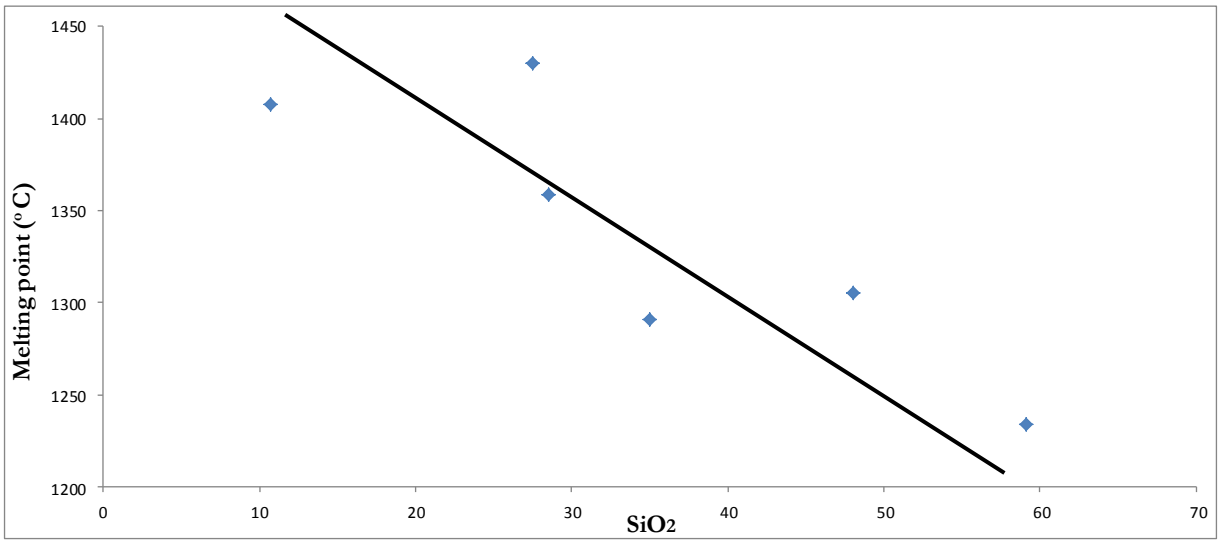

Figure 35: Effect of SiO_2 content on melting temperature (see Appendix B) as predicted by Giordano's thermodynamic model [100]

- From the above, it can be deduced that SiO_2, Fe_2O_3 and Al_2O_3 contents would have a dominant effect on sintering resistance and phase stability of 7YSZ thermal barrier coatings. Even very small amount of these oxides result in more rapid sintering of TBCs [110].
- Miller and Shott [113] examined the influence of basicity on the leaching rate of molten slag in steel making. Re-examining their results showed that CMAS induced damage as a result of leaching increased with increasing basicity. Theoretically, "standard" CMAS and volcanic ash are expected to have similar degradation mechanism (as both belong in the low B.I. category, B.I. < 2). However, the damage caused by CMAS is expected to be more severe compared to volcanic ash attack, since CMAS has higher basicity index than volcanic ash, 1.08 and 0.46 respectively, should all other factors be equal.

2.10 Melting Properties of Synthetic CMAS and Eyjafjallajokull Volcanic Ash

Differential Scanning Calorimetry (DSC) was used to study the glass transition temperature (T_g) and the crystallisation temperature (T_c) of the synthetic CMAS and volcanic ash. Figure 36 illustrates a DSC trace of melt transition for Eyjafjallajokull volcanic ash. Eyjafjallajokull ash has a melting temperature in the range of ~11300 - 1145 °C, which is less than the operating gas temperature of a turbine engine, about 1400 to 1600 °C. At this temperature, ash ingested in the engine will melt to form a glass and because there is a temperature gradient continuously across the engine, on cooler surfaces, the molten ash will form a solid, but glassy, deposit on the TBC top coat.

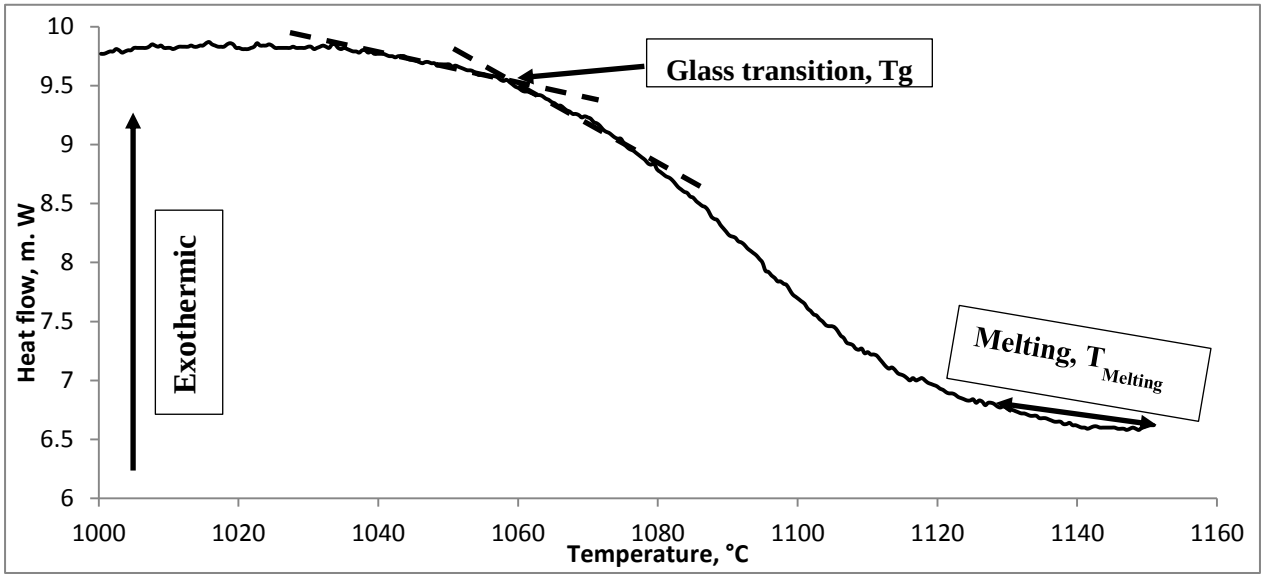

Figure 36: DSC trace of Eyjafjallajokull volcanic ash

In a high temperature gas turbine environment, volcanic glass would tend to melt first, because it has the lowest transition temperature, and consequently the lowest melting temperature. Molten volcanic glass has a high viscosity, which inhibits crystallisation as the material cools and loses volatiles. When volcanic ash is ingested into operating aircraft

engines, it is the melting temperature of volcanic glass particles that will determine the operating temperatures below which the ash will remain solid in the engine [114].

Both transition and melting temperatures are critical for molten deposit attack. Solid state diffusion of CMAS species may attack the TBC in situations where the TBC surface temperature (T_{TBC}) is less than the CMAS melting temperature ($T_{Melting}$), but close enough to the transition temperature (Tg) of the melt ($T_{TBC} < T_{Melting}$, but $T_{TBC} \approx Tg$). However, where T_{TBC} (TBC surface temperature) > $T_{melting}$ (melting point of the deposit), melting occurs and the TBC is infiltrated by the CMAS melt. This liquid form of CMAS attack turns to be faster compared to the slow, long-term solid state attack.

2.10.1 Physical Aspects of the Eyjafjallajökull Ash

Studies carried out by the Institute of Earth Sciences, University of Iceland, Sturlugata on the Eyjafjallajökull volcanic ash showed a pattern in the physical characteristics of the ash. Using electron microprobe analysis (EMPA), these authors found that, the early ash from the hydromagmatic, explosive ash (termed in this paper as small particles, but often referred to as phreato-magmatic ash) was surprisingly soft, light, and powdery [114]. The explosive character of volcanoes is caused by the silica-rich melt, which often contains dissolved volatile components, such as H_2O or SO_2 [114]. Explosive ash has distinct characteristics, as a direct result of its explosive origin, the particles appear cohesive with the consistency of flour. The Institute of Earth Sciences, University of Iceland, also concluded that the later, magmatic ash particles were more typical (referred to here as large particles); it was granular with the consistency of dry sand.

2.11 Role of Volcanic Ash in Gas Turbine Engine

Jet engines require large amounts of air in order to generate thrust. The Trent 800 bypass engines ingest 1000m^3 of air every second and the air includes sand, dust and volcanic dust particles, if the aircraft has travelled through the path of volcanic plumes. These particles will cause severe degradation to components of the turbine engine [115]. Molten volcanic ash has a detrimental effect on turbine blades due to its chemical attack of TBCs. Material degradation is a major problem since components have to operate in an environment that will invariably degrade their performance. Modern jet engines operate at temperatures well in excess of the melting point of volcanic ash, at least 300 ^{o}C hotter than the melting point of volcanic ash. The volcanic ash melts in the combustion chamber and the molten glass sticks onto the turbine blades in the right conditions (not 100% of the molten ash entering the turbine will adhere to the blade). The basic conditions for ingested volcanic ash to 'stick' on the surface of a turbine blade are discussed in more detail in section 2.11.1. The turbine blades will then be covered by a layer of molten glass, forming a coating layer of molten ash on the surface of the turbine blade, which degrades the thermal barrier coating. Understanding the various degradation mechanisms and their effect on overall life of the engine is paramount.

Elsewhere in the engine, volcanic ash can erode the compressor, block cooling holes and interfere with combustion through the disruption of air flow.

Turbine engines ingest 1000m^3 of air every second

1m^3 of air = 1kg

1000m^3 of air = 1000kg.

The limit of tolerable volcanic ash density set by the Civil Aviation Authority is 2×10^{-3} grams of volcanic ash per cubic metre of air (2×10^{-3} g/m^3 → 2 mg/m^3), although this figure has since been doubled to 4 mg/m^3 by the aircraft industry and engine manufacturers. This amounts to 4 g/s of volcanic ash passing through the engine. An aircraft engine is designed to operate in 78% nitrogen, 21% oxygen and some trace gases. In a dense ash cloud, there is a possibility of the air mixture falling short of the 78/21 split.

Calculating at the maximum permissible limit (4 mg/m^3), per second;

The engine's bypass ratio determines the actual amount of ash that passes through the combustion chamber and subsequently enters the turbine section. The bypass ratio is the ratio between the mass flow rates of air which bypasses the engine core (un-combusted air), to the mass flow rate of air passing through the engine core and is involved in the combustion process to produce mechanical energy. The Trent 800 engine has a bypass ratio of 6.2-5.7 [2], meaning for every 1kg of air that passes through the combustion chamber, ~6kg of air passes around it through the ducted fan alone.

An aircraft engine will ingest 1000m^3 of air per second, meaning 4000 mg (4 g) of volcanic ash particles enter the engine every second, at an ash load of 4 mg/m^3. However, with a ~6:1 bypass ratio, assuming everything else being equal, 3.4 g of ash contained in the 1000 m^3 of air bypasses the engine core and remains un-combusted, whilst 0.6 g passes through the engine core and into the turbine section before possibly being deposited on the turbine blades.

Trent 800 bypass ratio 6.2 – 5.7

Per second, 1000 m^3 of air ⟶ 4 g of volcanic ash

~6:1 bypass ratio ⟶ 3.4:0.6 volcanic ash ratio

∴ 0.6 g of volcanic ash gets into the core of the engine every second.

Therefore, for every minute, the engine swallows;

$0.6 \times 60 = 36$ g/min

And for a seven hours flight to New York;

$0.6 \times 60 \times 60 \times 7 = 15.12$ kg of volcanic ash passes through the engine core, at the allowable limit.

This amount of ash is likely to cause serious damage to an aircraft engine in terms of erosion (compressor section) and molten slag attack (combustion and/or turbine section). For this reason, it is important to establish a threshold of ash density that an aircraft can tolerate safely and to establish a correlation between ash density and exposure time. Volcanic ash can cause both short term and long term damage to engines that have passed through volcanic ash plumes.

- Short term damage: If volcanic ash density exceeds the critical threshold level. This causes severe compressor erosion, cooling holes blockage and engine surge.

- Long term damage (below threshold level): Progressive damage to the combustor and turbine through molten slag attack. How often should aircraft engine be serviced? How long should turbine blades last?

Overall, this result in a difficult decision for aircraft industry, as two vital but opposite factors are intertwined, Safety and Costs. Grounding an aircraft for repair is costing airline companies in terms of lost revenue and the cost of repair, whereas the decision not could jeopardise passenger safety.

2.11.1 Adhesion of Environmental Dust to Turbine Engine Components

There are several conditions that must be satisfied in order for particles ingested by a gas turbine engine to "stick" on engine hardware, including sufficient service temperatures to instigate melting or at least soften of the particles. For this to occur, the service temperature has to be greater than or equal to the glass transition temperature ($Ts \geq Tg$). Three factors are said to affect the probability of particulate adhering to engine hardware [116]. These are the particle temperature, gas temperature and the turbine surface temperature, at the point of impact. The gas temperature defines the particle temperature, which then determines the physical state of the particles (a factor related to the hardness of the particle); solid, liquid or partially molten - and in the latter case the melt fraction becomes significant. The state of the particle influences whether they rebound from the surface (causing erosive damage) or instead are likely to stick. The heating and acceleration behaviour is also a function of particle size. Particle size also determines the amount of inertia a particle has, and when it is carried by a fast moving gas stream, this will affect whether the particle will follow the streamline or deflect away from it, if the flow happens to turn rapidly [116].

2.11.2 Effect of Volcanic Ash and CMAS Ingestion in the Compressor Section – Erosion

Volcanic ash particles of various sizes enter the engine and first impinge on compressor blades at a variety of angles. The erosion behaviour of two typical compressor materials (IN718 and Ti64) were studied in this project and results presented in a later chapter. Figure 37 shows samples in the "as received" condition and after an erosion run.

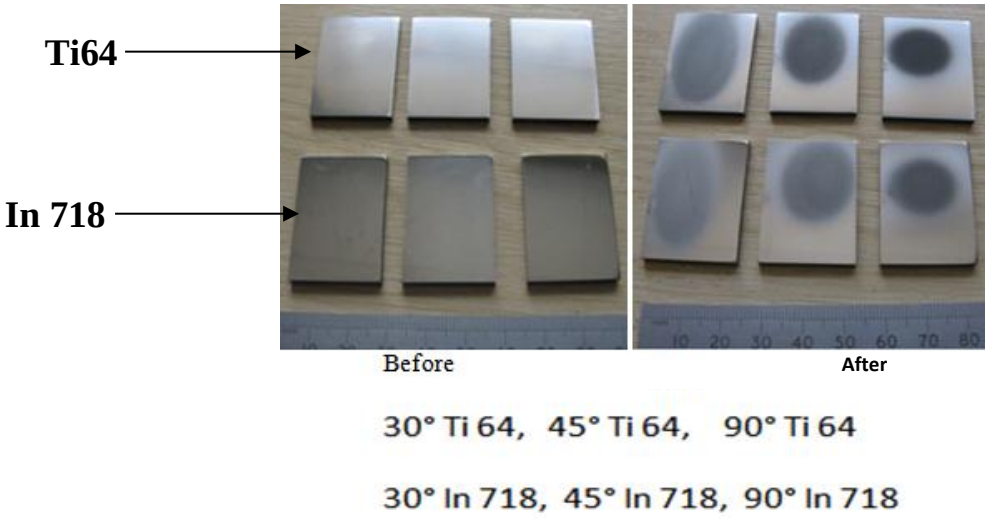

Figure 37: Erosion samples before and after test.

The compositions of these two alloys are given in Table 10.

Table 10 : Chemical compositions of Ti 6Al-4V and In 718 alloys

Ti64	**Al**	**V**	**C**	**N**	**O**	**H**	**Fe**	**Y**	**Others**	**Ti**
Wt.%	6.75	4.5	0.08	0.5	0.2	0.0125	0.3	0.005	0.1	Balance

In 718 Wt.%	**Cr**	**Ni**	**Mo**	**Nb**	**Ti**	**Al**	**C**	**Mn**	**Si**	**Co**	**Fe**
	21.0	55	3.3	5.5	1.15	0.8	0.08	0.35	0.35	1	Balance

Erosion-induced degradation: In a gas turbine engine, erosion damage occurs in the compressor section (cold section, temperature up to 700^{o}C). Sand and volcanic ash that impacts the surface of a compressor blade will result in slow but steady loss of material. Volcanic ash that gets sucked into a gas turbine engine are carried in the airstream and can cause severe erosion damage by solid particle impacts to compressor components whilst travelling through the engine. Volcanic ash particles can be sharp edged and highly abrasive, especially when larger particles are fragmented by impact. The extent of the damage caused depends upon factors such as; particle size and density of VA, the angle of impact, velocity (blade tip speeds and impact velocities) and operating temperature.

Solid particle erosion is the subsequential loss of material by the impact of small solid particles suspended in the gas stream [117]. Due to the tight tolerance with which modern turbine engines are built, the problem of erosion cannot be avoided, as illustrated in Figure 38.

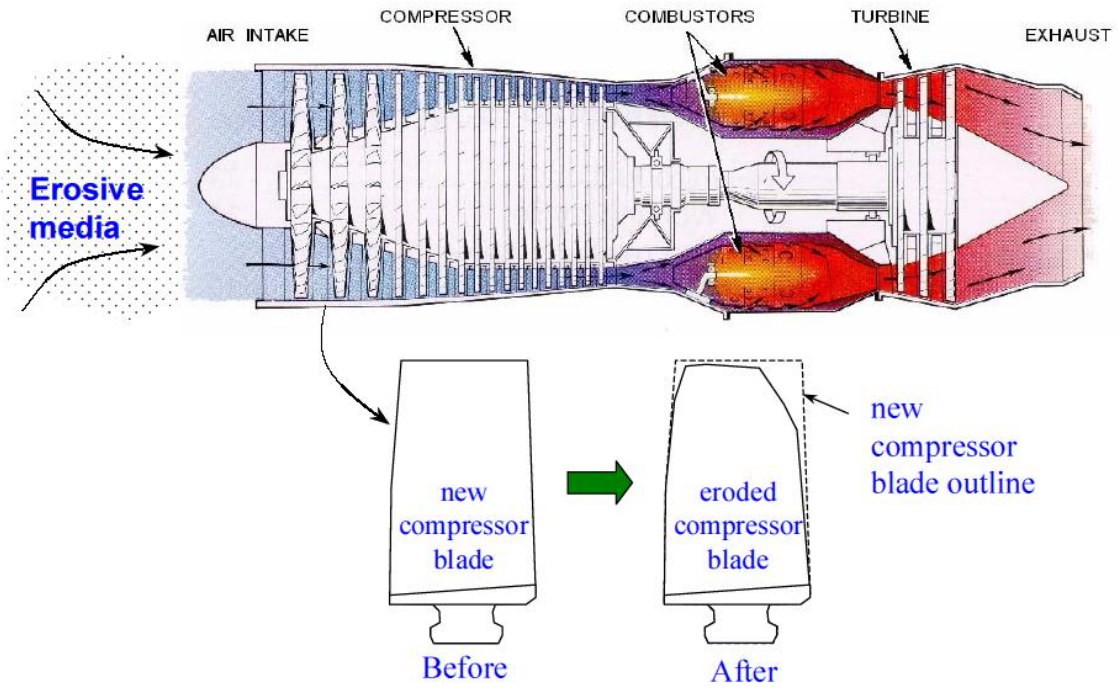

Figure 38: Erosion problem in a gas turbine engine [118]

Erosion damage of compressor components increases with total mass of impacting particles, flow turning and gas velocity, and with decreasing blade size. The erosion rate (E) for solid particle impact is given as a function of mass of material loss against the mass of impacting material. However, for a true comparison between different materials with different physical properties, the volume of materials is preferred to the mass of material loss because it takes into account the difference in density between them [119]-[120]. The rate at which erosion occurs is measured in units of (g/g), (cc/g), (g/kg), (cc/kg).

$$Erosion\ rate\ (E) = \frac{Mass\ of\ material\ removed\ from\ substrate}{Mass\ of\ impinging\ particles}$$ Equation 3

Particles size also has an effect on the occurrence of erosion, a minor effect on erosion rate and may influence the mechanism. Fine particles (<1-2 µm) will generally flow within the gas stream and cause little erosion [121]-[122]. Particles size between 2 µm and 10 µm may impact angular surfaces, where significant local aerodynamic effects modify the particle impact conditions. Medium sized particles (10-20 µm) cause erosion to the trailing edge of turbine aerofoils [123]. Coarse particles (>40 µm) move relatively slowly in the gas flow and can be hit by the rotating turbine hardware damaging the leading edges [124]-[125]. The graph in Figure 39 shows the steady state erosion rate as a function of impact angle and particle size. The graph also shows a small dependency of the erosion rate on particle size when volcanic ash is the erodent. In this case, medium sized particles are more erosive than fine and coarse size fractions at all impact angles, with the fine particles being more erosive than the coarser particles at all impact angles for IN718, but for Ti6Al4V this is only at 30° impact angle. In an engine, this would further be modified by aerodynamic behaviour as a function of particle size.

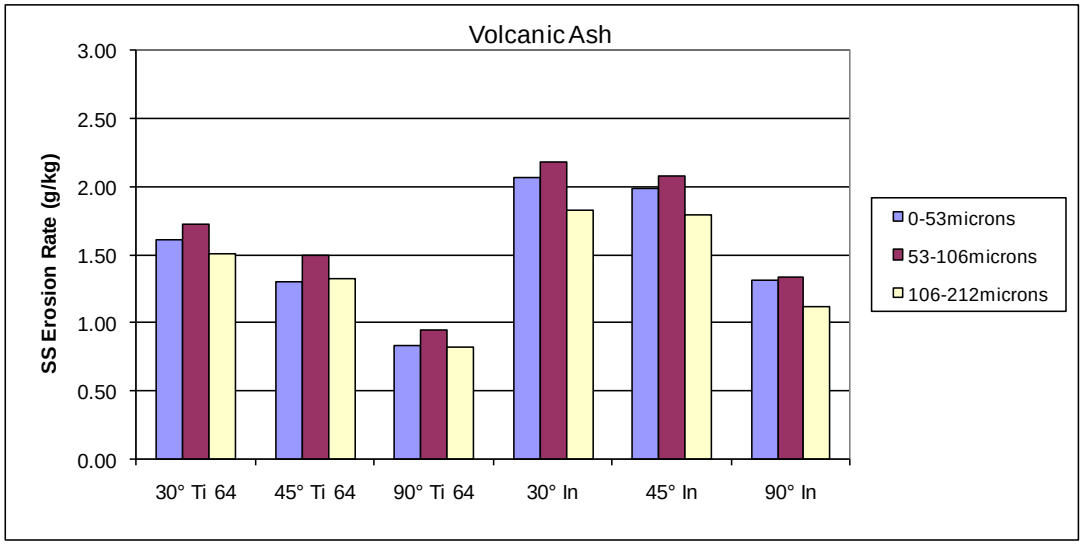

Figure 39: Bar chart of steady state erosion rates as a function of particle size with volcanic ash as the erodent, test at 6.5 bar, estimated gas velocity 252m/s.

In order to better understand how small solid particles, suspended in a gas stream, are able to cause damage in an aircraft engine, the mechanisms of solid particle erosion and factors affecting them will be discussed.

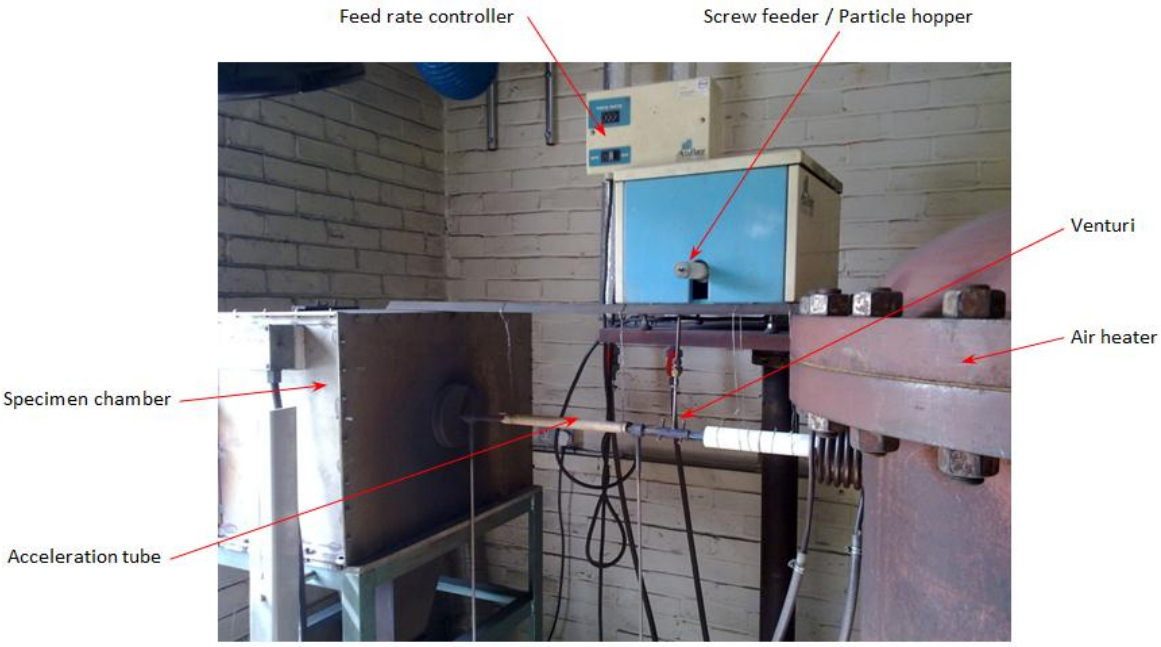

Figure 40: Erosion rig at Cranfield University

2.11.2.1 Mechanisms of Erosion

Erosion damage by solid particle impacts can occur in several ways, depending on the material properties and the angle of impact. Material removal occurs by micromechanical deformations and fracture processes such as; cutting, ploughing, extrusion and fragmentation [119; 120].

Finnie [126] developed a relationship between a material's hardness and its erosion resistance for pure metals, as can be seen on Figure 41. It can thus be concluded that higher hardness results in higher erosion resistance of the material, unless the material has undergone thermo-mechanical processes in order to increase its hardness, such as work hardening or heat treatment, where upon the erosion rate is less dependent on the increase in Hv. From this

figure, one would deduce that the erosion rate (E) is inversely proportional to the hardness (H), as shown by Equation 4.

$$E \propto \frac{1}{H}$$ Equation 4

Where the performance coefficient may depend on the alloy crystal structure, number of slip systems, hence ductility.

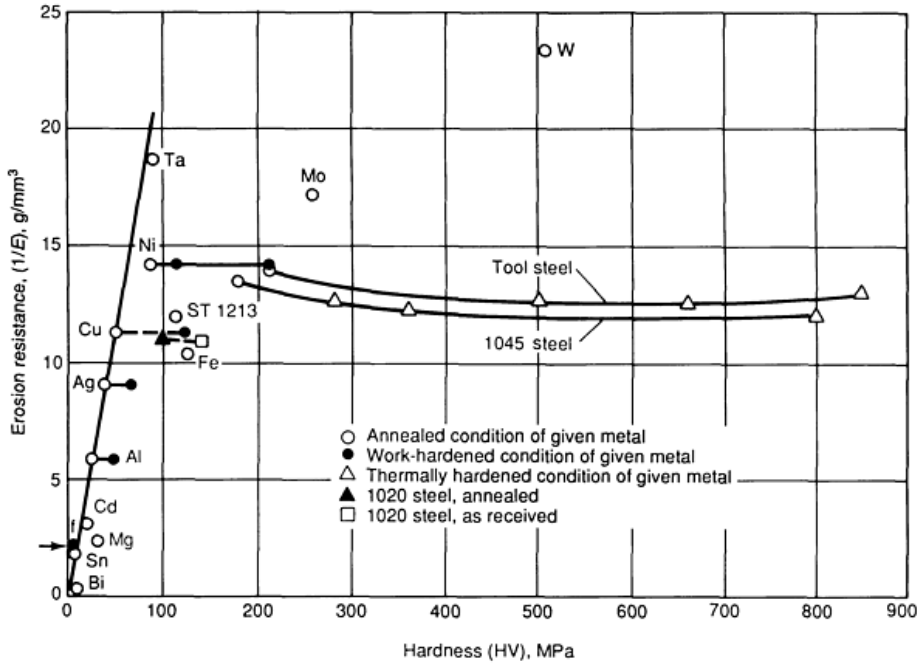

Figure 41: Correlation between hardness and erosion resistance for pure metals [126]

Erosion mechanisms fall under the following categories;

- Ductile erosion
- Brittle erosion
- Erosion of multilayers
- Erosion of dual phase materials
- Erosion-corrosion

The two main mechanisms of erosion are ductile erosion and brittle erosion. The former involves plastic deformation and cutting processes, while the later involves crack formation, propagation and then interaction. Experimentally, ductile and brittle erosion can be identified depending on the angle at which maximum erosion occurs, as shown in Figure 42. If maximum erosion occurs at low impact angles, then the material is said to behave in a ductile manner, whereas a material will exhibit brittle behaviour if maximum erosion is associated with maximum impact angles of 90^{o}, i.e. normal incidence [127]. Brittle-to-ductile transition behaviours have also been recognised by various authors [128].

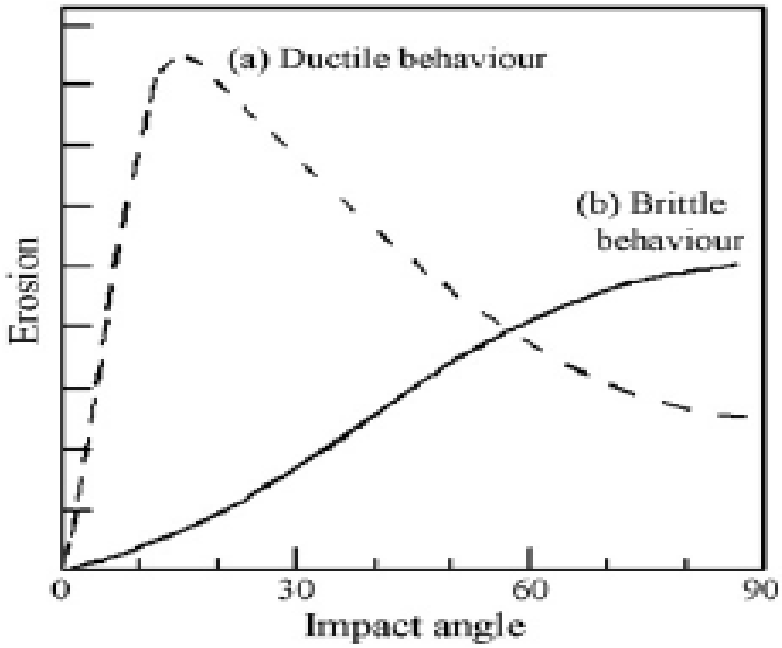

Figure 42: Ductile and brittle erosion behaviour with varying degree of impact angle, [127].

When particle velocity and size is decreased, eventually the particles are not able to initiate cracking and will only plastically deform the material. This change in mode of erosion is known as the ductile–brittle transition [128].

2.11.2.1.1 Ductile erosion mechanisms

The erosion of ductile materials is predominantly due to localised plastic deformation and it is related to the particle impact angle and velocity. At low impact angles (below 30° to 60°),

the predominant mechanism of solid particle impact is by cutting wear. On the other hand, particles impacting at a greater angle will cause loss of material by an extrusion mechanism or ploughing. However depending on the particle size and velocity, fragmentation of the particles can also occur and damage the surface for a second time [129].

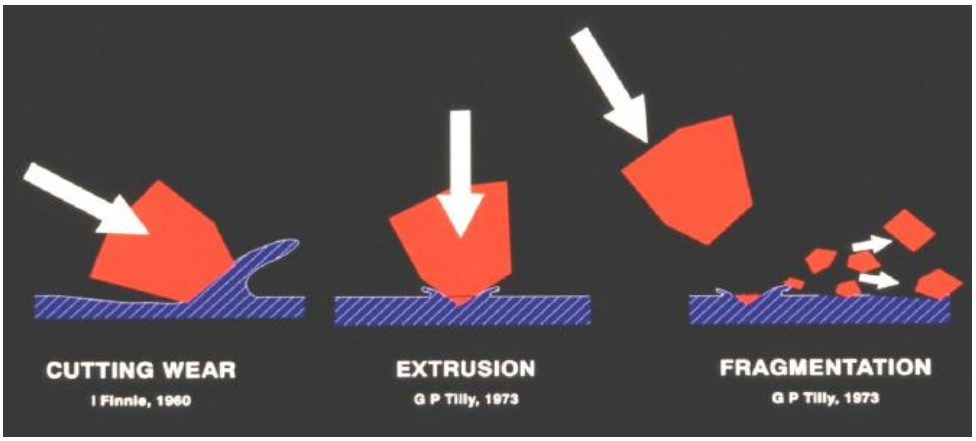

Figure 43: Ductile erosion mechanisms, [130]

2.11.2.1.2 Brittle erosion mechanisms

Brittle erosion is characterised by cracks that radiate out from the point of impact. An impacting particle will lose kinetic energy and as a result, will rebound with less mechanical energy. This irreversible kinetic energy loss is theoretically available to cause a deformation in the shape of a crack and/or the removal of a piece of previously cracked material, prior to conversion into internal energy [127]. However, the degree of damage will depend on certain factors such as impact angle, temperature, impact velocity, particle shape and size. For brittle erosion the peak rate occurs at normal impact angles.

The crack morphology can be classified as radial and lateral cracks or Hertzian cracks, depending on the shape of the impacting particle and the deformation caused during impact. Radial and lateral cracks are created when the target material is impacted by sharp edged particles, and can also result due to local plastic deformed zone. Hertzian cracks, meanwhile, are created by rounded particles impacting the target material, with no post impact plastic

deformation zone [117]; [131]-[132]. The extent of fracture of the impacted material depends on its mechanical properties (in particular its resistance to crack initiation and its fracture toughness) and on the energy transmitted by the projectile (function of its velocity, density and shape) [133].

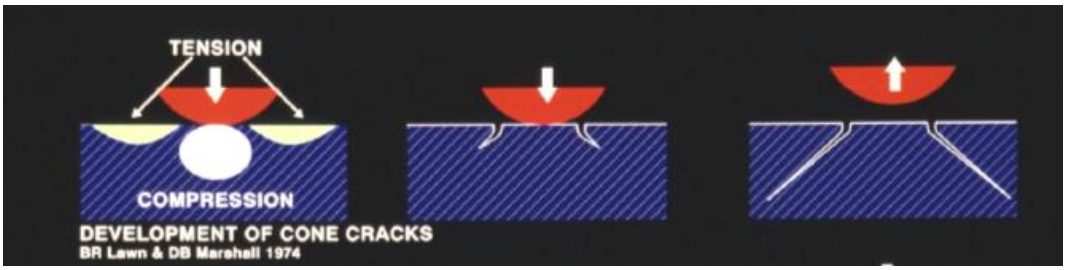

Figure 44: Brittle erosion mechanism, [134]

2.11.3 Factors that Affect Erosion Rate of a TBC

As seen above, solid particles erosion are different depending on whether the material is ductile (compressor materials) or brittle (ceramic TBCs). Thus there are several factors that affect the rate of erosion;

- Microstructure of the coating, that is, for TBC systems, laminar plasma sprayed coating versus columnar EB-PVD coating
- Porosity of the TBC top layer
- Size, hardness, velocity and flux of the impacting particles
- Impingement angle
- Exposure temperature [135]

2.11.4 Erosion Resistance

Erosion resistance can be expressed in relation to the mechanism of erosion involved. This takes into consideration the effects of process variables on erosion, such as impact angle and velocity, with respect to the erosion mechanism involved.

2.11.4.1 Ductile Materials:

As mentioned above, ductile erosion involves the removal of material due to localised plastic deformation and is related to the energy absorbed by the system (related to the kinetic energy). Finnie [126] proposed the following model for the ductile erosion mechanism:

Given the volume of material removed:

$$V = \frac{c \cdot M}{p} \cdot f(\alpha) \cdot \mathrm{v}^n \qquad \text{Equation 5}$$

But he found that:

$$p = Const \cdot H \qquad \text{Equation 6}$$

Furthermore:

$$E = \frac{Mass\ of\ material\ removed}{Mass\ of\ impinging\ particles} = \frac{V \cdot \rho}{M} \qquad \text{Equation 7}$$

Thus:

$$E = Const \cdot \frac{\rho}{H} \cdot f(\alpha) \cdot \mathrm{v}^n \qquad \text{Equation 8}$$

Where: V = Volume of material removed from the surface
E = Erosion rate (volume loss / impact mass)
ρ = Density of the target material
H = Hardness of the target material
c = Fraction of particles which cut in idealised manner
M = Mass of abrasive particles
p = Plastic flow stress of the material
f(α) = Function of impact angle
v = Particle velocity
n = Velocity exponent (typically in the range 2.2 – 2.4 for metals)

2.11.4.2 Brittle materials:

Several models for brittle erosion have been proposed, involving the inverse proportionality to the hardness and fracture toughness principle. The model below was that proposed by Evans et al. to predict the volume of material removed for normal impacts [136].

Volume of material removed:

$$V_i = Const \cdot \mathrm{v}^{3.2} \cdot {r_p}^{3.6} \cdot {\rho_p}^{1.6} \cdot {K_c}^{-1.3} \cdot H^{-0.25} \quad \text{Equation 9}$$

Applying the assumption:

$$E = \frac{M}{V_p \cdot \rho_p} \cdot V_i \cdot f(\alpha) = \frac{M}{{}^{4}/_{3}\,\pi \cdot {r_p}^{3} \cdot \rho_p} \cdot V_i \cdot f(\alpha) \quad \text{Equation 10}$$

Thus:

$$E = Const \cdot M \cdot v^{3.2} \cdot {r_p}^{0.6} \cdot {\rho_p}^{0.6} \cdot {K_c}^{-1.3} \cdot H^{-0.25} \cdot f(\alpha) \quad \text{Equation 11}$$

Where: V_i = Volume of material removed per impact
V_p = Volume of a particle
E = Erosion rate (volume loss / impact mass)
M = Mass of abrasive particles
v = Particle velocity
r_p = Particle radius
ρ_p = Particle density
K_c = Fracture toughness of the material
H = Material hardness
$f(\alpha)$ = Function of impact angle

In summary, the above models show the primary impingement parameters influencing the erosion process; impact angle, mass of erodent (given by the duration of exposure), particle velocity and density, material fracture toughness and hardness. Others parameters such as particle shape, testing temperature are important as well.

2.11.5 Erosion of EB PVD TBCs

As can be seen from Figure 38, solid particle impact has a detrimental effect in the compressor section of a gas turbine engine, by eroding the leading edge of the compressor blade. Studies into the erosion behaviour of thermal barrier coatings are somewhat more limited in the open literature, especially studies looking at the effect of erosion on the lifecycle of an electron beam physical vapour deposited TBC. This is because the stress due to thermal expansion mismatch between the TBC topcoat and the substrate, and the TGO at the top coat/bond coat interface were identified as the primary life limiting factor of the coating system. For this reason, understanding the erosion behaviour of coating was perceived as being of secondary importance. From Figure 45, EB-PVD TBCs have a higher erosion rate compared to bulk zirconia, but performed better when compared to APS TBCs due to their columnar microstructure which gives them a superior strain tolerance over APS TBCs [6].

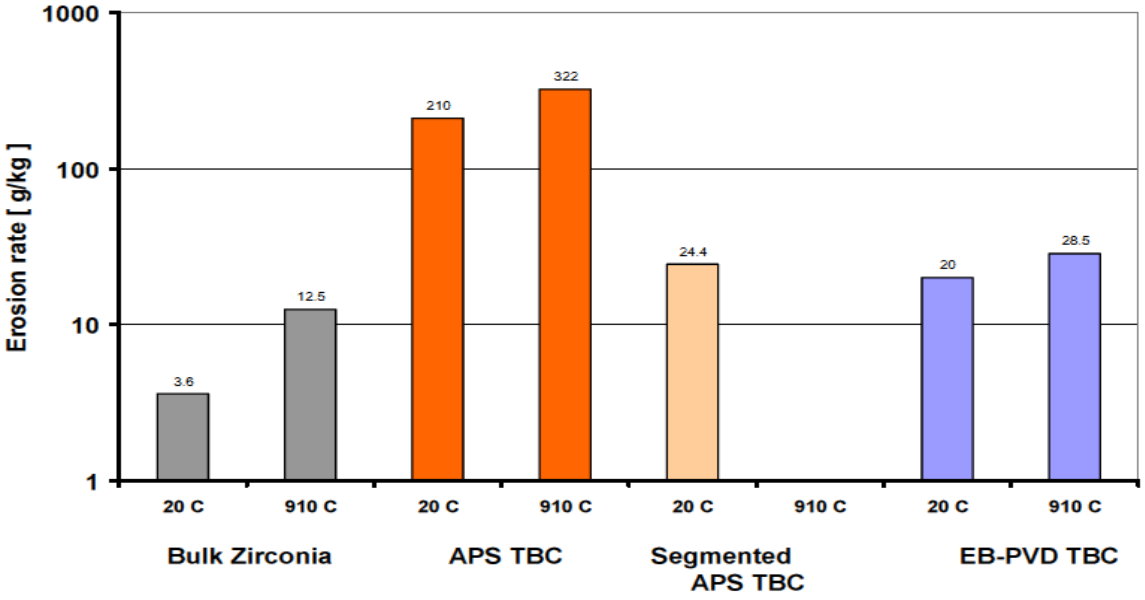

Figure 45: Comparison of the erosion performance of APS, EB-PVD and segmented APS coatings at room temperature and 910ºC. Bulk ZrO_2-7wt%Y_2O_3 ceramic reference is included [6].

It can be noted from Figure 45 that, both the APS and the EB-PVD coatings show a variation in the extent of erosion response. From Figure 45, it can also be said that at room temperature (20ºC) and high temperature (910ºC), the splat-like APS microstructure have an erosion rate greater than the columnar microstructure of EB-PVD coating by a factor of approximately x10, under normal (90º) impact conditions. For the EB-PVD columnar microstructure, the erosion rates were 20 g/kg (20ºC, 140m/s) and 28.5g/kg (910ºC, 230m/s) compared to 210 g/kg (20ºC, 140m/s) and 322g/kg (910ºC, 230m/s) for that of the APS splat-like microstructure. Nicholls and Wellman [6] also noted that bulk zirconia was significantly more erosion resistant than both the APS and EB-PVD coatings (the EB-PVD ceramic erodes at x 2 to x 5 the rate of bulk zirconia, depending on test temperature).

Fleck et al. [137] used finite element analysis to explore the elastodynamic response of EB-PVD TBC columnar structure to normal and oblique impact by an erosive particle. It was found that the TBC columnar layer acts as a set of independent wave guides. The magnitude of the tensile stress was found to be in the order of ρcV, sufficient to cause columnar fracture due to lateral propagation of pre-existing flaws near the top of the coating. Erosion response was found to be sensitive to size, shape and approach direction of the incoming particle and to the details of the TBC geometry, whereas the peak tensile stress was found to be sensitive to the level of friction between columns and between particle and top of the TBC [137].

2.11.6 The Need for an Erosion Resistant TBC

Initially, TBC applications were restricted to non-critical applications [138]. However, with the push for greater turbine engine efficiency, coupled with the drive for lower emissions and high operating temperatures, TBCs are increasingly finding use on load-critical applications. TBCs are critical in the race to achieve improved engine performance and durability of next generation turbine engines, because of their ability to allow increased engine gas temperatures and reduced cooling requirements. In order to meet the stringent requirements

of future engine design and desired performance, extensive research efforts have been invested in developing advanced TBC compositions, processing techniques and erosion mechanism models, to improve the erosion resistance and impact toughness of the coating [139].

Although significant advances have been made in thermal barrier coating technologies for reduced thermal conductivity, increased temperature capability and improved cyclic durability, erosion and impact resistance improvements of the coating systems have remained one of the most significant challenges for turbine thermal barrier coating developments and applications [139]. Erosion problems under such conditions can lead to loss of the ceramic topcoat and subsequent increase in the operating temperatures of the metallic substrate. This effect could have disastrous consequences to the components being protected, in terms of the performance and overall engine integrity [140].

Thermal barrier coatings are particularly prone to foreign object damage and erosion. In gas turbine engines, the source of the particulates inducing erosion may come from ash or runway sand ingested with the air intake during take-off and landing of the aircraft. These particulates often may be generated within the combustor of the gas turbine engine as a by-product of incomplete fuel combustion. Depending on the size, particles are initially entrained in the aerodynamic flow contour of the gas path. However, centrifugal load in the engine eventually forces them to deviate and impinge at various angles on engine parts in their path [135].

The overall effect of erosion is the gradual thinning of the TBC, resulting in reduction of thermal insulation and aerodynamic efficiency. This may result to partial or complete loss of ceramic top coat, exposing the underlay bond coat and metallic substrate to aggressive gas temperature which will eventually accelerate the process of oxidation [135]. The following approaches have been proposed for improving the impact and erosion resistance of TBCs.

- Composition modifications and composite toughening
    - low thermal conductivity compositions
    - fracture toughness improvement
    - composite toughening
    - TGO/bond coat interface toughening
- Microstructure modifications
    - Porosity effect
    - Modulated/wavy TBC structures
- Deposition, infiltration and reaction with CMAS particles
    - Thermomechanical effect
    - Thermochemical effect

2.12 Chemical (Molten Deposit) Attack of TBC's caused by Volcanic Ash and CMAS Infiltration – Turbine Section

Volcanic ash and CMAS-type material constituents ingested by the fan of a gas turbine engine will cause various damages to the engine, erosion in the compressor section and molten deposit attack (including blockage of the cooling holes shown in Figure 46) in the turbine section being the most severe. When for example volcanic ash is ingested by the engine, it will first cause erosion problems in the compressor section while those particles that make it pass the compressor section will be carried in the airstream to the combustor, where they melt and are projected on the surface of turbine blades in a molten state hence, attacking the TBC (also known as CMAS/molten deposits attack mentioned previously). Relatively cool air (~600-700 °C) is bled from the compressor into the cooling holes of turbine blades and the ash contained within the cooling air may melt and eventually freezes (due to thermal gradient across the blade) to block the cooling passage.

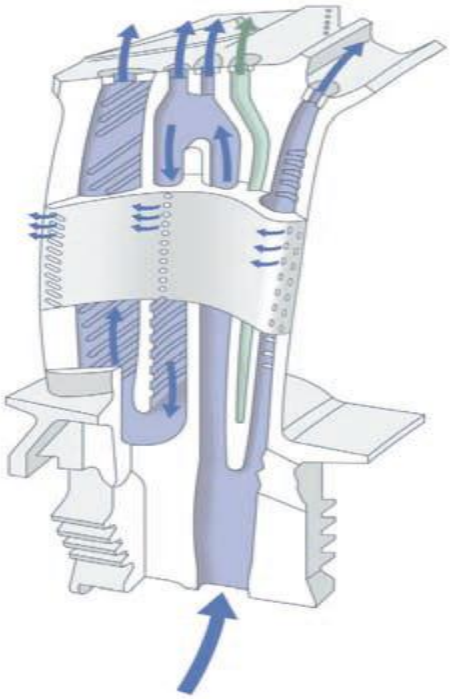

Figure 46: HP turbine blade cooling flows. Courtesy of Rolls-Royce [2]

This thesis investigates the outcome when volcanic ash and CMAS materials are ingested into an engine, their journey from the compressor section (where the engine temperature is not hot enough to induce melting) to the turbine section (it is expected that different stages of the compressor will mill the ash into fine particles and propelled them into the combustion chamber and eventually deposited on the surface of the coating or alternatively travel with the cooling air and block the fine cooling passeges within the blade).

3 CMAS vs. VA: Introducing the Concept of Basicity Index for TBCs

Although the major discussion over the concept of Basicity Index will be addressed in the discussion section, it is introduced here as part of the background to the project. The ideas surrounding the application of the concept of Basicity to TBCs was formulated during the early stages of this thesis and is formed a significant part in the planning of the testing, to test and validate the concept.

Molten deposit in this work refers to a glass-like product, with calcium, magnesium, aluminium and silicon as its main elements and some other minor oxides. The composition and properties of the molten deposits found in an aircraft engine can greatly affect the severity of damage caused. CMAS is the term given to oxides known as **C**alcia-**M**agnesia-**A**lumino-**S**ilicates, formed from siliceous material ingested with the air intake (sand, dust, volcanic ash and runway debris). SiO_2, Al_2O_3, CaO and MgO are the common oxides found in both volcanic ash and CMAS (Table 9), although in different fractions. Volcanic ash may also contain iron oxides and various other trace elements and alkali-metal oxides.

$CaO + SiO_2 + MgO + Al_2O_3 \longrightarrow$ Model CMAS

$CaO + SiO_2 + MgO + Al_2O_3 + Fe_2O_3 + TiO_2 + Na_2O$ + others $\longrightarrow$ Volcanic ash

} Molten Deposit

The composition and properties of the molten slags found in an aircraft engine can greatly affect the severity of damage caused [65]. At elevated temperatures (temperatures around or above 1240 °C, depending on composition) siliceous debris can deposit on the top of the TBC ceramic and then melt, yielding a molten, glassy deposit of CMAS.

Analysis of volcanic ash particles can provide important information necessary to understand the problems associated with volcanic ash clouds; such as aircraft engine damage, visibility,

atmospheric dispersion, and ash deposition. By using the latest analytical techniques, particles can be characterised in terms of morphology (size and shape), density, mineralogy and chemical composition [146]. Volcanic ash can cause serious damage to an aircraft engine, if the ash reaches the flight path used by an aircraft. This damage can be terminal or, at a minimum, very expensive to repair. [146].

Improvements in monitoring techniques and better tracking of volcanic ash clouds are necessary in order to avoid a repeat of what happened in April 2010, where there was an unprecedented closure of most airspaces right across Europe, due to the presence of volcanic ash in the atmosphere, generated from the active Icelandic Eyjafjallajokull volcano [147; 148]. This prompted those involved in the aviation industry and engine manufacturers to establish a safe level of ash ($2mg/m^3$) which their product can tolerate without causing significant damage to the aircraft. Since volcanic ash (akin to CMAS) attack is a Time-Temperature dependent reaction, further studies were commissioned, to better understand the potentially damaging effect of volcanic ash.

3.1 Interacting Parameters Affecting the Severity of CMAS Attack

Findings of this research and the work by Whitman et al. [13] stipulate that, simulated CMAS and VA caused varying degrees of damage to coating microstructure, which agrees with published literature [7; 68; 69; 73; 76]. So far, it can be concluded that, time and temperature will affect the depth of attack (factor which may be attributed to wetting characteristics and viscosity of VA/CMAS) but neither attack mechanism nor the severity of the attack have been related to the degree of exposure. Therefore, it was vital to build an understanding as to the conditions that favour this mode of attack. Five inter-related parameters are proposed in this work that may influence both the attack mechanism and the severity of degradation of an EB-PVD coating by molten deposits. The proposed parameters are Basicity, Wettability,

Viscosity, Time and Temperature. However, the individual effects of these parameters as well as their collective effect on damage mechanism is part of the ongoing study and their interactive behaviour and severity shall be investigated as part of future studies. Based on these parameters, the model in Figure 47 is proposed, which is a schematic of the expected inter-relationship of Basicity, Wettability, Viscosity, Time and Temperature.

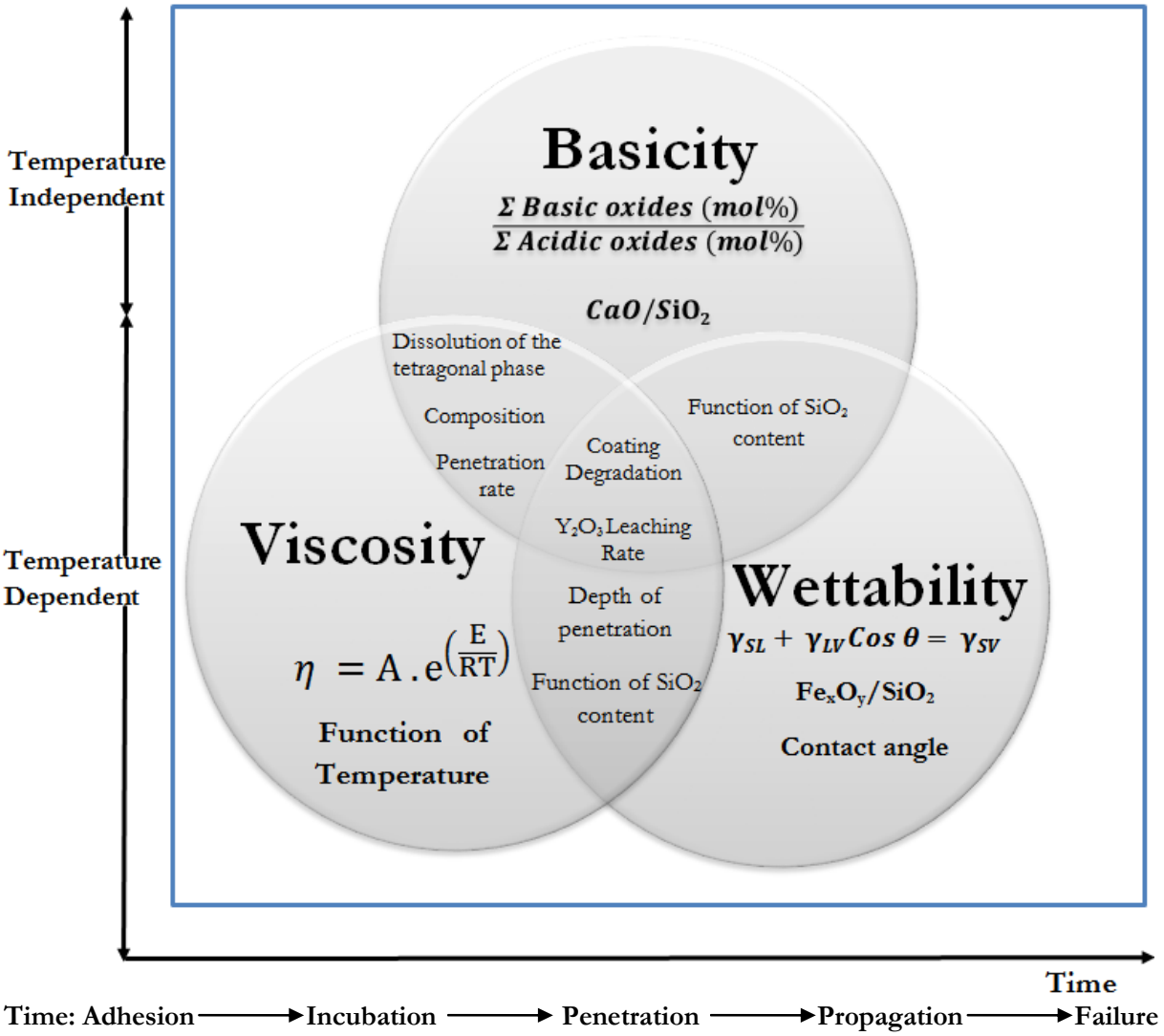

Figure 47: Five interacting parameters that determines the severity of damage to TBCs caused by molten oxides

While for a given chemical composition, time at temperature will determine the depth of penetration and the Y_2O_3 leaching rate. However, the chemical composition (especially

CaO/SiO_2 ratio) of the slag is equally important in determining the degree of degradation, as the composition will determine the Basicity, Viscosity and Wettability of the slag.

Depth of penetration is most likely a function of Viscosity and Wettability (together with time at temperature). Whilst viscosity describes the melt's resistance to flow, wettability is the tendency for the melt to spread on and adhere to or "wet" the surface of the TBC. However, more research is needed to determine which of these parameters has a more dominant effect on the depth of penetration. It is clear, though, that if the molten CMAS or volcanic ash is non-wetting it will not adhere or infiltrated and would be expected to be removed by high velocity gas stream through the engine.

A new and novel concept of Basicity Index, with regard to CMAS, to evaluate the degree of molten deposits degradation is introduced in this project. An in-depth study to understand the effect of a slag's Basicity Index on the severity of coating degradation was undertaken as a key objective of this work, in an effort to support the model featured in Figure 47. Here, Basicity is defined as the ratio of calcia to silica (CaO/SiO_2). However, in general terms, a slag's Basicity Index must be defined as the molar ratio of basic oxides to acidic oxides.

From the graph in Figure 49, it is evident that there exist variations in the Basicity Index of the deposits used by various referenced authors and this reflects in the results presented (they are presented in identical units), mechanisms observed and severity of damage. Research by Stott et al. [65] showed that engine debris compositions (i.e. CMAS) vary considerably between regions of the world. Basicity Index as a unit is expected to play a vital role in categorising these different degradation mechanisms observed and the severity of damage. Ternary phase diagrams (Figure 48) was used in conjunction with a DSC (Figure 74) to study the glass transition temperatures (T_g) and the crystallisation temperatures (T_c) of the different slag compositions reproduced in Table 13.

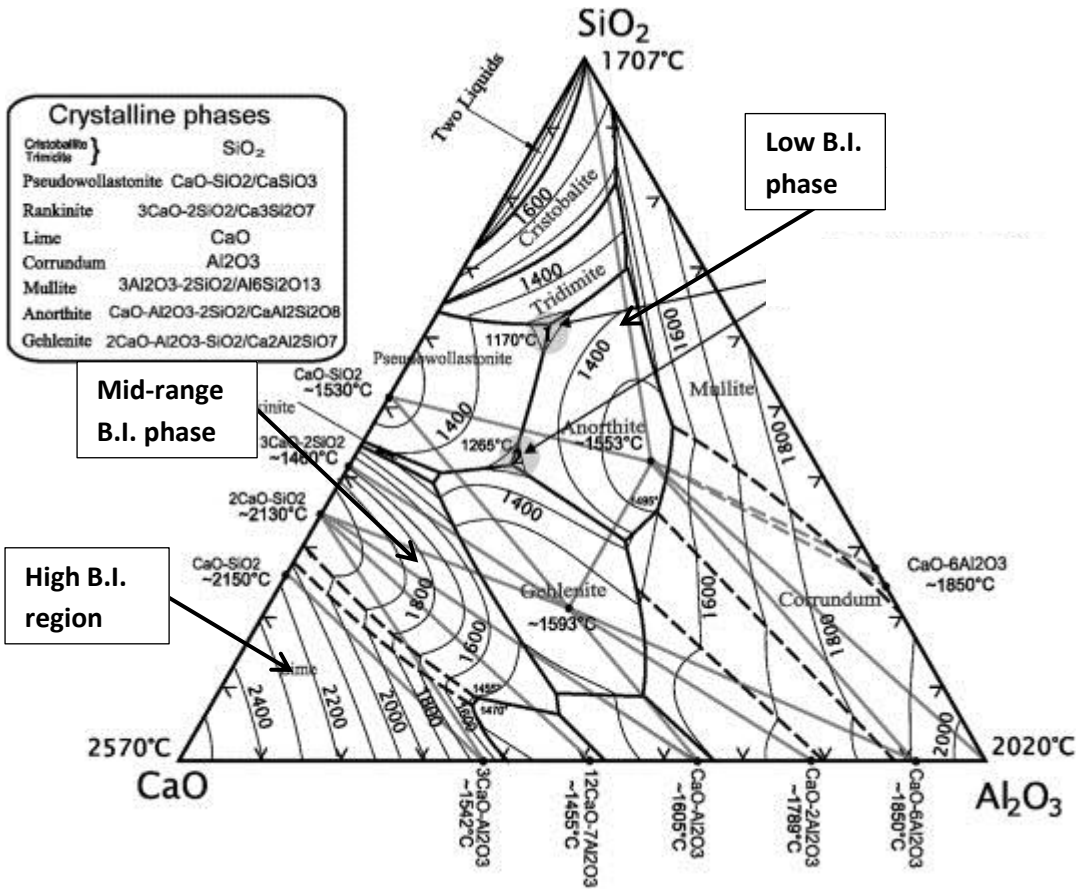

Figure 48: Ternary phase diagram of system CaO–SiO_2–Al_2O_3 [103].

The variation in melting temperatures can be confirmed by comparing these compositions to a ternary phase diagram, where the lower B.I. composition are found within the Anorthite region compared to the high B.I., lime region. This confirms Stott et al. [65] study which noted that CMAS melting temperature will vary depending on composition.

A set of experiments were designed to test this concept of Basicity, each performed under isothermal heat treatment condition at a fixed temperature above the melting point of the deposit used. The melting temperature of each composition is mentioned in Table 13 and the temperature differential (ΔT) above their melting points was set to 50 °C. 50 °C was chosen as the ΔT in order to ensure sufficient over temperature in the furnace that all slags would reach molten state. All the samples were exposed for 30 minutes, 1, 2, 4 and 8 hours at temperature and then analysed.

It has been reported in the literature that damage caused by molten deposits and slag penetration rates relate to Basicity [149]. Basicity was a term first coined within the steel industry to measure the slag chemistry within the ceramic blast furnace and is now accepted within blast furnace design and relates to molar ratio of basic and acidic oxides [110]. However, with respect to CMAS attack in the aerospace industry, Basicity was first proposed by Ndamka in 2011 [150] and then later accepted and referenced by Levi et al in 2012 as part of their review paper [71]. Basicity and melt viscosity may also be inter-related [110]. The predominant indicator in slag basicity is the CaO/SiO_2 ratio, as the CaO/SiO_2 ratio is thought to determine the overall behaviour of the slag system [110]. In this study, Basicity is modified to acknowledge that amphoteric oxides may exhibit either acidic or basic roles. Thus, the Basicity Index is found to vary among different compositions of CMAS and using data from previous studies, this is illustrated in Table 11.

Table 11: Comparison of CMAS compositions from previous authors with associated calculated Basicity Index

Elements (mol.%)	**Wellman et al. (2010)** [13]	**Aygun et al. (2007)** [73]	**Borom et al. (1996)** [70]	**Kramer et al. (2006)** [11]	**Smialek et al. (1994)** [72]	**Rai et al. (2010)** [12]	**Wolfgang Braue (2009)** [75]
CaO	35	38	32.1	33	20.9	32.7	33.6
MgO	10	5	10	9	9.5	9.4	9.9
Al_2O_3	7	4	6.9	6.5	7.5	6.8	10.1
SiO_2	48	50	46	45	49.8	46.2	22.4
TiO_2	-	-	-	-	1.8	-	-
FeO	-	-	-	-	-	-	-
Fe_2O_3	-	1	3.2	-	4.7	3.2	-
NiO	-	-	1.6	-	4.2	1.7	-
Na_2O	-	1	-	-	1.5	-	
K_2O	-	1	-	-	-	-	-
B. I.	**1.08**	**1.00**	**1.17**	**1.08**	**0.94**	**1.16**	**1.90**
Melting temp °C	**1235**	**1121**	**1290**	**~1200**	**1136**	**~1190 – 1260**	**1135**

In general, slag compositions can be classified according to the oxide groups as follows [105];

- Modifiers (Basic oxides) – CaO, MgO, Na_2O and K_2O
- Glass formers (Acidic oxides) – SiO_2 and P_2O_5
- Amphoteric oxides – Al_2O_3, TiO_2 and Fe_2O_3.

Acidic oxides tend to enhance polymerisation, while basic oxides tend to disrupt the process of polymerisation in the melt. The amphoteric oxides can act either as acidic or basic oxides [105]. In this study, a slag Basicity Index (B.I.) was defined using Equation 12 and it is proposed that if the melt is basic, amphoteric oxides behave as an acid until the B.I. reduces to 2; if the melt is acidic, amphoteric oxides behave as a base until the B.I. increases to 2; in neutral melts the amphoteric oxides can be considered neutral (this explanation is based on a neutral Ca_2SiO_4 slag composition). In this study, the slag Basicity Index was defined as:

$$\text{Slag Basicity index (B.I.)} = \frac{\sum Basic\ oxides\ (mol\%)}{\sum Acidic\ oxides\ (mol\%)} \qquad \text{Equation 12}$$

In a binary $CaO{-}SiO_2$ slag system, neutral composition corresponds to the formation of the ortho-silicate composition $2CaO.SiO_2$ [104]. A $CaO{-}SiO_2$ dominant slag system will become neutral when two moles of lime (CaO) are present for each mole of silica (SiO_2) to give two Ca^{2+} cations and one SiO_4^{4-} anion. Since one molecule of the oxide of a bivalent element forms one cations and one oxygen ion, the neutral melt here contains cations and oxy-acid silica groups in the ratio of 2:1. This applies if Na_2O or K_2O alkali oxide groups are incorporated in the melt. In a neutral melt, all the oxygen bonds of the silicon ion are satisfied and an increase in the CaO concentration results in the presence of free oxygen ions. Conversely, if the CaO content is reduced, some of the SiO_4^{4-} ions become unsaturated and degenerate into $Si_2O_7^{6-}$ or similar groupings [104].

In light of the foregoing considerations, a neutral melt can be defined as one with CaO content of 66.7 mole% and the system will be basic only when CaO content is more than 66.7

mole% [151]. For a slag system to become neutral, enough oxygen ions will have to be present to ensure that each tetrahedron remains independent of each other. Based on the ortho-silicate composition of a neutral slag system, the Basicity Index (B.I. from Equation 12) for a neutral slag is equal to 2. Since amphoteric oxides can behave either as an acidic or basic oxide, depending on the composition of the system, then if the CaO/SiO_2 ratio < 2, amphoteric oxides will behave in a basic manner. In this case, it is proposed that amphoteric oxides are treated the same as basic oxides. Similarly, if CaO/SiO_2 ratio > 2, amphoteric oxides will act in an acidic manner and therefore will be treated as an acidic oxide. The implication of this is that amphoteric oxides provide a buffer such that a neutral slag may exist over a range of compositions. In this study, the range is taken as 1.8 to 2.2, a ±10% variation on the neutral composition. The Basicity Index calculation (see Appendix A) from Equation 12 for Eyjafjallajokull volcanic ash and the standard CMAS used in this study is given in Table 12, both belonging in the acidic Basicity Index category, with the volcanic ash much more acidic than the standard CMAS composition, as proposed in other studies [13].

Table 12: Volcanic ash and CMAS Basicity Index values

Mineral	**Basicity index**
Eyjafjallajokull Volcanic ash	0.46
Standard CMAS [13]	1.08

The graph in Figure 49 is constructed from the CMAS main oxides compositions from the referenced authors (Table 11), plus the calculated Basicity Index (B.I.) using Equation 12, based upon the slag composition as shown within Figure 49. The most basic composition (still near to neutral) was that proposed by Wolfgang [12], while the most acidic composition was that used by Smialek et al. [72], with the composition proposed by Wellman et al. [13] in a region still acidic but midway between Wolfgang and Smialek's works. Apart from these,

the remaining compositions have a Basicity Index close to one. The B.I. within this study as defined by Equation 12 varies from 1-4, with three distinct regions associated within this Index. Values of 0-1.8 refer to Low Basicity Index melts, 1.8-2.2 refer to Mid-range (Near Neutral) Basicity Index and >2.2 refers to High Basicity Index melts.

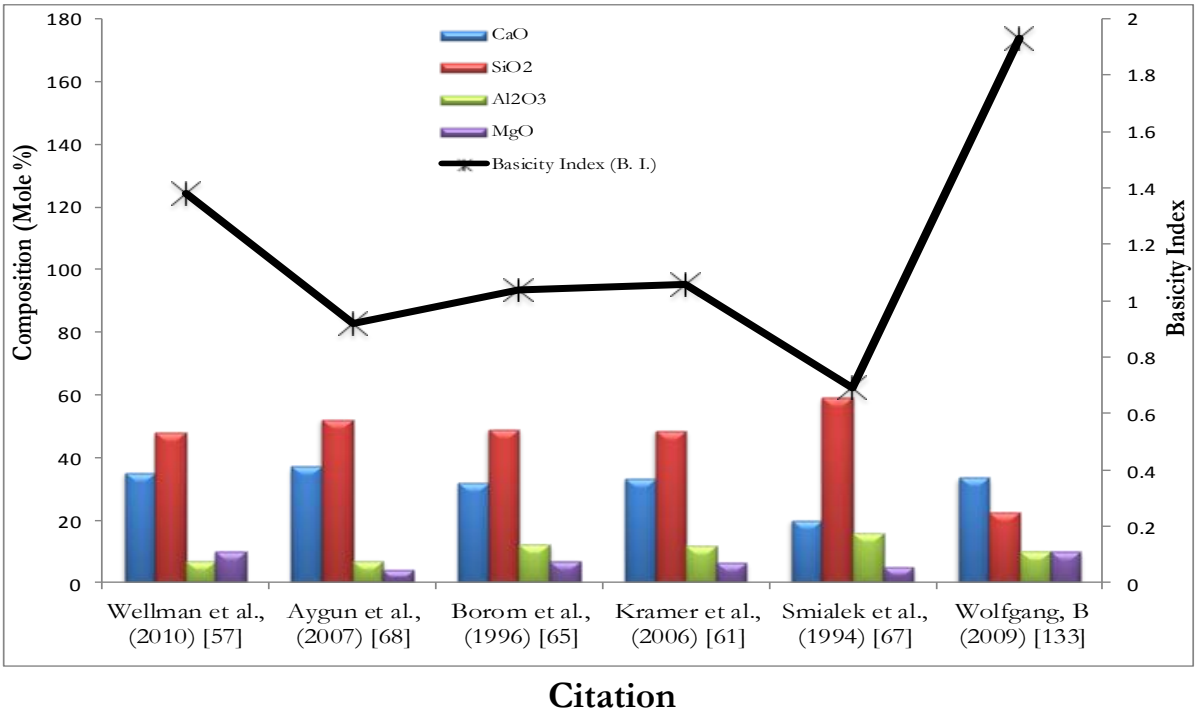

Figure 49: Comparison of CMAS compositions with Basicity [150]

The interrelationship between Basicity Index and the melting point of the slag was also investigated and the result is shown in the graph in Figure 50. A differential scanning calorimetry was used to determine the melting temperatures of the deposits and using the B.I. equation as defined in Equation 12, the plot in Figure 50 was generated. An increasing trend is observed, that suggests the melting point increases with Basicity Index of the molten slag up until a Basicity Index close to 2, where upon it remains approximately constant out to a value of 4.

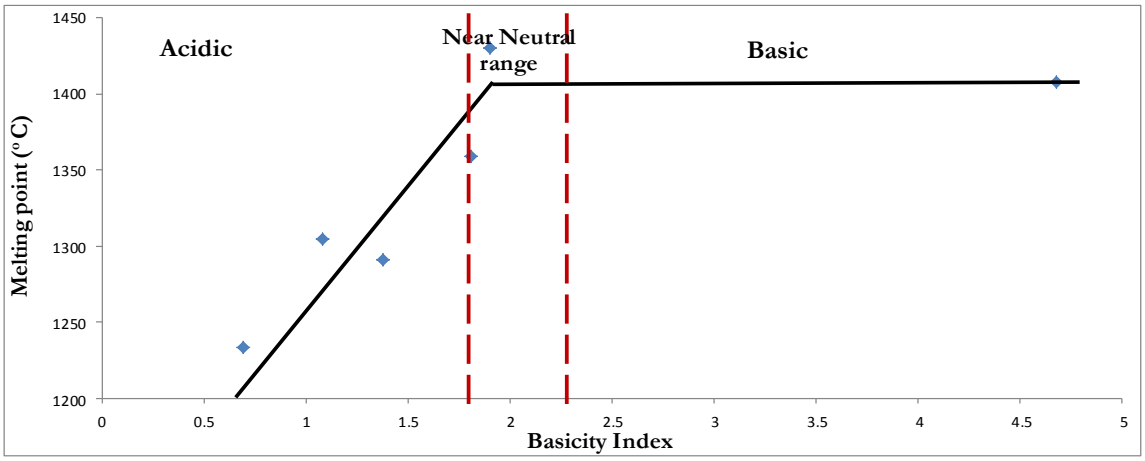

Figure 50: Interrelationship between deposit melting temperature and the Basicity Index of the melting.

3.1.1 Review of Basicity Index

The concept of Basicity Index (B.I.) is commonly used in industries including mining and steelmaking. In steelmaking, Basicity Index is used to detect the quality and the chemical composition of the slags formed [104]. Steelmaking relies on the formation of slags in order to remove unwanted elements from the metal and also purify the metal by forming oxides and floating them off the molten metal. Basicity Index is then employed to analyse the slag which will give an indication as to the foaminess/viscosity of the melt, the amount of FeO generated and the overall quality of the metal produced [152].

In welding, Basicity Index is used to describe the metallurgical behaviour of a welding flux. Basicity Index has a great influence on the impact toughness of the weld metal, by determining the level of impurities in the welded joint. Welding fluxes are divided into three groups based upon the definition of Basicity Index (the ratio between basic and acid compounds); Acid fluxes (Basicity <0.9), Neutral fluxes (Basicity 0.9 – 1.2) and Basic fluxes (Basicity >1.2) [153].

This study was the first to modify the concept of Basicity Index and adopt it in ceramic chemistry in order to investigate the effect of environmental dusts ingested by a gas turbine engine on thermal barrier coating systems, in terms of microstructural degradation.

4 Experimental Procedures

4.1 Analytical and Observation Tools:

Molten deposits (VA and simulated CMAS) can have a significant effect on the behaviour of EB-PVD TBC it comes into contact with. Therefore, it is important to characterise the chemical composition of the starting materials. The VA and CMAS samples were analysed using various techniques to determine their chemical compositions, particle size and distribution. Differential scanning calorimetry (DSC), X-Ray diffraction (XRD), optical microscopy, optical imaging microscopy, Raman spectroscopy, scanning electron microscopy (SEM), electron backscatter diffraction (EBSD) and focused ion beam (FIB) were the major characterisation techniques used in this work.

4.1.1 Optical Microscopy

Optical microscopy was a vital tool for first stage investigation and also for checking quality during sample polishing. The microscope used was a Nikon optical microscope equipped with a JVC CCD sensor camera for image acquisition. However, the optical microscope on its own was not relied upon because of the relatively low magnification (x100 to x1000) offered by the optical microscope and the thickness of the coatings throughout this study.

4.1.2 Scanning Electron Microscope (SEM)

Samples of volcanic ash are non-conductive which is why the Philips XL30 ESEM was used so as to avoid the need to coat the samples before analysis, which would have been the case if using an SEM rather than an environmental SEM. The Scanning Electron Microscope (SEM) uses a fine focused beam of electrons, which scans across the surface of the sample. An SEM produces images with a large depth of field, a characteristic which is useful in understanding the surface topology of a sample. The SEM requires the sample to be capable of conducting

electrons and cannot be used on a non-conductive specimen, as this will lead to the specimen charging which will continually deflect the beam from position. However, when it was deemed necessary for the samples to be examined at high magnification using a FEG-SEM, the samples were coated in gold/palladium to make them conductive then an XL30 Philips SFEG-SEM was used to carry out the examination. ESEM differs as it does not require samples to be conductive; the sample environment can be varied through a range of pressures, temperatures and gas compositions. The ESEM retains all of the performance advantages of a conventional SEM, but removes the high vacuum constraint on the sample environment, which means non-conductive samples can be examined in their natural state without further modification or preparation. ESEM was used to examine the microstructure of the samples in cross section and also the top view. ESEM was also used to determine the particle size and distribution of the volcanic ash used in the experiments.

4.1.3 Focused Ion Beam

The Focused Ion Beam (FIB) is an analytical technique similar to scanning electron microscope (SEM) except an ion beam of gallium ions is used to image the surface. The FIB 200XP by FEI Company was used throughout this study. The FIB uses a finely focused ion beam to mill the surface of the sample in order to modify and generate secondary electrons (or ions) which are collected to form an image of the surface of the sample of interest. Because the contrast mechanism for FIB is different to that of SEM/TEM, unique structural information can be obtained.

4.1.4 Electron BackScatter Diffraction (EBSD)

Electron BackScatter Diffraction is a relatively new, scanning electron microscope-based surface analysis technique used to characterise microstructures and textures (“texture” means degree and nature of alignment of the crystal lattices in a sample) in crystalline materials

(metals, ceramics). EBSD is an SEM based microstructural-crystallographic technique employed to measure the crystallographic orientation [141]. In EBSD, electrons are inelastically scattered in all directions from a high angle of incidence, optimally 70 degrees, towards the sample surface. Since nearly all SEMs have vertical columns, this is accomplished by tilting the sample on the SEM stage, mounting it on a pre-tilted sample holder, or a combination of the two. This glancing angle allows most incident electrons to penetrate, scatter and propagate from the surface with a minimal energy loss, important because a crisp diffraction pattern requires a small electron energy spread. Higher angles are less optimal because spatial resolution rapidly degrades, particularly in the uphill-downhill direction [142].

4.1.5 X-Ray Diffraction (XRD)

X-ray diffraction was used to carry out qualitative phase analysis. However, since XRD can only provide information about the crystal structure of the phases present, it was used in conjunction with EDAX to identify the chemical compositions and local distributions. The diffractometer was mainly used with a typical $\theta/2\theta$ layout. A Siemens D5005 system was used to obtain the XRD peaks, with Cu-Kα radiation (λ=1.5405 Å), 35 kV accelerating voltage and 20 mA of current. XRD operation follows Bragg's law in order to measure the cell parameters from diffracted peaks.

4.1.6 Differential Scanning Calorimetry (DSC)

The principle of DSC is to measure the difference in temperature (ΔT) between the sample and a reference (usually alumina), both placed in a small calorimeter crucible and subjected to the same heat treatment. When an exothermic reaction occurs, there is a subsequent increase in the temperature of the sample, resulting in an increase of ΔT (e.g. solidification of a liquid). On the other hand, an endothermic reaction is followed by a decrease in ΔT. This

method of thermal analysis is superior and gives the actual enthalpy of a reaction by integrating the peak areas. The apparatus used was a "SETSYS Evolution 16" manufactured by Setaram. It was designed for both DTA/DSC and thermogravimetry. The heating is provided by a high performance graphite furnace, with heating range up to 1600 °C.

4.2 Volcanic Ash and CMAS Chemistry

4.2.1 Volcanic Ash

The volcanic ash used in this study was collected some distance away from the volcano, which ultimately determines the size fraction of the ash. As expected fine ash particles travelled furthest away from the volcano while coarse ash (denser) particles fall close to the volcanic source. Volcanic ash size fractions decrease exponentially with increasing distance from the source [143]. Fine ash particles were those collected furthest from the volcanic source whereas coarse ash particles were collected closest to the volcano. In this study no volcanic ash aerosols were collected and analysed. However, smaller sized particles are expected to travel further and to last longer in the atmosphere. Therefore volcanic ash aerosols are expected to exhibit similar characteristics as "fine" ash particles in this study. This assumption is supported by the published composition by Sigfusson et al. [101] of Eyjafjallajökull volcanic ash aerosols, showing very similar composition to fine size volcanic ash.

However, the "as received" volcanic ash particles were sieved into three size fractions to obtain the desired grain size and then analysed using energy dispersive spectroscopy (EDAX), attached to an environmental scanning electron microscope. Microstructural analyses were also performed using an ESEM to reveal the size and distribution of the volcanic ash particles. The natural occurring volcanic ash is expected to exhibit a superior chemical complexity than laboratory grade synthetic CMAS often used in research. The

compositional variation of the different size fractions of volcanic ash is discussed in the result section.

4.2.2 CMAS Preparation

The CMAS compositions as reported by different authors are given in Table 11 while the compositions of CMAS that were used in all the experiments are shown in Table 13. The "standard" composition of synthetic CMAS used in Cranfield University for this purpose was $C_{35}M_{10}A_7S_{48}$, also referred to as "standard CMAS" composition. This composition was based on the average composition of molten slags that were found to have penetrated the TBC of an aircraft engine operated in a desert environment [70], but not including impurities believed to have originated from the engine (Ni, V, Ti, S, and Fe) [69]. This CMAS composition falls in the pseudo-wollastonite region in $CaO\text{-}SiO_2\text{-}Al_2O_3$ ternary phase diagram (see Figure 48). Pseudo-wollastonite has the stoichiometry formula $CaSiO_3$ and is a high-temperature crystal. However, with the introduction of this novel concept, Basicity Index, model CMAS of different compositions (Table 13) were prepared in order to rigorously tests the aforementioned concept. Ternary phase diagrams and DSC were used to identify the melting temperatures of these compositions. The synthetic CMAS compositions were made by mixing high purity fine powders of the individual oxides by ball milling, which were later transferred into a spray bottle and subsequently applied to the samples, by atomised spraying along with a solvent.

Table 13: Composition of model CMAS used in the Basicity Index study

Model CMAS Composition	Tg (°C)	Tc (°C)	Tm (°C)
$C_{73}M_{10}A_7S_{11}$	936	681.1	1407.9
$C_{55}M_{10}A_7S_{29}$	928	707	1358.5
$C_{56}M_{10}A_7S_{28}$	915	705.4	1430
$C_{24}M_{10}A_7S_{59}$	890	674.8	1234.2

4.3 Sample Preparation

Alumina (99.9% purity Al_2O_3) discs were used as the substrate material and were then coated with a ZrO_2 – 8wt% Y_2O_3 or an Er_2O_3-doped 8YSZ TBC, deposited by EB-PVD. The microstructure of EB-PVD coated TBC system has a higher porosity (approximately 70% of the theoretical density). This is representative of commercial production, but makes it susceptible to molten deposit attack. One outcome of such attack and penetration is a substantial reduction in thermal conductivity of the TBC can be expected [12]. These experiments were carried out under isothermal heat treatment conditions, as opposed to thermal gradient conditions in the real situation, where there is a temperature gradient across the system. In order to standardise this experiment, the amount of CMAS powder applied has to be controlled. To ensure a near even infiltration throughout, a repeatable and reliable method was required to quantify the amount of CMAS/VA applied to the sample.

Volcanic ash samples used were in the "as received" composition, with no extra preparation required. However, it is important to keep samples within specific size ranges, taking into consideration the size of the particle that is likely to travel into the path used by the aircraft and also across the continent, from the volcanic source. According to Smith et al. (2010) [143], particle sizes up to about 57 µm were reported to have reached countries across Europe from the eruption source in Iceland. Smaller particles are likely to be in the atmosphere longer and in the path taken by the aircraft, hence smaller particles are most likely to interact with aircraft. Thus the volcanic ash (VA) samples used throughout this study were blended from sub-50 µm particles.

A pneumatic spray gun was used to apply the VA and CMAS as consistently as possible onto the different samples. CMAS/VA was weighed and transferred into a spray gun bottle which was then filled with distilled water. The powder was suspended in distilled water and sprayed

onto the samples under a fume hood. The mixture was made up of 1.5g of powder (VA or CMAS) and approximately 50ml of distilled water. The spray gun was externally connected to a compressed air line and the assembly was held in a clamp to ensure it was in the same position when spraying the samples (Figure 51). The samples were preheated to 120 °C to encourage the instant evaporation of the water. The samples were then weighed and the weight recorded (W_o). The samples were held by tweezers approximately 30cm away from the spray gun during spraying, and were rotated throughout the process to ensure an even distribution of the solution. The samples weight were again measured and recorded (W_f) and the weight of deposit (W_d) on each sample was calculated by $W_f - W_o = W_d\,(g)$. W_d equates to the amount of coverage of VA or CMAS on the sample prior to thermal ageing. Figure 51b illustrates a schematic of CMAS deposition on the surface of an EB-PVD TBC sample.

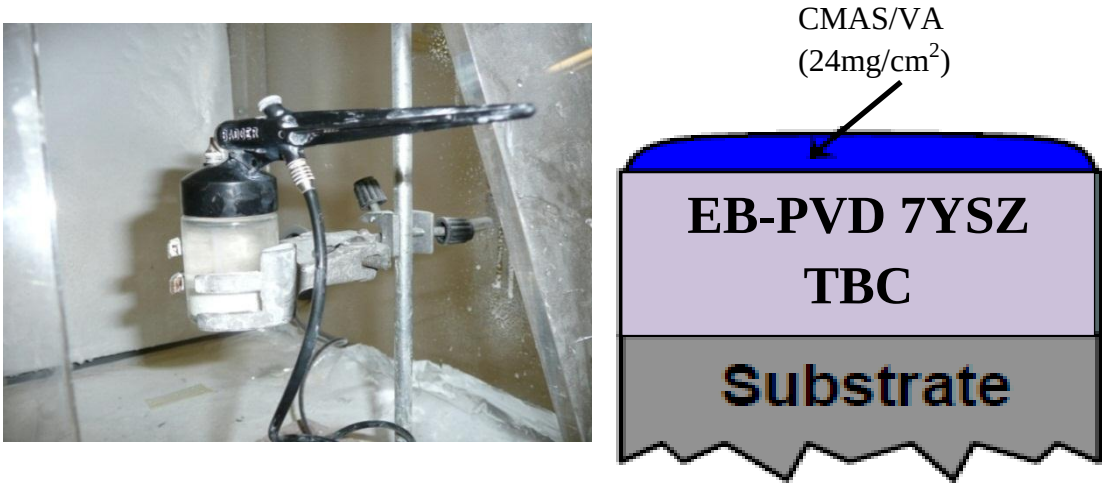

Figure 51: (a) spray gun bottle externally connected to a compressed air line and (b) Schematic of a CMAS deposited EB-PVD sample.

The experiments in this study were performed under isothermal conditions on EB-PVD TBC top coats with typical thicknesses of 170-210 µm, at temperatures in the range 1200-1500 °C for short term (1-24 hours at temperature) exposure and 1100 °C for long term (50 – 1000 hours at temperature) exposure. The experiments were divided into short-term and long-term

for time and temperature effects, variation in the amount of coverage and Basicity (compositional effect). The heat treatments were performed in a Pyro Therm furnace. Samples were removed from the furnace once the heat treatment was completed and were air cooled to room temperature.

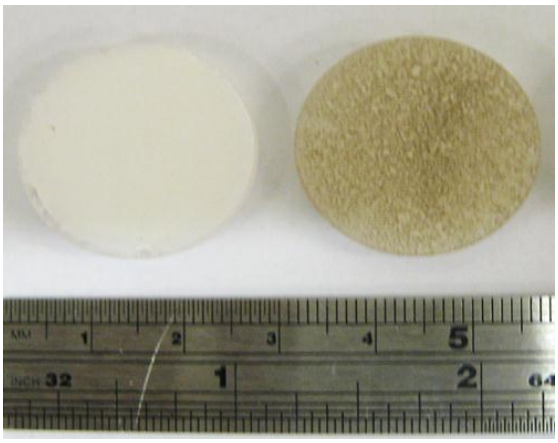

Figure 52: CMAS and VA (from left to right) on EB-PVD coated alumina discs.

4.3.1 CMAS and Volcanic Ash Interaction with YSZ EB-PVD TBC

Molten deposit interaction with YSZ thermal barrier coatings shows full penetration of the CMAS into the TBC, as shown by the cross-sectional micrograph in Figure 53. The resulting coating morphology (Figure 53) is drastically different to the "as-deposited" coating in Figure 17, indicating an interaction between CMAS and YSZ. Also noticed were Si and Ca from CMAS throughout the entire coating, indicating that CMAS has penetrated the entire TBC thickness. Viscosity and wetting characteristics of CMAS plays a role in CMAS penetration. The viscosity values for standard CMAS composition was calculated based on the viscosity model proposed by Giordano et al. [100], at two separate temperatures (their melting points and melting points + 50 ºC). Depending on the wetting behaviour of the molten deposit, CMAS will wet the surface of the coating and penetrate by capillary action into the pores and cracks. It will also attack the grain boundaries and dissolve part of the coatings resulting in

full penetration of the coating. The finding here that 7YSZ EB-PVD coatings have little resistance to CMAS penetration are consistent with what others have seen and reported.

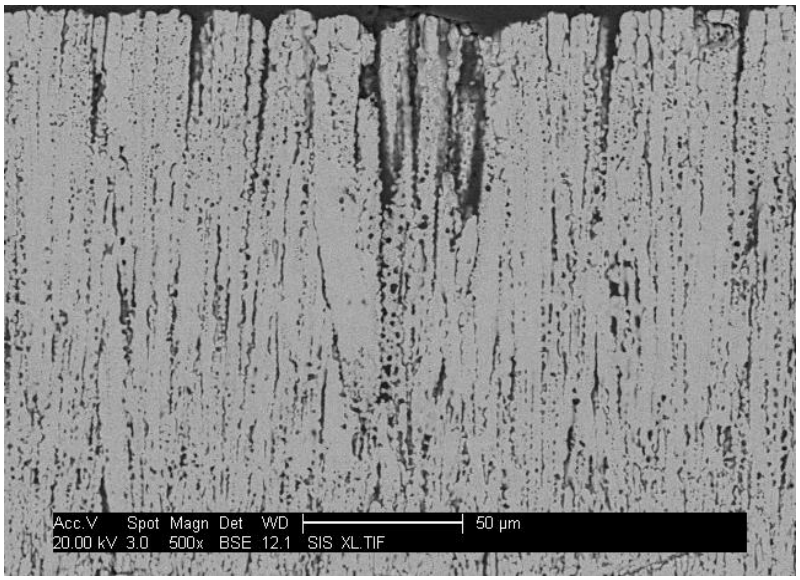

Figure 53: Scanning electron image of YSZ showing molten deposit induced degradation of entire TBC.

4.4 Mechanical Studies

4.4.1 Nanoindentation

Nanoindentation tests were performed on the top surface of a whole sample using a Zwick Roell Auto indenter. Nanoindentation is a method of measuring the mechanical properties (elastic modulus, hardness, fracture toughness and creep) of small volumes of materials and consists of imprinting a diamond indenter into the sample under investigation at a specified loading rate whilst monitoring the variation in the indentation depth. A dwell time at maximum load was included, to prevent gross errors due to creep [144]. In this study, the maximum load was 100 mN, the loading rate was 2.0 mN s^{-1} and the dwell time at maximum load 60 s. The deformation on the specimens upon loading and unloading of the indenter is a combination of both elastic and plastic strain [145]. Loading is attributed to both elastic and plastic deformation, whereas, unloading is linked to material recovery and

is principally an elastic phenomenon. Hardness, fracture toughness and elastic modulus of the material can be determined using this method.

4.4.2 Erosion Test

A series of erosion tests were performed using volcanic ash and MIL spec silica sand of similar sized fractions for comparison purposes. The volcanic ash (VA) used in this experiment was collected in the Eyjafjallajokull Icelandic eruption, obtained by Rolls Royce. The VA was then separated into three different size fractions, by sieving. Two grades of MIL spec silica sand were also used, MIL-810D, 98.5% SiO_2, with particle size in the range of 0-150 μm, in this thesis termed as "fine sand". The second grade, MIL-E5007, had a particle size range of 76 - 212 μm, which is referred to as "coarse sand" in this study.

Erosion tests were grouped under three different phases, all carried out under different conditions. The first phase of the test was conducted at room temperature and three different impact angles (30° , 45° and 90°) and comprised of 5 separate runs assessing the effects of different grits (volcanic ash and silica), and different size fractions. Table 14 summarises the different particle sizes used in these experiments.

Table 14: VA and Silica size fractions

Volcanic Ash		**Silica**	
Particle size	Size Fraction (μm)	Particle size	Size Fraction (μm)
Small	0 - 53	Fine	0 - 150
Medium	53 - 106	-	-
Large	106 - 212	Coarse	76 - 212

Phase two involved testing at different impact velocities, achieved by changing the accelerating pressure. In this phase of the experiment, samples were only impacted at 30° because of the limited number of specimens available. Size fractions of 53 - 106 μm and 0 - 150 μm were used for volcanic ash and silica respectively in this phase of the test. 30° was

found to be the impact condition in this test programme that in the main produced the maximum erosion irrespective of particle type and size (Table 16 and Table 17 summarise these room temperature, change in gas velocity tests). It was also noticed that, peak erosion rate at 30° occurred at these size fractions for the different grit types. The gas velocities achieved were 155m/s at 3bar, 210m/s at 4.5 bar and 252 m/s at 6.5 bar.

Phase three was conducted at high temperature, 450 °C, using volcanic ash and silica as the erodent. Particle size of 53 - 106 µm (volcanic ash) and 0 - 150 µm (silica) were used during this part of the test, in order to achieve maximum predicted erosion rate. Table 15 to Table 17 summarise the condition of the three test programmes.

Table 15: Phase one – Test matrix of the room temperature erosion tests to determine the effect of particle size on the erosion rates

Room Temp	All tests at 6.5 bar pressure.						
Grit	Ti 64			In 718			Test No
Impact Angle	30°	45°	90°	30°	45°	90°	
VA 0-53µm	x	x	x	x	x	x	1
VA 53-106µm	x	x	x	x	x	x	2
VA 106-212µm	x	x	x	x	x	x	3
Silica Dust 0-150µm	x	x	x	x	x	x	4
Silica 76-212µm	x		x	x		x	5

Table 16: Phase two – Test matrix of the room temperature erosion tests to determine the effect of impact velocity

Room Temp	3 bar		4.5 bar		
Grit	Ti 64	In 718	Ti 64	In 718	Test No
Impact Angle	30°	30°	30°	30°	
VA 53-106 µm	x	x	x	x	6
Silica Dust 0-150 µm	x	x	x	x	7

Table 17: Phase Three – Test matrix of the high temperature erosion tests (450 °C)

450°C	All tests at 6.5 bar pressure.						
Grit	Ti 64			In 718			Test No
	30°	45°	90°	30°	45°	90°	
VA 53-106µm	x	x	x	x	x	x	8
Silica Dust 0-150µm	x	x	x	x	x	x	9

4.4.2.1 Erosion of CMAS infiltrated samples

The erosion rate of samples infiltrated with both volcanic ash and simulated CMAS of various compositions were analysed. Volcanic ash and standard CMAS [13] were aged at 1250 ^{o}C, whereas other CMAS compositions were heat treated 50 ^{o}C above their melting point. The experiments were performed using the Cranfield university erosion rig at various conditions as summarised in the matrix in Table 18.

Table 18: erosion tests to determine the effect of slag infiltration on the erosion rate of EB-PVD TBC

Condition	Impact angle	TBC Type
As received	30° and 90°	EB-PVD
VA infiltrated	90°	EB-PVD
CMAS infiltrated	90°	EB-PVD

The tests were conducted under the following test conditions:

Temperature	850 °C
Erodent	Al_2O_3 (90 – 125 µm)
Particle Feed rate	0.5 g/min
Pressure	5.6 bar

4.4.3 Method

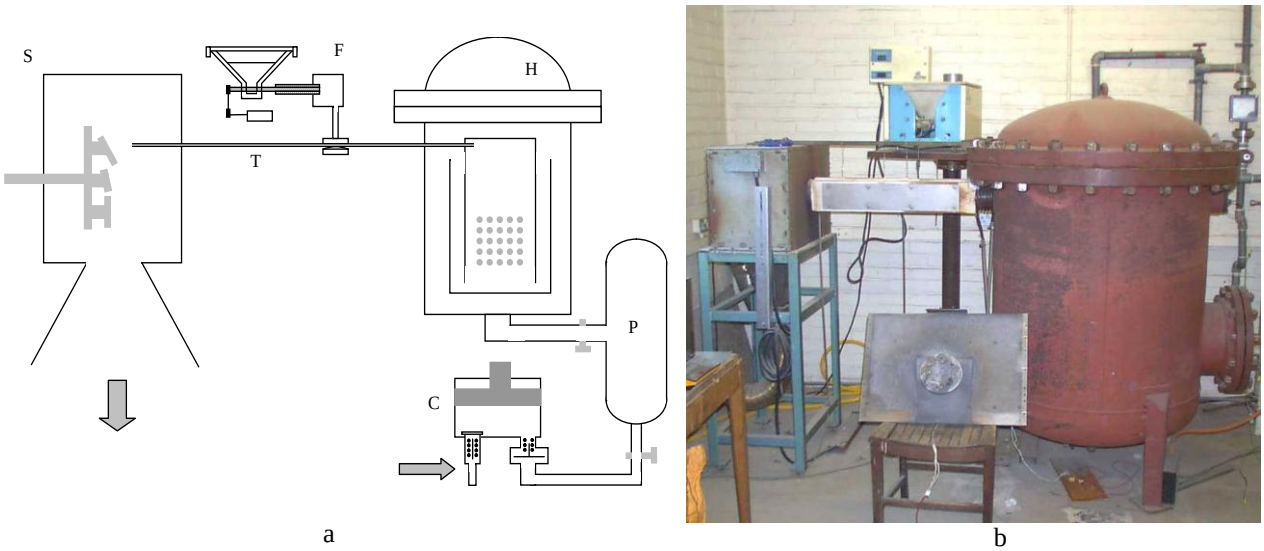

Figure 54: Cranfield University erosion rig a) Schematic and b) photograph by Wellman, R. G.

Figure 54 (a) is a schematic of the high temperature erosion rig that was used in this experiment. There are a number of key components in the operation of this machine, starting with the compressor (C), producing compressed air which supplies a pressure vessel (P). This is there to ensure that a constant amount of compressed air is supplied to the heating system (H). The air passes through a convoluted path in the pressurised heating system, which is electrically heated, before entering the acceleration tube (T). The erodent material is fed via a screw feeder and a venturi nozzle into the acceleration tube, where the compressed air accelerates the particles before they impact the test specimen in the chamber (S). The test samples are attached to a carousel, which is capable of holding six different specimens at different angles with respect to the impacting particles. Table 19 summarises the range of operating conditions attainable using this facility.

Table 19: Operating capabilities of the test rig

Temperature Range	RT-850°C
Particle Velocities	50-300 m/s (depending on particle size)
Particle Size Range	50-1,000 µm (affects the max velocity)
Impact Angles	30, 45, 60, 75 & 90°
Particle Feed Rate	0.2-3g/min

4.4.4 Metallographic Preparation

Cross sectioning of the samples were performed using a diamond cutting blade in a Brilliant 200 precision cutting machine, at a relatively slow speed, which allowed for a good surface finish to be achieved and ensuring that no brittle fracture or rough edges of the sample occurred. Cross sectional mounting of the CMAS/VA infiltrated TBC samples for microstructural evaluation were performed using Durocit powder and liquid resin before

polishing. Prior to ESEM examination, micrographic preparation of the cross sectioned samples were required in order to study the material's microstructure. The procedure involved grinding with a fixed diamond surface until planar, followed by additional grinding but this time starting with abracloth for 5 minutes before switching to planocloth for an additional 6 minutes. A summary of the microstructural preparation procedure is detailed in Table 20. Care had to be taken in order to avoid the unnecessary removal of material and smearing of small pores during the procedure. Extra polishing was required for EBSD samples, to remove any stressed top layer.

Table 20: Ceramic preparation procedure

Stage	**Surface**	**Abrasive**	**Pressure**		**Speed – Direction**	**Time**
Primary Grinding	Fixed Diamond	40 µm MB	Psi	N	500 – Comp	Until planar
			5	25		
Additional Grinding	Abracloth	9 µm (WB) PCD Diamond	5	25	250 – Comp	5 mins
	Planocloth	3 µm (WB) PCD Diamond	5	25	250 – Comp	6 mins
Polishing	Planocloth	0.06 µm Colloidal Silica	5	25	100 – Contra	6 mins

For nanoindentation, the top surface of the samples were lightly polished and cleaned to minimise surface roughness and ensure the surfaces are free from grease and dirt which can affect the results. The specimens were then mounted on removable metal studs using a heat softening glue. This was an important process because if too much glue was used, the compliance of the glued joint would affect the nanoindentation results. For this reason, it was important to ensure that the specimens make good mechanical contact with the mount and that the glue only fills in the asperities in the contact surface.

4.4.5 EBSD Specimen Preparation Techniques

The first step in obtaining EBSD data is sample preparation since EBSD is a near surface technique (5 – 20nm). Therefore, the condition of the sample surface is critical in order to obtain high quality EBSD patterns. Mechanical polishing alone is insufficient to obtain a strain-free and smooth surface for diffraction analysis, meaning the resulting EBSD patterns will be of poor quality or will not be visible at all. Bulk samples require cross-sectioning and polishing as mentioned above (sectioning, coarse grinding, fine grinding, rough polishing and final polishing), per normal SEM examination. In EBSD, an additional final step of fine polishing using colloidal silica suspension is necessary to remove any residual induced preparation damage, especially within a few nanometers of the surface.

4.5 Thermochemical Experiment

The effect of CMAS and volcanic ash interaction on TBCs was studied under an isothermal heat treatment condition, which involved placing the samples (from ambient temperature) in a calibrated furnace, pre-heated to 50 °C above the melting temperatures of the deposits. The samples were then allowed to soak at the set temperature and taken out at <1, 2, 4, 8, 50, 100, 200, 500 and 1000 hours interval before being air cooled to room temperature, prior to analytical examination.

4.5.1 Furnace Profiling

Due to the temperature dependence of molten slag attack, it was considered important to understand the thermal efficiency and to get accurate and comprehensive temperature profile of the furnace used in this study. In order to obtain these results, a 3-D thermocouple structure was built to fit the interior of the furnace and the furnace was then run to its maximum capacity (in this case 1600 °C) and the thermocouple readings were compared against those of the furnace. The result revealed that, there is a discrepancy across the

furnace, with a slight drop in temperature the further away from the heating elements in the back of the furnace, moving towards the door of the furnace. Results also showed a thermal gradient between base and top of the furnace. The closest temperature to the actual reading was achieved at points located at the top and back of the furnace, ~20 °C. With this knowledge in mind, thermal ageing tests were performed taking into account this thermal discrepancy across the furnace. Allowances were made to compensate for the temperature delta within the furnace.

Figure 55: Thermal profiling using thermocouple arrays monitored using MatLab computer software system.

Results and Discussion

5 Effect of CMAS Ingestion in the Compressor Section (Erosion): Results and Discussion

5.1 Volcanic Ash Characterisation

The images in Figure 56 are SEM micrographs of the different size fractions of the "as-received" Eyjafjallajökull volcanic ash. The chemical analyses given in Table 21a-c are the analyses of the different size fractions of the ash and are an average of 15 analyses, taken randomly across each size fraction.

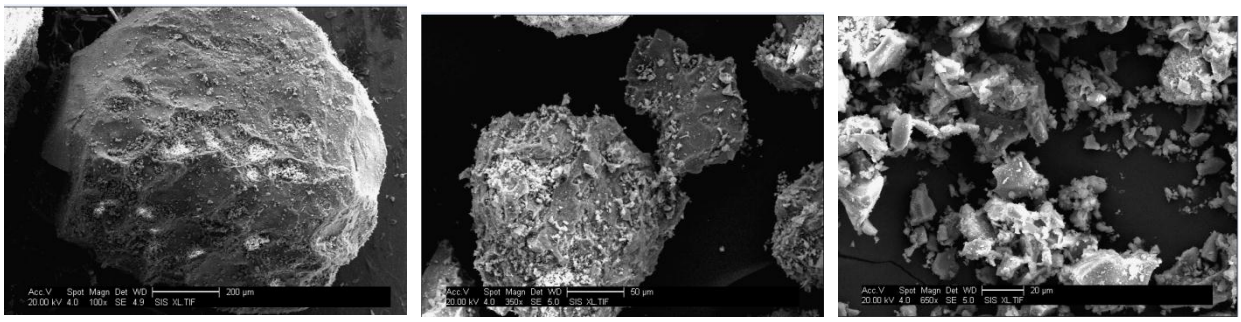

(a) (b) (c)

Figure 56: SEM Micrographs of volcanic ash: a) greater than 300 µm, b) 90-300 µm and c) less than 50 µm.

Table 21: SEM EDAX analysis of (a) Coarse, (b) Medium and (c) Fine size fractions of volcanic ash

Element	Wt. %	At. %
C	7	12.4
O	38.3	51.3
Na	3.2	3
Al	7.7	6.1
Si	25.1	19.1
K	2.1	1.1
Ca	3.7	2
Ti	1.3	0.6
Fe	11.7	4.5
Total	100.1	100.1

(a)

Element	Wt. %	At. %
C	5.8	9.9
O	45.4	57.8
Na	2.2	1.9
Mg	1.1	0.9
Al	7.4	5.6
Si	25.3	18.4
K	1.1	0.6
Ca	3.6	1.9
Ti	1.3	0.6
Fe	6.9	2.5
Total	100.1	100.1

(b)

Element	Wt. %	At. %
C	5.8	9.3
O	51.8	62.3
Na	4.1	3.5
Al	6.4	4.6
Si	26.5	18.1
K	2.3	1.1
Ca	0.7	0.3
Fe	2.4	0.8
Total	100	100

(c)

These analyses permit the mass fraction of the different oxide phases to be calculated, from which the following mean compositions have been obtained, see Table 22.

Table 22: Calculated mass fraction (%) by oxide phases in the volcanic ash used in the Cranfield erosion tests

Particle Size	SiO_2	Al_2O_3	Fe_2O_3	TiO_2	Na_2O	K_2O	MgO	CaO
>300 µm	57.0	15.1	11.4	1.5	5.2	2.1	2.9	4.7
90-300 µm	58.2	14.7	11.5	1.6	5.6	2.3	1.5	4.6
< 50 µm	59.6	15.1	10.1	1.5	5.7	2.4	1.3	4.4

5.2 Variation of Particle Size on Erosion Performance

Erosion test results are presented as mass loss per mass of impacting particles, from which the erosion rate is then calculated. Erosion rate is a dimensionless parameter, but usually quoted at g/kg or mg/g. Results showing the effect of volcanic ash and silica on the erosion rates are shown on Figure 57 – Figure 58, for different size fractions.

$$Erosion\ rate, (g/kg) = \frac{mass\ loss\ of\ sample}{mass\ of\ erodent} \times 1000$$

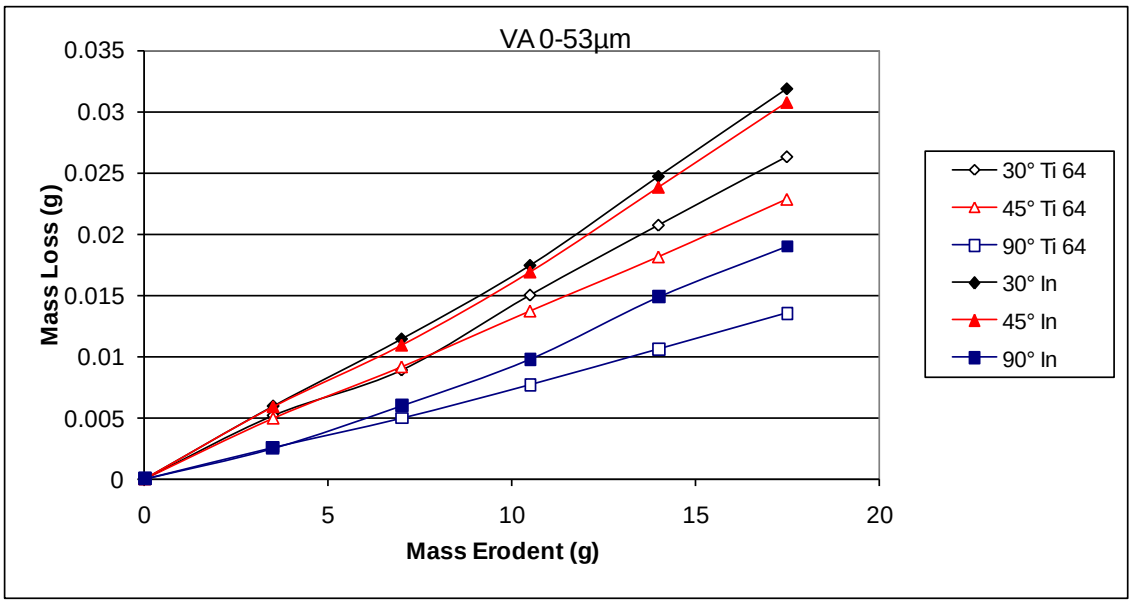

Figure 57a: Mass Loss vs. Mass Erodent graph for VA 0-53 µm.

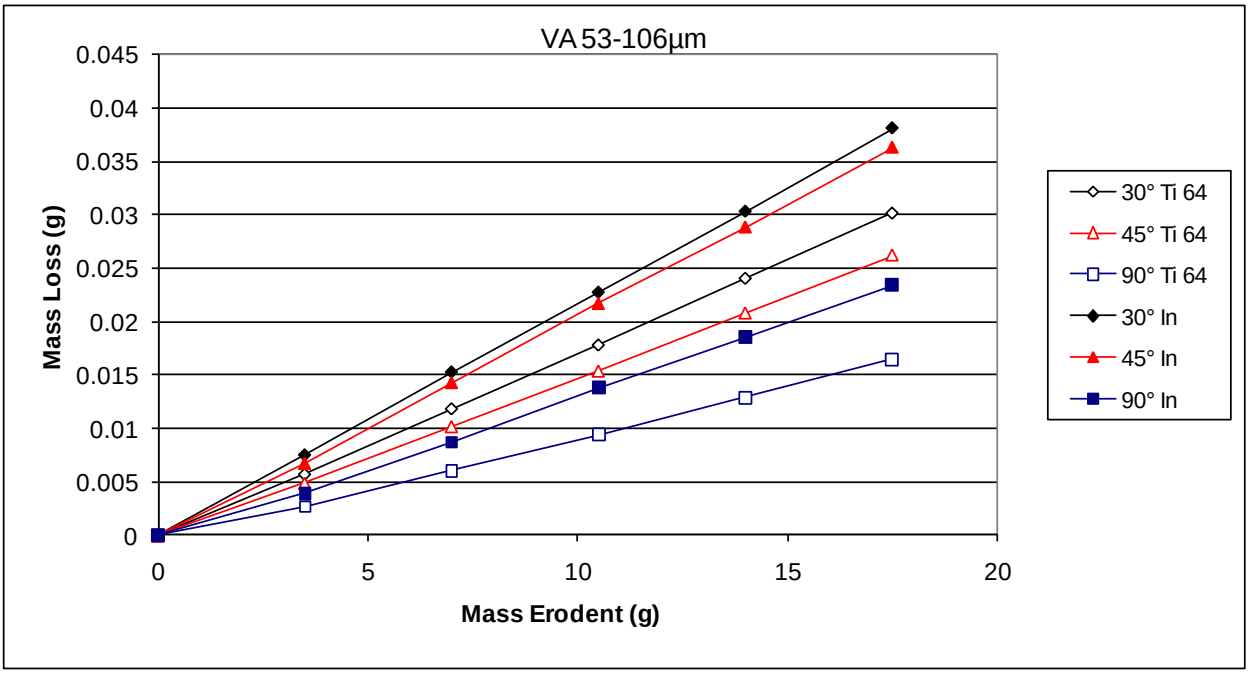

Figure 57b: Mass loss graph for VA 53-106 µm test.

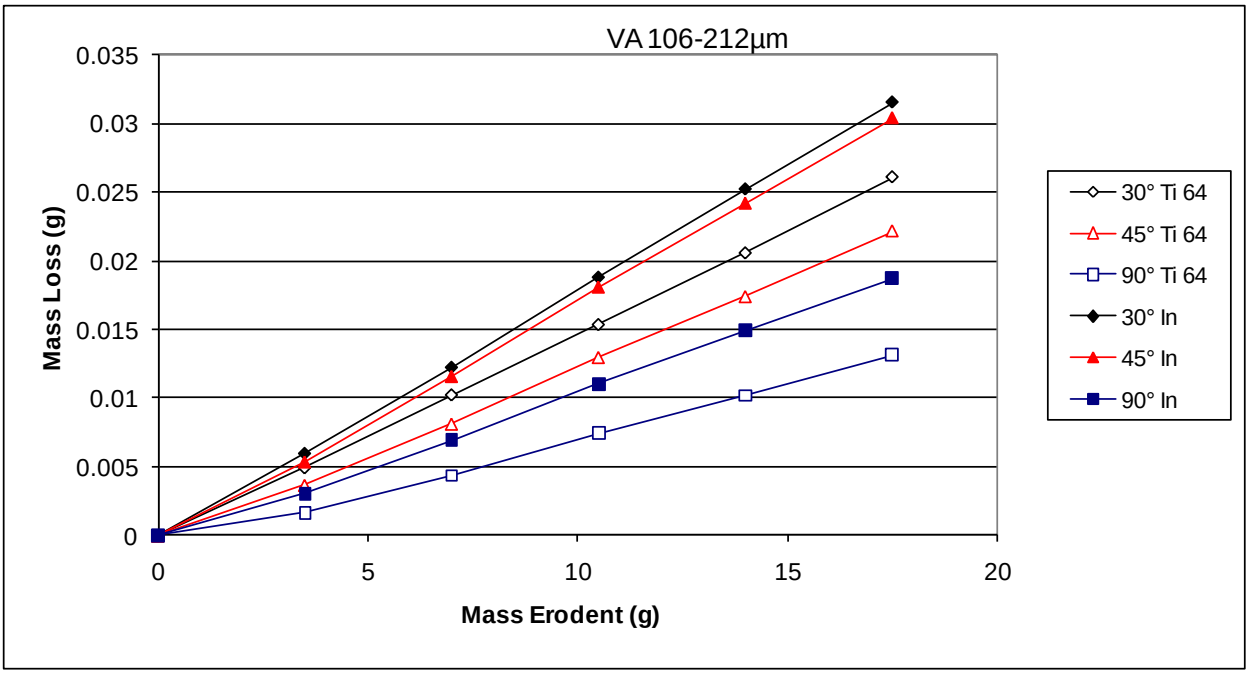

Figure 57c: Mass loss graph for VA 106-212 µm erosion test.

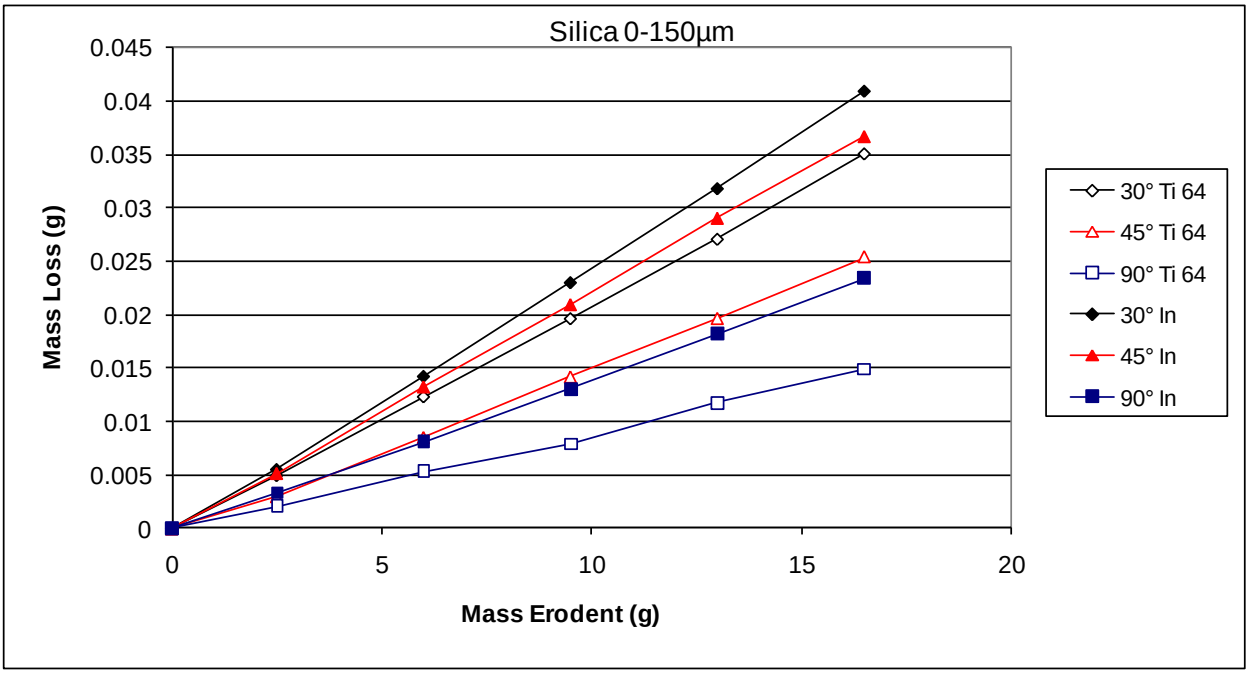

Figure 58a: Mass loss against Mass Erodent graph for silica 0-150 µm erosion test.

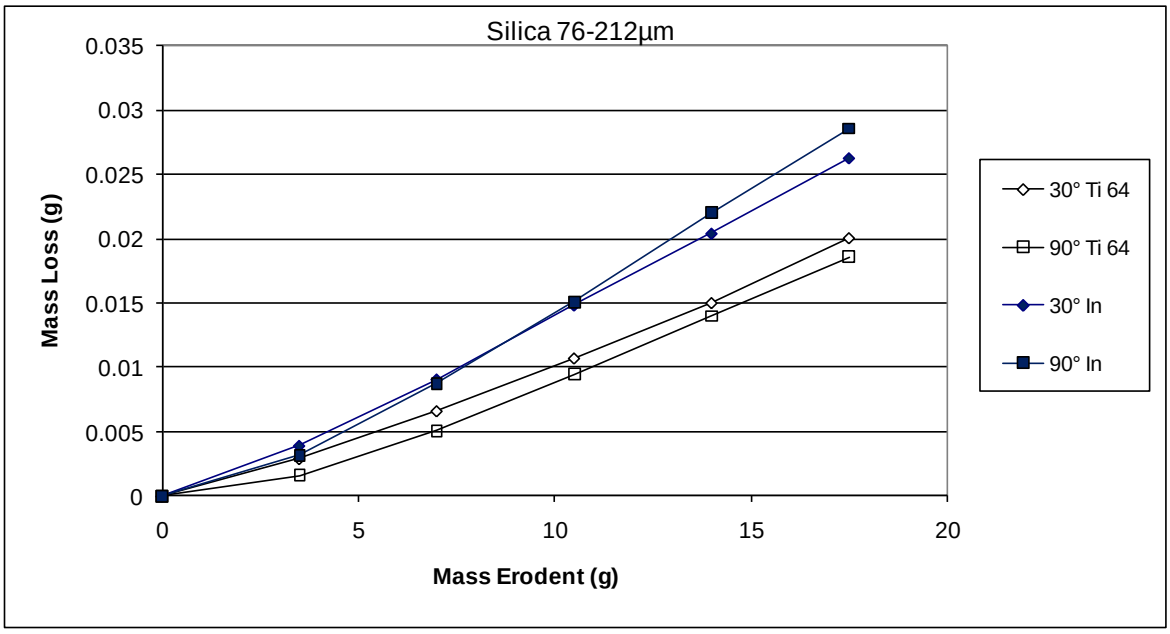

Figure 58b: Mass loss graph for silica 76-212 µm erosion test.

On examination, it is evident that Figure 57a – Figure 57c and Figure 58a – Figure 58b have slight curvature. This reflects the early accumulation of damage in the surface before "steady state" erosion is achieved. In the early stages some particle embedment may occur (mass gain) as well as mass loss due to erosion and thus the measured early rate of erosion is less

than that at steady state. Steady state erosion rates, i.e. the rate achieved after some initial incubation period, were reported rather than the erosion rate determined from some end point measurement. The bar chart in Figure 59 plots the steady-state room temperature erosion rate between fine, medium and coarse volcanic ash and silica particle size for comparison purposes.

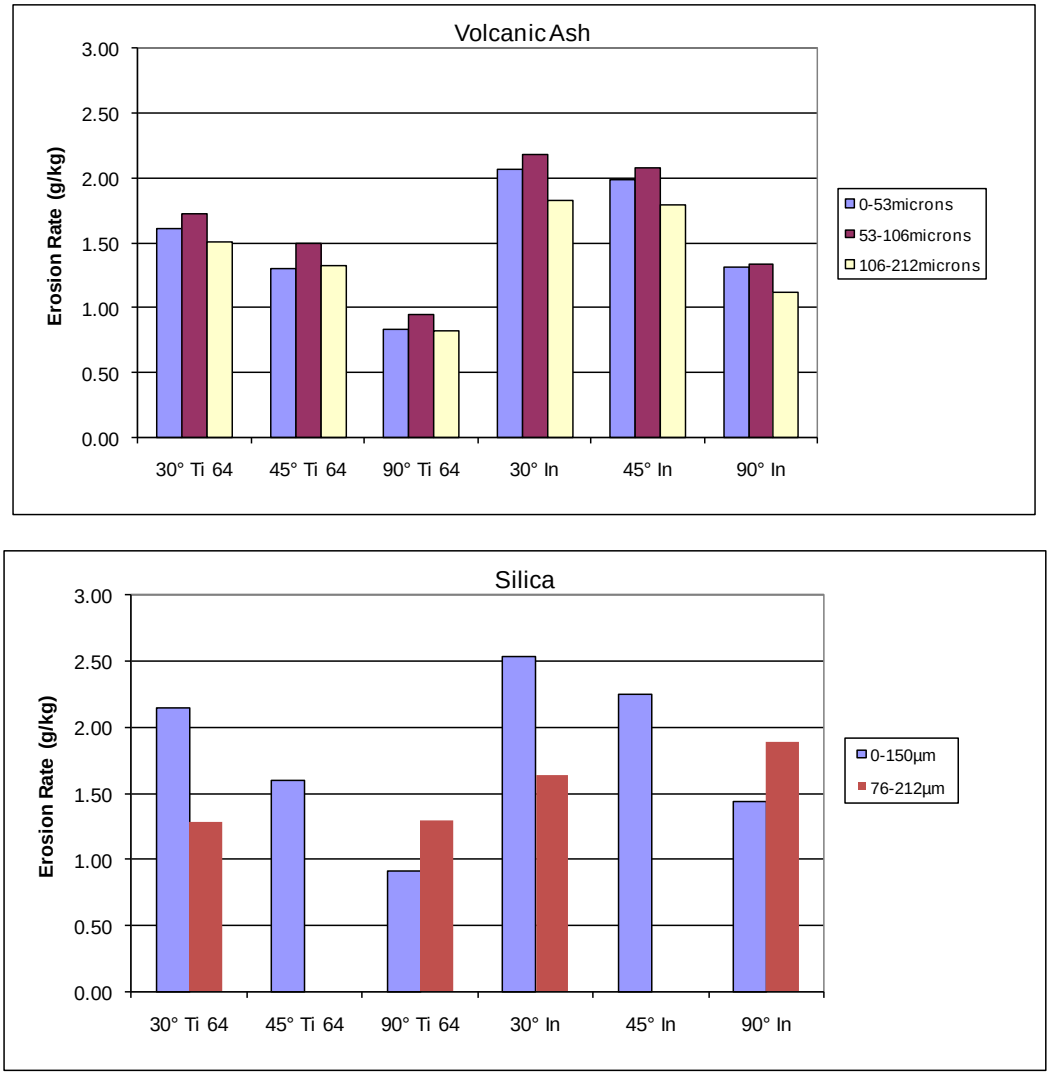

Figure 59: Bar chart of steady state erosion rates as a function of impact angle with volcanic ash (top) and silica (bottom) as the erodent, test at 6.5 bar, estimated gas velocity 252m/s.

As expected for both volcanic ash and silica sand (Figure 59), the maximum erosion rate is at low impact angles, indicating a ductile erosion mechanism. Further, there appears to be only a small dependence of steady state erosion rate on particle size for the volcanic ash (VA) as

can be seen in Figure 59. The erosion rates are all reported as mass loss per mass of erodent (g/kg), however, it must be borne in mind that there is a big difference in density between Ti64 (Ti-6Al-4V) and IN718 (4.43 to 8.22 SG respectively) and this would alter the relative performance between these two materials should volume loss per mass of erodent be used as the measure of erosion damage.

For fine and coarse silica sand, the fine silica sand would appear more erosive than the equivalent VA at all impact angles, whereas the coarse silica sand is less erosive than VA at 30° impact, but more erosive at 90° impact. The corresponding erosion rate values are tabulated below (Table 23).

Table 23: Steady State' Erosion Rates for Room Temperature Tests

Test conditions	**Ti6Al4V**	**IN718**
Volcanic Ash		
0-53 µm 30°	1.61	2.06
0-53 µm 45°	1.30	1.98
0-53 µm 90°	0.83	1.31
53-106 µm 30°	1.75	2.18
53-106 µm 45°	1.52	2.11
53-106 µm 90°	0.99	1.40
106-212 µm 30°	1.51	1.82
106-212 µm 45°	1.32	1.79
106-212 µm 90°	0.82	1.12
Silica Sand		
0-150 µm 30°	2.15	2.53
0-150 µm 45°	1.60	2.25
0-150 µm 90°	0.91	1.49
76-212 µm 30°	1.28	1.64
76-212 µm 90°	1.29	1.89

5.3 Variation of Velocity on Erosion Performance

Variation in gas velocity is achieved by changing the accelerating pressure in the erosion rig. The rig gas velocity is controlled by the pressure in the gas reservoir, prior to particle injection; this was maintained at 3.0, 4.5 and 6.5 bar giving room temperature gas velocities of 155, 210 and 252m/s respectively. Increasing the accelerating pressure equates to increase in the gas velocity, which can be calculated using Fanno flow theory [154]. Erosion rate is dependent upon the impacting velocity, and the rate is expected to be different with different impacting particle, particle size and different materials. Figure 60 gives the erosion rates of the two alloys (Ti64 and IN718) with different impacting particles, plotted as a function of accelerating pressure at a 30° impact angle.

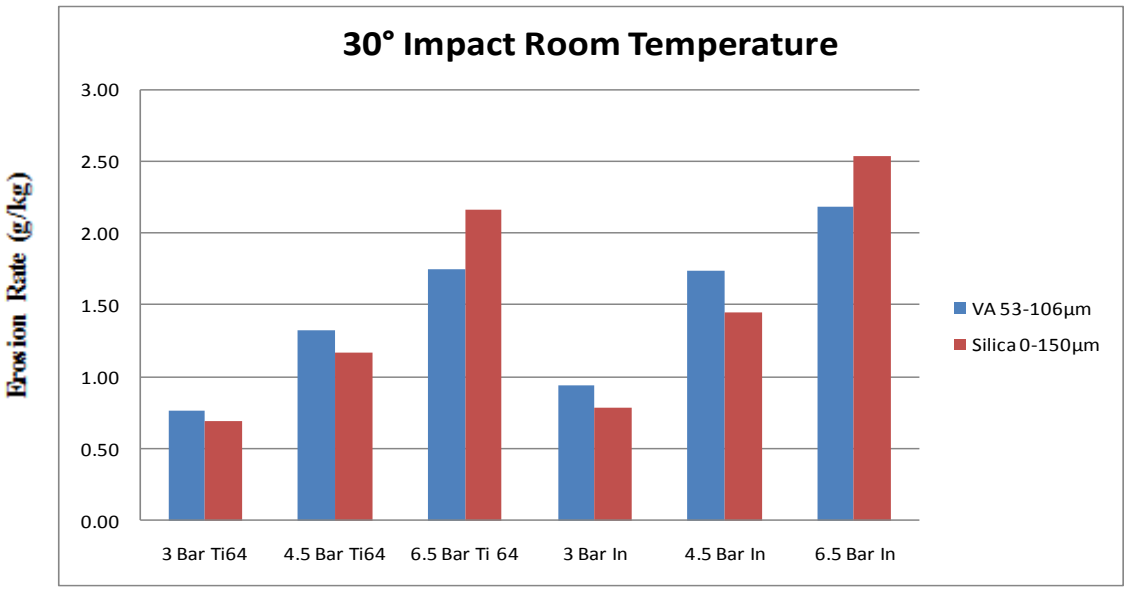

Figure 60: Bar chart of the erosion rates at different accelerating pressures using volcanic ash and silica as the erodent at 3 bar, 4.5 bar and 6.5 bar.

Figure 61 and Figure 62 plot the erosion behaviour of Ti64 and IN718 as a function of gas velocity when eroded by volcanic ash. Similar figures using silica sand are presented in Figure 63 and Figure 64. All four figures show that the dimensionless erosion rate (g/kg) follows a power law dependence on gas velocity, with an exponent close to 2.4. This

behaviour is consistent with and as one would expect from a ductile erosion mechanism, where erosion rate would have a power law dependence on particle velocity with an exponent between 2.0-2.4.

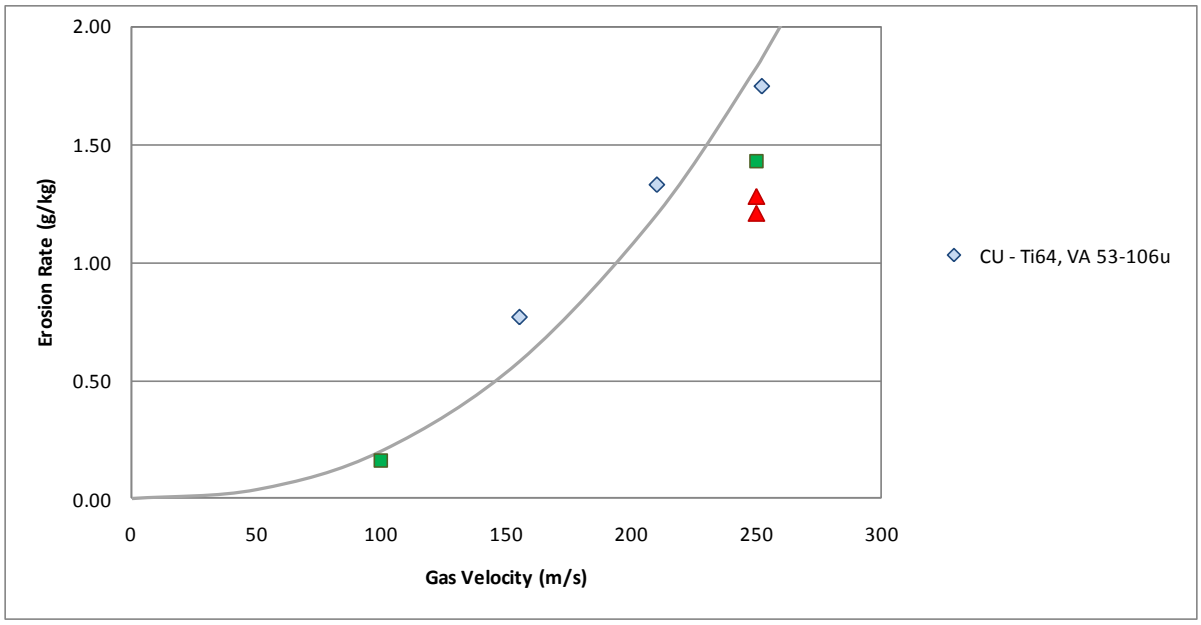

Figure 61: Erosion Rate of Ti-6Al-4V (Ti64) by Volcanic Ash, Effect of Gas Velocity

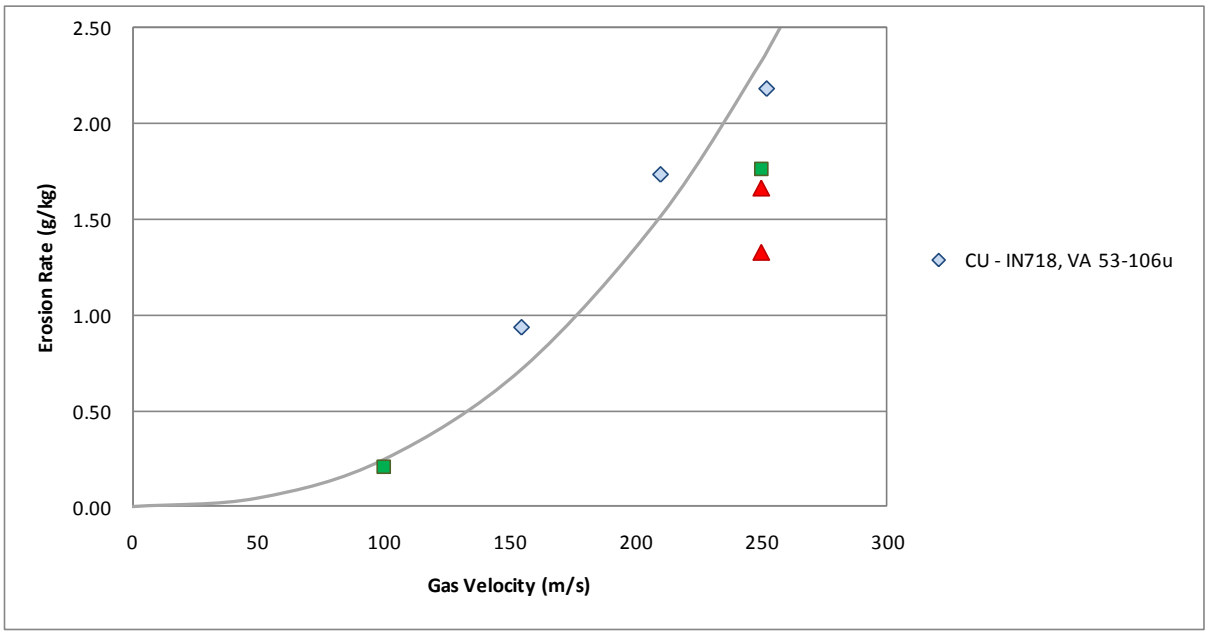

Figure 62: Erosion Rate of IN718 by Volcanic Ash, Effect of Gas Velocity

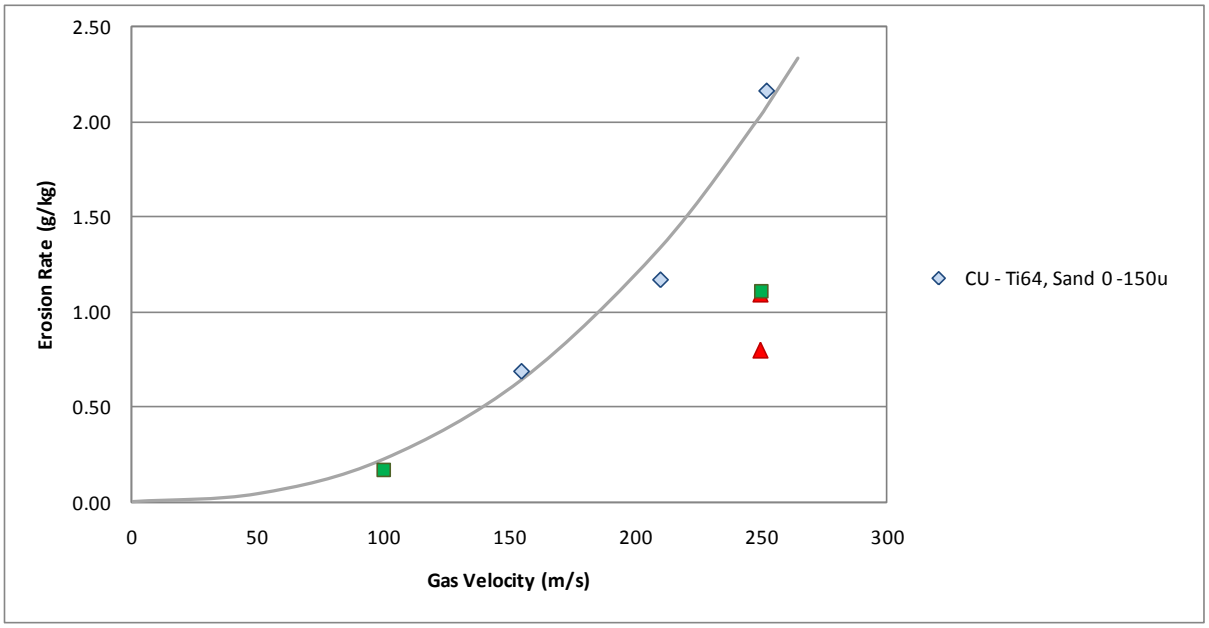

Figure 63: Erosion Rate of Ti-6Al-4V (Ti64) by MIL Spec Sand, Effect of Gas Velocity

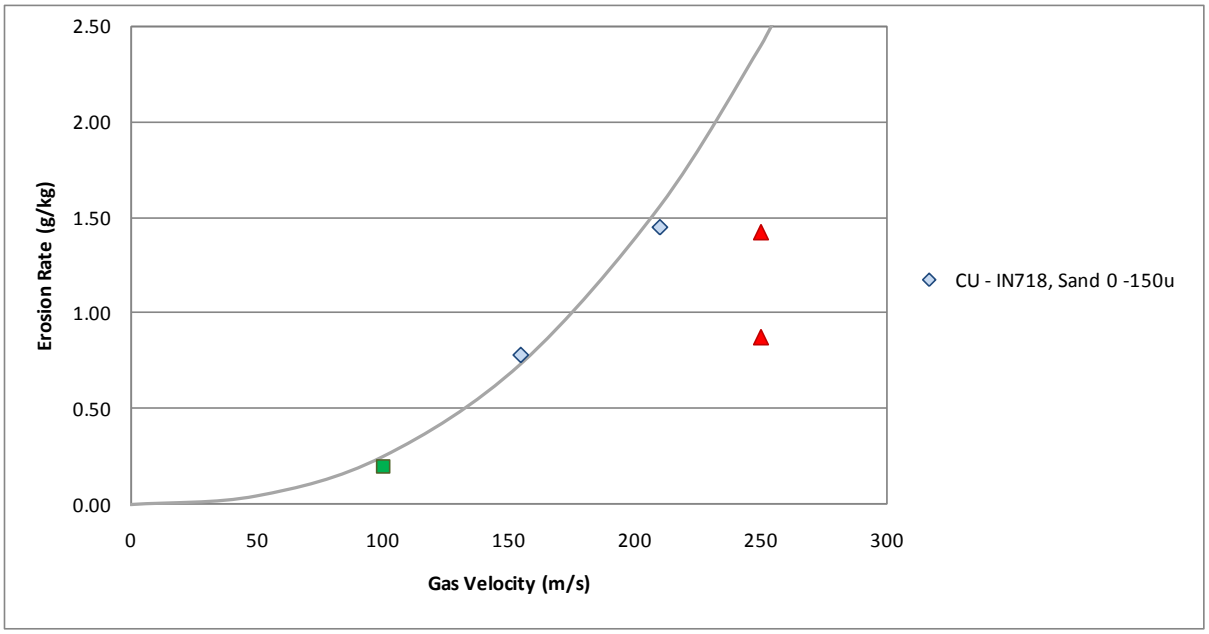

Figure 64: Erosion Rate of IN718 by MIL Spec Sand, Effect of Gas Velocity

Thus, the following equations may be used to predict the erosion rate of volcanic ash and MIL spec sand for Ti-6Al-4V (Ti64) and IN718, when eroded at a 30° impact angle (peak erosion condition for ductile erosion).

For volcanic ash;

Ti64 erosion can be modelled with the following equation, when eroded under ductile erosion conditions (30° impact):

$$E = 3.23 \times 10^{-6}. V^{2.40} \quad \text{Equation 13}$$

For IN718 the equation is:

$$E = 3.11 \times 10^{-6}. V^{2.45} \quad \text{Equation 14}$$

For silica sand;

Ti64 erosion can be modelled with the following equation under ductile erosion conditions (30°C):

$$E = 3.40 \times 10^{-6}. V^{2.41} \quad \text{Equation 15}$$

For IN718 the equation is:

$$E = 2.92 \times 10^{-6}, V^{2.47} \quad \text{Equation 16}$$

Where V is the gas velocity in m/s and E is the dimensionless erosion rate in g/kg. It can be seen that the velocity models fit well to the erosion data plotted in Figure 61 to Figure 64.

5.4 Effect of Substrate Temperature on Erosion Performance

Variation in temperature (room temperature and 450^{o}C) tests was conducted at impact angles of 30, 45 and 90° at 6.5 bar, on Ti64 and IN718 substrates. The high temperature erosion rig at Cranfield University operates at constant acceleration pressure rather than constant velocity. Increasing the operating temperature will increase the gas volume flux (the gas mass flux remained much the same), resulting in a much higher calculated value of gas velocity. Figure 65 present results comparisons of the high temperature tests.

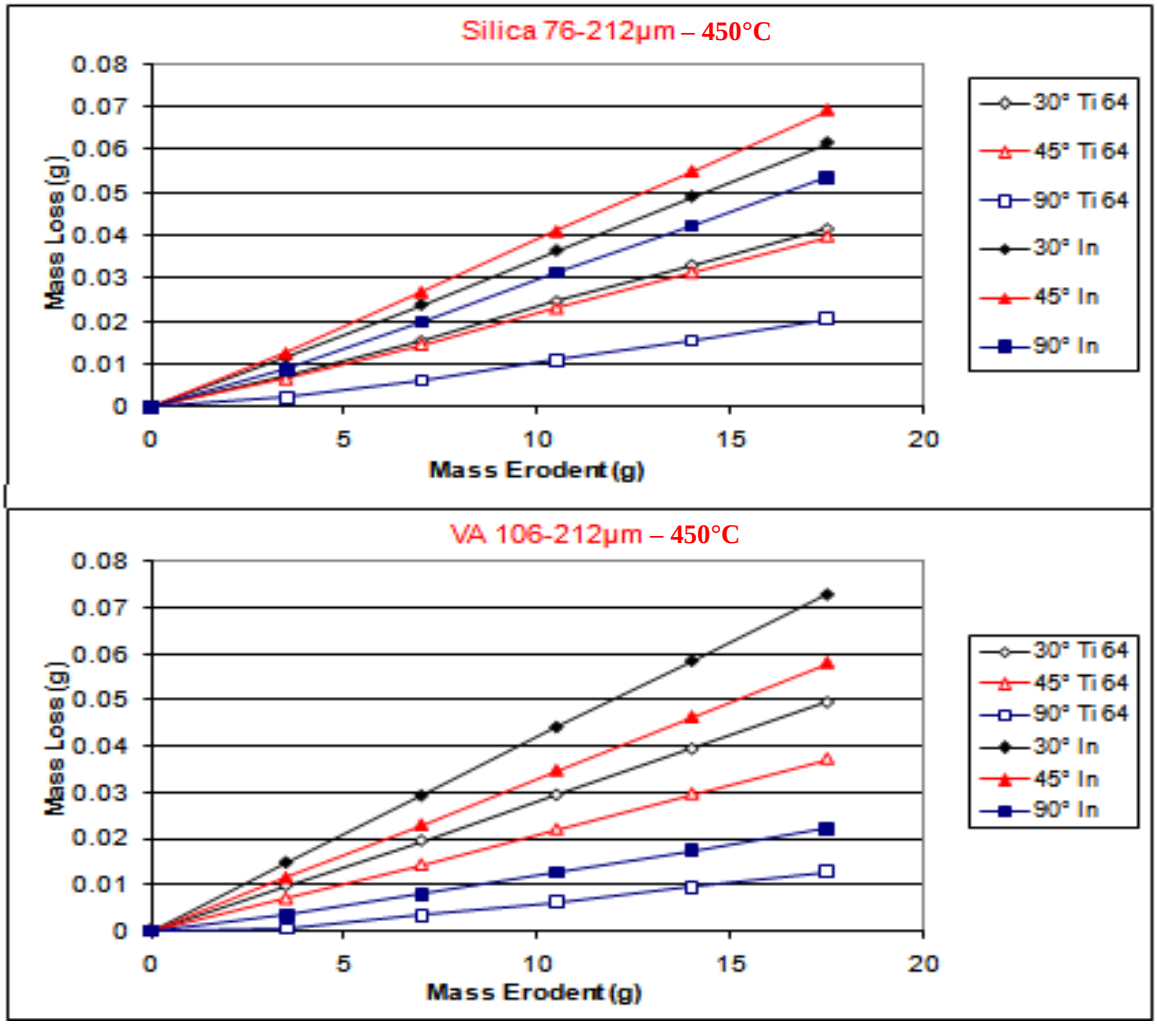

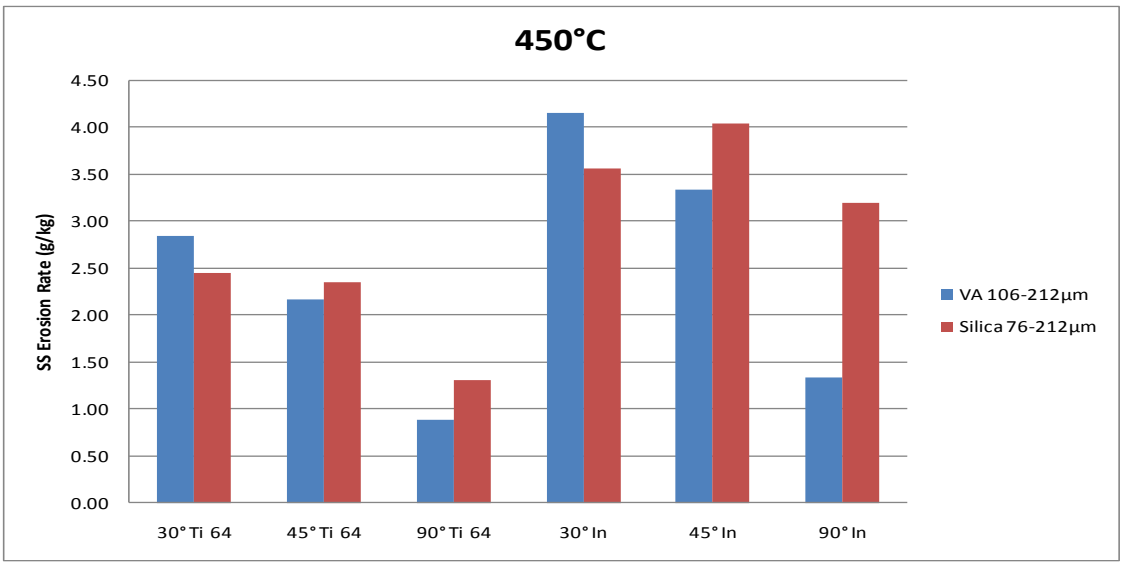

Figure 65: Erosion rate at different impact angles at 450 °C, 6.5 bar, using volcanic ash and silica as the erodent

The calculated erosion rates suggest that when testing at higher temperature, the erosion rates with volcanic ash are highest at room temperature, decreasing as the gas temperature is increased. This behaviour applies both for glancing angle impact (20 – 30°) and normal impact (90°). Similar trends were observed with both Ti64 and IN718. Erosion rates at 250m/s gas flow, under ductile erosion conditions, were calculated from the test results. Thus Ti64 is expected to erode at a rate of 0.94g/kg at 450 °C and a gas velocity of 250m/s, compared with 1.49g/kg measured at room temperature. For IN718 the erosion rate calculated was 1.35g/kg at 450 °C and 250m/s, compared to 1.80g/kg measured at room temperature.

The hypothesis that in the compressor section, variations in temperature, impact velocity and particular size will affect the rate of erosion of compressor materials is supported based on the results discussed in this section. However, the dependency of erosion mechanism on temperatures, impact velocity and particle size was not fully established. Temperature, impact velocity and particle size have all shown to be important parameters in determining the erosion rate.

5.5 Erosion behaviour of CMAS modified EB-PVD TBC

5.5.1 Method and Results

This section was done as a joint collaboration with a second year PhD student (Arthur Hawkins). Arthur's thesis was studying and modelling the erosion mechanism of aero engine coatings. Arthur performed the erosion tests, while the CMAS chemical attack and discussion of the erosion results was done as part of this project.

For the purpose of this study, the amount of coverage was kept at a minimum in order to measure the erosion properties of a sample that had been sufficiently degraded rather than measuring the erosion rate of a glassy layer formed at the surface of the sample. CMAS glaze has been shown to have excellent erosion properties [155]. 4.8mg/cm^2 (0.2g per coupon) of

CMAS was selected to be the amount of coverage because it was deemed necessary for the samples to have uniform degradation. Whitman et al. [13] reported this level of coverage to cause uniform attack characterised by the formation of globular particles to approximately 35 µm depth within the TBC, with no excess CMAS on the surface. The erosion testing was performed under the following conditions:

- Erodent – Al_2O_3 (90 – 125 µm)
- Pressure – 5.6 bar (Approx. 100m/s velocity of gas stream)
- Temperature – 850 °C
- Erodent feed rate – 0.5 g/min
- Samples weighed at 30 second intervals to give a steady state erosion rate.

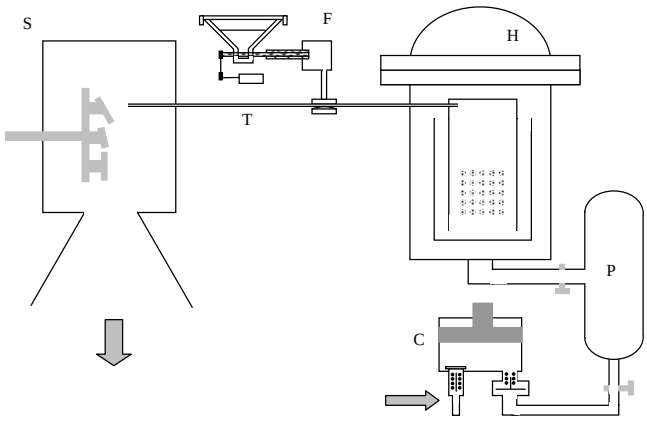

Figure 66: Diagram of erosion test rig (Courtesy of Wellman, R. G.)

5.5.2 Discussion

CMAS infiltrated samples have a significantly higher initial erosion rate than the reference samples with no CMAS, which then reduces slightly when it settles into a steady state rate. The steady state erosion rate shown in Figure 67 was calculated from the steady state erosion test data, eliminating the ambiguous initial erosion rate. The predominant mode of material loss for CMAS infiltrated samples was found to be the near surface cracking mechanism. The CMAS attack on the EB PVD columns causes degradation of microstructure which leads to

an increase in erosion rate because cracks can easily propagate from one column to another where sintered together.

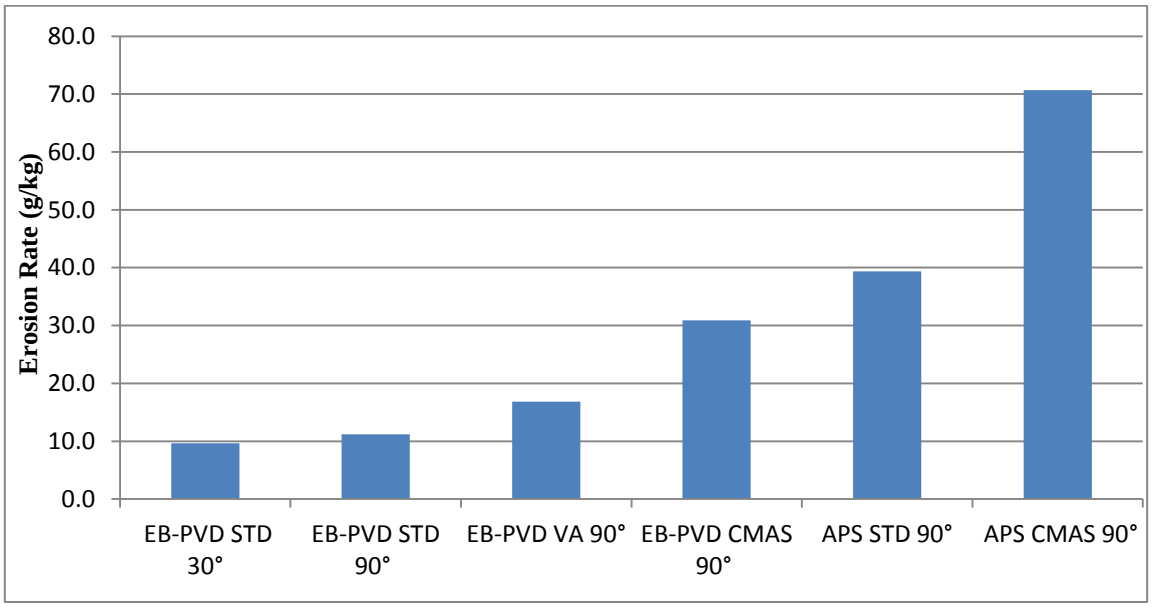

Figure 67: Showing the erosion rates of the infiltrated samples.

However, the reference EB PVD sample exhibited enhanced erosion resistance, as shown in Figure 68, since its columnar microstructure allows for columns to erode and fracture almost independently of each other thus reducing horizontal cracking per impacting particle (an erosion mechanism more predominant in PS TBC's [6; 156; 157]). The columnar boundaries in EB-PVD TBC microstructure have been shown to inhibit crack propagation [158; 159].

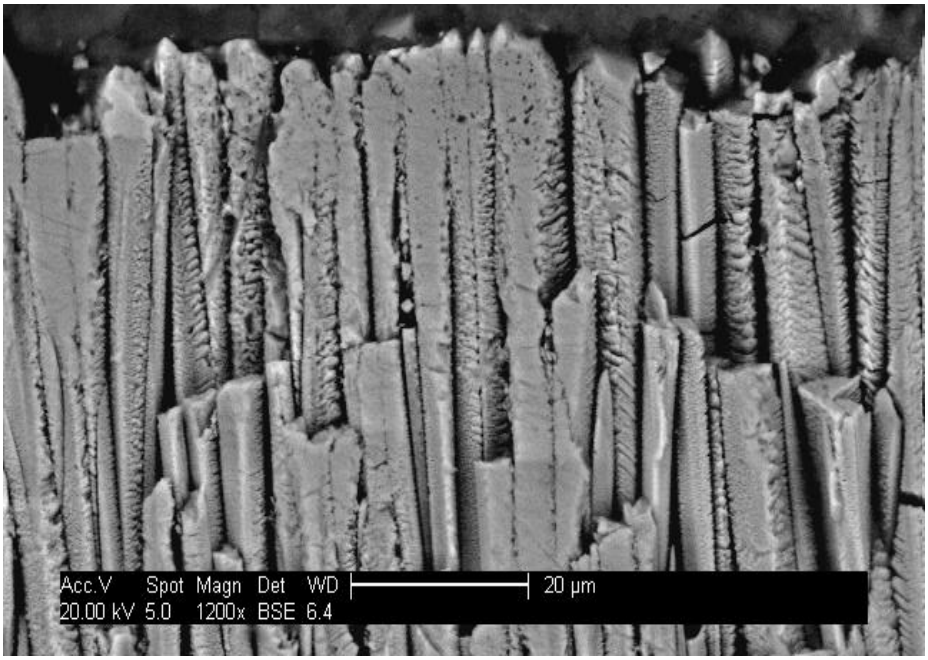

Figure 68: Micrograph of an eroded EB-PVD sample, showing less damage to the more independent columns

The addition of CMAS to an EB PVD TBC causes neighbouring columns to "stick" together and during particle impact, more than one column is damaged leading to an increase in the erosion rate. Therefore, CMAS infiltrated samples are more susceptibility to horizontal cracking (Figure 69). Additionally, the globular pores in the coating caused by CMAS attack create points of weakness within the structure and upon particle impacts results in cracks which may eventually merge with other pores (accelerating crack propagation), leading to spallation of the TBC. CMAS attack of PYSZ TBC will instigate a phase transformation from tetragonal to the brittle monoclinic phase thereby increasing the erosion rate.

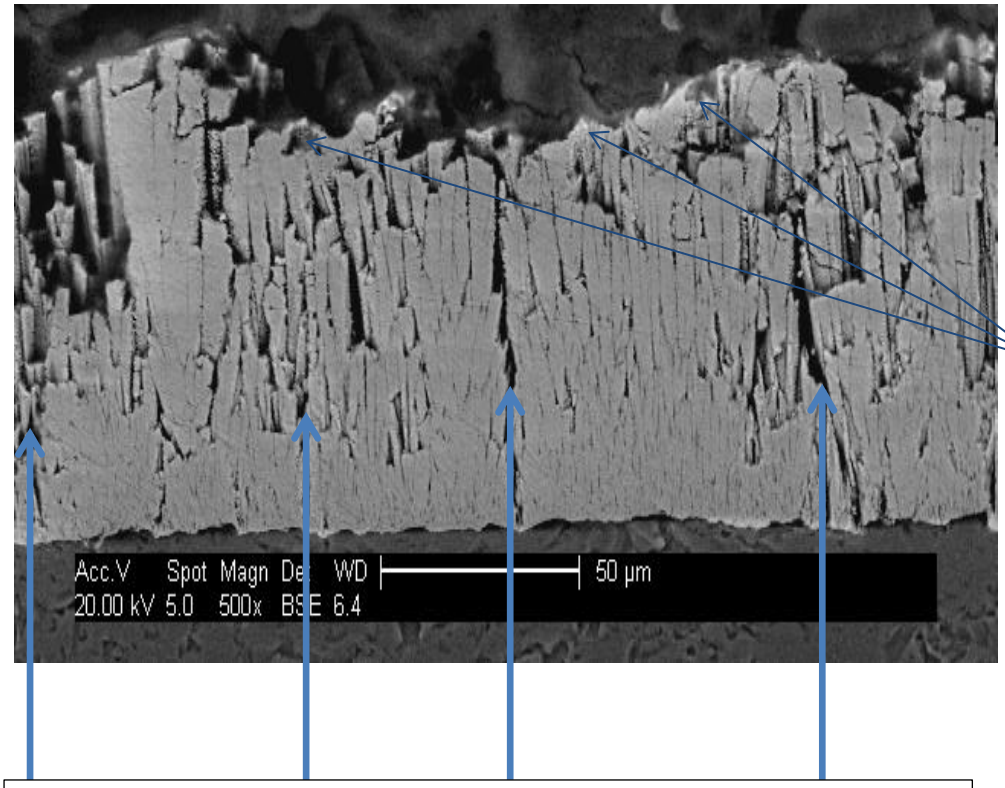

CMAS infiltration causing 'sticking' of neighbouring columns.

Segmentation cracks; a characteristic feature of erosion of molten deposits (CMAS and VA) infiltrated EB-PVD TBCs due to the eradication of the accustomed strain tolerance associated with columnar structures. Components in the molten deposits (especially CaO) act as sintering aid causing the columns to stick together and upon impact, segmentation cracks are generated as an energy release mechanism.

Figure 69 Increase in erosion rate of CMAS infiltrated sample caused by sintering of columns

6 Chemical (Molten Deposit) Attack of PYSZ in the Turbine Section: Results and Discussion

In the compressor section, debris (volcanic ash and sand) impacting components of the compressor section may cause erosion problems. Concurrently, these debris are being efficiently milled during compression into fine particles which are carried in the gas stream beyond the compressor and subsequently into the combustion chamber. The air is therefore heated in the combustor where melting of the fine volcanic ash and sand occurs. The molten deposit is propelled into the turbine section where it is deposited on the surface of turbine blades. The molten deposit will chemically attack the TBCs on the surface of turbine blades. This chemical attack of TBCs is discussed in this chapter.

6.1 Effect of Varying the Amount of Coverage, Time and Temperature on Severity of Standard CMAS and Volcanic Ash Attack of PYSZ

6.1.1 Short-term Exposure to Standard CMAS and Volcanic Ash

Short-term in this study refers to short exposure time at temperatures above the melting point of the deposit and exposed for between 1 and 24 hours. Therefore it was very important to accurately establish the melting points of the deposits used. Figure 36 is a DSC trace of a sample of the Eyjafjallajokull volcanic ash with a melting point of ~1200 °C, whilst Figure 74 illustrates DCS curves of two synthetic CMAS (Low and High B.I. compositions). Short-term exposures were performed at different times by varying the coverage to determine the effect of times at temperature on standard PYSZ EB-PVD TBC. The following analytical techniques were used to characterise the results and enabling to map the degradation mechanism.

6.1.1.1 Visual Examination

Visual examination of the samples after testing revealed no obvious evidence of coating degradation as well as no evidence of a glassy layer of molten slag on the top of the coating. However, various authors [11; 13; 66] have reported the formation of this glassy layer on the surface of the coating which is due to the excess coverage of CMAS (saturated coverage) used in testing. In order to ascertain the thermochemical effect of molten slag, microscopic investigation was required. These experiments were performed using the minimum level ($5mg/cm^2$) of CMAS/VA necessary to cause attack (as determined by Whitman et al. [13]). ESEM equipped with energy dispersive X-ray spectroscopy (EDAX) was used to analyse the samples.

6.1.1.2 X-Ray Diffraction (XRD)

The XRD spectrum of the as-received yttria stabilised zirconia TBC is shown in Figure 70. The "as-received" 7-8wt% YSZ top coat is composed of the non-transformable t' tetragonal phase zirconia, which is in agreement with the expected composition based on the Y_2O_3–ZrO_2 phase diagram. The t' phase is not an equilibrium phase and it is formed by a diffusionless transformation mechanism of the high temperature cubic phase, due to rapid solidification during the deposition process. The t' phase differs from other possible phases (monoclinic and transformable tetragonal) notably it's higher yttria content, hence further confirmation of the constituent phases can be drawn from an EDAX analysis. However, for VA/CMAS infiltrated samples, the X-ray data showed a transformation from the t' phase and mainly consisted of the monoclinic and tetragonal phases of the zirconia polymorph. The tetragonal peaks appeared in different positions (Figure 71) due to them having different amount of yttria content within the tetragonal phase. This slight difference in yttria content

affected their lattice parameter hence the tetragonal peaks are not in exactly the same position.

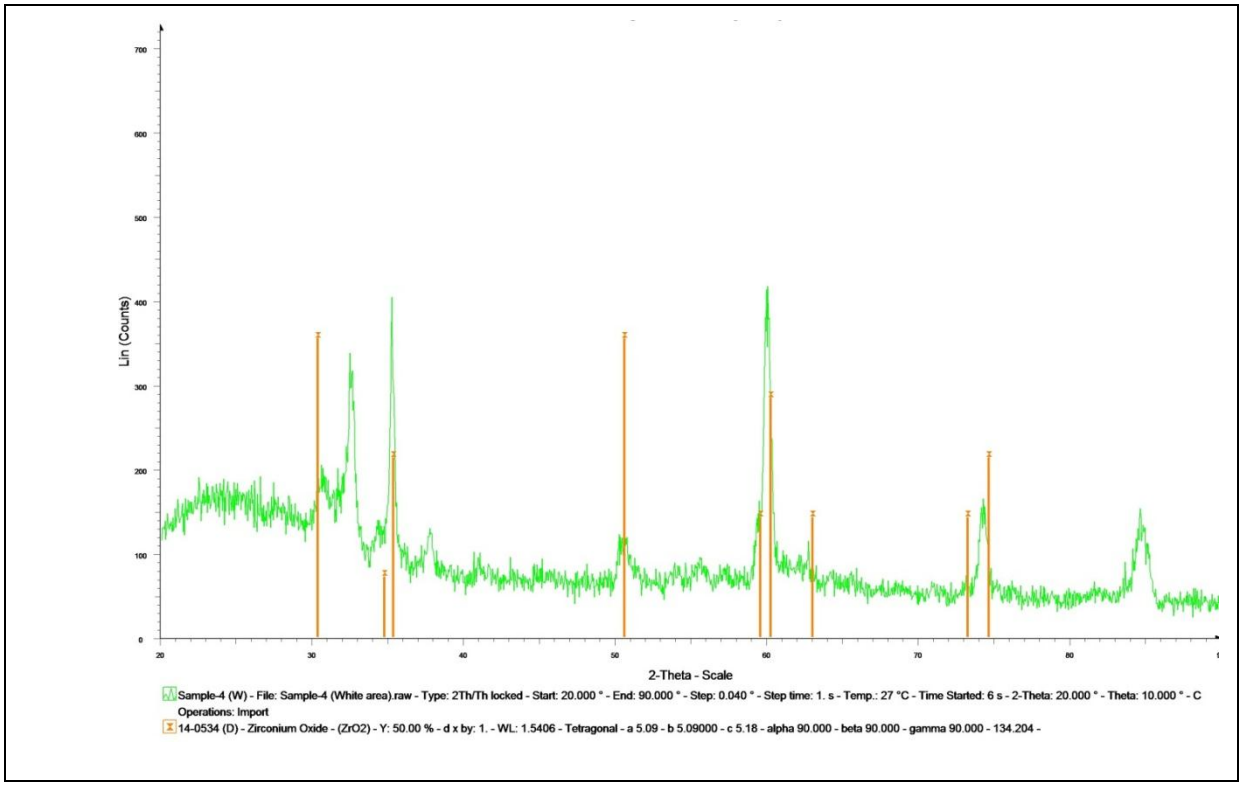

Figure 70: XRD spectrum of the as-received 7-8wt% YSZ top coat.

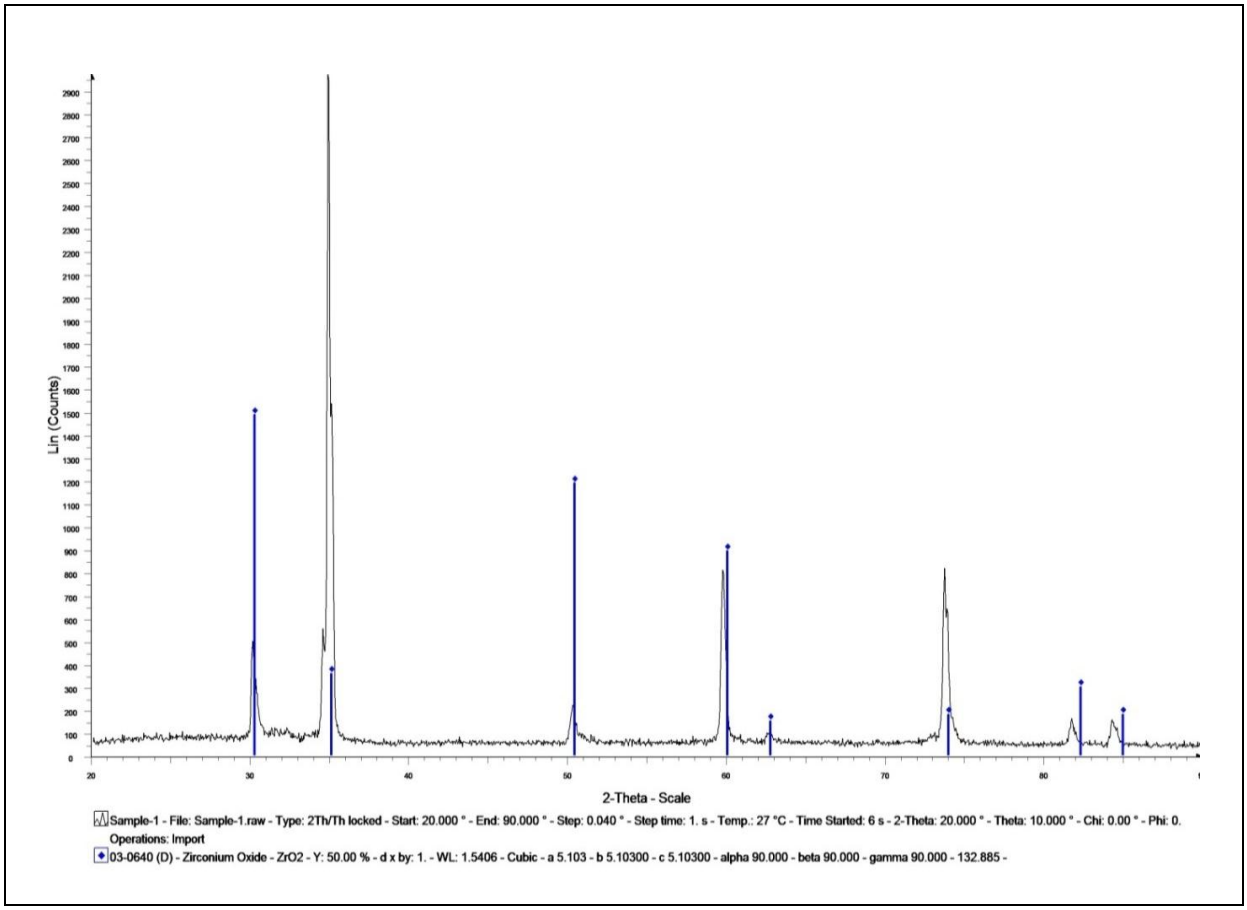

Figure 71: XRD spectrum of slag infiltrated 7-8wt% YSZ top coat.

6.1.1.3 Scanning Electron Microscope (SEM)

Comparison of the as-received YSZ XRD spectrum (Figure 70) with the slag infiltrated spectrum (Figure 71) revealed that the position of the tetragonal peaks in both spectra is not in exactly the same position. This is an indication of different phases (or stress) in the samples suggesting that there is a variation in yttria content between the samples due to the presence of oxides impurities (CMAS). In order to investigate these differences, destructive evaluation (in the form of cross-sectioning, polishing and microstructural analysis in the SEM) was necessary. For delicate samples, where extra conductive coating if applied to the surface may interfere with results, ESEM was used to examine for changes in microstructure and morphology of the TBC and also to analyse for compositional changes across the samples. Otherwise, the samples were coated with gold/palladium and examined in an SEM

using high resolution. Figure 72 shows the microstructure of a reference YSZ sample, in top and cross-sectional view before infiltrated with standard CMAS, note the pyramidal nature of the top of the columns.

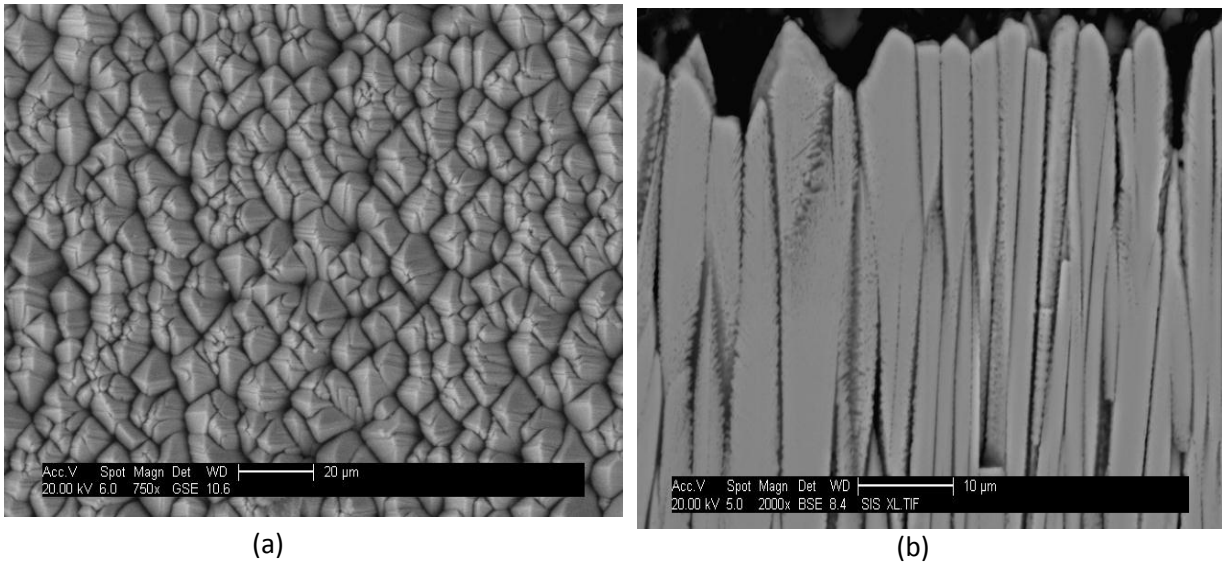

Figure 72: 7-8wt% YSZ TBC microstructure a) top and b) cross-sectional view before infiltration.

Samples infiltrated with volcanic ash and CMAS were studied. The results showed that, overall CMAS induced greater coating degradation than volcanic ash (Figure 73). It is evident from Figure 73 that CMAS reacted more with the TBC than volcanic ash, under similar conditions of exposure time, temperature and amount of coverage, with composition of the deposit being the only variable. At first glance after four hours exposure, samples that were covered with standard CMAS composition showed severe damage to the tips of the TBC columns, whereas volcanic ash samples showed a minimal degree of damage, with the column tips almost intact. 50 °C above melting temperature was selected to be the exposure temperature, in order to ensure melting of the volcanic ash and CMAS occurred.

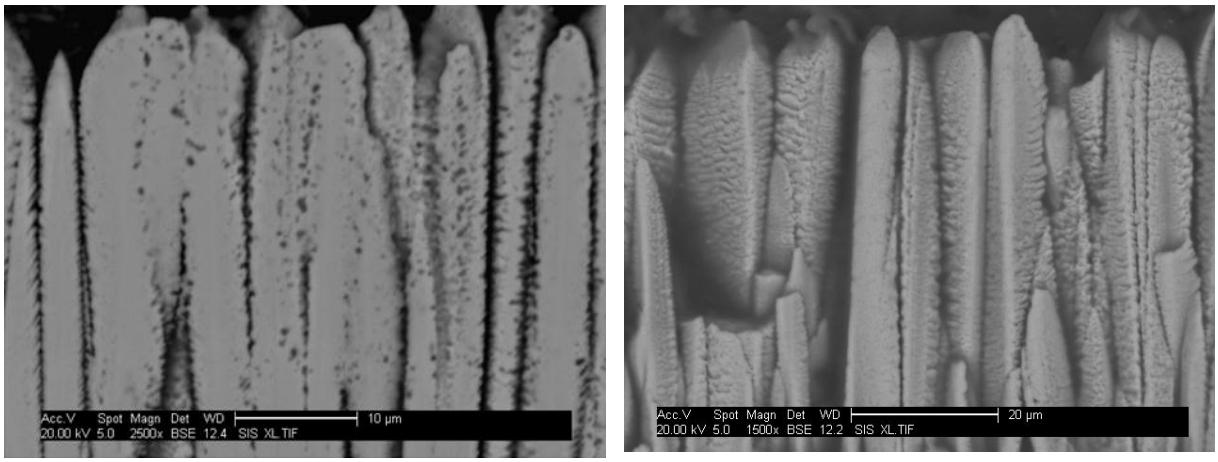

Figure 73: 7-8wt% YSZ TBC infiltrated with 5mg/cm^2 a) CMAS, and b) volcanic ash, heat treated at melting point + 50 °C (1300 °C) for 4 hours.

6.1.1.4 Differential Scanning Calorimetry (DSC)

Differential Scanning Calorimetry (DSC) was used to study the glass transition temperature (T_g), the crystallisation temperature (T_c) and the melting temperature (T_m) of the different compositions used throughout this study. Figure 74 illustrates a DSC trace of the melt transition of a "standard" CMAS composition, which has a melting temperature of ~1258 °C.

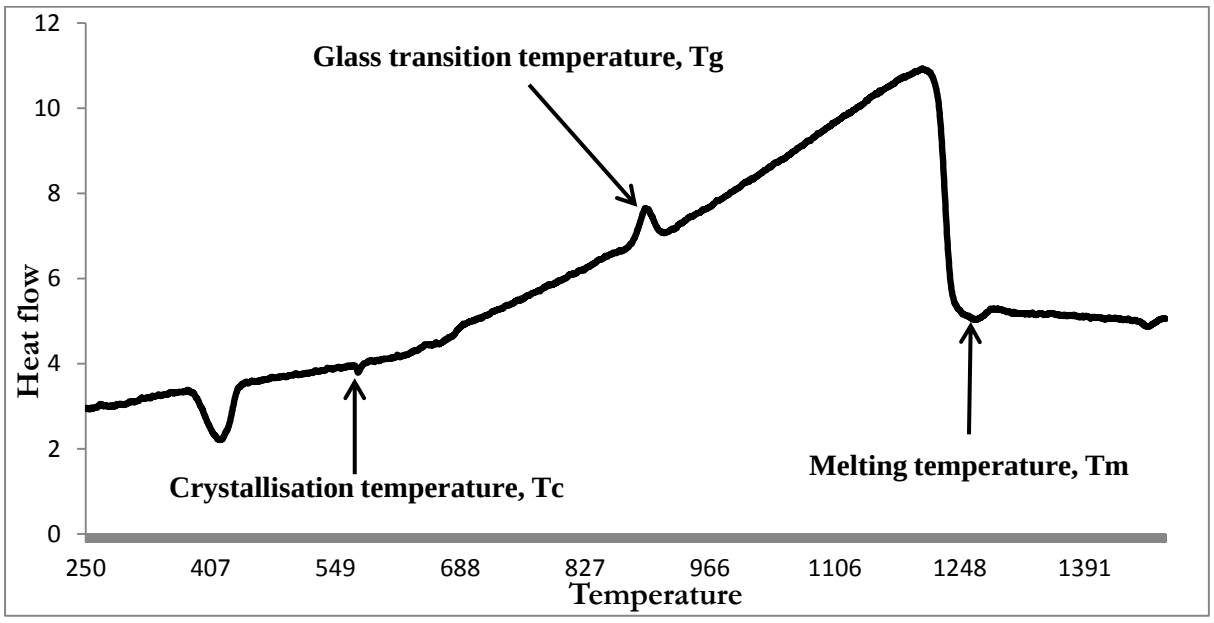

Figure 74: DSC curves of synthetic CMAS with composition $C_{24}M_{10}A_7S_{59}$, in mole%.

The variation in melting temperatures can be confirmed by comparing various CMAS compositions to a ternary phase diagram [13], where the standard CMAS composition is found within the Anorthite region compared to the High B.I. CMAS which sits in the lime region. This confirms the study by Stott et al. [65] which noted that CMAS melting temperature may vary depending on composition.

6.1.2 Effect of Time on Standard CMAS and Volcanic Ash Attack

The columnar, high porosity microstructure of electron beam physical vapour deposited (EB-PVD) TBCs make them susceptible to CMAS and volcanic ash attack. The molten deposit is able to penetrate the TBC columns by capillary action and by so doing, creating an interaction zone where yttria is sufficiently depleted from the bulk TBC, allowing the detrimental phase transformation from monoclinic to tetragonal. However, the columnar microstructure is important as it improves the strain tolerance of the system caused by the mismatch of thermal expansion, although this characteristic of the coating deteriorates with infiltration of molten deposits. Standard CMAS and volcanic ash attack mechanism is reported in literature [10; 11; 22; 68; 76; 160] to be driven by diffusion kinetics (dissolution and re-precipitation), which is a time and temperature dependent phenomenon.

To determine the time dependency of this method of TBC failure, a series of samples were exposed for different exposure times whilst keeping the temperature and amount of coverage constant. This research is a follow up from previous study by a Cranfield University MSc student, Gemma Whitman [13], looking at the minimum level of CMAS necessary to initiate CMAS attack. Whitman et al. [13] found that when the amount of CMAS deposited on the EB-PVD TBC samples were below 0.02g (4.8mg/cm^2), the samples showed very minimal degradation, with no great loss of microstructural identity, all columnar tips remaining fully intact. However, above this minimum concentration of CMAS (>4.8mg/cm^2), the coating

showed extensive microstructural evolution, with substantial degradation to the column tips. The result also showed that, time and concentration plays an important role in CMAS and CMAS-type (volcanic ash) degradation mechanism.

The thermochemical degradation mechanism was found to be attributed to the wetting characteristic of CMAS. Kramer et al. [11] also explained that standard CMAS composition has an affinity for 7YSZ TBC, and can easily wet and dissolve the TBC into the CMAS melt which re-precipitates with a different morphology and composition upon cooling.

In order to study the effect that time has on coating degradation, concentration was kept constant at minimum coverage (4.8mg/cm^2). Since Kramer et al. [11] indicated that full infiltration of CMAS occurs at 1300 °C, this was the temperature chosen for this set of experiments. The rate at which CMAS infiltrated the TBC was reported to be very high when the amount of coverage was in excess [11]; [13]. Excess CMAS coverage in this thesis refers to deposit above the minimum level (>4.8mg/cm^2), sufficient to cause significant coating degradation and enough to form a glassy layer on the surface of the coating. It was noticed for this set of tests that the exposure time plays an important role in molten deposit attack, especially initiating the attack. However, the effect of exposure time was significantly less in the second phase of the attack; propagation to completion, other factors being equal. Standard CMAS attack mechanism of TBC was found not to be an instantaneous phenomenon, meaning time is required for the deposits to react with the coating and also for phase transformation to occur. Since the mechanism is diffusion related, exchange of species will also take place. This theory is supported by the observation that for the first two hours of ageing at 1300 °C, the samples showed minimal damage, apart from the obvious feathering attack which is expected after one hour of ageing at this temperature (Figure 75). As can be seen from the micrographs in Figure 75, both samples retained their microstructural

identities, except for minor tips degradation which was progressed further after two hours exposure.

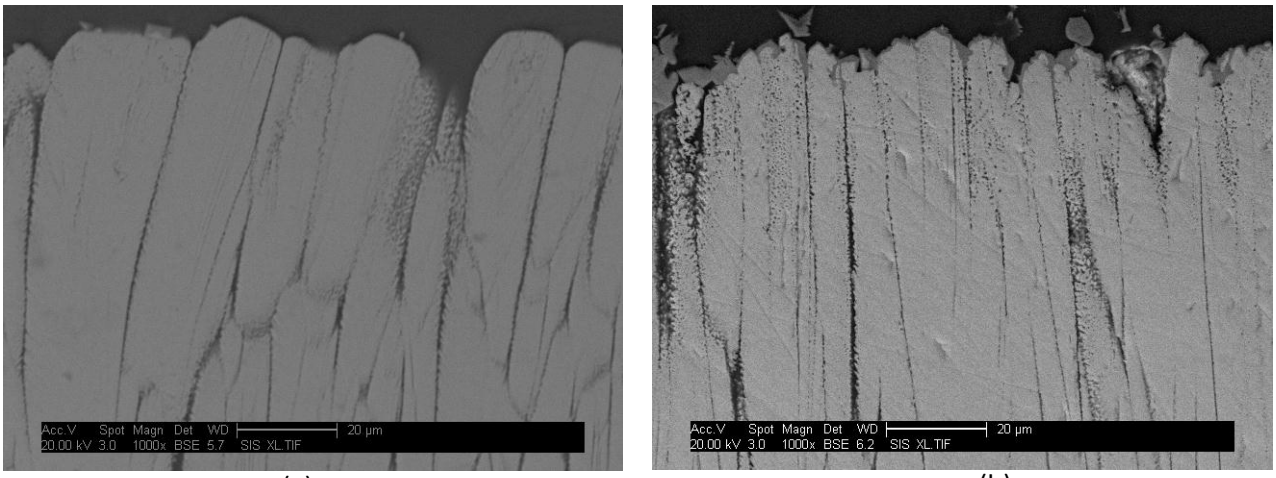

Figure 75: ESEM images of an EB-PVD TBC sprayed with 4.8mg/cm^2 of VA deposit then heat treated at 1300 °C for a) 1h, and b) 2h.

6.1.3 Effect of Temperature on Standard CMAS and Volcanic Ash Attack

In order to investigate the effect of temperature on volcanic ash and CMAS attack, it was vital to first determine the melting temperatures of each deposit. This was achieved by DSC analysis. Once their melting points were established, experiments were then designed to determine whether or not temperature has an effect on this mode of attack. For the purpose of temperature effect, the experiments were split into two sub-category; low temperature and high temperature experiments.

6.1.3.1 Long-term; Low Temperature Experiments

Low temperature in this study refers to thermal exposure below the transition temperature (below melting point) of the deposit. In these experiments, samples were heated to 1100 °C. Due to the nature of these tests, amount of coverage was not considered to be a variable hence these experiments were performed using relatively high amounts of VA/CMAS

coverage (24mg/cm^2) to try and induce significant damage. Figure 76 shows that, both deposits did not melt at 1100 °C test temperature but sintering of the CMAS deposit was noted. This was expected based on the melting point analysis obtained by the DSC revealing the melting point to be ~1258 °C. Figure 76 also showed that both VA and CMAS reacted differently depending on the exposure time, since VA/CMAS induced degradation is time dependent mechanism.

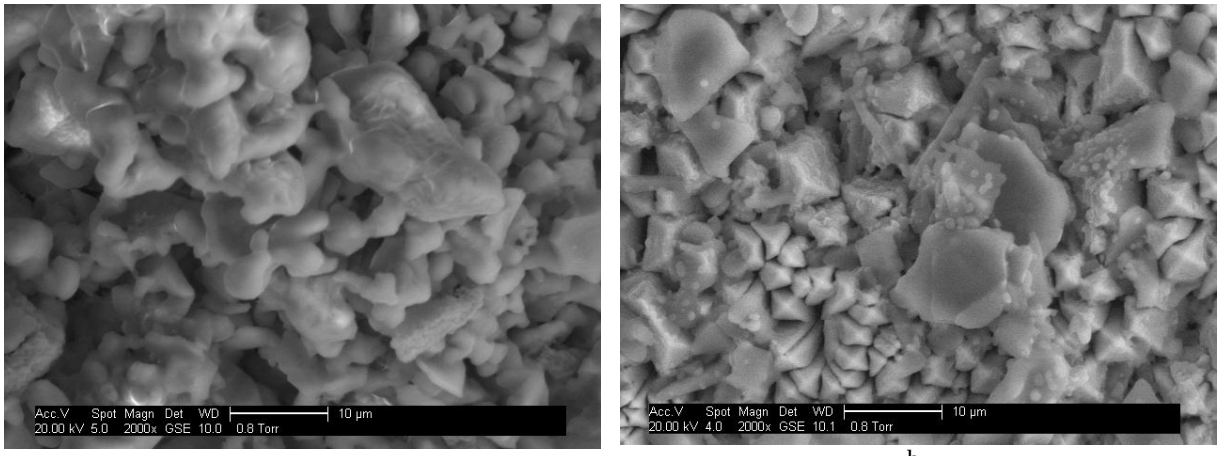

a b

Figure 76: ESEM analysis of TBC samples coated with 24mg/cm^2 of a) CMAS and b) VA, after ageing at 1100 °C for 100h showing solid particles sitting on the surface of the coating.

Low temperature tests were conducted for 8, 50, 100, 200, 500 and 1000 hours at 1100 °C in a box furnace. Two samples were used for each programme – one standard electron beam physical vapour deposited 7-8 wt% YSZ (standard/white TBC) and one Er-doped PYZ (pink TBC) sample. Firstly, the samples were examined to determine whether any melting of VA/CMAS had occurred (Figure 76). Cross section examination showed no apparent microstructural damage to both the standard YSZ and doped samples sprayed with volcanic ash and aged below 200 hours. However, SEM micrographs showed visible changes to the microstructure for samples sprayed with volcanic ash and aged above 200 hours, as illustrated on Figure 77. Samples with CMAS sprayed on the surface showed no major microstructural damage even when heat treated for 1000 hours. The reason for this being the temperature

differential (ΔT) between the test temperature and the melting point of CMAS was wider (~ 160 °C) compared to volcanic ash. The proximity of VA melting point was within ~5% of the test temperature while for CMAS it was more than double, ~12%.

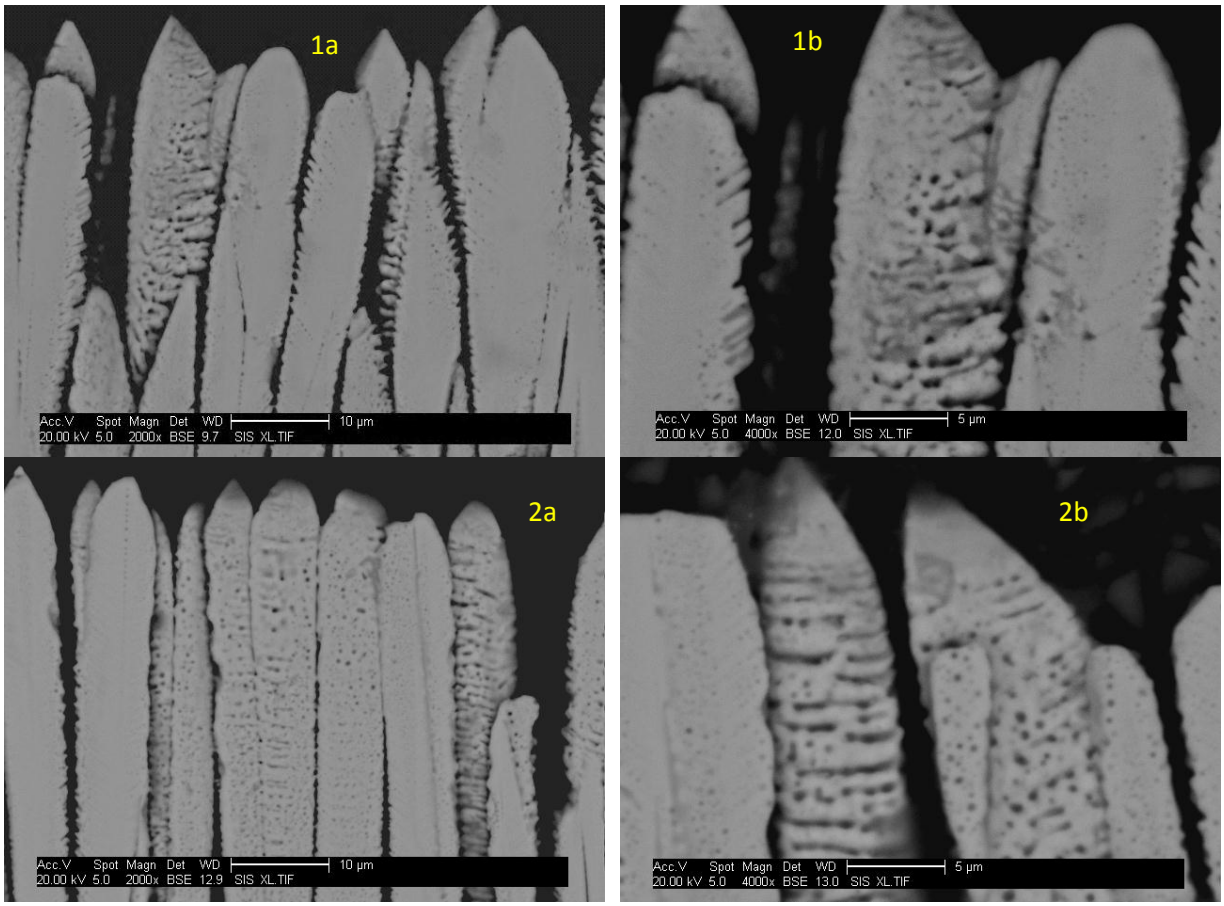

Figure 77: Cross-sectional scanning electron micrograph of an EB-PVD 7-8wt% YSZ samples 1) standard/white and 2) Er-doped/Pink TBC, heat treated for 1000 hours at 1100 °C, showing low temperature, long term damage.

Low temperature molten deposits induced degradation takes place by means of solid state diffusion. The diffusion mechanism was mostly along line (channels along the grain boundaries) and surface defects, (sintering, cracks, porosity). Solid state diffusion in oxides is a function of the temperature, activities of the constituents of the compounds, the microstructure, grain size, porosity and the presence of cracks. Due to the nature of the microstructure of EB-PVD TBC (columnar structure full of micro-pores and nano-pores), EB-PVD coatings are particularly susceptible to solid state diffusion.

6.1.3.2 High Temperature Experiments

High temperature refers to temperatures above the melting point of the deposit used. It was noticed that, temperature has an effect on the rate and depth of coating degradation, but not necessarily impacting on the mechanism of damage and the severity of attack. As the temperature increased above the melting point, the rate of reaction speeds up, meaning that the deposit is being used up at a quicker rate and the depth of penetration is faster. As seen on Figure 78, the melt has infiltrated the entire TBC thickness, yet the damage mechanism was similar to that observed for low temperature attack. The images in Figure 78 are indicative of a phase transformation from t' to monoclinic, as a result of increased Y_2O_3 leaching rate. EDAX later confirmed that substantial amount of yttria had been leached out in this area (spectrums 1-4, Figure 89), which instigated a phase transformation as stated earlier.

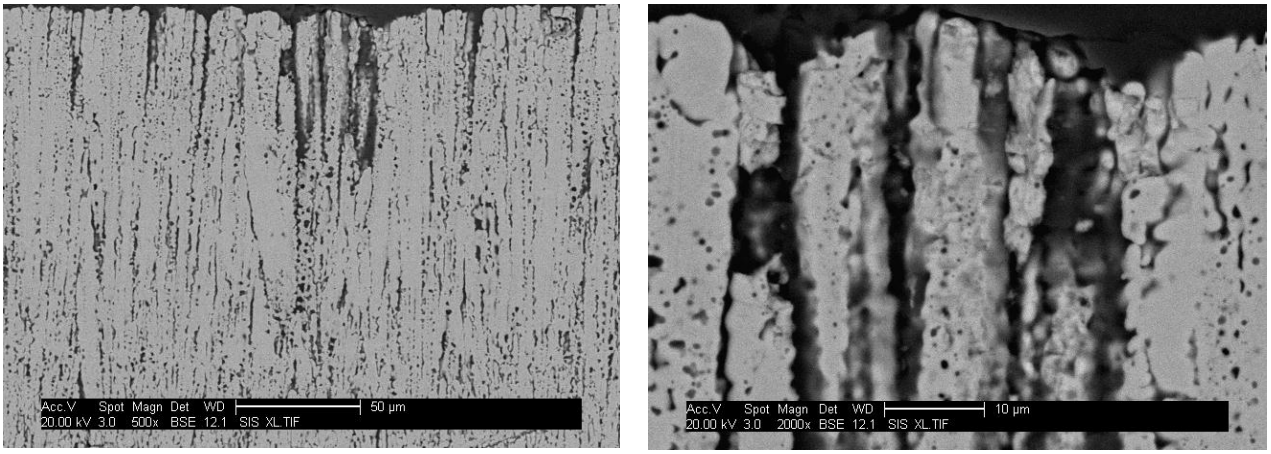

Figure 78: VA infiltrated thickness of TBC, 4h at 1400 °C, 24mg/cm^2. Similar damage mechanism but extensive slag penetration

The effect of temperature on reactions below the melting temperature of slag was found to be much higher than above the melting point. Reason being that the energy barrier necessary to initiate solid state reactants (in the case of low temperature reaction) is far higher than in liquid-solid reactant (high temperature experiment). The major difference increasing temperature was found to have on high temperature experiment was the increased in the pace of the reaction, however following the same reaction route. As per the results discussed in

this section, the formulated hypotheses that changing the amount of CMAS deposited and time at temperature (Severity of exposure) will both affect the rate of CMAS attack is proven to be valid. CMAS deposits get used up during the chemical attack hence by varying the quantity of CMAS available the rate of CMAS attack also changes. Study of the effect of time at temperature was divided into two sections; low and high temperature effects. It was found that, increasing the exposure temperature accelerates the rate of attack.

6.2 Stages of Standard CMAS and Volcanic Ash Attack

The theory proposed in this thesis is that, the system is required to attain a certain activation energy state for the reaction to commence. Initially, the system absorbs energy in order to get to an equilibrium state to excite the reactants and favour a reaction between the deposit and TBC structure. This stage is termed the initiation phase and is quickly proceeded by an adhesion phase. Adhesion plays an important role in determining whether a fluid in the presence of a solid has the correct energy to bind to the solid surface (i.e. whether or not both the slag and the coating surface have suitable surface energies to facilitate sticking of the molten slag to the coating surface). Adhesion is a function of wettability (surface tension/surface energy) of the system. Wettability is defined as the tendency of a fluid to spread on and preferentially adhere to or "wet" a solid surface in the presence of other immiscible fluids. Wetting behaviour gives an indication of the ability to penetrate, and a measure of the driving force for penetration, but not necessarily the degree of chemical attack. Wettability can be measured by the contact angle in a sessile drop (SD) test for which,

$$\gamma_{SL} + \gamma_{LV} Cos\,\theta = \gamma_{SV} \qquad \text{Equation 17}$$

when the liquid wets the surface. Here $\boldsymbol{\theta}$ = contact angle, less than 90° when wetting the surface; and $\boldsymbol{\gamma_{SL}}$, $\boldsymbol{\gamma_{LV}}$ and $\boldsymbol{\gamma_{SV}}$ are the surface energies (tensions) of solid - liquid, liquid - vapour and solid – vapour respectively.

The measurement of the contact angle can be taken as a good indicator of wettability; it actually measures the change in surface energy as a result of melt penetration (see Equation 17). The larger the contact angle, the more difficult it is to wet a given solid with the particular liquid. If $\theta < 90°$, then the liquid exhibits an affinity for the surface, it can lower the surface energy by wetting the surface. If $\theta = 0°$, the surface is strongly wetting (perfectly wetting liquids). If $\theta > 90°$, the liquid exhibits an aversion for the surface (degree of non-wetting). If $\theta = 180°$, then the liquid is non-wetting. Volcanic ash (VA) and CMAS are expected to have different wetting behaviour, which is influenced by the chemical composition of the compound. A compound with higher chemical complexity is expected to have lower wettability compared to a compound with less chemical complexity. On this basis, CMAS would be expected to have better wetting characteristics than volcanic ash because there are fewer elements in CMAS compared to VA, hence CMAS is expected to have a greater depth of penetration. However, this was contrary to the observations made in this study, where volcanic ash had infiltrated the entire TBC (~200 µm) after just four hours at 1300 °C with excess amount of coverage, whereas CMAS can only penetrate ~82 µm (~41% penetration depth) under similar conditions, as is seen in the images in Figure 79. One likely explanation for this observation may be attributed to the fact that VA has a lower B.I. (0.46). This low B.I. composition is less viscous, hence will penetrate further compared to standard CMAS which has a much higher B.I. value (1.08) and therefore was expected to be more viscous, other factors being equal.

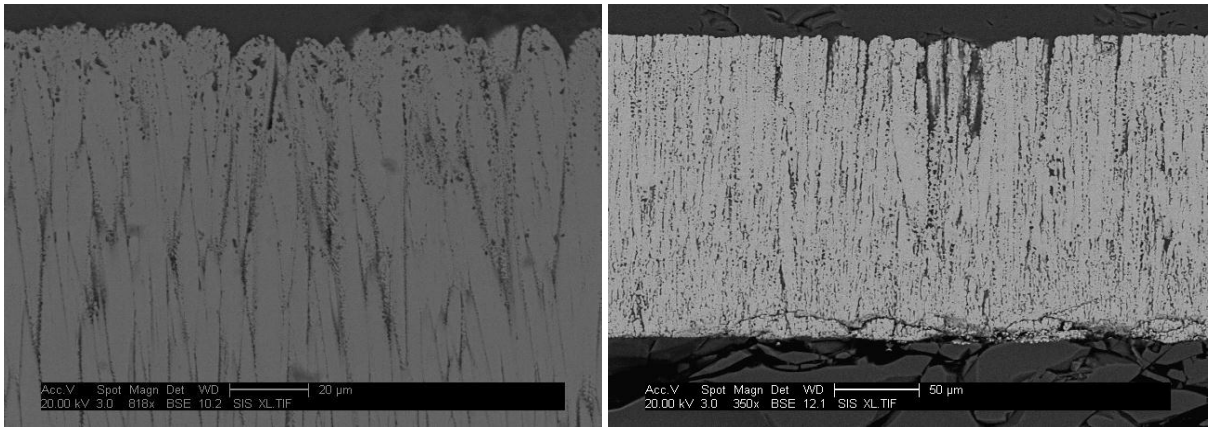

(a) (b)

Figure 79: The depth of penetration of standard/white TBC aged for 4h at 1300 °C. (a) CMAS and (b) VA showing penetration through entire TBC.

Once all conditions are favourable for an attack to take place, the reaction then enters into an incubation phase. The incubation period refers to the time it takes for the reaction to stabilise, to the time it takes for the reaction to show first symptoms of damage. All the above stages occurred within the first two hours of thermal ageing before any symptoms of severe degradation. This initial stage of attack is a very slow process due to the high energy barriers involved and influence of heat over time (diffusion kinetics) that is necessary to overcome the energy barrier.

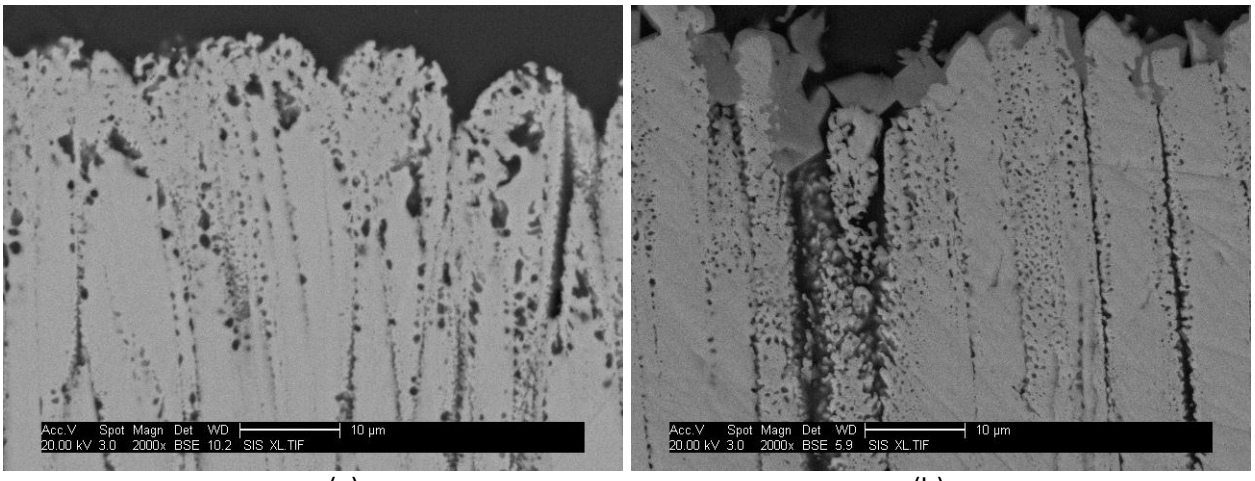

(a) (b)

Figure 80: Cross-sectional SEM micrograph of standard/white TBC heat treated for 4h at 1300 ℃ a) 4.8mg/cm^2 CMAS showing complete degradation of columnar tips b) 4.8mg/cm^2 VA showing severe coating degradation.

Figure 80 shows that both VA and CMAS have infiltrated the TBC columns, with varying degree of damage after 4h of exposure. However, CMAS attack showed a more adverse attack, with complete degradation of the tips, whereas volcanic ash tends to form a reactive phase (~5 µm around the column tips), but with less damage observed to the TBC microstructure. Elemental analysis of this region revealed this area to be a silica-rich phase, zirconium silicate ($ZrSiO_4$), as shown on Figure 81.

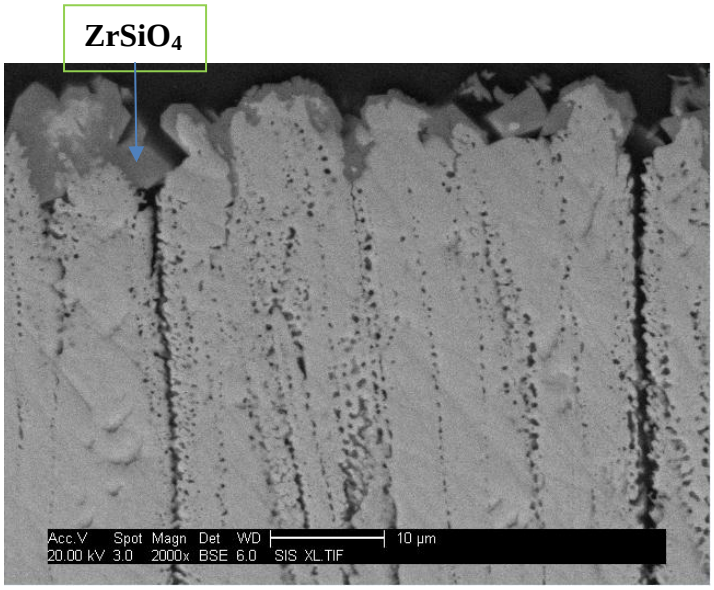

Figure 81: EDAX analysis of the protective phase formed by VA attack on 7-8% YSZ TBC.

For the level of degradation observed in Figure 80 to occur, all conditions mentioned above (minimum coverage at 1300 ℃) and reaction path (initiation, adhesion and incubation phase) must be satisfied and the reaction must have exceeded the "two hours" threshold. In the case of Figure 80, the samples were exposed for four hours and the reaction had entered the next phase of attack, the penetration phase. Melt penetration mechanism proceeds via TBC pores and down column boundaries, given that standard 7YSZ TBC is about 30% porous (thereby giving the coating its strain tolerance), this can be rapid. This melt penetration mechanism involves silica in the melt reacting with the TBC by leaching Y_2O_3 from the ZrO_2 grains, so

destabilising the TBC, so that it transforms from a tetragonal to a monoclinic phase. Figure 82 shows an EDAX analysis performed in the globular regions, confirming that CMAS has infiltrated the pores and formed a reacted composition (phase). EDAX analysis revealed that, the deposit composition filling the pores results in 1:1 and 1:9 CaO/SiO_2 mole ratios for CMAS and VA samples respectively. These atomic ratios indicate that, samples with CMAS form a phase transformation from pseudo-wollastonite to an anhydrite phase, whereas VA infiltrated samples result to anorthite transformation (based on the phase diagram in Figure 48).

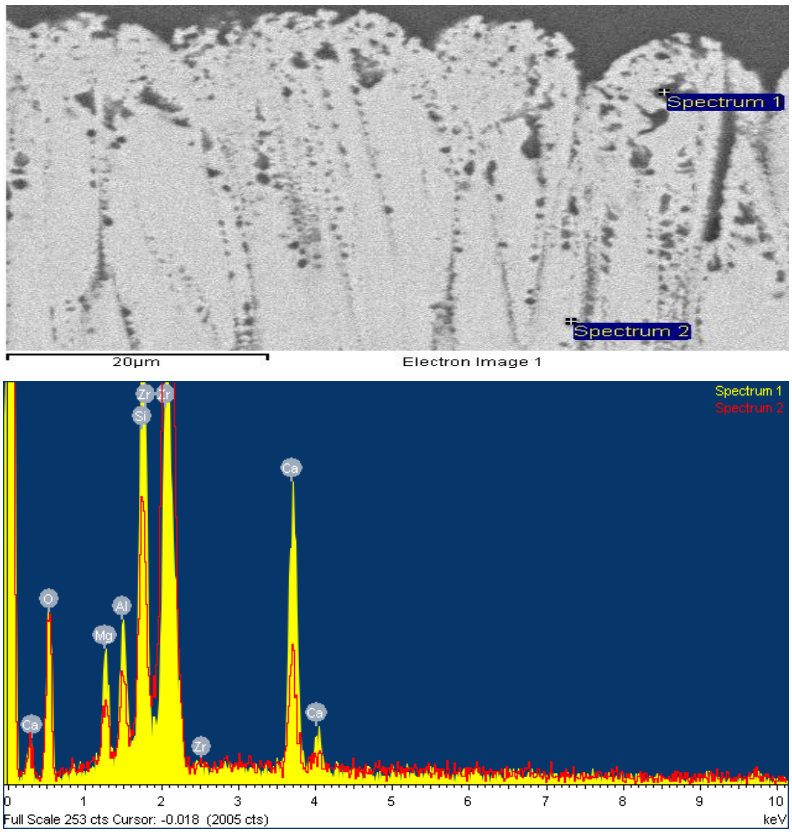

Figure 82: SEM-EDAX elemental analysis of globular pore deposits of CMAS.

When the pores are infiltrated with molten deposits, the coating can no longer adjust to the thermal cycle, and it spalls. Penetration rate is a function of chemical composition, temperature and time. The penetration depth was measured using an analytical package built in the environmental scanning electron microscope.

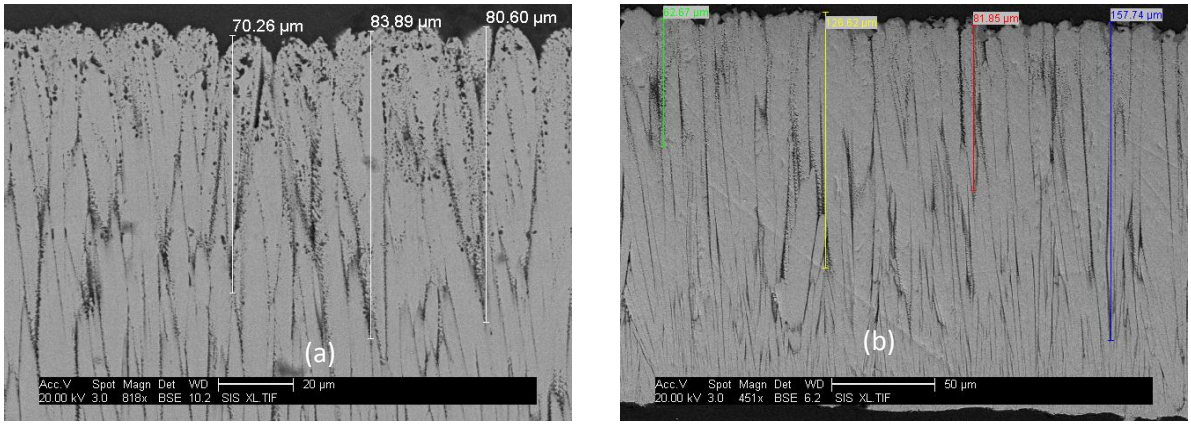

Figure 83: ESEM images showing depth of penetration of CMAS and VA infiltrated samples shown on a and b respectively.

Figure 83 revealed that volcanic ash had a greater rate of penetration compared to synthetic CMAS, when exposed for 4h at 1250 °C, with VA samples averaging 187 µm depth while CMAS infiltrated samples have an average penetration depth of 76 µm. Table 24 and Table 25 show the depth of penetration of both VA and CMAS with their calculated Median Rank (MR) values.

Table 24: Statistical Analysis and Ranked-Ordered depth of penetration for CMAS (probability values relate to chance of greater depth)

Depth of penetration, µm	**Rank**	**Median Rank (MR)**
62.8	1	0.109
70.3	2	0.266
80.6	3	0.422
81.9	4	0.578
83.9	5	0.734
126.6	6	0.891

Table 25: Statistical Analysis and Ranked-Ordered depth of penetration for VA (probability values relate to chance of greater depth)

Depth of penetration, µm	Rank	Median Rank (MR)
180.9	1	0.109
180.9	1	0.266
181.4	3	0.422
192.7	4	0.578
195.3	5	0.734
195.3	5	0.891

Bernard's Formula was used to estimate the Median Rank for each depth of penetration after four hours exposure with CMAS (Table 24) and volcanic ash (Table 25). The Median Rank is the point on the distribution at which the failure value is equally expected to fall above or below. A range of penetration depths were sampled and the cumulative probability distribution for CMAS revealed that the probability of the depth of penetration being less than 62.8 µm is 11% and 89% probability of CMAS to have penetrated up to 126.6 µm of the TBC (Table 24). With VA, one would expect 11% of the sample as a whole to have a penetration depth of 180.9 µm and 89% of the sample to the sample to have a penetration depth of up to 195.3 µm (Table 25).

Once penetration has occurred and these reacted phases are formed, the reaction then proceeds to the propagation phase should all other factors be equal. The propagation phase creates a chain of reaction until the reaction goes to completion, which in this case is degradation of the TBC performance. The penetration and propagation stage is where the coating degradation mechanism takes place. The damage mechanism is time-temperature dependent and it is driven by dissolution of the TBC and diffusion (leaching out) of yttria, resulting in a phase transformation from metastable tetragonal phase (t') to monoclinic phase (m) (t' → m + F), as shown by Whitman [83].

So far, exposure time has proven to play a significant role in short-term CMAS degradation, from initiation to failure. At same condition of 4.8mg/cm^2 slag concentration and an ageing temperature of 1300 °C, VA and CMAS samples were heat treated for eight hours and examined. The samples were quite similar to the four hours samples, with the only noticeable difference being a slight increase in the depth of penetration (Figure 84). This observation agrees well with that made by Whitman [13], in which she noted that the depth of formation of the globular particles being the major difference. It can be said that, time dependency of molten slag attack is significant until the reaction gets into the propagation phase (2 – 4 hours exposure; with minimal concentration), beyond this duration, an exponential increase in exposure time is not respondent with proportional increase in the degree of damage. However, as mentioned earlier, the depth of penetration is time dependent hence the reason there was a slight increase in the penetration depth, up to the point where the deposits are eventually "used up" or "reacted" to form different phases. Exposure time may influence the depth of CMAS penetration but does not influence or alter the mechanism of attack.

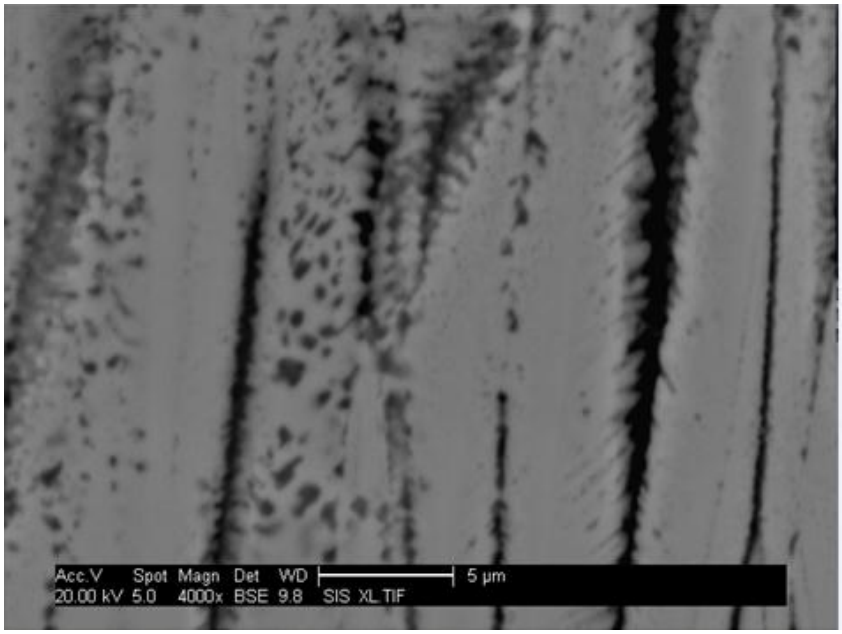

Figure 84: 8h showing increased depth of penetration of globular particles near base of TBC.

The map on Figure 85 summarises the reaction process of short-term/minimum level coverage attack mechanism. Time is a very important parameter in terms of initiating the reaction of molten deposits and coating chemistry, and propagating the attack to the point of coating failure. This process is believed to take 2 – 4 hours when the amount of coverage applied is minimum (meaning there is no formation of the glassy coating after heating). However, it was noted that, once the reaction has gone beyond the propagation phase, the effect of time as a factor of molten deposits attack was diminished.

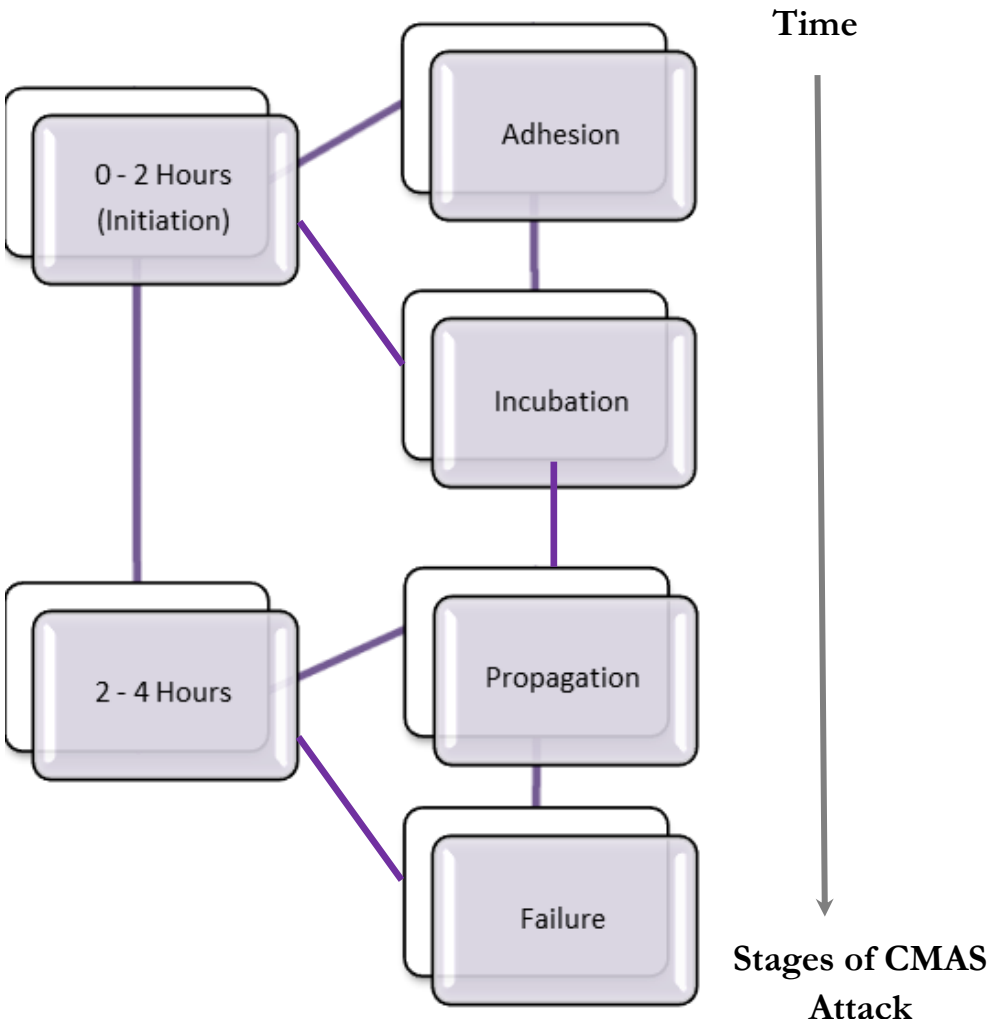

Figure 85: Reaction path of TBC attack with minimum amount of CMAS, to demonstrate exposure time effect on molten deposits attack.

6.3 Attack of PYSZ by Low Basicity Index (Acidic) deposits: B.I. < 1.8

Whilst the initial objective of this study was to investigate the interaction of volcanic ash and "standard CMAS" with EB-PVD TBC, simulating chemical attack in the turbine section of the engine, it became evident early on that the chemical composition of the melts would affect how the PYSZ reacts. Seok et al. [13] reported attack of the ceramic lining in blast furnace by molten slag, by-product of steel making. They also reported that the reaction product changes depending on the Basicity of the slag. Hence very earlier in this study, the question was posed; would the Basicity of different CMAS compositions affect its degradation mechanism? Would Basicity have an effect on the severity of damage? In order to answer these questions, Seok et al. [110] theory of Basicity was adopted and experiments were designed to investigate zirconia reactivity in acid-base slag.

Low B. I. deposits are CMAS compositions mainly found in temperate regions like in Europe, thereby most likely to be found in aircraft engines travelling across European airspace. Low B. I. refers to a CaO/SiO_2 ratio < 1.8. Generally, almost all model CMAS compositions used by previous authors fall into this low Basicity Index region (Figure 49) category and therefore the damage mechanisms observed were very similar, although varying degrees of the severity of attack were observed. The Low B. I. composition used in this category was $C_{24}M_{10}A_7S_{59}$ mol%, B.I. = 0.69, having a melting temperature of 1234 °C. However, the "standard" CMAS ($C_{35}M_{10}A_7S_{48}$ mole%, B.I. = 1.08) and Eyjafjallajokull volcanic ash (B.I. = 0.46) compositions also studied belong to the Low B.I. category and comparison will be drawn between the three Low B.I. attack mechanism. The top view of a low B.I. deposited sample after ageing can be seen from the image in Figure 86. In the case, excess coverage of Low B. I. CMAS (24mg/cm^2) was employed.

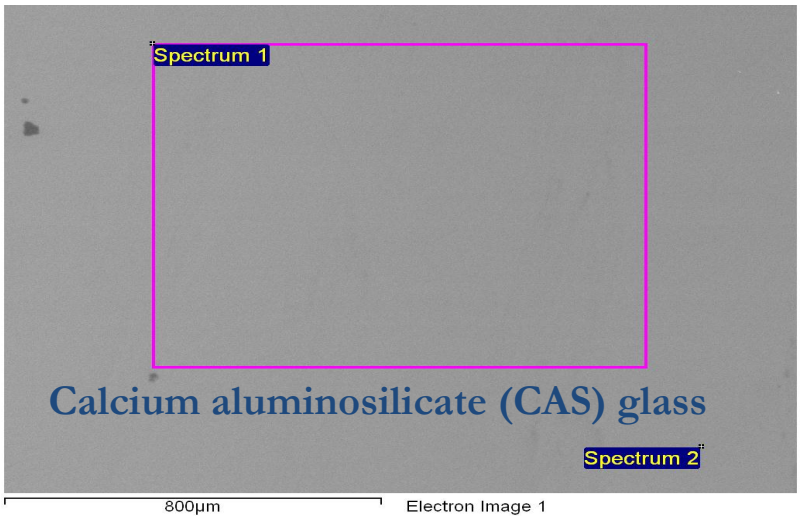

Spectrum	O	Mg	Al	Si	Ca	Y	Zr
Spectrum 1	63.76	3.12	5.88	19.13	6.09	1.06	0.96
Spectrum 2	63.62	2.96	6.75	18.91	5.97	0.80	0.99

All results in atomic%

Figure 86: Top analysis of Low B.I. deposited sample after 4h at 1285 °C, showing formation of a glaze at the surface.

Low B.I. deposit was found to form a glassy layer on the surface of the TBC (Figure 86). This is a "classic CMAS" attack characteristic, as widely reported in the open literature [110]. Analysis of this region (shown on Figure 86) revealed a viscous layer, possibly calcium aluminosilicate (CAS) glass. The attack as shown in Figure 87 and Figure 88 is less in the bulk of the coating but shows severe degradation of the columnar tips, near the surface and also along the column boundaries. Low B.I. CMAS ($C_{24}M_{10}A_7S_{59}$ mol%) infiltration of PYSZ TBC showed a similar degradation mechanism to "standard" CMAS and Eyjafjallajokull volcanic ash, although with varying degree of severity (Figure 87). This was expected since all three compositions belong in the same B.I. category.

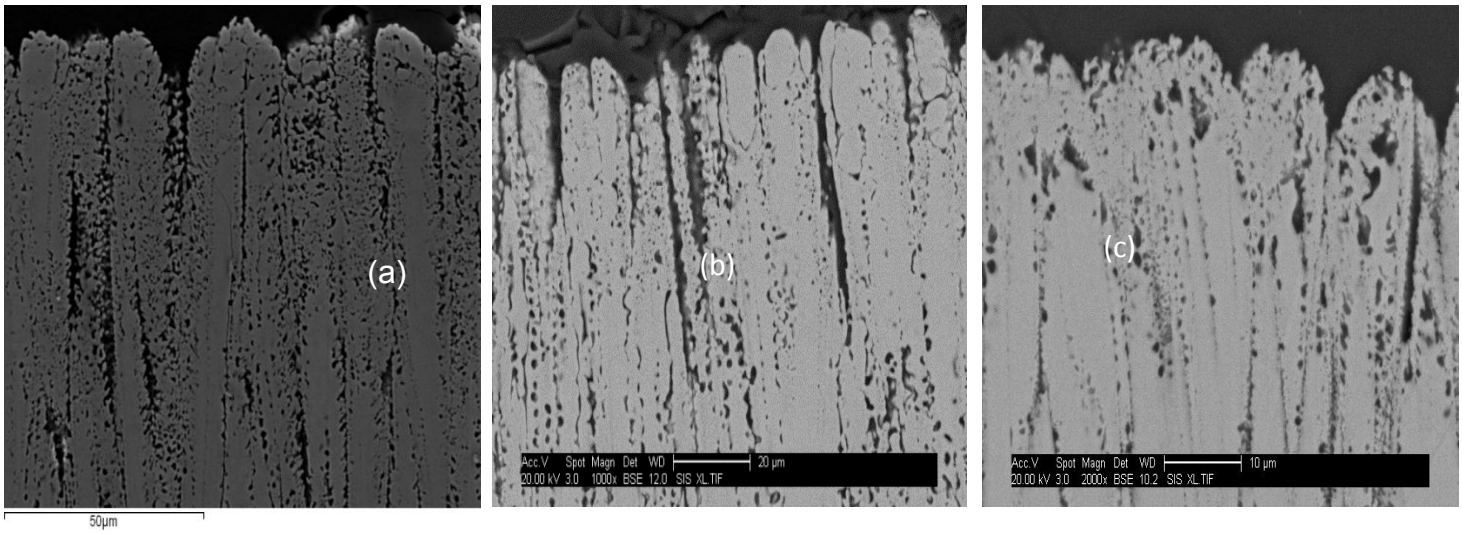

Figure 87: (a) C24M10A7S59 mole% (B. I. ~0.7), (b) Eyjafjallajökull volcanic ash (B.I. ~0.5) and (c) Standard CMAS, $C_{35}M_{10}A_7S_{48}$ mole% (B.I. = 1.08)

Figure 88 illustrates micrograph images of an EB-PVD sample sprayed with Low B.I. slag and aged for four hours. The thermochemical attack mechanism for this mode of attack has been extensively studied and the results observed herein were similar to that published in the literature [11; 13; 68; 69; 150] which can be thought of as "classic CMAS attack" i.e. that reported by previous authors. The mechanism is that of dissolution of the YSZ coating and re-precipitation of zirconia, resulting in Y_2O_3 depleted zones and a disruptive phase transformation from t'-zirconia to monoclinic zirconia. As can be seen, the attack mechanism comprises of leaching of Y_2O_3 and forming dark globules of a CMAS related phase.

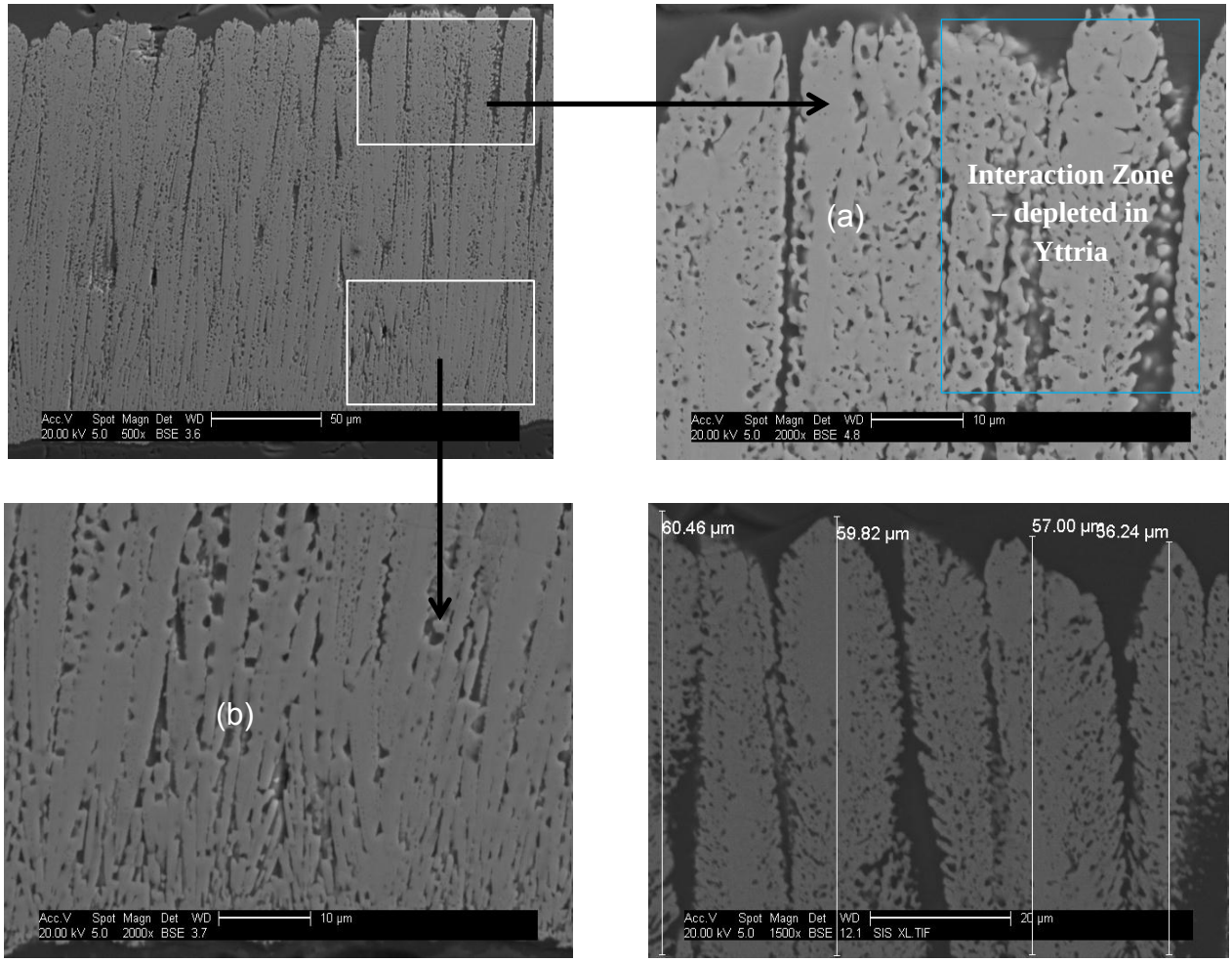

Figure 88: EB-PVD TBC infiltrated with $C_{24}M_{10}A_7S_{59}$ mole% aged for 4 hours at 1285 °C (B. I. = 0.69).

The yttria depleted zone is depicted on the image in Figure 88 (interaction zone) which was confirmed by EDAX analysis (results in Figure 89). Yttria depletion is indicative of the detrimental phase transformation from t'-zirconia to monoclinic zirconia. The evidence of evolution to monoclinic is shown further in Figure 89 where leaching of yttria near the surface of the coating (spectrums 1-4) can be observed.

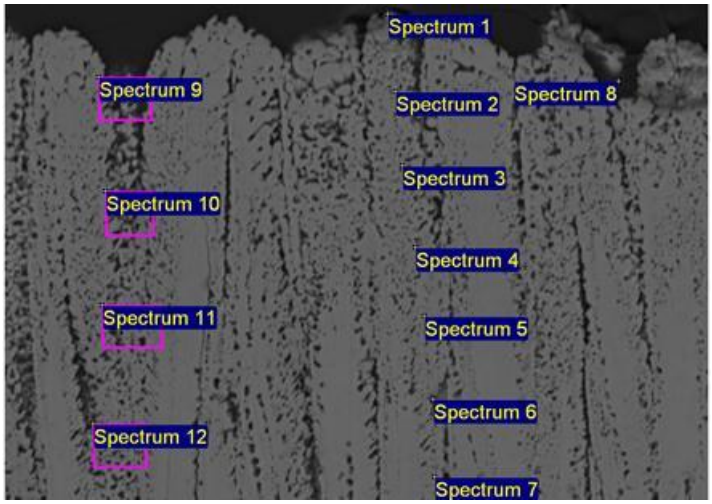

Spectrum	O	Mg	Al	Si	Ca	Y	Zr
Spectrum 1	69.5	0.8	1.7	4.6	1.8	0.0	21.5
Spectrum 2	67.5	0.3	0.7	1.2	0.6	0.0	29.7
Spectrum 3	67.7	0.5	1.0	1.9	0.9	0.0	28.0
Spectrum 4	70.2	0.6	0.7	1.4	0.6	0.4	26.1
Spectrum 5	66.0	0.2	0.5	0.0	0.2	1.2	31.9
Spectrum 6	69.3	1.7	2.5	7.5	2.6	0.7	15.7
Spectrum 7	65.4	0.0	0.5	1.2	0.7	1.2	31.0
Spectrum 8	71.2	2.9	3.8	13.9	3.9	0.5	3.9
Spectrum 9	69.3	1.7	2.5	7.6	2.7	0.0	16.2
Spectrum 10	67.9	1.1	2.1	5.7	2.1	0.0	21.1
Spectrum 11	65.6	1.1	1.5	4.3	1.7	0.7	25.2
Spectrum 12	65.7	0.8	1.4	3.6	1.5	1.0	26.0

All results in atomic%

Figure 89: Low B.I. sample – indicative phase transformation from metastable tetragonal phase (t') to monoclinic (m)

EDAX elemental mapping (Figure 90) showed that all the oxides involved in the deposit are present in the core of the TBC. Additionally, it shows that once in a liquid state the CMAS infiltrates via the columns first. EDAX mapping results also illustrates that slag penetrated the thickness of the coating, particularly down the grain boundaries. It is believed that Low B.I. attack can be thought of as classical CMAS attack.

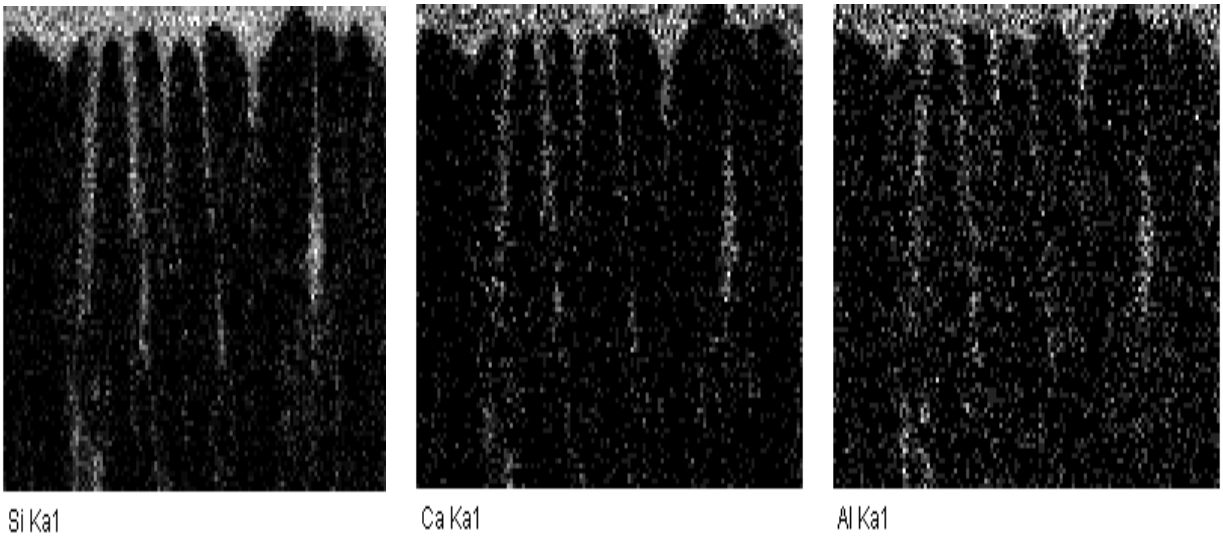

Figure 90: EDAX elemental mapping of $C_{24}M_{10}A_7S_{59}$ mole% (B. I. = 0.69).

Focused Ion Beam (FIB) was used to study the bottom of the Low B.I. samples, with special attention paid to the TBC/Substrate interface which in real life situation would correspond to the TBC/TGO interface.

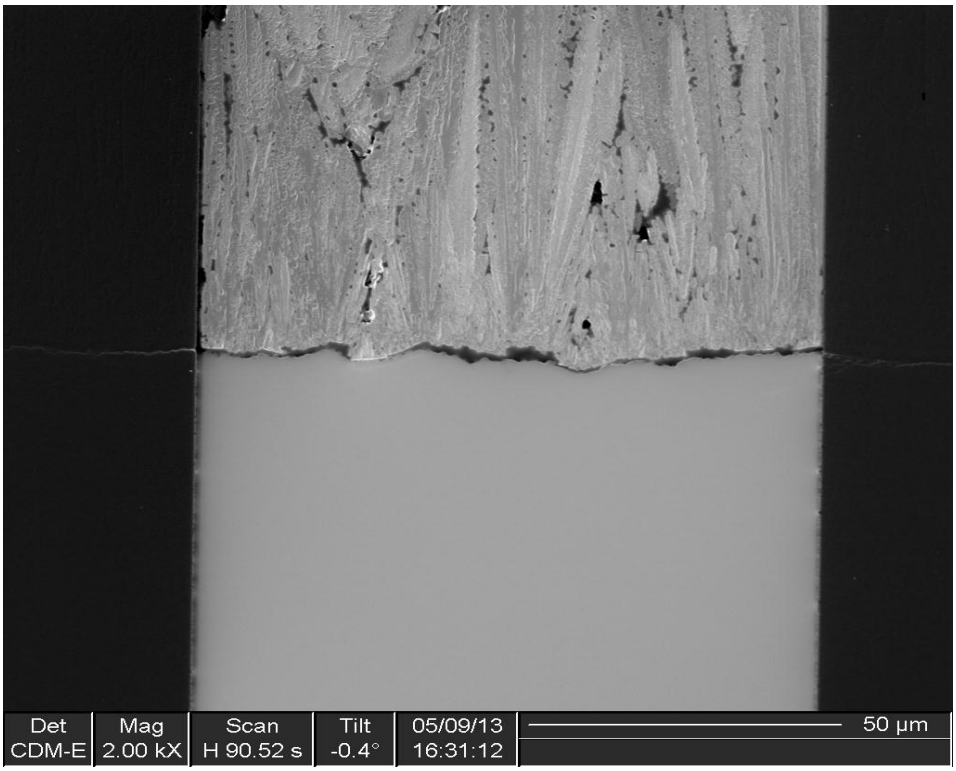

Figure 91: FIB image of a Low B.I. sample after 4h exposure at 1285 °C, showing minimal attack at the bottom of the coating.

Figure 91 shows minimal degree of attack on the TBC, characterised by classic CMAS attack footprint of dark globules although the alumina substrate is seen to have no damage and no evidence of CMAS penetration into the substrate. Hence in service operation, Low B.I. attack is not expected to form a melt pool at the TBC/bond coat interface and potentially damaging the alumina TGO or attack through to the bond coat/substrate. A similar result was also noticed with eight hours exposure with Low B.I. CMAS, even though there was noticeable increase in the degradation at the bottom of the TBC columns, the alumina substrate remained intact (Figure 92).

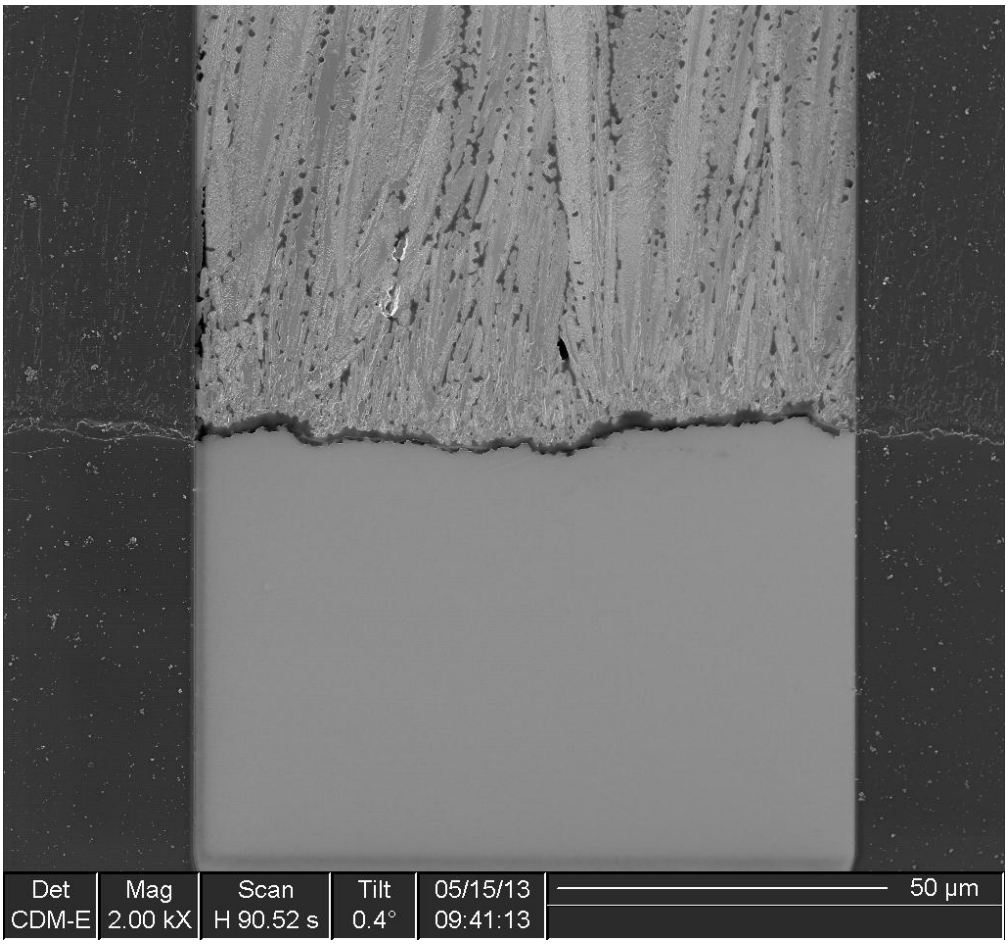

Figure 92: FIB image of Low B.I. sample after 8h exposure at 1285 °C, showing increased activities of classic CMAS attack at the bottom of the coating.

6.4 Free-Standing TBC; Eliminating the Effect of the TBC Substrate

Free-standing TBC was obtained from within the EB-PVD coater at Cranfield University, which was the residual TBC layer formed from a number of previous deposition runs. The composition of the free-standing TBCs was very similar to the standard EB-PVD samples used throughout this study. Figure 93 is a scanning electron micrograph looking at the top of a free-standing TBC reference sample, aged at 1480 ºC with no CMAS. The columnar microstructure of an electron beam physical vapour deposited process is evident from the image in Figure 93, although not a perfect columnar structure.

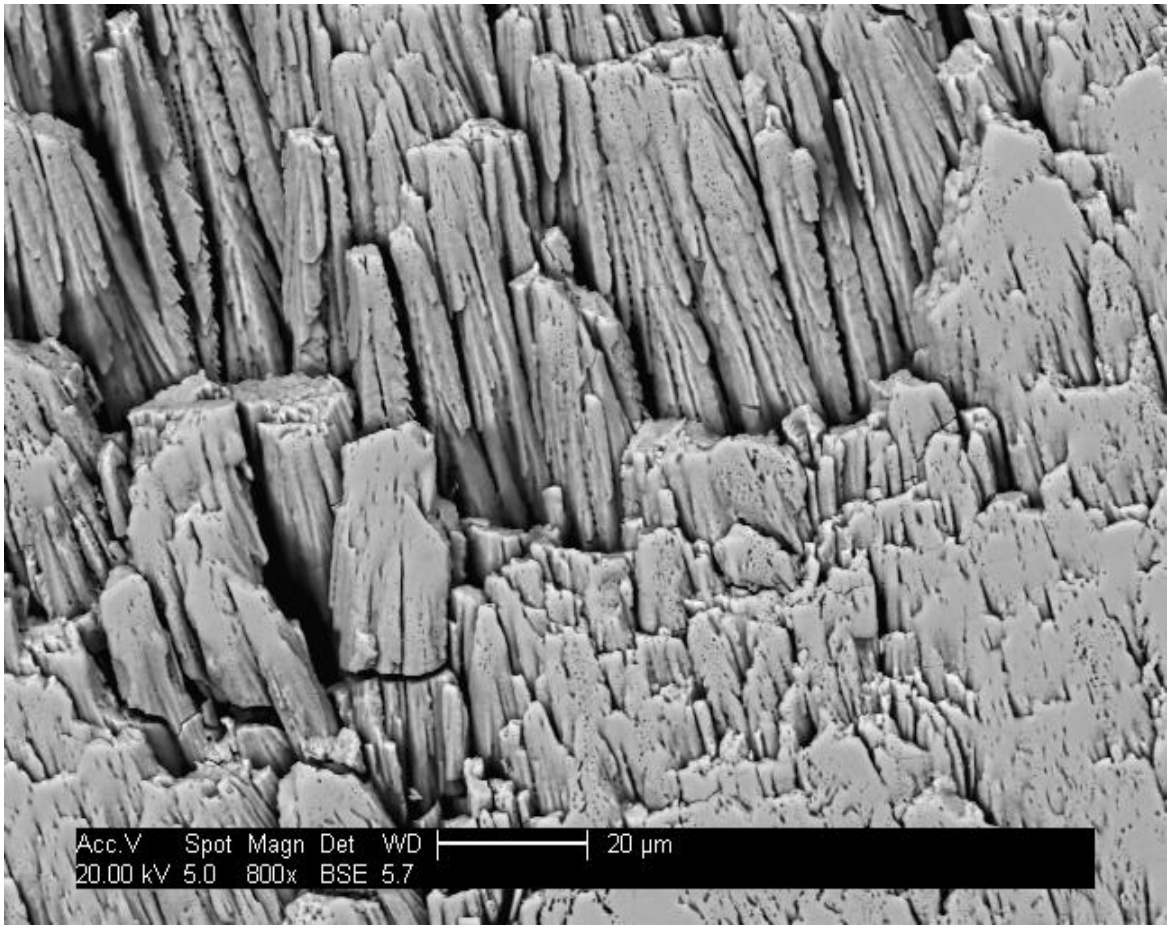

Figure 93: Top view of a free-standing TBC reference sample aged at 1480 ºC for 4h, without CMAS.

Free-standing sample sprayed with Low B.I. deposit and heat treated for four hours was examined using SEM and EDAX spot analysis, as shown in Figure 94. The cross-sectional

image shows characteristic globular particles formation associated with "classic" (Low B.I.) CMAS attack, linked to the exchange of materials between CMAS and TBC (yttria leaching out from the TBC and into the CMAS melt while CMAS particles formed phases in the TBC structure). Even though the initial microstructures were not identical, it was very clear that the degradation mechanism was similar to that observed with standard CMAS and Low B.I. deposits. This shows that, the lack of a substrate material did not play an important role in the overall degradation mechanism.

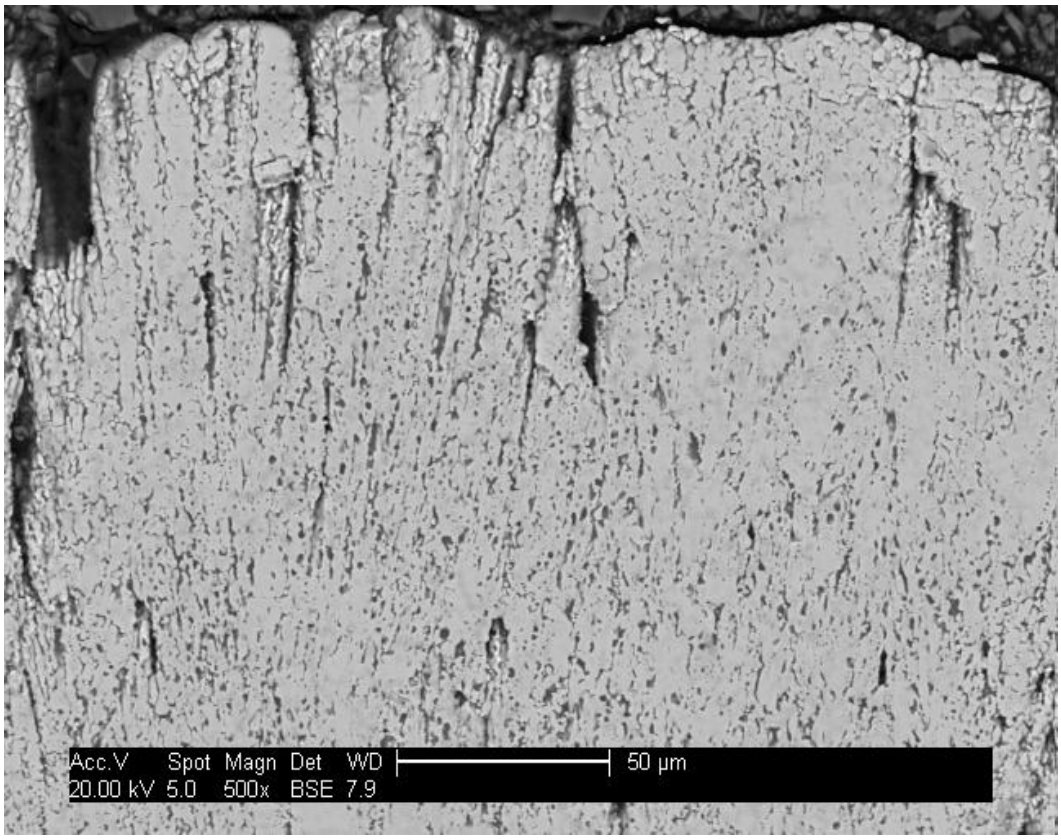

Figure 94: Free-standing sample sprayed with Low B.I. deposit and aged for 4h at 1480 ºC, showing characteristics of classic CMAS attack.

Low B.I. attack is characterised by a phase transformation from the "as-deposited" tetragonal phase to the detrimental monoclinic zirconia, due to the depletion of yttria from the TBC. The ZrO_2-$YO_{1.5}$ ratio is an indication of the phase transformation that has occurred as a result of slag attack. The ratio is calculated from Equation 18;

$$\frac{[YO_{1.5}]}{[ZrO_2]+[YO_{1.5}]}, \text{ in mole\%} \qquad \text{Equation 18}$$

For an "as-received" TBC, the ratio calculated using Equation 18 is 0.08, whereas after ageing with Low B.I. deposit for four hours, the ZrO_2-$YO_{1.5}$ ratio is reduced to 0.01 (Figure 95), a suggestion that the system has undergone a phase transformation yielding monoclinic zirconia as a result of yttria leached out from the TBC and into the CMAS melt.

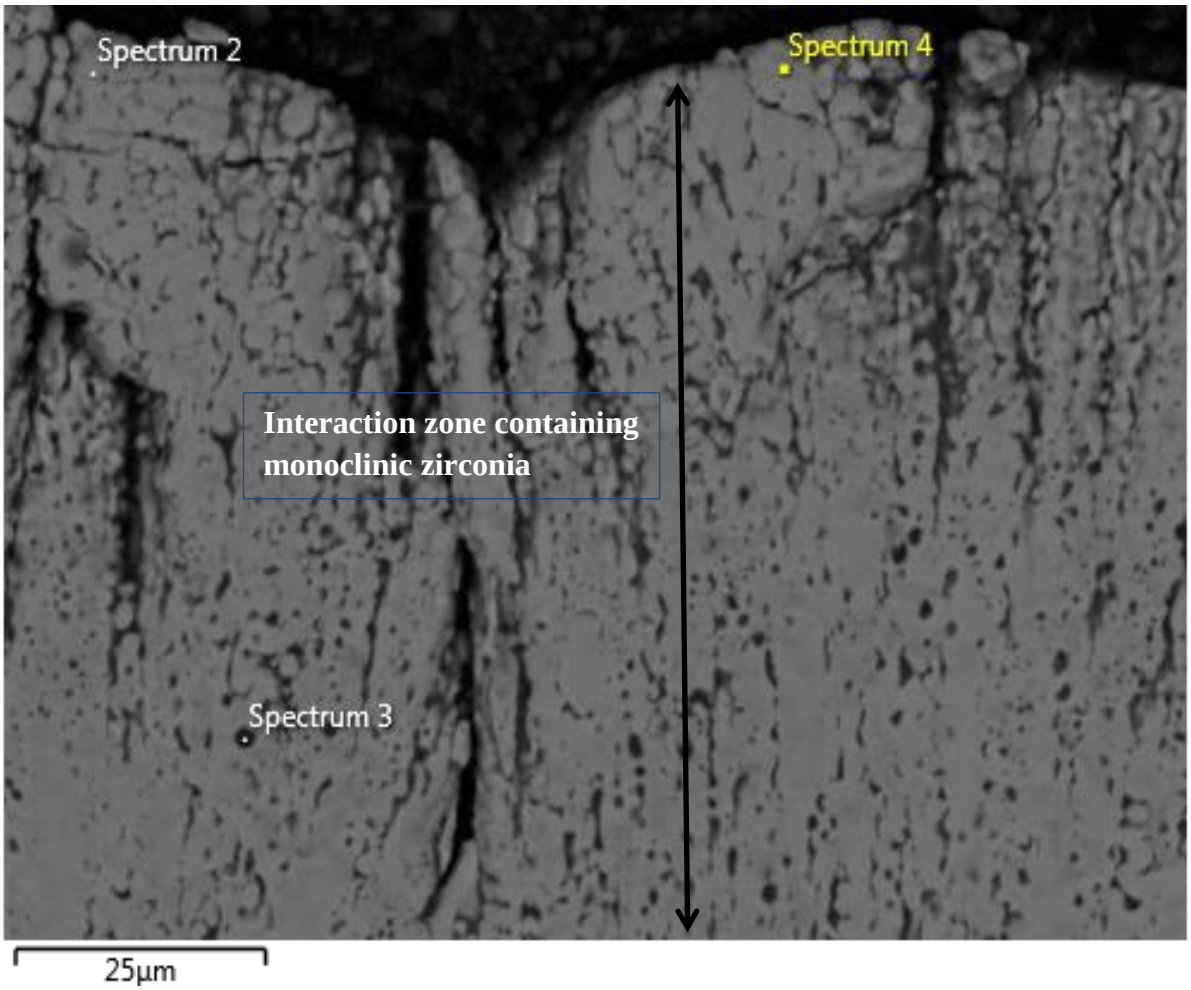

Spectrum	O	Mg	Al	Si	Ca	Y	Zr
Spectrum 2	66.4	0.2	0.3	0.0	0.1	0.6	32.4
Spectrum 3	58.1	2.2	3.3	14.4	6.5	2.0	13.6
Spectrum 4	69.8	0.0	0.4	0.1	0.1	0.5	29.1

All results in atomic%

Figure 95: Indicative phase transformation in the interaction zone (spectrums 2 & 4) of Low B.I. attack of free-standing TBC.

6.5 Mechanism of Attack

It is evident from examining the infiltrated microstructures that at operating temperatures above the melting temperature of Low B.I. deposits (~1235 °C), melting occurs and by capillary action in a cooled (thermal gradient) system, the melt penetrates through the columnar microstructure of PYSZ TBC to a point where the TBC temperature is less than the melting temperature of the deposit and the melt freezes, introducing strain into the system. However in an isothermal system, the melt penetrated to the bottom of the sample, attacking the coating in the process. Low B.I. melt was found to readily "wet" PYSZ TBC and penetrate the columnar structure, chemically attacking the ceramic whereupon yttria is leached from PYSZ and into the melt, creating an yttria depleted interaction zone. The attack is minimal in the bulk of the coating but severe near the surface, with complete degradation of the column tips. These observations are consistent to that made by other authors investigating the effect of CMAS melt on TBCs [11; 13; 68; 69; 150].

6.6 Summary

Low B.I. refers to CMAS compositions with Basicity Index ratio < 1.8. Generally, almost all CMAS compositions used by previous authors fall into this low B.I. category and therefore the damage mechanism observed were very similar, although varying degrees of the severity of attack were observed. The thermochemical attack mechanism for this mode of attack is extensively studied and the results observed were similar to that published in the literature [9; 11; 13; 34; 68] - [13].

The attack is less in the bulk of the coating but shows severe degradation of the columnar tips, near the surface and also along the column boundaries. The mechanism involves silica in the melt reacting with the TBC by leaching Y_2O_3 from the ZrO_2 grains, so destabilising the

TBC and instigating a phase transformation. This can be thought of as “classical CMAS” attack [12].

Low B.I. deposit showed attack to the bottom of the TBC but did not interfere with the interfacial chemistry, since Low B.I. deposit does not form a melt pool at the interface and thereby not attacking the alumina substrate, as was revealed by FIB images in Figure 91 and Figure 92. However, when the amount of coverage used was saturated, Low B.I. sample formed a silica-rich glaze on the surface of the TBC.

Low B.I. attack of PYSZ was found to be similar irrespective of whether the coating was on a substrate or free standing. In both cases, the “classic CMAS” footprint of dark globules of CMAS related phase, as a result of exchange mechanism with yttria going the other way.

7 Mid-range Basicity Index (Near Neutral deposit): B.I. = 1.8 – 2.2

Mid-range B.I. was calculated based on the Basicity Index of a CaO – SiO_2 dominated slag composition, with B.I. in the range of 1.8-2.2. The composition used in this category was $C_{56}M_9A_7S_{28}$ in mole% (B.I. = 1.9). Mid-range Basicity Index was not only selected based on the neutral composition of a CaO – SiO_2 [9; 11; 13; 34; 68], but also based on results from experiments to determine the Basicity Index of the transitional composition. A range of CMAS compositions with different B.I. were prepared and applied onto EB-PVD samples to study their microstructural evolution with Basicity Index.

It was identified from the literature review that, research with deposits of B.I. = 1.6 [104] yielded characteristics of a typical Low B.I. degradation, producing an interaction zone with yttria leaching out of the bulk TBC, leading to a monoclinic phase transformation. Equipped with this knowledge, model CMAS compositions with B.I. in the range of 1.6 – 2.0 were manufactured and used in this phase of the research. A B.I. value of 2.0 corresponds to the stoichiometric composition of a CaO-SiO_2 dominant slag system with balanced acid and basic groups (a neutral composition), meaning the formation of a $2CaO.SiO_2$ compound [75]. Hence the reason 2.0 was selected as the upper limit to determine the transitional composition from Low B.I. to Near Neutral B.I.

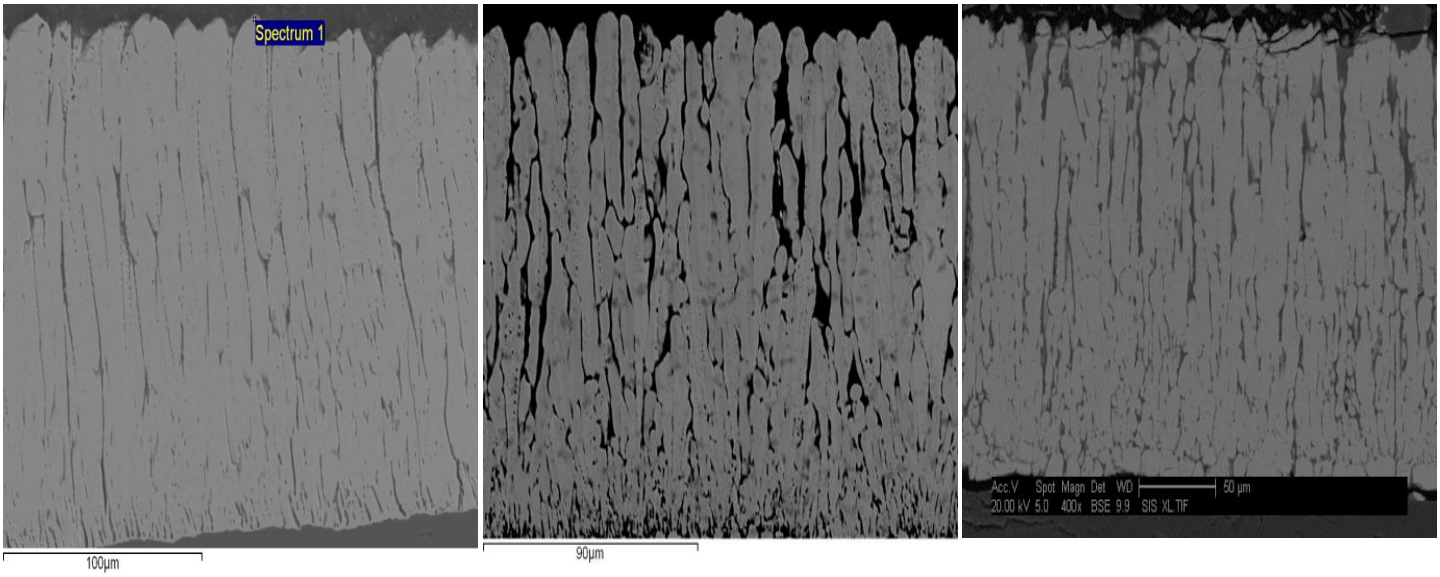

(a) (b) (c)

Figure 96: CMAS compositions with B.I. = (a) ~1.6, (b) ~1.76 and (c) ~1.8, all aged for 4h at their respective mpt + 50 °C.

Unlike Low B.I. attack with excess deposit (Figure 86), Near Neutral deposits do not form a glassy coating on the surface of the TBC under similar conditions (coverage and 50 °C above melting point). Instead, it was observed that Near Neutral deposits melt and quickly penetrate through to the base of the TBC, leaving a shallow melt lock between grains boundaries on the surface, as can be seen from Figure 97.

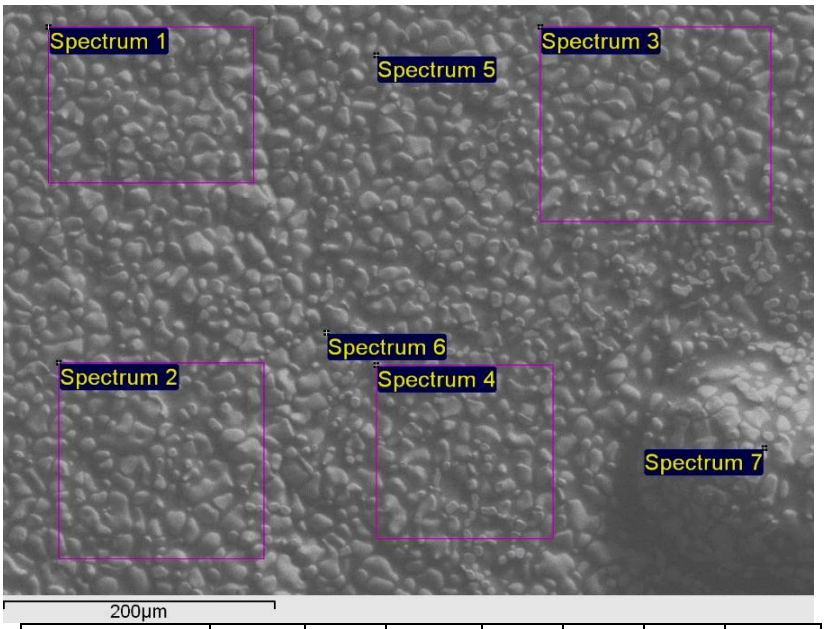

Spectrum	O	Mg	Al	Si	Ca	Y	Zr
Spectrum 1	67.8	1.0	8.2	3.4	5.3	0.6	13.9
Spectrum 2	68.3	0.9	8.4	3.4	5.4	0.5	13.1
Spectrum 3	68.0	1.0	9.0	3.6	5.7	0.4	12.4
Spectrum 4	67.7	1.0	8.9	3.7	5.6	0.6	12.7
Spectrum 5	67.0	0.8	5.7	2.0	4.2	0.9	19.5
Spectrum 6	68.8	0.8	5.7	2.0	4.2	0.7	17.8
Spectrum 7	67.4	1.1	11.0	4.6	6.5	0.8	9.1

All results in atomic%

Figure 97: Surface analysis of Near Neutral B.I. deposited sample after 4h at 1480 °C heat treatment.

The micrograph images in Figure 98 show the different morphology of attack observed with the Near Neutral (Mid-range) B.I. CMAS deposit. Here, the attack is mainly along the TBC columns, with almost no dark globular pores of CMAS reacted phases as observed in the Low B.I. attack. Mid-range B.I. deposits also showed a change in damage mechanism from primary column attack to columns plus sub-boundary attack, through the TBC thickness.

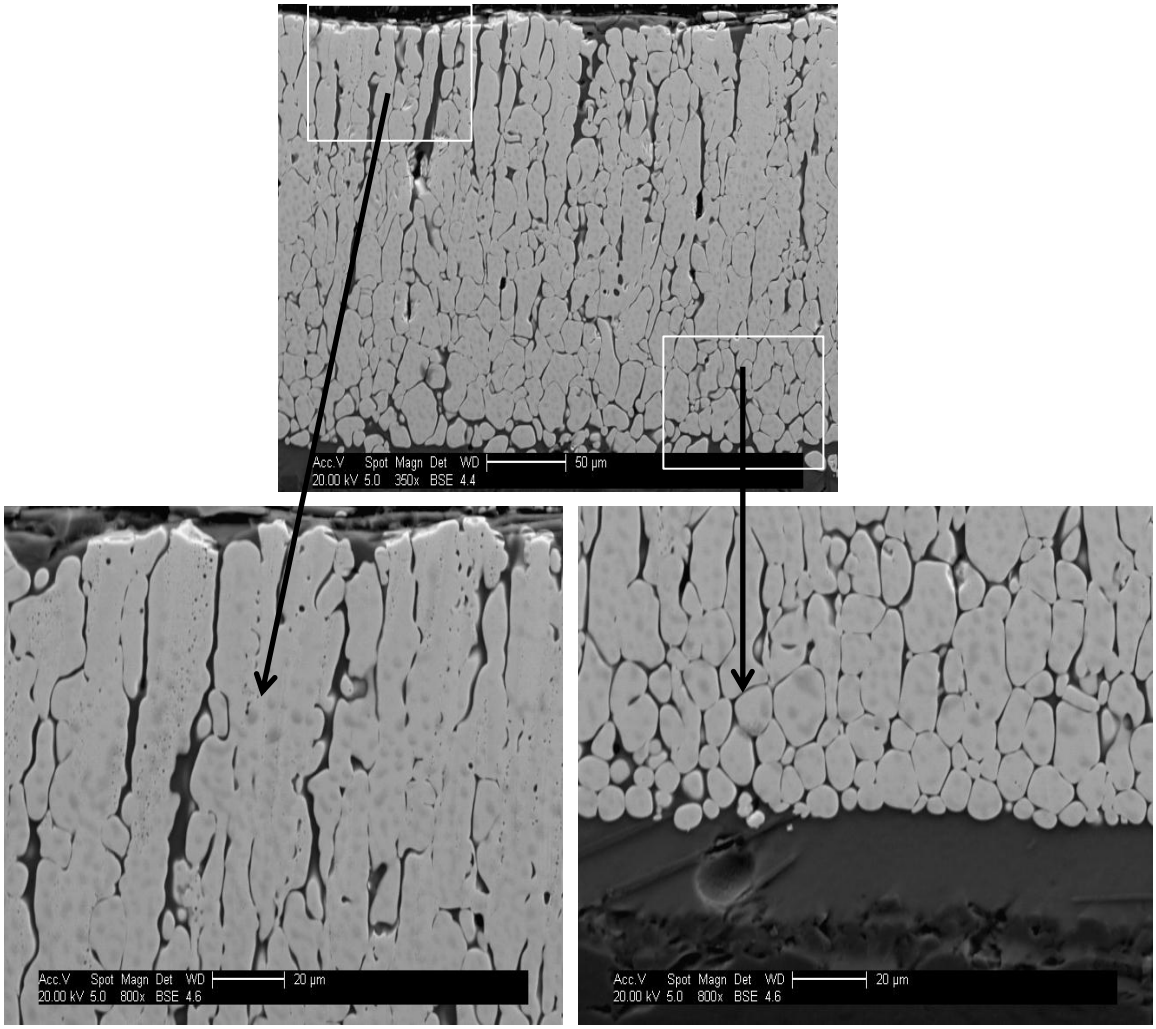

Figure 98: Cross-sectional scanning electron micrograph of a PYSZ – 8 wt% yttria EB-PVD TBC sprayed with $C_{56}M_9A_7S_{28}$ mole% (B.I. = 1.9), and heat treated for 4h at 1480 °C.

7.1 30 Minutes Exposure at 1480 °C

Near Neutral deposits rapidly penetrate to the bottom of the coating, after about an hour after becoming molten, where it forms a melt pool at the TBC/substrate interface. Near Neutral deposits also accelerate the sintering rate, as shown in Figure 99, which after only 30 minutes of ageing, create open inter-columnar gaps which act as reservoir for the melt to travel through to the base of the TBC.

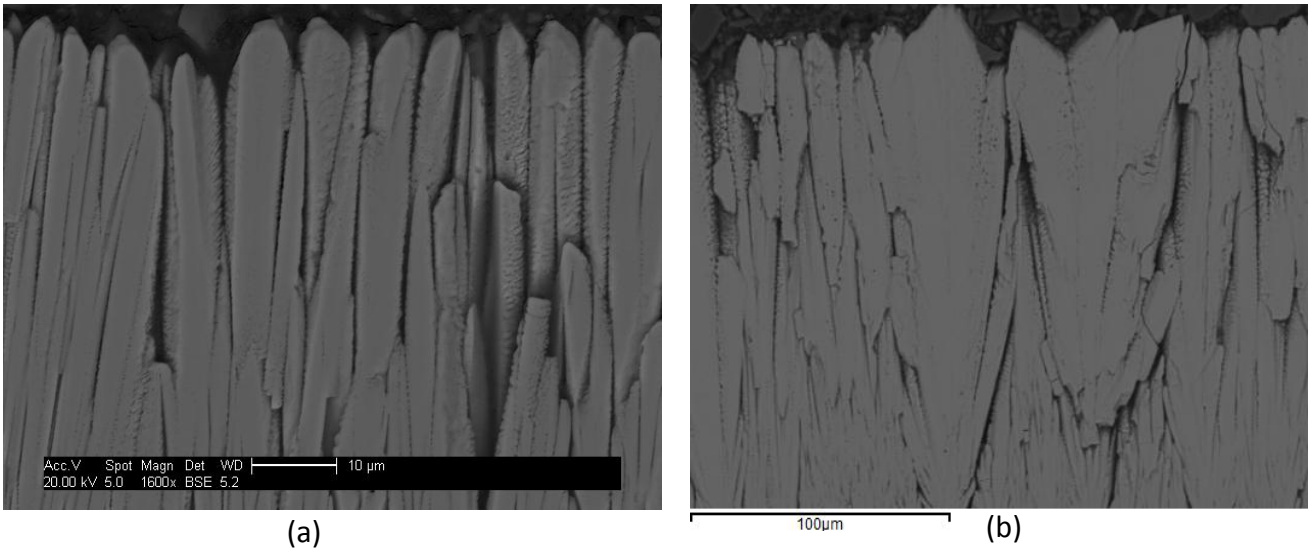

Figure 99: Mid B.I. analysis (a) Reference sample aged for 4h at 1480 °C without CMAS and (b) 30 minutes exposure at 1480 °C showing accelerated sintering of columns.

After 30 minutes heat treatment, Near Neutral deposit did not cause an obvious deviation in TBC composition. Feathering of the TBC microstructure was noticed after 30 minutes, which may have resulted in yttria leaching out from the columns and could account for the deviation in yttria content seen in Figure 101. Also, elemental EDAX mapping displayed in Figure 100 showed no evidence of a melt pool formed at the interface under these conditions. The Ca map indicated that the Near Neutral melt penetrated the newly created inter-columnar boundaries formed as a result of accelerated sintering of the TBC columns.

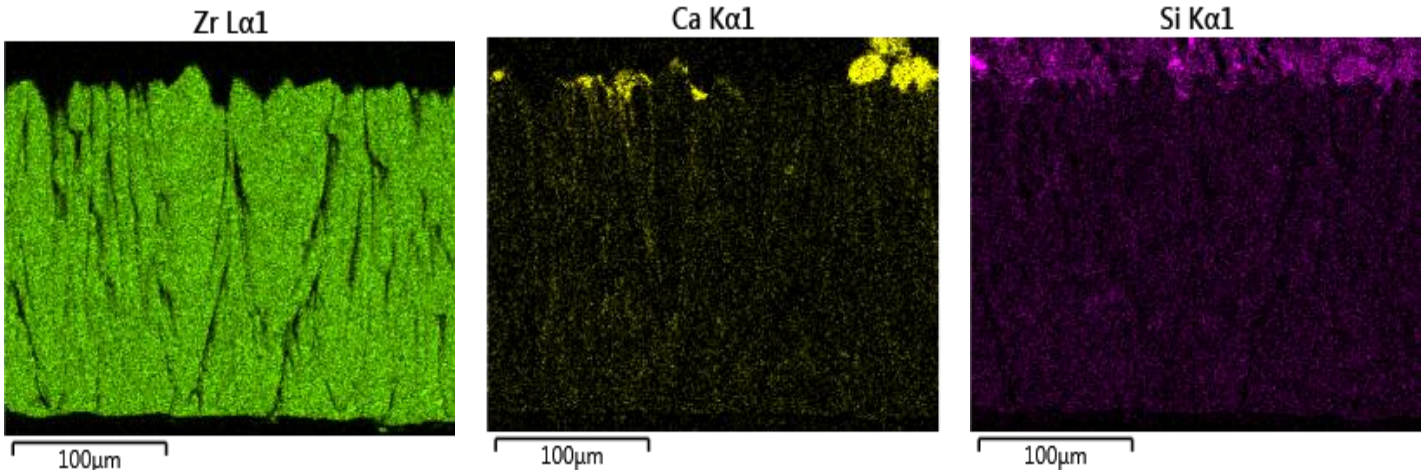

Figure 100: EDAX elemental mapping of Near Neutral deposit after 0.5h at 1480 °C showing no melt pool at the interface.

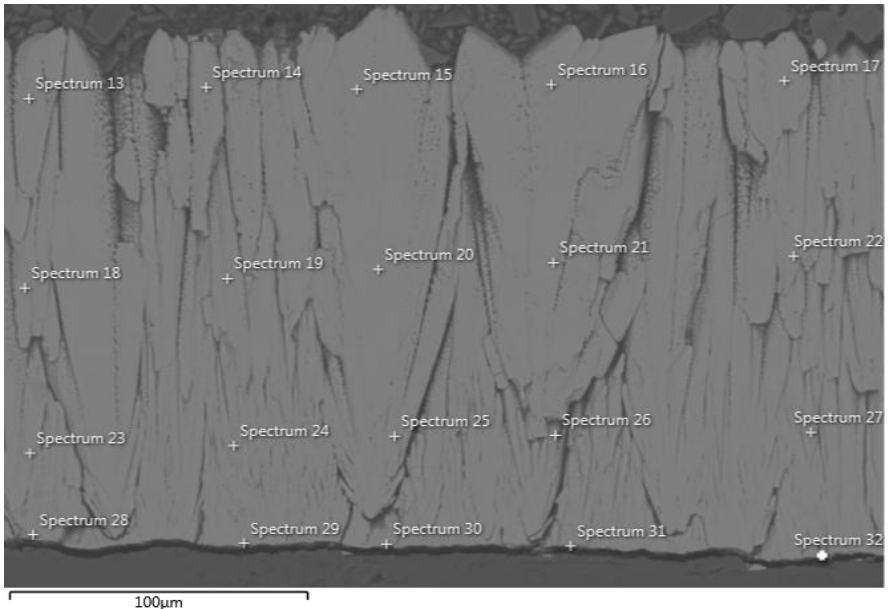

Spectrum	O	Mg	Al	Si	Ca	Y	Zr
Spectrum 13	57.3	0.2	0.0	0.7	0.9	3.3	37.6
Spectrum 14	60.1	0.2	0.0	0.6	0.8	3.1	35.1
Spectrum 15	58.8	0.2	0.0	0.2	0.5	3.3	37.1
Spectrum 16	59.0	0.2	0.0	0.3	0.3	3.4	36.7
Spectrum 17	60.9	0.2	0.0	0.2	0.3	3.3	35.1
Spectrum 18	58.1	0.2	0.0	0.0	0.0	3.5	38.2
Spectrum 19	57.9	0.4	0.0	0.8	0.9	3.2	36.7
Spectrum 20	58.8	0.4	0.0	0.7	1.0	3.5	35.6
Spectrum 21	60.5	0.5	0.0	0.2	2.2	3.2	33.4
Spectrum 22	58.6	0.4	0.0	0.2	0.9	3.9	36.0
Spectrum 23	58.6	0.2	0.0	0.2	0.2	2.8	37.9
Spectrum 24	57.2	0.2	0.5	0.7	1.1	2.8	37.5
Spectrum 25	59.0	0.2	0.0	0.3	0.7	2.7	37.0
Spectrum 26	55.7	0.2	0.5	0.9	1.1	2.8	38.9
Spectrum 27	61.4	0.2	1.1	0.8	1.1	2.6	32.9
Spectrum 28	58.1	0.2	0.8	1.0	1.6	2.2	36.1
Spectrum 29	58.6	0.2	0.8	0.5	1.0	2.2	36.7
Spectrum 30	67.3	0.2	0.1	0.1	0.3	1.8	30.1
Spectrum 31	58.6	0.2	1.0	0.8	1.1	2.0	36.3
Spectrum 32	57.5	0.0	0.3	0.3	0.5	2.2	39.1

All results in atomic%

Figure 101: EDAX analysis of Near Neutral deposit after 0.5h at 1480 °C.

7.2 One Hour Exposure at 1480 °C

An hour of heat treatment at 1480 °C showed clear evidence that the molten deposits have penetrated to the base of the TBC, formed a melt pool at the TBC/substrate interface (Figure 102). First layer transformation of the bulk TBC was also noticed at this stage, where the PYSZ TBC have dissociated and recrystallized, forming new spheroidal polycrystalline structures.

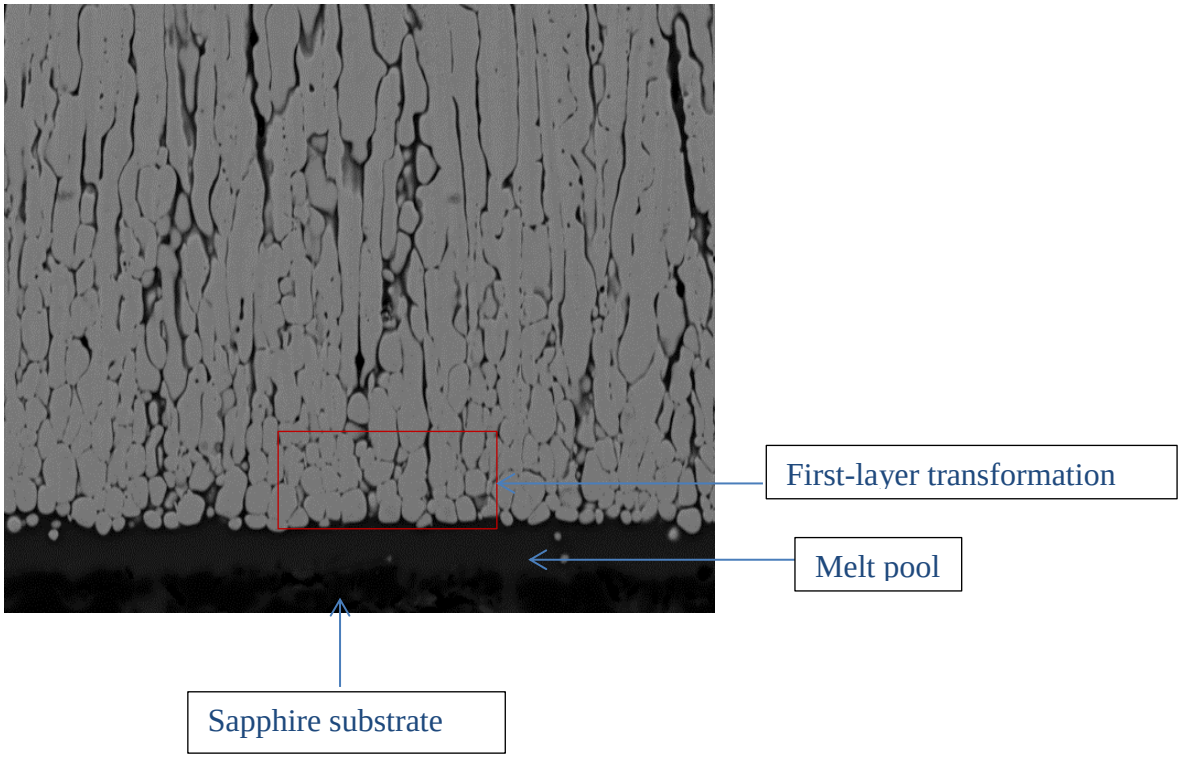

Figure 102: Mid B.I. micrograph – one hour at 1480 °C

Unlike the low B.I. attack mechanism, where CMAS/TBC interaction produced an yttria depleted zone, resulting in large amount of monoclinic phase being present in the bulk TBC. The Near Neutral attack mechanism on the other hand was observed to have less interaction with the bulk PYSZ TBC, with no sporadic leaching of yttria into the melt and diffusion of CMAS products into the bulk TBC. Hence, Near Neutral attack does not form CMAS-reacted globules in the coating as a result of material transfer between the TBC and the melt, therefore does not instigate the detrimental tetragonal to monoclinic phase transformation.

Instead, due to the viscosity of the melt, the molten deposits travelled along the grain boundaries and formed a melt pool at the bottom of the TBC. Here, due to the local chemistry of the melt (hence the local B.I. of the deposit), it reacts with the TBC and recrystallized into a new polycrystalline grains of tetragonal zirconia and calcium zirconate. Hence, the Near Neutral degradation mechanism initiate at the base of the TBC. Evidence of calcium zirconate transformation is shown in the compositional analysis in Figure 103.

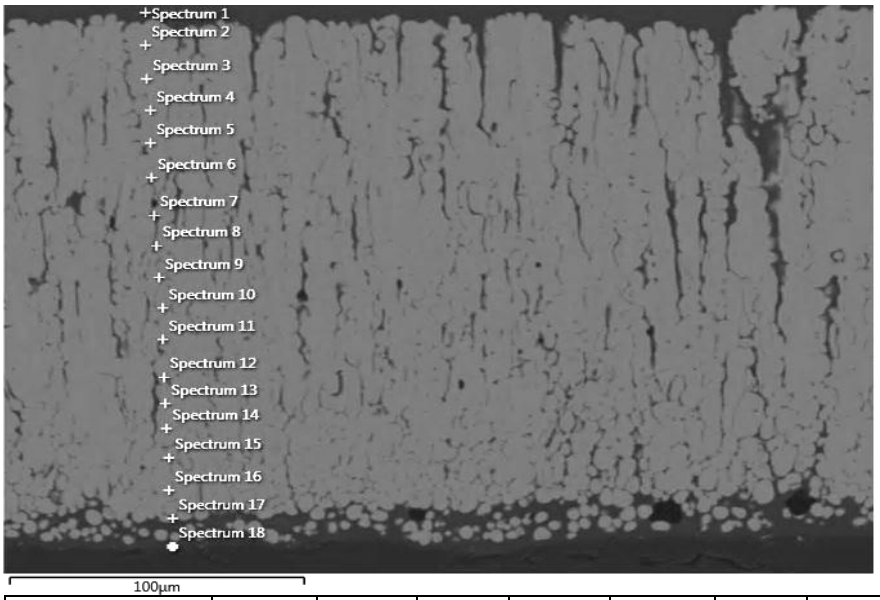

Spectrum	O	Mg	Al	Si	Ca	Y	Zr
Spectrum 1	56.4	3.6	7.1	14.1	17.3	0.4	1.1
Spectrum 2	64.5	0.0	0.0	0.0	0.1	2.8	32.6
Spectrum 3	63.5	0.2	0.0	0.0	0.2	2.9	33.2
Spectrum 4	64.4	1.1	1.5	2.3	4.4	2.0	24.4
Spectrum 7	61.7	2.6	5.2	8.7	12.1	0.8	8.8
Spectrum 8	63.9	0.5	0.3	0.0	4.6	2.3	28.4
Spectrum 9	63.6	0.5	0.2	0.0	4.6	2.4	28.8
Spectrum 10	63.8	0.5	0.1	0.0	4.5	2.3	28.7
Spectrum 13	64.8	0.3	0.6	0.4	2.0	2.0	29.6
Spectrum 15	64.3	0.3	0.5	0.0	3.4	2.0	29.5
Spectrum 16	64.1	0.5	0.9	0.7	5.0	1.8	27.1
Spectrum 17	61.7	2.6	6.0	7.7	12.9	0.5	8.5
Spectrum 18	59.0	7.5	20.4	4.1	8.7	0.1	0.2

All results in atomic%

Figure 103: EDAX analysis of Near Neutral deposit after one hour at 1480 °C, with significant amount of Ca diffused into the newly formed structures.

EDAX elemental mapping analysis shows CaO and SiO_2 are enriched at the column boundaries (Spectrum 7) and at the base of the TBC (Spectrum 17 and 18), as can be seen in Figure 104.

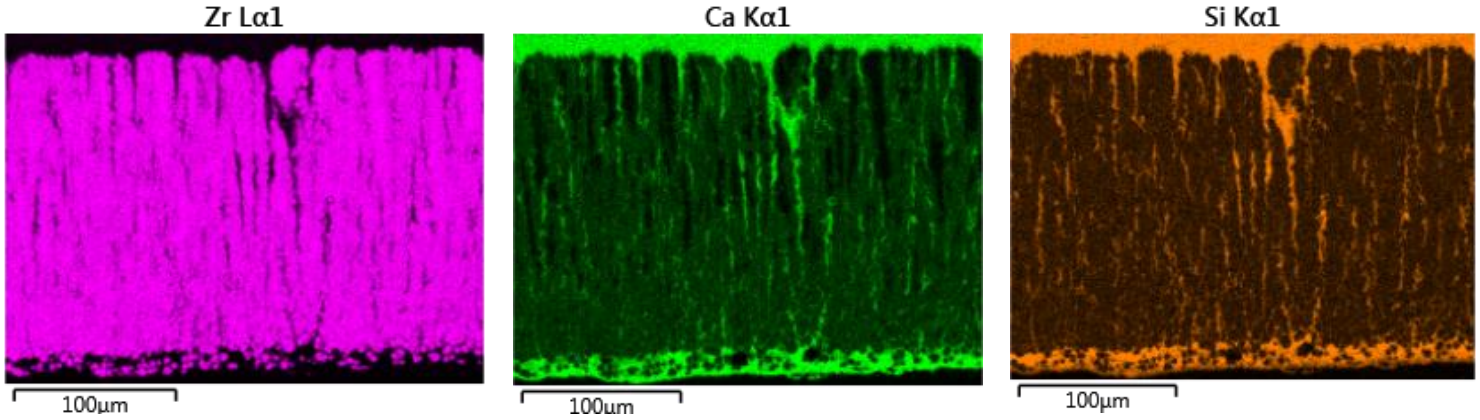

Figure 104: EDAX elemental mapping of $C_{56}M_9A_7S_{28}$ (B. I. = 1.9) – one hour at 1480 °C, clearly showing the melt pool at the TBC/substrate interface.

Line scan result on Figure 105 revealed TBC/Near Neutral deposits interaction to have fairly steady amount of zirconia across the TBC thickness, while the content dropped towards the root of the TBC, which is where the grain transformation is initiated. However EDAX analysis later found the zirconia content to be averaging ~30at.% in the bulk TBC. Yttria was also found to follow similar pattern across the entire TBC. Again, there was a slight decrease in the amount of yttria in areas that have undergone structural transformation and this was consistent throughout the coating. EDAX analysis revealed the amount of yttria averaging the bulk structure to be ~2at.%, enough to prevent phase transformation. However, extra CaO absorbed in the new grains will also help to stabilise the zirconia.

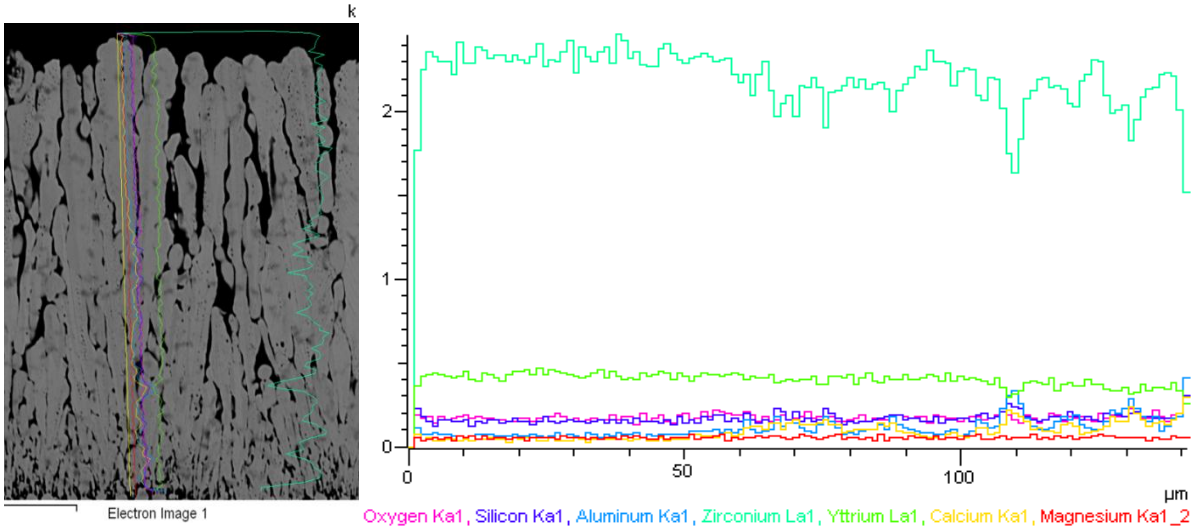

(a)

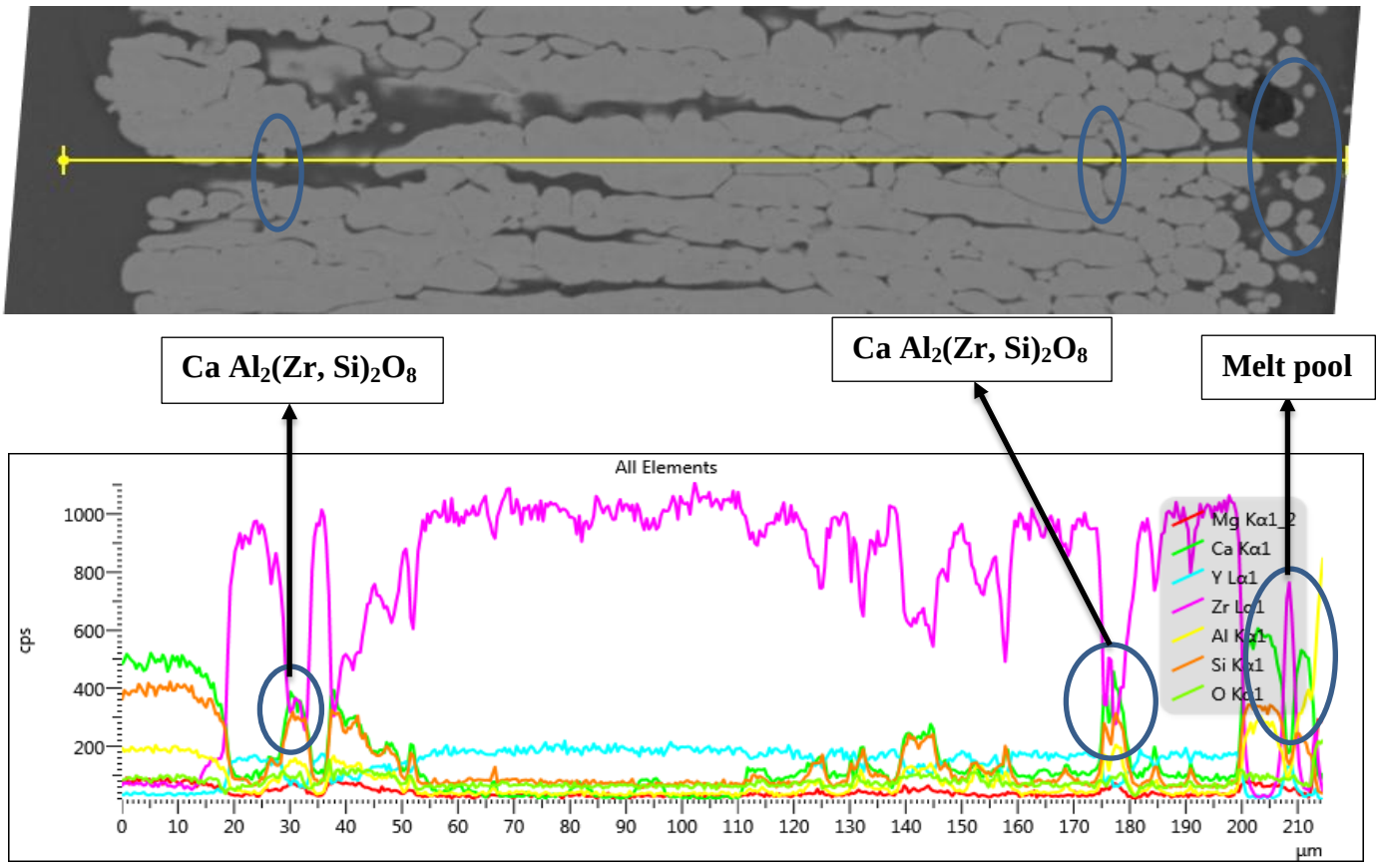

(b)

Figure 105: Line scan results of Near Neutral slag composition (a) B. I. ~1.76 and (b) B.I. = 1.9

7.3 Two Hours Exposure at 1480 °C

Two hours of heat treatment at melting point + 50 °C (1480 °C) resulted in second layer transformation. This time, the new grains are larger than was observed after an hour ageing, as it is shown in the micrograph on Figure 106.

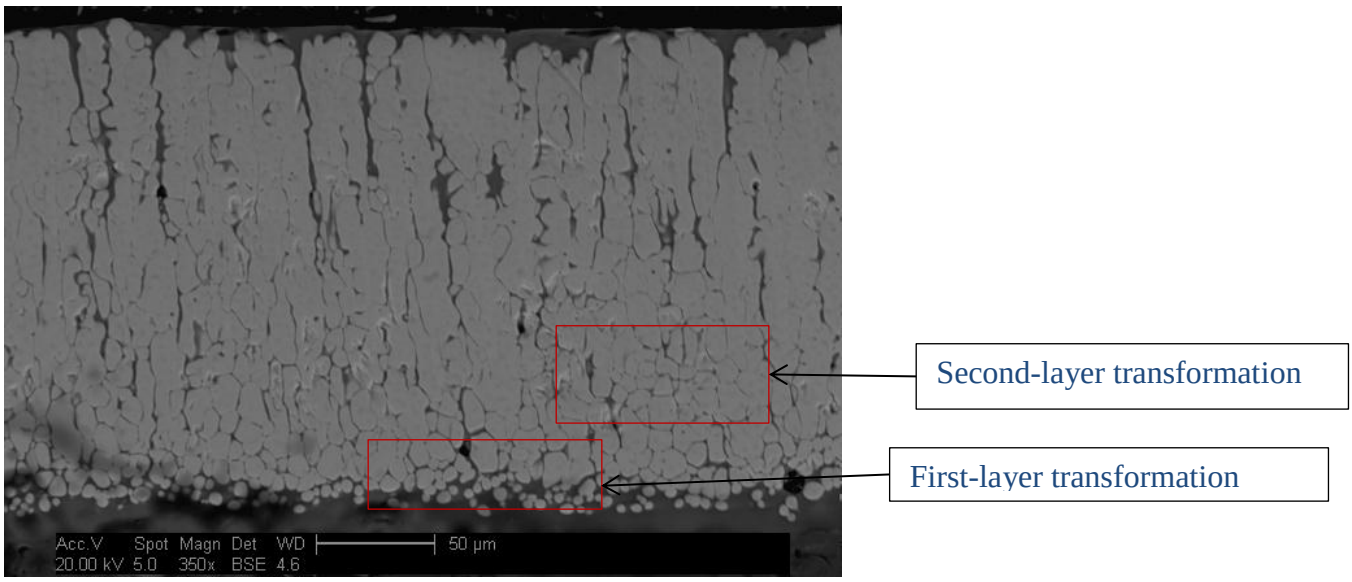

Figure 106: Near Neutral B.I. micrograph – two hours at 1480 °C

Near Neutral attack mechanism showed a time dependency, which was found to be a diffusion controlled process, similar to the Low B.I. attack mechanism. The transformation zone (indication of severity of attack) was found to increase with increase in the exposure time (Figure 106). CaO and $YO_{1.5}$ content were noticed to always add up to ~6 at% (Figure 107) in the newly formed grains, which helps to stabilise zirconia in the tetragonal phase.

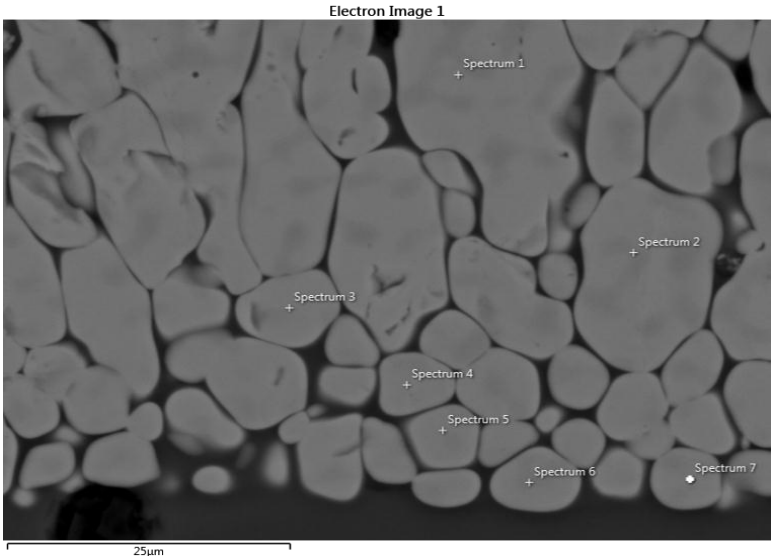

Spectrum	O	Mg	Al	Si	Ca	Y	Zr
Spectrum 1	59.7	0.4	0.3	0.0	3.1	2.4	34.1
Spectrum 2	58.7	0.4	0.3	0.0	4.1	2.2	34.4
Spectrum 3	59.6	0.4	0.3	0.0	3.3	2.2	34.1
Spectrum 4	59.6	0.4	0.3	0.0	3.5	1.9	34.3
Spectrum 5	57.6	0.2	0.3	0.0	4.1	2.0	35.7
Spectrum 6	56.9	0.2	0.5	0.0	4.7	1.9	35.8
Spectrum 7	58.9	0.5	0.3	0.0	3.4	2.1	34.7

All results in atomic%

Figure 107: 2h at 1480 °C – Near Neutral B.I. micrograph showing CaO and $YO_{1.5}$ in the new grains add up ~5-6 at%.

Elemental mapping of the Near Neutral sample (Figure 108) after two hours showed the CMAS rich content penetrated along the columnar boundaries to the bottom of the coating where a melt pool was formed.

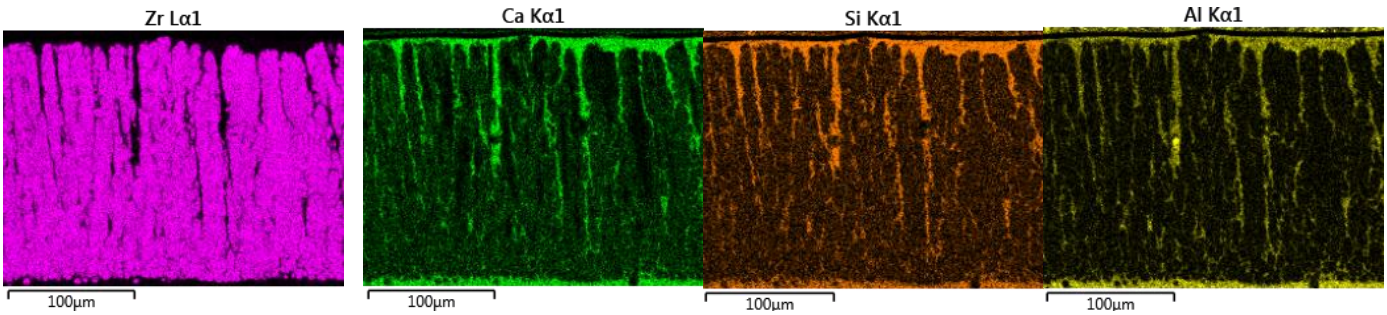

Figure 108: EDAX elemental mapping of Near Neutral B.I. – 2h at 1480 °C, showing penetration along boundaries to deposit at the TBC/substrate interface to form a melt pool.

EDAX analysis of the melt pool is illustrated in Figure 109, showing high Al_2O_3 content in the melt, which is an indication that Al has diffused from the alumina substrate into the melt pool, forming a low melting eutectic.

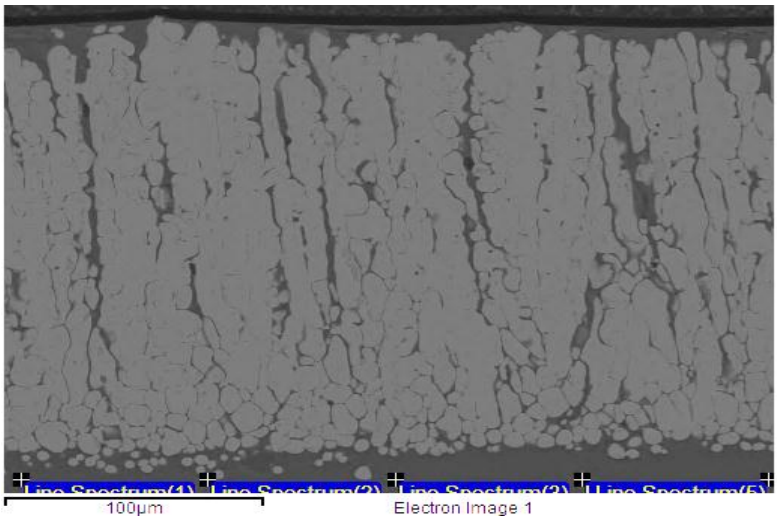

Spectrum	O	Mg	Al	Si	Ca	Y	Zr
Line Spectrum(1)	59.2	1.0	16.9	10.7	11.4	0.0	0.8
Line Spectrum(2)	59.7	1.0	16.5	10.5	11.6	0.0	0.7
Line Spectrum(3)	58.4	0.9	16.7	10.8	11.9	0.1	1.2
Line Spectrum(4)	59.6	0.9	16.3	10.7	11.4	0.0	1.1
Line Spectrum(5)	59.6	0.7	16.4	10.7	11.2	0.0	1.2

All results in atomic%

Figure 109: EDAX of Near Neutral melt pool – two hours at 1480 °C

Again zirconia was found to maintain a high intensity throughout the entire TBC structure but for a slight decrease towards the root of the coating. This was further confirmed by EDAX spot analysis (Figure 107) and line scan analysis shown on Figure 110. This pattern was similar with yttria, although at a much smaller intensity compared to zirconia.

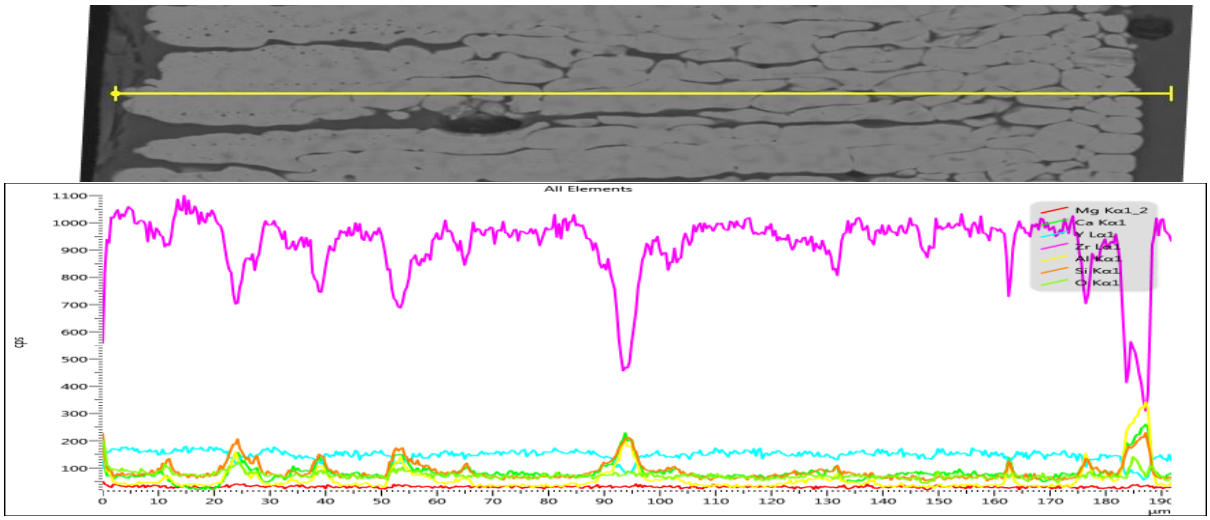

Figure 110: Line scan results of Near Neutral slag composition after two hours at 1480 °C

7.4 Four Hours Exposure at 1480 °C

Increasing exposure time resulted in an increase in the size of the transformation zone as was observed after four hours of heat treatment at 1480 °C. Figure 111 shows that the sample has undergone a third-layer transformation, with almost 75% of the coating transformed into a spheroidal structure.

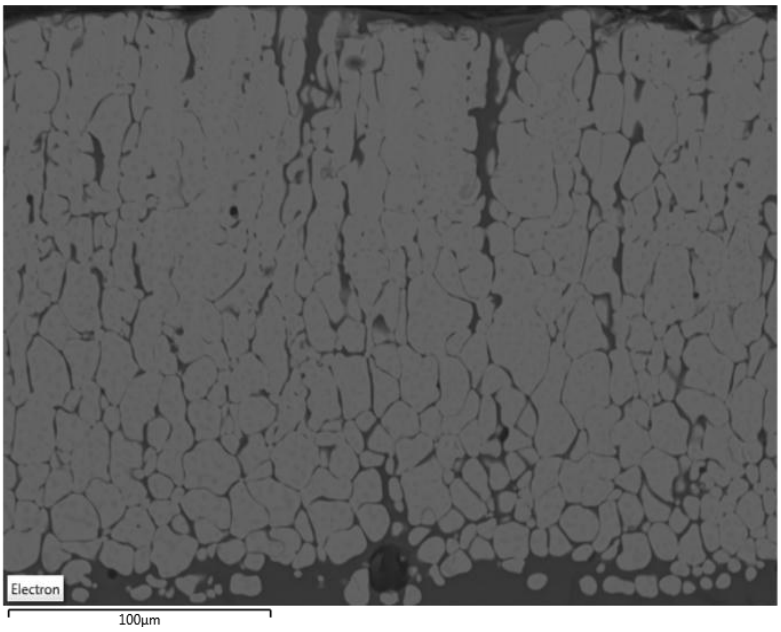

Figure 111: Near Neutral B.I. micrograph – Four hours at 1480 °C, showing about 75% grain fragmentation.

It was also observed that the amount of CaO and $YO_{1.5}$ in the newly formed grains, which had an average of ~7 at% (Figure 112a) compared to two hours exposure time where the value was found to be ~6 at%. As calcia and yttria are capable of stabilising zirconia, Near Neutral deposits do not result in monoclinic phase transformation. However, there was very little calcia in the TBC structure in regions outside the transformation zone, as can be seen from spectrum 20-22 in Figure 112b.

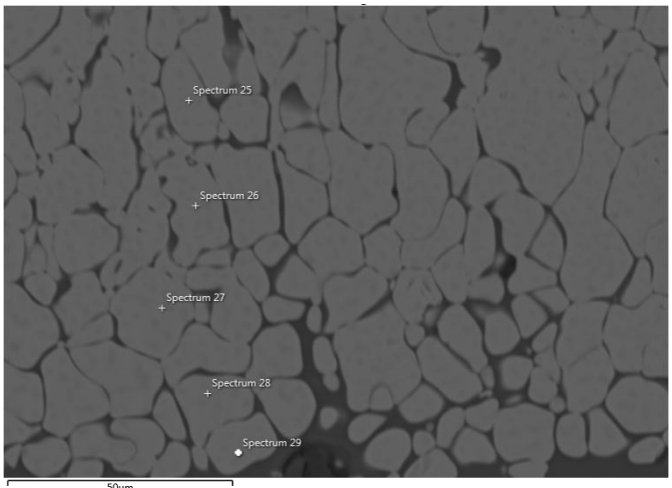

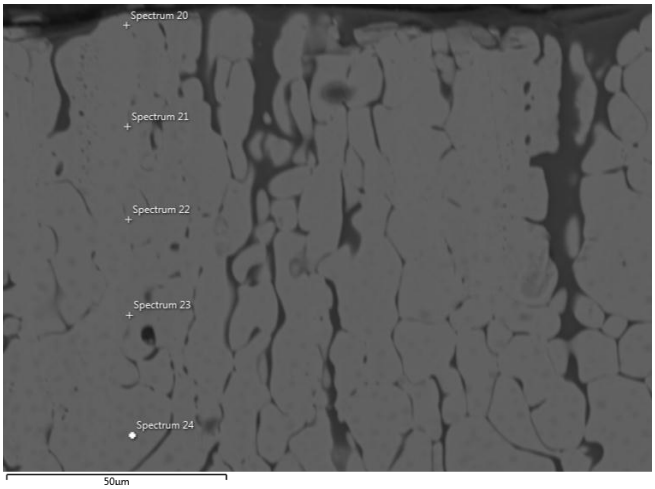

Spectrum	O	Mg	Al	Si	Ca	Y	Zr
Spectrum 25	56.2	0.2	0.3	0.0	3.4	3.1	36.8
Spectrum 26	58.5	0.4	0.3	0.0	3.6	2.6	34.6
Spectrum 27	56.9	0.6	0.3	0.0	5.0	2.3	34.9
Spectrum 28	57.2	0.4	0.3	0.0	5.7	2.4	33.9
Spectrum 29	57.9	0.5	0.3	0.0	5.0	2.1	34.2

a

Spectrum	O	Mg	Al	Si	Ca	Y	Zr
Spectrum 20	61.3	0.2	0.3	0.0	0.0	3.2	35.0
Spectrum 21	60.6	0.2	0.5	0.0	0.2	3.1	35.4
Spectrum 22	59.4	0.2	0.5	0.0	1.9	2.6	35.4
Spectrum 23	58.3	0.4	0.5	0.0	3.7	3.0	34.2
Spectrum 24	58.4	0.5	0.2	0.0	4.7	2.8	33.4

b

All results in atomic%

Figure 112: EDAX analysis of Near Neutral B.I. micrograph – Four hours at 1480 °C. (a) Transformed grains at bottom and (b) non transformed columns at the top, showing no interaction at the top of the coating

The Near Neutral degradation mechanism showed an interesting characteristic, where MgO, SiO_2 and Al_2O_3 were not retained by the newly formed grains. However, CaO, SiO_2 and Al_2O_3 are seen entrapped between grain boundaries and eventually migrating to the interface to form a melt pool, whereas Ca is the only element absorbed from Near Neutral melts by the new grains, thereby influencing the chemistry of the resultant microstructure. Near Neutral attack results in Ca doped PYSZ being formed in the transformation zone. Unlike Low B. I. attack of PYSZ TBCs where yttria leached out from the TBC and into the melt, forming yttria depletion zone, the yttria content was retained in the TBC in Near Neutral attack. From the elemental maps in Figure 113, it is clear that SiO_2 and Al_2O_3 meander around the microstructure without actively being involved in the reaction. However, Ca map gives a very

bright indication at the lower half of the TBC, suggesting that CaO has been absorbed into the newly formed grains.

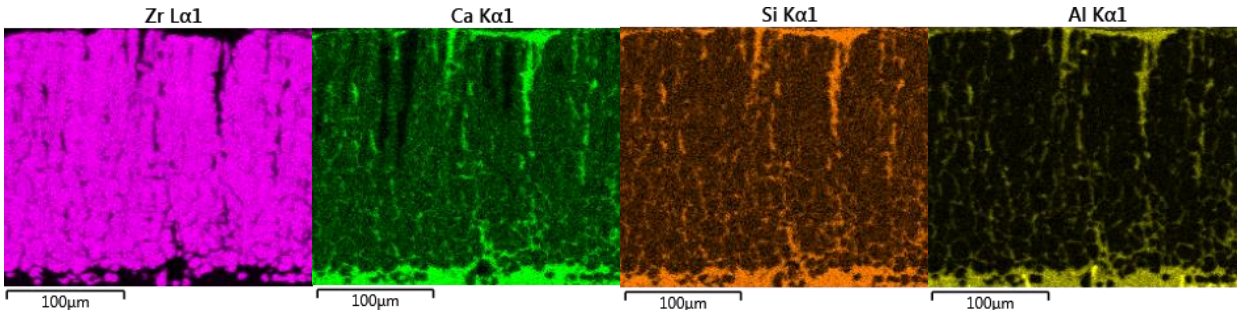

Figure 113: EDAX elemental mapping – 4h at 1480 °C.

7.5 Eight Hours Exposure at 1480 °C

It has been established that time plays an important role in this category of molten deposits degradation of TBCs. Therefore a similar pattern of growth of the transformation zone was expected after eight hours exposure. The results showed that after 8h heat treatment, the transformation was through the entire TBC (Figure 114), with a complete loss of columnar identity. Instead, the entire coating comprised of spheroidal grains, with little evidence of the "as deposited" columnar microstructure of an EB-PVD TBC.

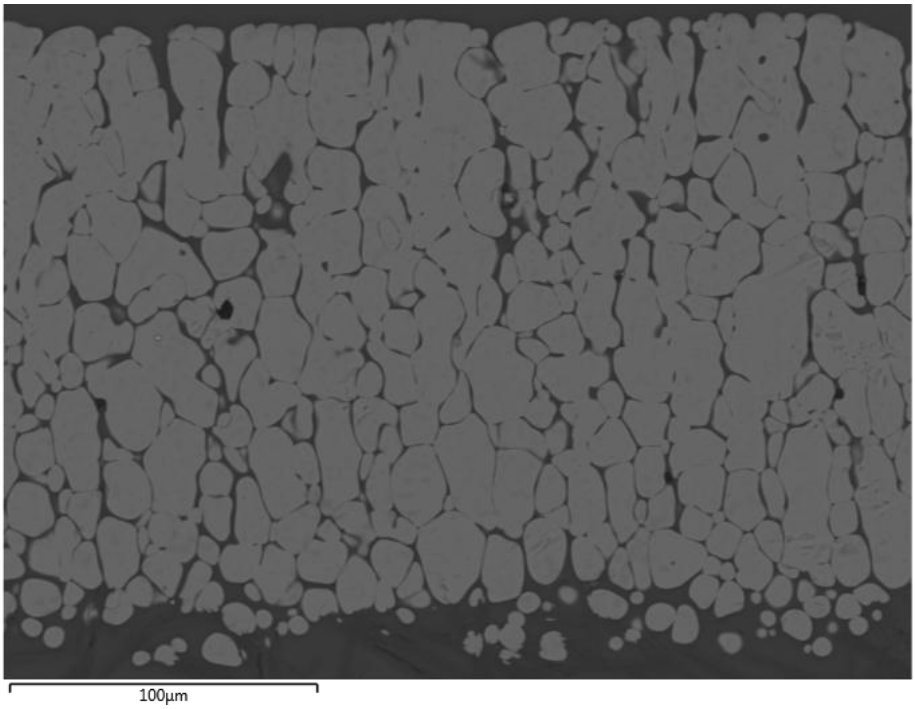

Figure 114: Through thickness transformation of Near Neutral B.I. after 8h at 1480 °C.

Near Neutral degradation mechanism remains the same irrespective of time. However, the severity of damage increases with time, in the form of growth of the transformation zone. An eight hours exposure was expected to result in ~6-7 at% content of ($CaO + YO_{1.5}$) within the spheroidal grains, which would avoid the induced stresses caused by monoclinic phase transformation, which is the case with Low B.I. degradation. From the EDAX analysis shown in Figure 115, the $CaO + YO_{1.5}$ value was found to match the expected value of ~6-7 at%. As was expected with this category of attack, SiO_2, MgO and Al_2O_3 did not interact with the bulk zirconia (spectrums 2-9, Figure 115) but were instead locked in solution in the CMAS matrix.

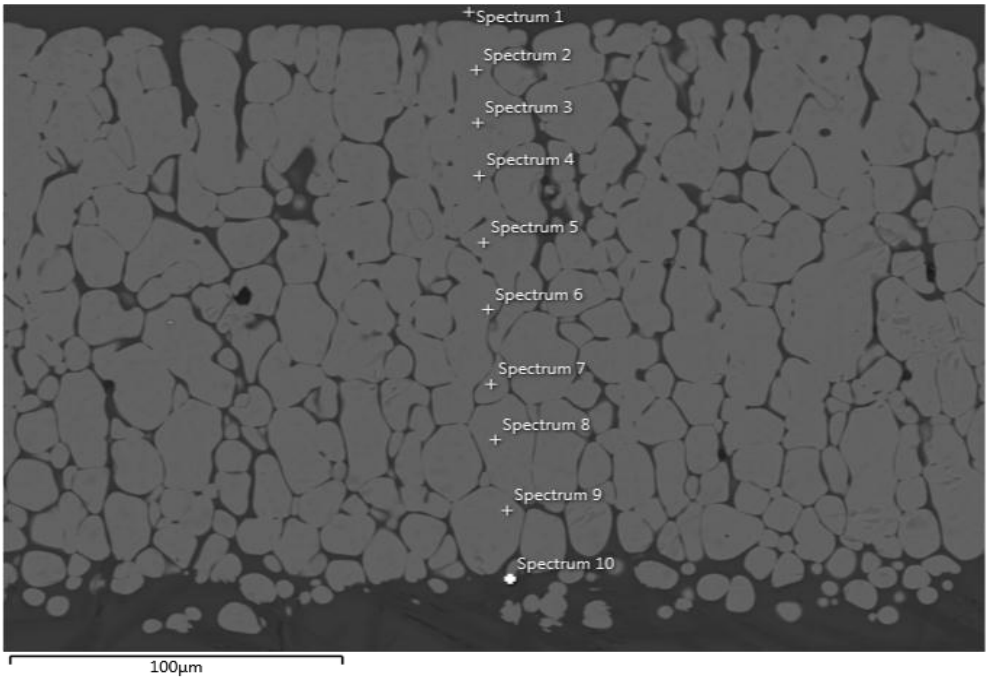

Spectrum	O	Mg	Al	Si	Ca	Y	Zr
Spectrum 1	55.2	1.1	18.7	11.0	13.1	0.0	0.9
Spectrum 2	56.1	0.2	0.2	0.0	3.5	2.9	37.1
Spectrum 3	56.9	0.4	0.3	0.0	6.2	2.3	34.0
Spectrum 4	58.2	0.4	0.5	0.0	6.1	2.3	32.5
Spectrum 5	56.9	0.4	0.3	0.0	5.1	2.9	34.5
Spectrum 6	58.2	0.4	0.3	0.0	3.7	2.8	34.5
Spectrum 7	58.3	0.4	0.3	0.0	3.4	2.6	35.0
Spectrum 8	58.6	0.4	0.3	0.0	4.2	2.6	33.9
Spectrum 9	58.7	0.4	0.3	0.0	3.4	2.4	34.8
Spectrum 10	55.9	1.2	18.4	10.7	12.5	0.1	1.2

All results in atomic%

Figure 115: EDAX analysis of Near Neutral sample exposed for 8h at 1480 °C.

As can be seen from Ca, Si and Al elemental maps in Figure 116, the alumina substrate was attacked by the Near Neutral deposit melt pool and aluminium was diffused from the substrate and into the melt, by so doing forming a low melting point phase. As mentioned earlier, SiO_2 and Al_2O_3 are not involved in the chemistry of the resultant structures. However, they formed rich phases at the newly created grain boundaries and are also present in the melt pool at the bottom of the coating.

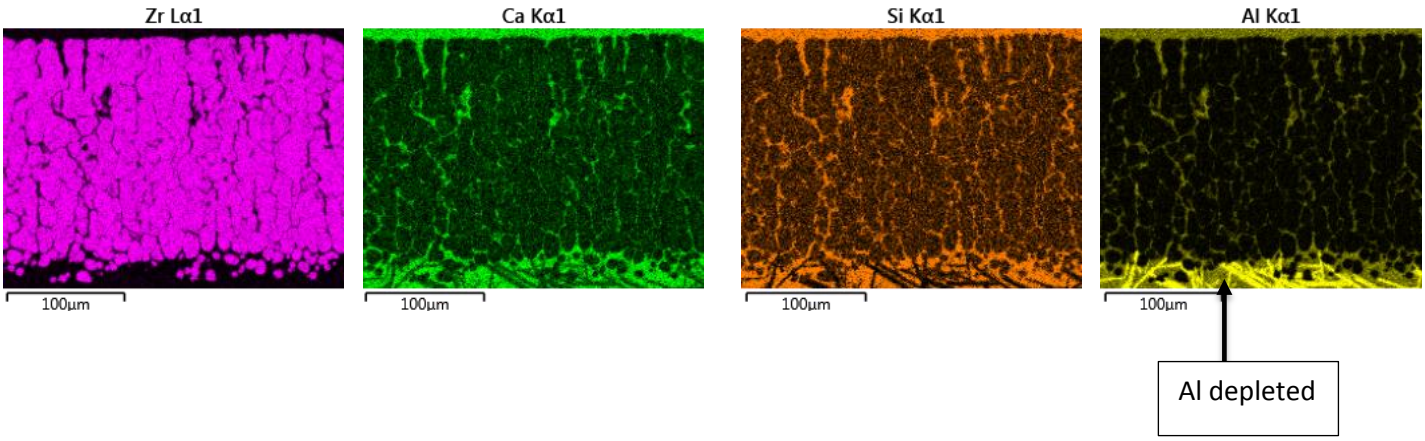

Figure 116: EDAX elemental mapping – 8h at 1480 °C, showing areas depleted of Al in the Al_2O_3 substrate.

EDAX line scan (Figure 117) was used to determine the through composition of the coating. It was observed that, zirconia maintained a constant composition through the entire coating, averaging at about 35 at%. Yttria also maintained a constant composition through the coating thickness, again an indication that zirconia is stabilised in the tetragonal phase.

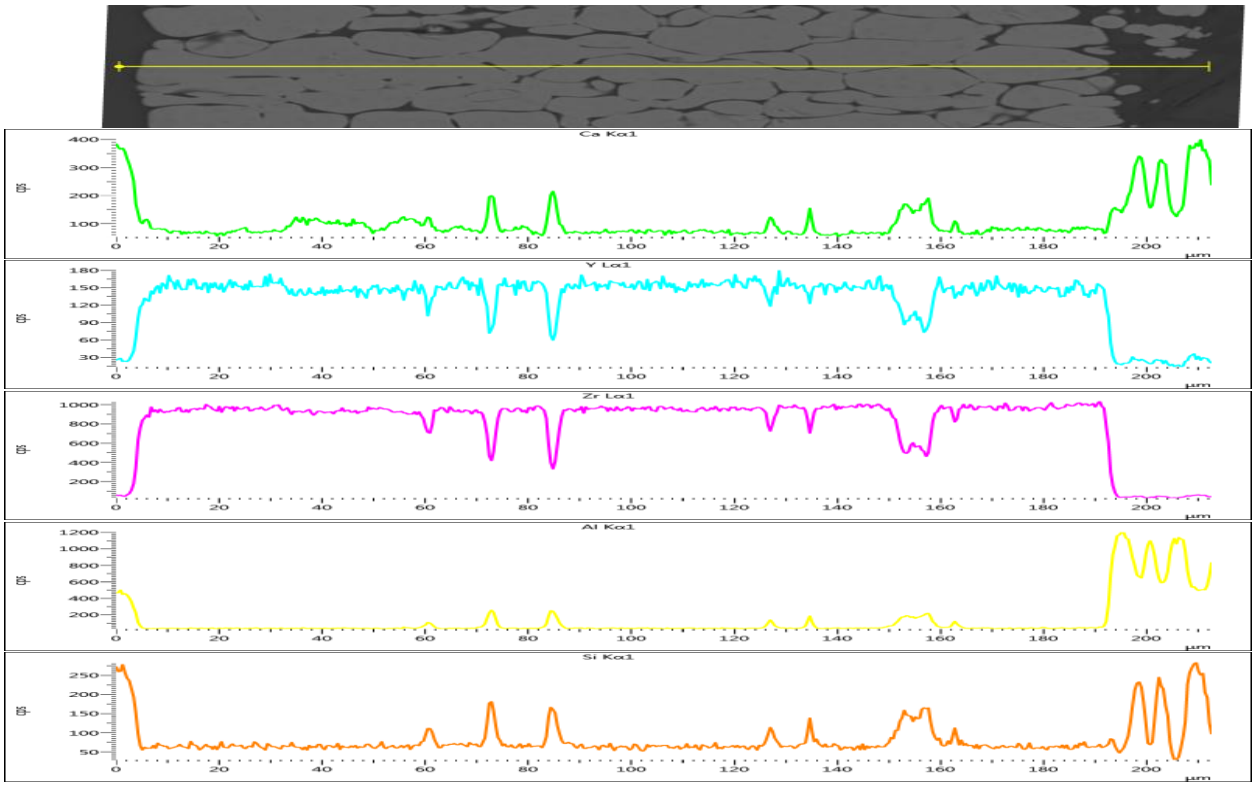

Figure 117: Line scan results of Near Neutral slag composition after 8h at 1480 °C

Near Neutral deposit was found to be less viscous and more aggressive than Low B.I. CMAS composition. Near Neutral melt formed a melt pool at the TBC interface and was therefore relevant to further investigate whether molten melt has penetrated to the substrate. FIB images provide unique structural information in understanding the mechanism of attack.

Near Neutral samples showed a new feature at the bottom of the sample from attack by the molten deposit. Similar to Low B.I. attack, there was no evidence of the melt penetrating and damaging the alumina substrate. Instead, the coating was found to have completely de-bonded from the substrate, with magnesium spinel sitting on the surface of the substrate (spectrums 1-3, Figure 118). The presence of the spinel phase indicates that melt pool was formed at the TBC/substrate interface. This implies that, PYSZ interaction with Near Neutral melt not only caused chemical attack to the coating but also thermo-mechanical (adhesion) problem, between the TBC and bond coat/TGO in a real life situation, resulting not only in ceramic failure but also spallation of the entire coating system.

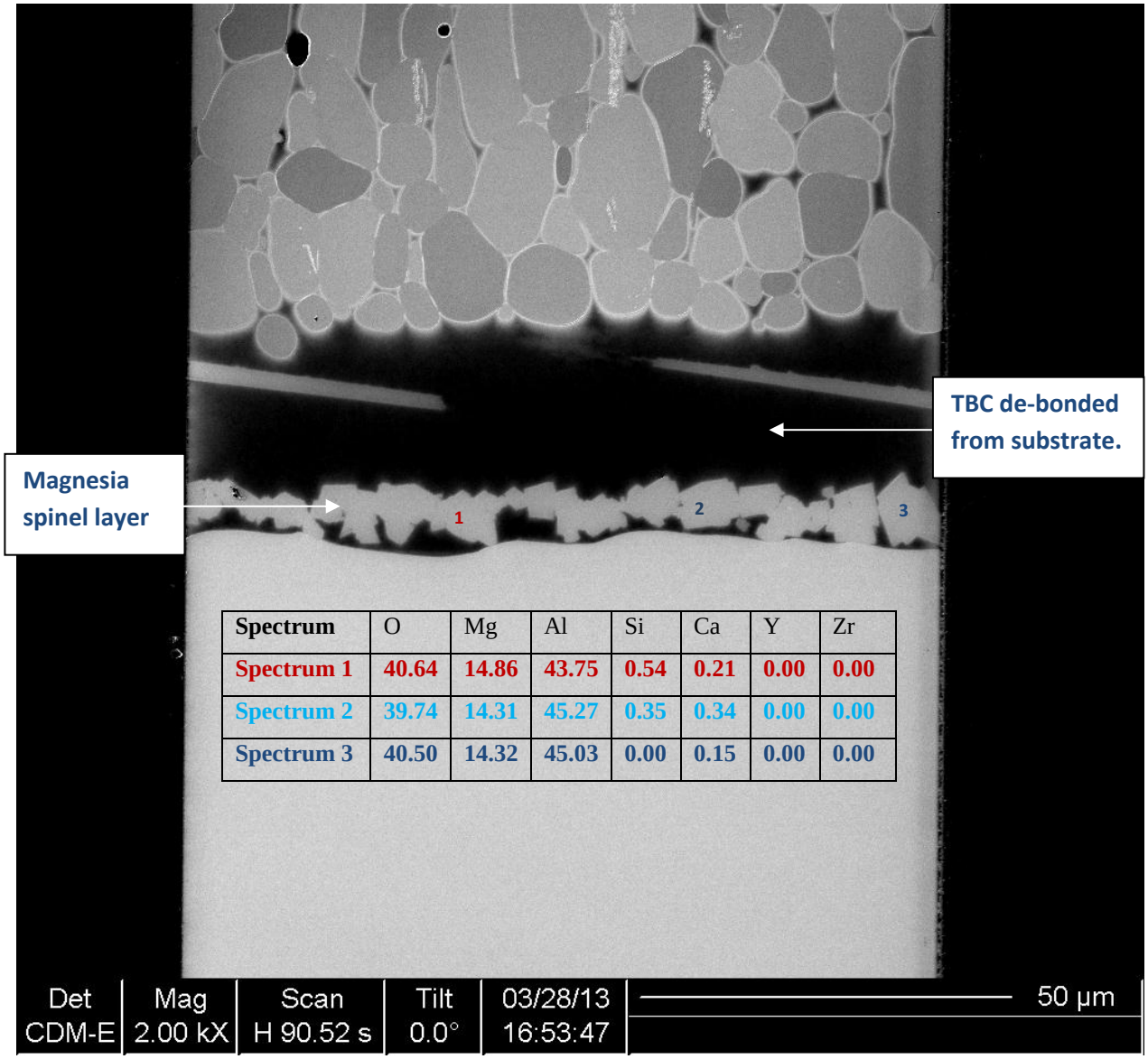

Spectrum	O	Mg	Al	Si	Ca	Y	Zr
Spectrum 1	40.64	14.86	43.75	0.54	0.21	0.00	0.00
Spectrum 2	39.74	14.31	45.27	0.35	0.34	0.00	0.00
Spectrum 3	40.50	14.32	45.03	0.00	0.15	0.00	0.00

Figure 118: FIB image of PYSZ interaction with molten Near Neutral deposit, resulting to de-bonding of the ceramic (enclosed: elemental analysis in at% revealing the magnesia alumina spinel layer at the interface).

7.6 Free-Standing TBC Eliminating the Effect of Excess Aluminium Leached out from the Substrate

PYSZ TBCs degradation by Near Neutral molten deposit showed intense activities at the bottom of the TBC, as shown in the FIB image in Figure 118. Hence it was deemed necessary to isolate the effect of variations in B.I. of the deposit used and microstructural evolution

solely due to the composition of CMAS and not because of destabilisation of the alumina substrate, subsequently releasing aluminium into melt.

Near Neutral degradation mechanism of free-standing TBC samples showed similar patterns to that observed in the Near Neutral category above. The morphology of attack was characterised by microstructural transformation from columnar to fragmented grains, as a result of dissolution of the TBC and recrystallization into new rounded grains (Figure 119), rich in calcia content. Due to their low viscosity, Near Neutral melts quickly penetrated through the coating and, depending on the coating thickness, formed a melt pool at the bottom of the coating. However, there was no evidence of a melt pool with the free-standing samples which was attributed to the thickness of the structure (about 3 mm).

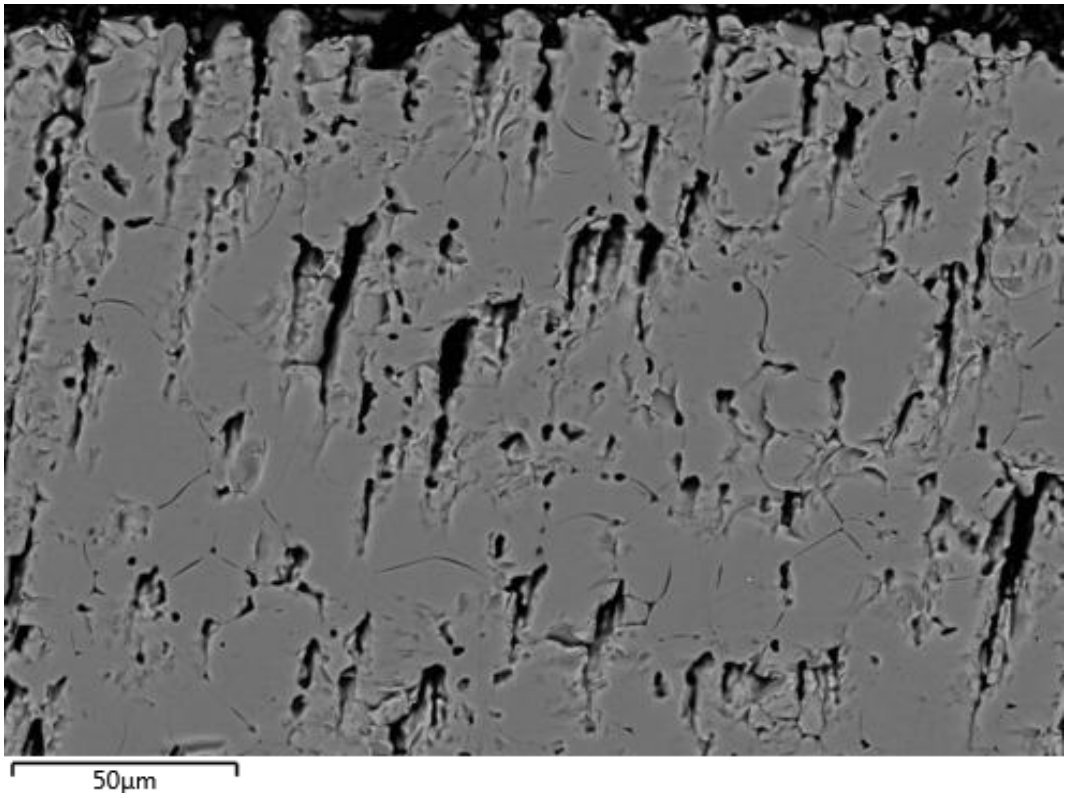

Figure 119: Free-standing TBC samples sprayed with Near Neutral deposit for 4h at 1480 °C, showing completely different mechanism of attack to the Low B.I. sample in Figure 94 .

The Near Neutral sample maintained a high yttria content averaging above 3 at% throughout the entire coating, with significant amount of calcium absorbed into the newly formed grains (~4 at%), as can be seen in Figure 120. The ($CaO + YO_{1.5}$) value for Near Neutral free-standing sample adds up to about 6 at%, which is enough to stabilise the t-zirconia hence preventing the formation of monoclinic zirconia.

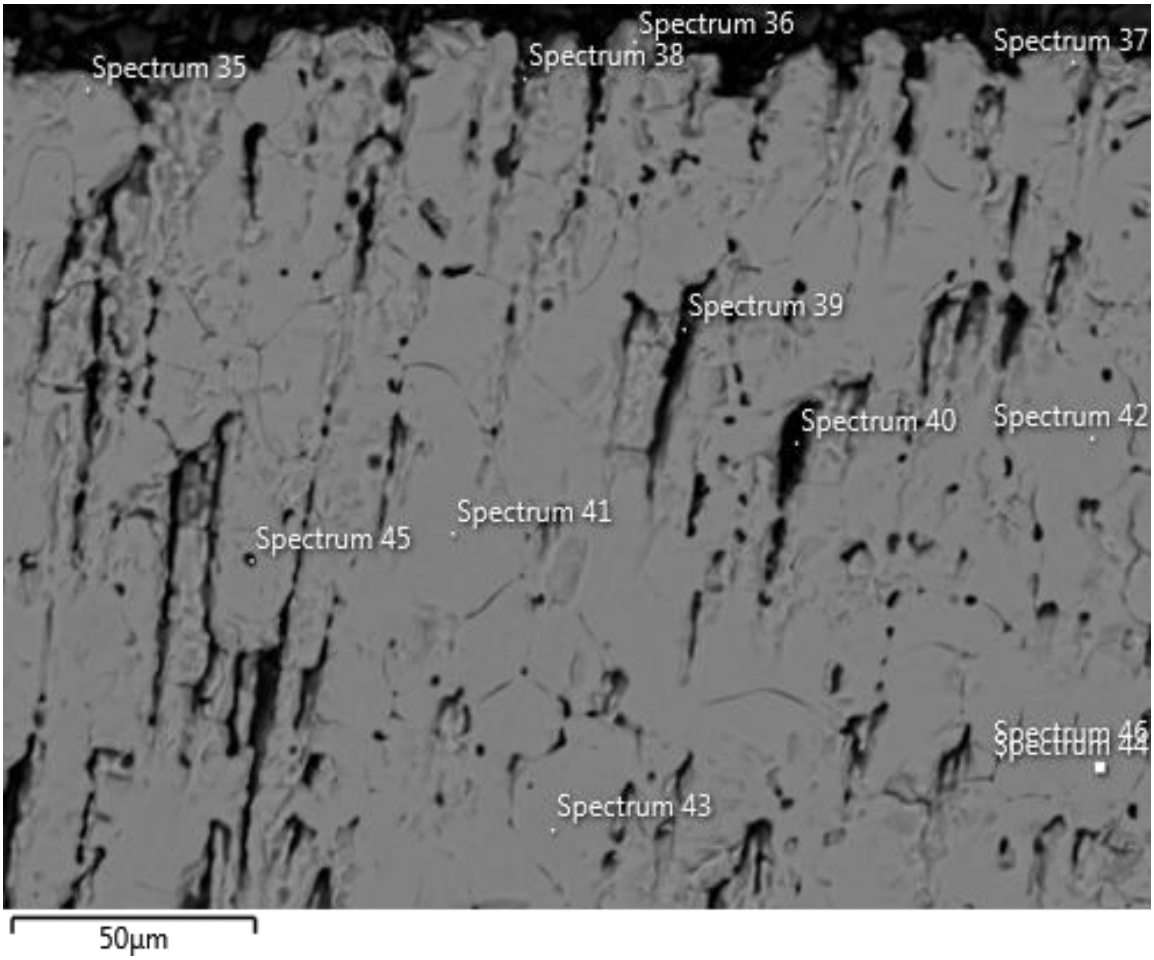

Spectrum	O	Mg	Al	Si	Ca	Y	Zr
Spectrum 35	58.2	0.2	0.0	0.0	4.4	2.0	35.2
Spectrum 36	43.2	0.4	2.6	0.0	5.3	2.4	46.1
Spectrum 37	64.8	0.3	0.0	0.0	3.5	1.9	29.4
Spectrum 38	70.7	0.1	3.1	0.5	2.4	1.2	22.0
Spectrum 39	45.5	0.0	0.2	0.0	4.0	3.6	46.7
Spectrum 40	57.4	0.7	3.0	1.7	2.7	2.4	32.0
Spectrum 41	59.1	0.4	0.2	0.0	3.0	2.6	34.8
Spectrum 42	58.8	0.0	0.0	0.0	3.6	2.8	34.8
Spectrum 43	59.6	0.7	0.0	0.0	3.5	2.7	33.5
Spectrum 44	60.5	0.2	0.0	0.0	2.7	2.7	34.0
Spectrum 45	59.2	0.4	0.2	0.0	3.4	2.7	34.2
Spectrum 46	60.4	0.2	0.2	0.0	2.3	2.6	34.3

All results in atomic%

Figure 120: Analysis of Near Neutral attack of free-standing TBC – 4h at 1480 °C, showing no evidence of preventing monoclinic phase transformation.

7.7 Mid-range (Near Neutral) B. I. Mechanism of Attack

Near Neutral deposits interaction with 7YSZ TBCs showed a completely different mechanism of attack compared to that observed with Low B.I. degradation. Near Neutral attack was found to transform the coatings microstructure, with the resulting microstructure being rounded grains high in CaO content thereby avoiding the detrimental monoclinic phase transformation (Figure 114). The attack mechanism is characterised by accelerated sintering as a result of high CaO content (with the excess CaO acting as a "sintering aid" binding the columns together), as was observed after 30 minutes of heat treatment with Near Neutral deposits (Figure 99). Viscosity was found to be an important parameter as it will influence the degradation mechanism, which has been shown to reduce with increasing B.I. value (Figure 31), thereby influencing the penetrating rate of the melt, the ability to form a melt pool at the interface and the rate at which it does so.

In order to understand the phenomenon of this mode of attack, the reaction products formed on the top, bottom and inter-grain boundaries were studied and so too were the newly formed grains. It was evident from the onset that Near Neutral B.I. samples do not form the glassy layer on the surface (irrespective of the amount of coverage) as was the case with Low B.I. samples under similar conditions. A melt pool was noticed to have formed after one hour exposure with Near Neutral deposit at the coating/substrate interface (Figure 102). The composition of the reaction products were mapped across the entire coating and were compared to the composition of the initial deposit (Figure 121).

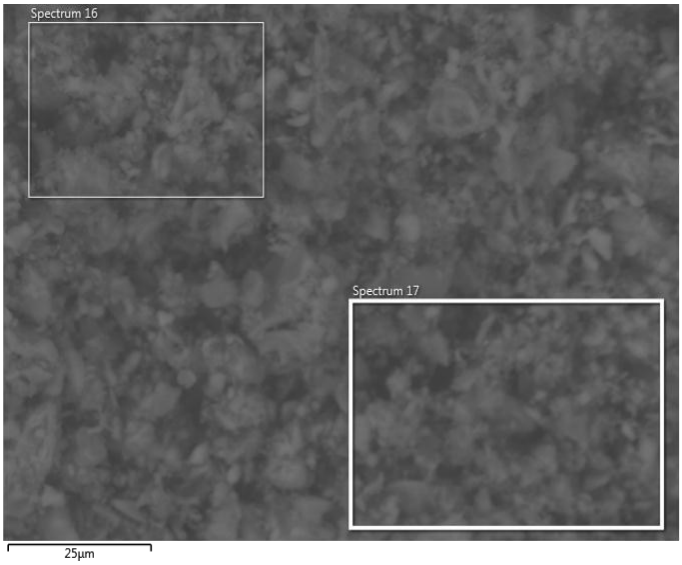

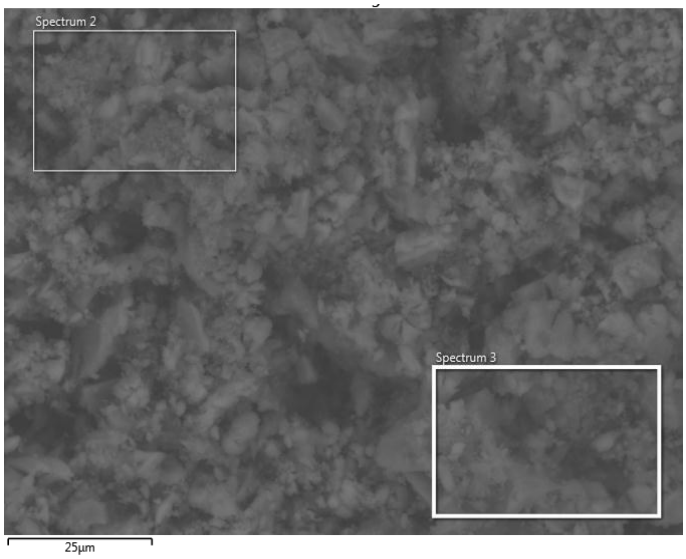

Spectrum	**C**a	**M**g	**A**l	**S**i
Spectrum 16	40.7	13.8	16.1	29.4
Spectrum 17	37.2	13.2	16.5	33.1

(a)

Spectrum	**C**a	**M**g	**A**l	**S**i
Spectrum 2	68.6	12.3	11.2	7.9
Spectrum 3	58.3	15.9	11.3	14.5

(b)

All results in atomic%

Figure 121: Analysis of (a) Near Neutral and (b) High B.I. deposits.

Near Neutral samples showed major compositional variation between the top of the coating and the melt pool at the bottom. The Al_2O_3 content increased significantly in the melt pool, due to the destabilisation of the alumina substrate resulting in Al diffusing from the surface of the substrate into the melt. Also, the amount of MgO in the melt pool was noticeably more than in the melt matrix, with the MgO at the interface combining with Al_2O_3 to form magnesia spinel (Figure 118). However, the CaO content in the melt, in the transformation region, is significantly lower than at the surface of the sample, since Ca is continuously absorbed from the melt by the new grains, resulting in a high CaO content in the grains in the transformation region whereas the CaO content in the melt depreciates, as illustrated in Figure 122.

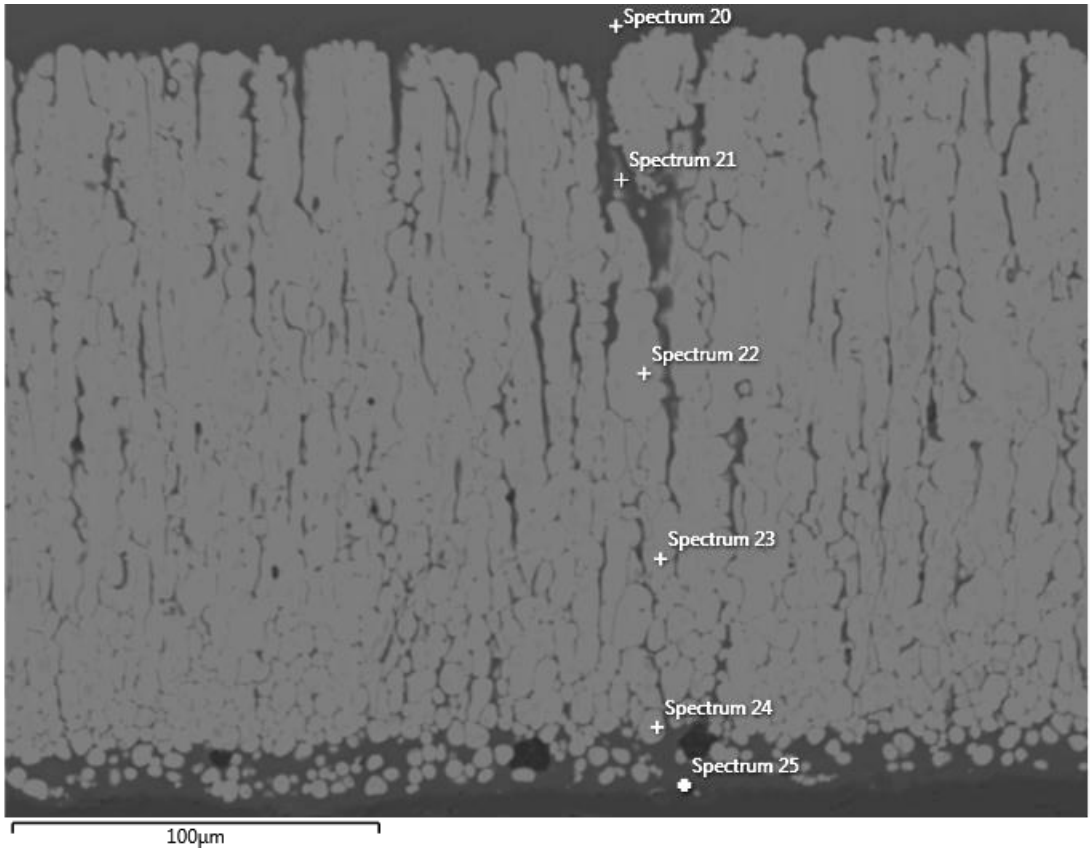

Spectrum	O	Mg	Al	Si	Ca	Y	Zr
Spectrum 20	38.6	3.7	8.0	16.3	27.5	1.1	4.8
Spectrum 25	41.1	4.6	19.0	9.0	24.9	0.6	0.8

All results in atomic%

Figure 122: Analysis of the melt on top (Spectrum 20) and bottom (Spectrum 25) of Near Neutral sample after one hour at 1480 °C.

An Al diffusion gradient is established between the surface and the Al_2O_3-rich bottom of the sample, due to excess Al_2O_3 leached into the melt pool from the substrate. As the exchange mechanism is diffusion driven, the amount of Al_2O_3 upward in the structure increases with time meanwhile the CaO content on the surface of the coating and in the melt matrix stabilises with time, as an all through grain transformation is achieved. It has been shown that Ca from the melt will diffuse into the new grains in the transformation zone therefore if the entire coating has been transformed, then the CaO content in the melt matrix is expected to be fairly steady throughout the structure. This is similar to the study by Stott et al. [104]. The

sample in Figure 123 has been treated for two hours and the Al content in the top melt was found to be more than double that of one hour exposure. On the other hand, the amount of CaO has decreased (Spectrum 20 on Figure 122 and Spectrums 21-23 on Figure 123) as more Ca is diffusing into the cells in the ever increasing transformation zones.

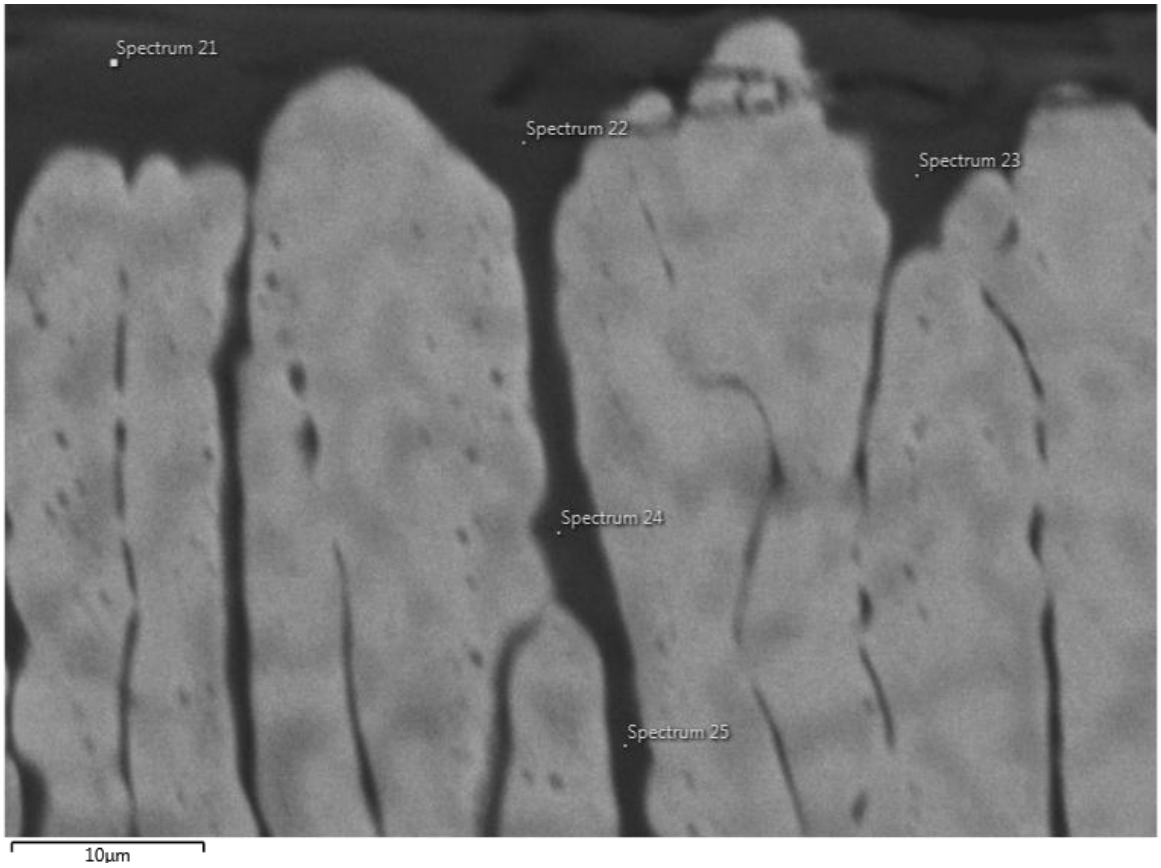

Spectrum	O	Mg	Al	Si	Ca	Y	Zr
Spectrum 21	37.3	1.8	22.6	16.9	20.2	0.2	**1.1**
Spectrum 22	36.2	1.6	23.0	17.7	20.7	0.0	**0.8**
Spectrum 23	39.6	1.5	21.3	16.3	19.5	0.2	**1.5**
Spectrum 24	38.8	1.3	19.3	14.6	17.6	1.2	**7.3**
Spectrum 25	36.8	1.3	18.6	15.2	18.2	1.7	**8.3**

All results in atomic%

Figure 123: Near Neutral sample after two hours exposure, showing significantly more Al in the melt compared to Figure 122.

As mentioned above, Al content in the entire structure increases with time, as Al diffuses from the Al_2O_3-rich melt pool into the melt matrix while the Ca content was found to be similar in all regions except in the transformation zone where Ca concentration in the surrounding melts matrix drops sharply as more CaO is absorbed by the recrystallized grains.

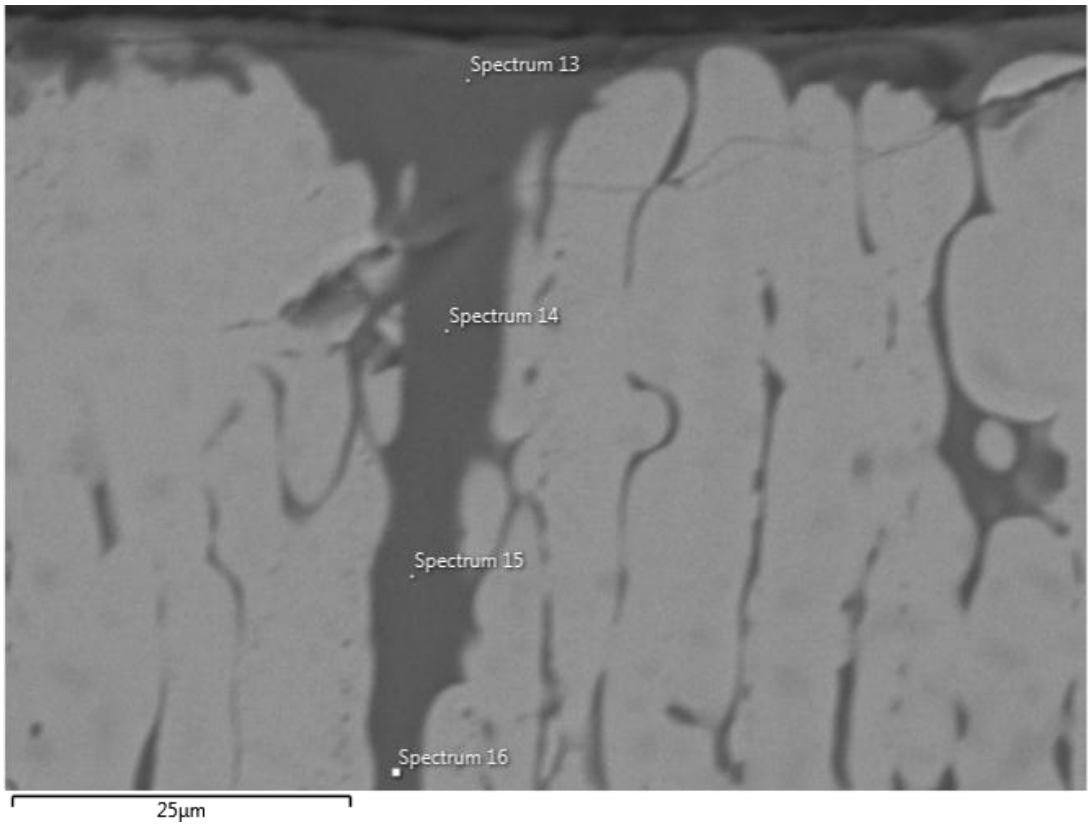

Spectrum	O	Mg	Al	Si	Ca	Y	Zr
Spectrum 13	38.1	1.6	24.7	15.1	19.5	0.2	0.9
Spectrum 14	37.5	1.6	25.2	15.4	19.8	0.1	0.4
Spectrum 15	38.1	1.4	25.0	15.2	19.6	0.0	0.7
Spectrum 16	39.6	1.6	22.5	14.4	18.9	0.3	2.7

All results in atomic%

Figure 124: Near Neutral sample – four hours at 1480 °C showing Ca content stabilising as transformation zone grows. The noticeable Al enrichment is due to excess Al migrating from the melt pool.

The melt analysis in Figure 124 suggests that the Ca content in the melt intercolumnar boundaries stays similar before transformation which leads to Ca being absorbed by the new structure. It is clear from their respective initial compositions (Figure 121) that the Al content

has increased substantially, especially with increasing exposure time. However, it cannot be concluded that the increased Al_2O_3 content, due to the destabilisation of the substrate, plays a role in the observed degradation morphology, since similar results were obtained with free-standing samples.

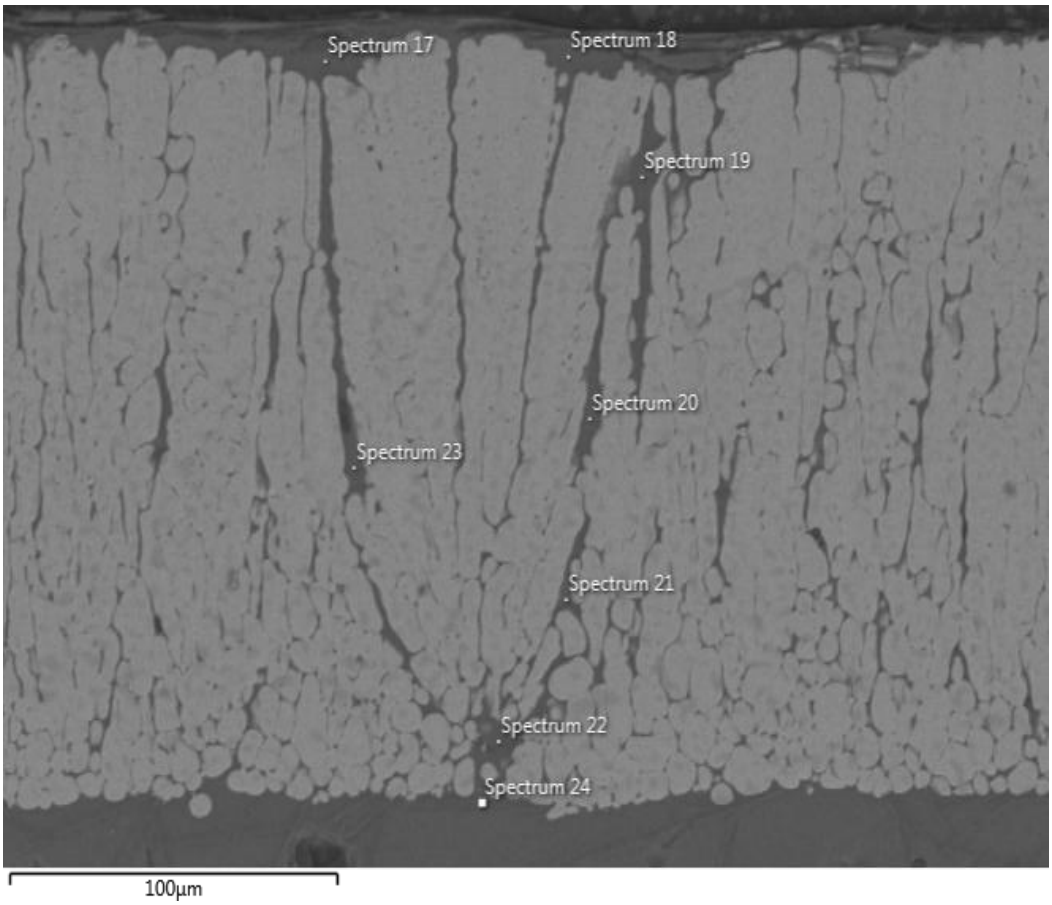

Spectrum	O	Mg	Al	Si	Ca	Y	Zr
Spectrum 17	34.7	1.4	25.4	15.7	21.4	0.2	1.3
Spectrum 18	39.1	1.4	24.0	14.8	19.4	0.2	1.1
Spectrum 19	38.0	1.5	24.3	15.3	20.0	0.3	0.6
Spectrum 20	35.9	1.5	25.6	15.7	20.6	0.1	0.7
Spectrum 21	36.9	1.3	23.9	15.7	20.6	0.1	1.4
Spectrum 22	40.9	1.5	43.3	3.4	10.5	0.0	0.4
Spectrum 23	38.7	1.5	24.2	15.0	19.9	0.1	0.6
Spectrum 24	40.4	1.2	45.9	3.8	8.5	0.0	0.2

All results in atomic%

Figure 125: Distinct composition of Near Neutral sample after four hours at1480 °C.

The following conclusions can be drawn based on Figure 125;

- The composition in the upper part and middle of the TBC (Spectrums 17-21 and 23) are very similar.
- Substantial reduction in CaO content (Spectrums 22&24) was noticed in the surrounding melt matrix in the transformation zone.
- Al content at the upper part and middle of the TBC are vastly more than the initial composition of the deposit, indicating excess Al_2O_3 has diffused from the substrate. In the melt pool (Spectrums 22&24), Al_2O_3 content was more than 5x that of the initial composition.

It is fair to say that the composition of the reaction products in the melt matrix stays fairly constant right up to the transformation zone, where the amount of Ca in the melt falls considerably. Also, Al increases which can be accounted for by destabilisation of the alumina substrate freeing Al into melt pool. The addition of excess Al in the melt pool reduces the melting point of the melt, hence creating a thermal gradient between the upper melt matrix and the melt pool. This explains the reason Near Neutral degradation of PYSZ deposited on a substrate showed attack initiation from the bottom of the coating, as can be seen in Figure 122. However, for free standing samples without the ability to form a melt pool as there was no substrate, attack were found to be uniform, with complete transformation in the middle of the sample.

As the transformation zone increases, the composition stabilises through the TBC reaction product. When transformation is complete, the composition becomes constant throughout the TBC. For the samples used in this study with a thickness of ~200 µm, Near Neutral samples showed all through transformation at the eight hours exposure time, as illustrated in Figure 126. Analysis of this sample revealed the reaction product between grain boundaries to be

constant or very similar (Spectrums 26, 27, 29-31, Figure 126), with Al content higher than usual, for the reason mentioned previously.

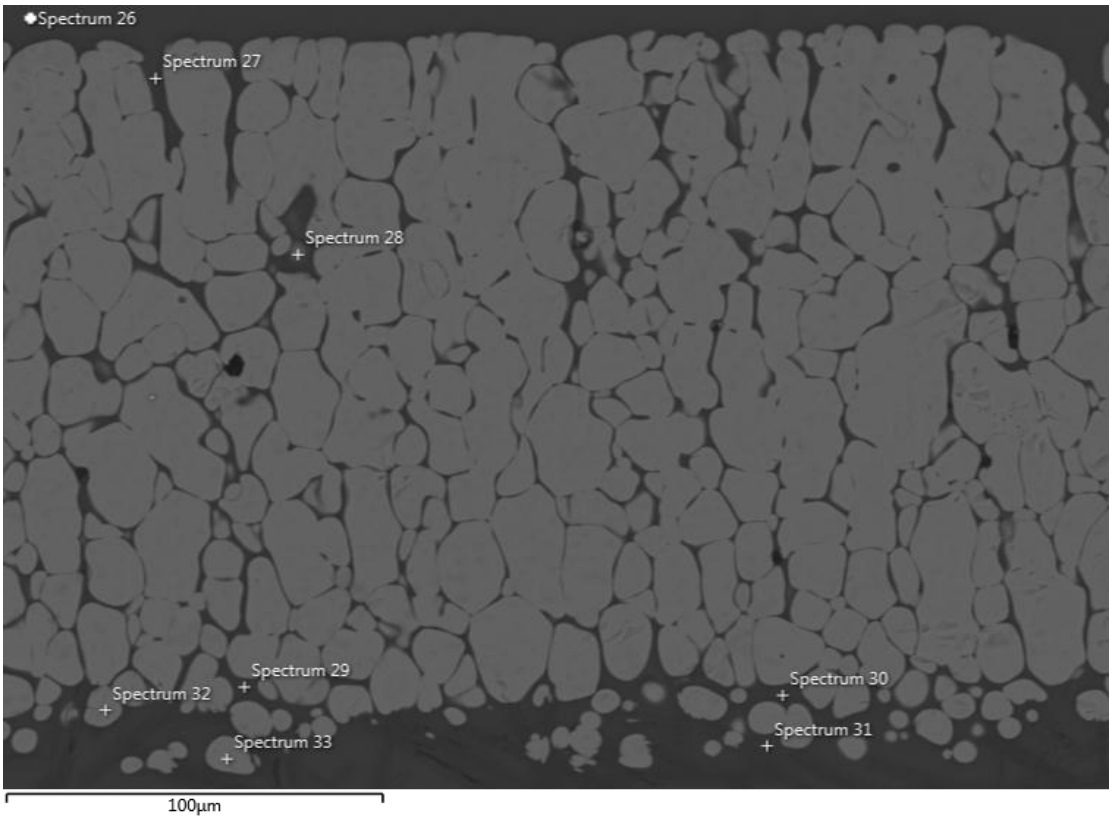

Spectrum	O	Mg	Al	Si	Ca	Y	Zr
Spectrum 26	37.5	1.3	21.5	13.2	22.3	0.2	4.1
Spectrum 27	40.0	1.3	20.8	13.1	21.2	0.3	3.4
Spectrum 29	39.3	1.2	21.0	13.4	21.6	0.3	3.2
Spectrum 30	39.1	1.4	21.6	13.9	22.2	0.0	1.7
Spectrum 31	38.6	1.2	22.2	12.9	23.2	0.0	2.0

Top half of sample

Bottom half of sample

All results in atomic%

Figure 126: All through transformation showing constant CaO value across the TBC after 8h heat treatment.

7.8 Summary – Mid-range Basicity Index (Near Neutral Deposits): B.I. = 1.8 – 2.2

Mid-range B.I. was calculated based on the Basicity Index of a CaO – SiO_2 dominated slag composition, with B.I. in the range of 1.8-2.2. The composition used in this category was $C_{56}M_9A_7S_{28}$ in mole% (B.I. = 1.9).

Near Neutral deposit was found to form a melt pool at the TBC/substrate interface. This caused boundary diffusion of Al from the surface of the substrate into the melt. There was no evidence that Near Neutral melts penetrated into the substrate. The FIB image in Figure 118 provides detailed features of the bottom of the sample, suggesting that the alumina substrate is not severely attacked by the melt. Uniquely, the sample showed complete de-bonding from the substrate, indicating a dual failure mode of coating degradation and spallation.

By using free-standing samples, the effect of B.I. variation was isolated mainly to CMAS/TBC interaction, with respect to time and temperature and the potential influence of the substrate was negated. Because the results of the free-standing experiments were similar to the PYSZ samples with alumina substrate, it can then be concluded that the excess alumina in the melt pool and melt matrix have little or no effect on the dissolution and recrystallization mechanism of the coating. However, it alters the local chemistry of the melt, creating a low temperature melting phase at the bottom of the sample. The low temperature melt pool at the bottom creates a thermal gradient in the melt between the top of the sample and the bottom, attack is hence initiated at the low temperature, super-saturated bottom of the sample. The microstructural evolution of PYSZ degradation by Near Neutral melt can be seen in Figure 127.

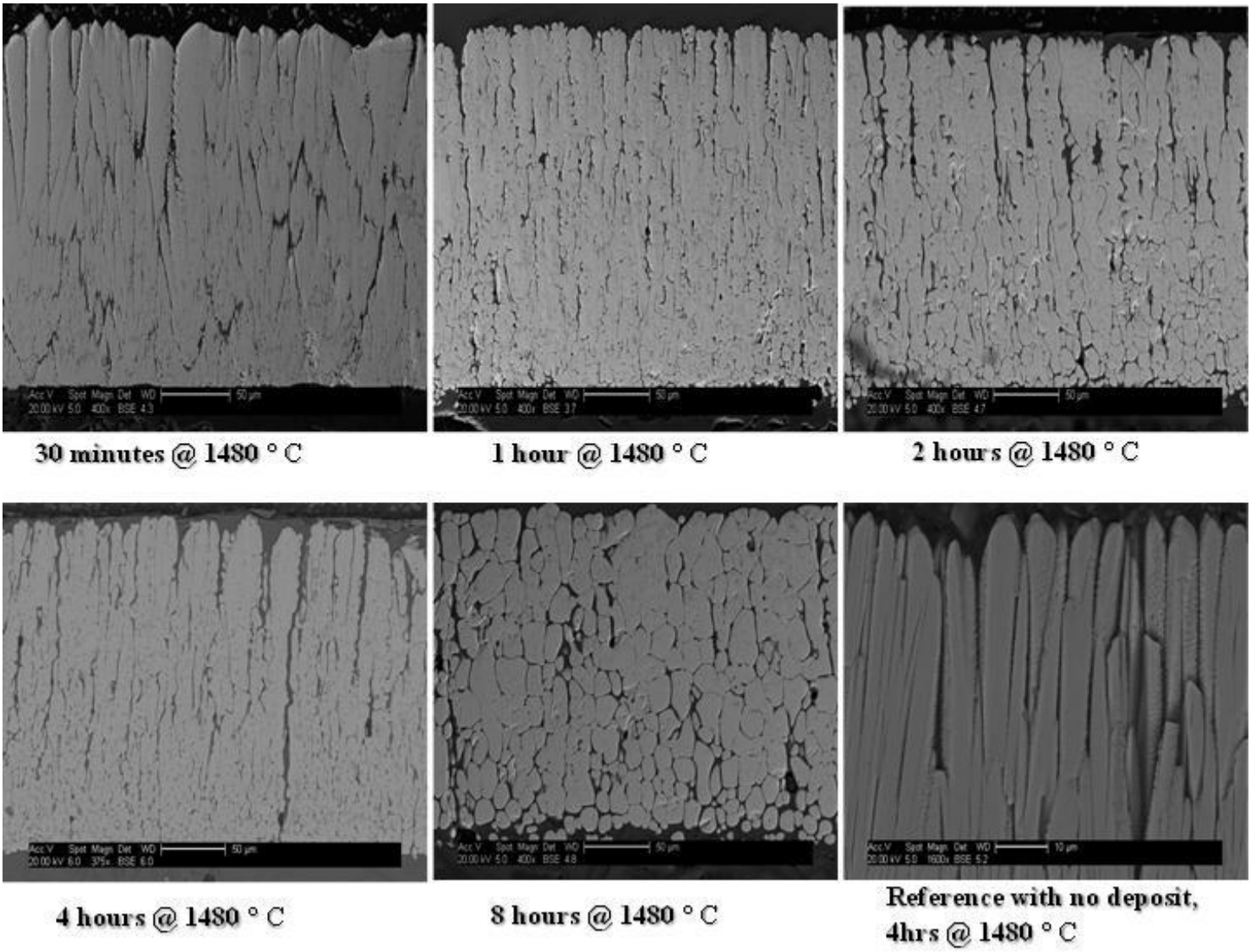

Figure 127: Summary – Near Neutral Deposits

8 High Basicity Index (Basic deposit): B.I. = 2.2 or above

High B.I. deposits are calcareous soils in arid regions of the world such as Middle East, North Africa and UAE. High B.I. in this study refers to Basicity Index with ratios greater than 2.2. In this test, the CMAS composition used was $C_{73}M_9A_7S_{11}$ in mole% (B.I. = 4.68). The glass transition temperature (T_g), the crystallisation temperature (T_c) and the melting temperature (T_m) of the High B.I. deposit used in this experiment can be seen from the DSC curve in Figure 128. The melting temperature of the deposit is ~1430 °C, which is within range of the upper operating gas temperatures of a turbine engine, about 1400 to 1600 °C.

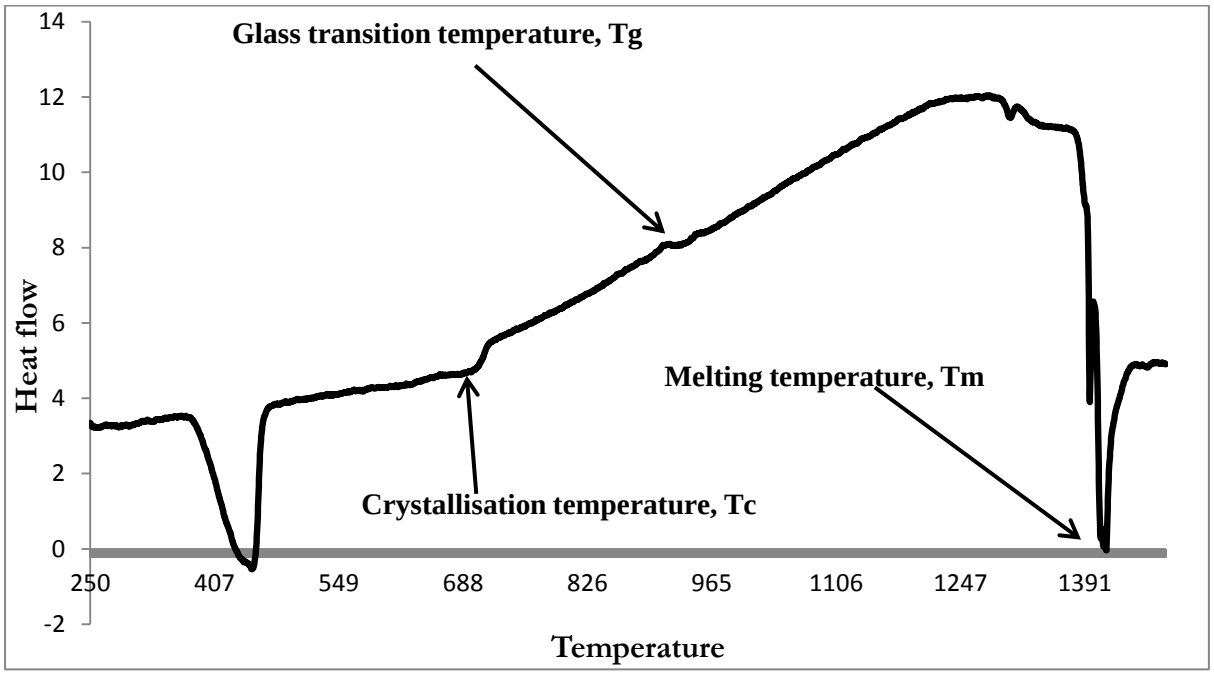

Figure 128: DSC curves of High B. I. CMAS with composition $C_{73}M_9A_7S_{11}$, in mole%.

It was heat treated under similar conditions to that used for the previous two deposits (Low and Mid-range Basicity Index) which involved ageing at 50 °C above the deposit melting point for 30 minutes, 1, 2, 4 and 8 hours. The High Basicity Index composition showed a completely different mode of attack, as shown in Figure 129.

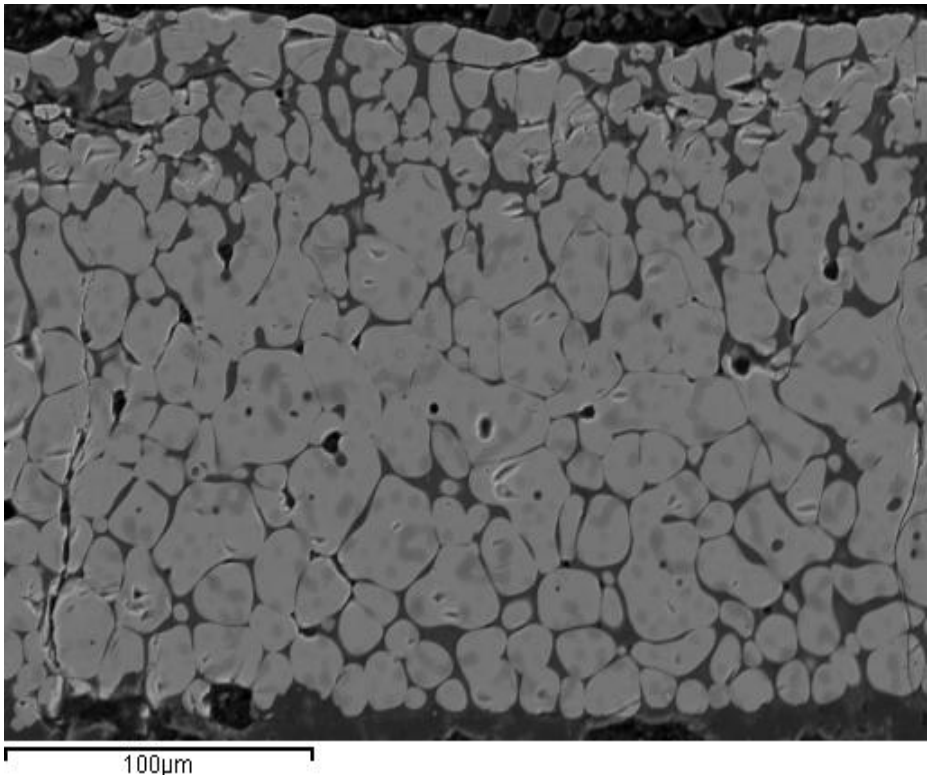

Figure 129: Zirconia – 8 wt% yttria EB-PVD TBC sprayed with $C_{73}M_9A_7S_{11}$ mole % (B. I. ~ 4.7), aged for 4h at 1458 °C; showing a different mode of attack to both Low and Mid-range Basicity Index slag attack.

Figure 129 shows complete dissolution of the columnar coating integrity after 4h at 1458 °C. Dissolution of the entire coating, plus recrystallization through the coating thickness has occurred. The presence of significant amounts of zirconia in the resulting melt pool confirms the partial or complete dissolution of bulk TBC into the molten slag deposit, changing the local chemistry of the slag, as can be seen in Figure 130. The resulting microstructure consists of dense ceramic rounded grains, attributed to the relative wetting characteristics of the TBC/CMAS system; aimed at minimising the surface energies of the reacted TBC/CMAS system. It can therefore be concluded that, wetting behaviour of zirconia based TBC and CMAS system is expected to vary with Basicity Index of the slag/deposit.

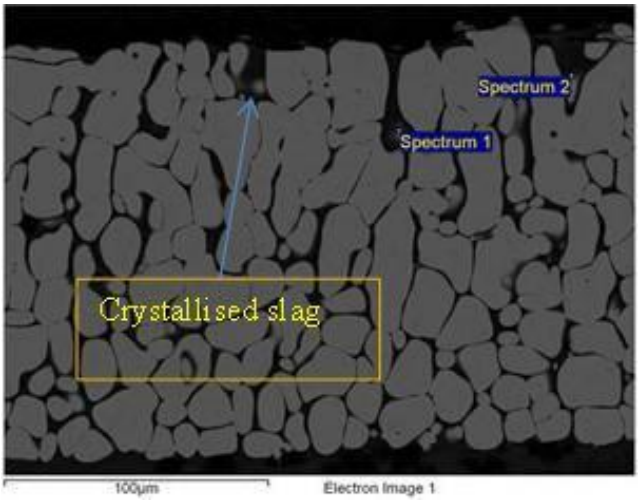

Table 26: Local chemistry of molten slag showing a high concentration of dissolved Zr in the melt.

Spectrum	O	Mg	Al	Si	Ca	Zr
Spectrum 1	69.6	1.3	10.0	4.5	4.9	9.8
Spectrum 2	68.7	1.4	11.1	5.3	5.2	8.4

All results in atomic%

Figure 130: EDAX image of spectrum1&2, showing solidified melt regions after ageing for 4h at 1458 °C.

The rounded grains microstructure of high Basicity Index slag attack is also associated with a phase transformation, believed in this case to be only between calcium oxide, which is absorbed by the bulk coating and reacted to form calcium zirconate. Figure 131 confirms the formation of calcium zirconate within the reaction product.

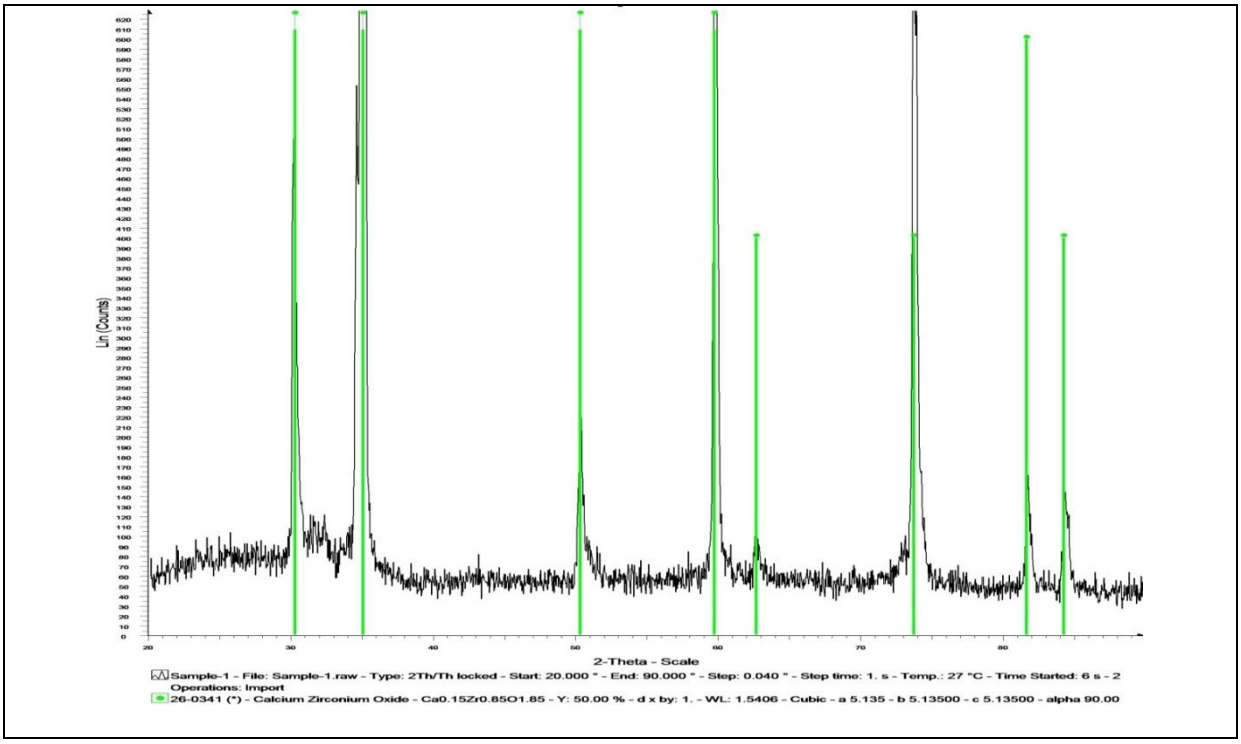

Figure 131: XRD analysis of reaction products formed when high B.I. infiltrated sample react, showing the detected transformed calcium zirconate phase.

Also present in the coating were yttria and calcia, which continue to stabilise the zirconia tetragonal phase. The remainder of the constituent oxides present in the slag are found along the newly formed grain boundaries, as can be seen in Figure 132.

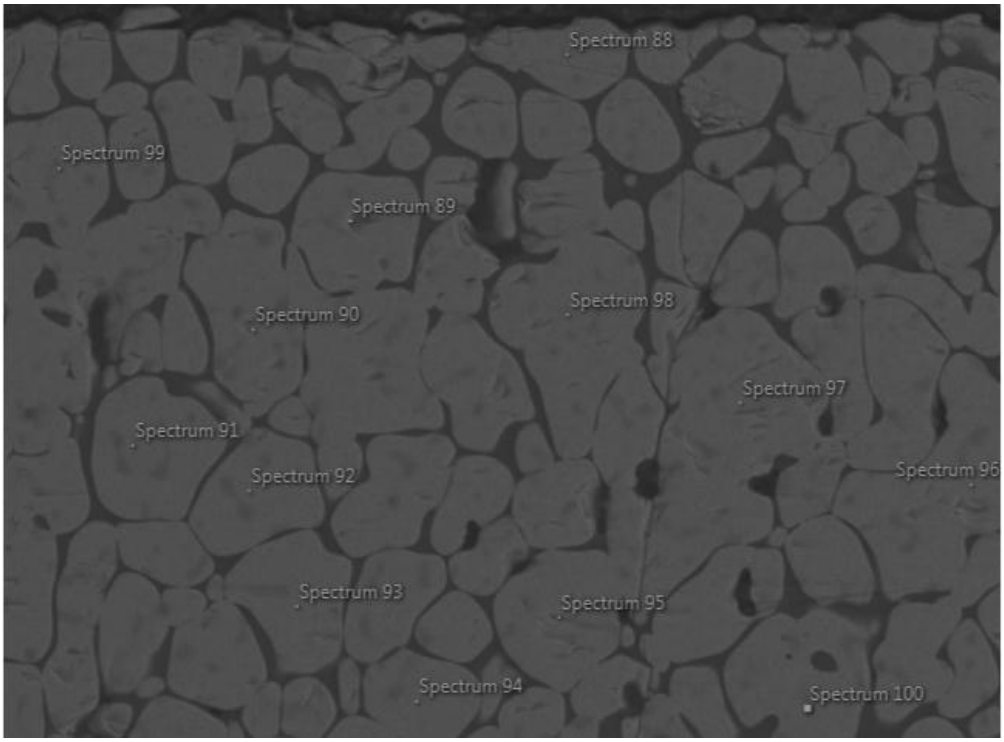

Spectrum	O	Mg	Al	Si	Ca	Y	Zr
Spectrum 88	59.0	0.6	0.6	0.0	5.6	3.6	30.6
Spectrum 89	34.9	0.6	1.4	0.0	9.2	5.8	48.2
Spectrum 90	68.6	0.5	0.4	0.0	4.2	2.8	23.5
Spectrum 91	62.3	0.3	0.4	0.0	4.6	3.5	29.0
Spectrum 92	63.5	0.3	0.6	0.0	4.4	3.3	28.0
Spectrum 93	62.5	0.5	0.4	0.0	4.6	3.6	28.4
Spectrum 94	62.3	0.3	0.2	0.0	4.3	3.5	29.0
Spectrum 95	53.2	0.4	0.7	0.0	6.1	4.3	35.3
Spectrum 96	62.2	0.4	0.3	0.0	4.3	3.5	28.9
Spectrum 97	61.5	0.5	0.3	0.0	4.8	3.4	29.4
Spectrum 98	62.0	0.5	0.3	0.0	4.8	3.4	29.0
Spectrum 99	62.6	0.2	0.5	0.0	4.6	3.3	28.7
Spectrum 100	62.0	0.4	0.4	0.0	4.6	3.9	28.9

All results in atomic%

Figure 132: EDAX analysis of high B. I. infiltrated standard YSZ EB-PVD TBC (4h at 1458 °C).

EDAX elemental mapping (Figure 133) revealed that, high Basicity Index damage mechanism forms a $CaO+Al_2O_3$ rich phase along the grain boundary, possibly of a low melting eutectic composition ((Ca, Mg) Al_2O_4 and $Ca_2Al_2SiO_7$). The zirconia TBC is dissolved in the process and with the rich calcia and alumina melt chemistry, a residual Ca

$Al_2(Zr, Si)_2O_8$ local phase is formed. This was further evident from line scan results in Figure 134.

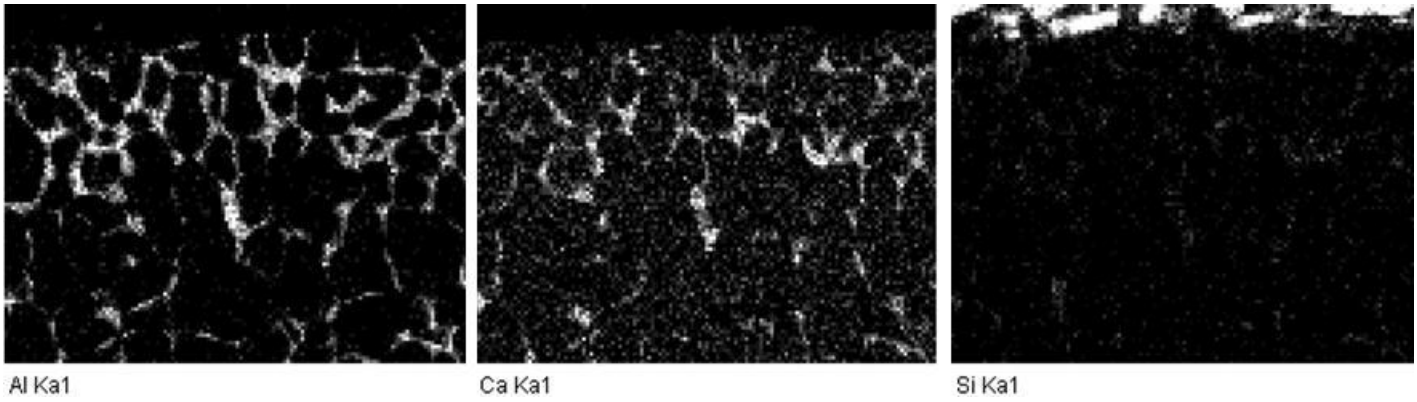

Figure 133: EDAX elemental mapping (4h at 1458 °C) of C73M10A7S11 (B. I. = 4.68)

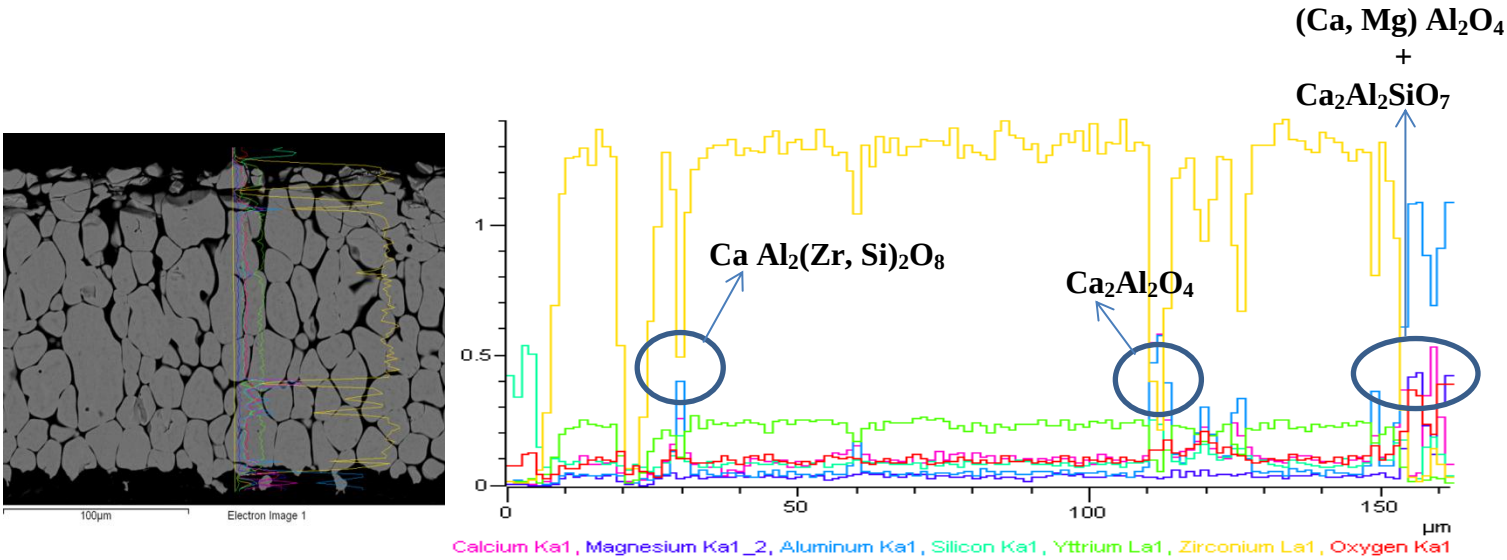

Figure 134: EDAX line scan results for C73M10A7S11 (B. I. = 4.68).

It has been demonstrated that, Basicity Index has a direct effect in the viscosity of the resulting melt. Low B.I. melt was found to be more viscous than its Near Neutral counterpart, which too was expected to be more viscous than High B.I. melt. Low B.I. deposits formed a glass at the surface of the sample while Near Neutral deposits had almost its entire melt penetrated to the bottom of the TBC, where very shallow melt was seen to be locked between grains. However, the topology of High B.I. sample showed that the melt has fully penetrated the entire TBC and formed a melt pool at the bottom of the coating. This is an indication that,

High B.I. melt is less viscous than Low and Near Neutral deposits, and after only 30 minutes, the sample was seen to have already formed a melt pool at the interface. Figure 135 shows a top analysis of a High B.I. infiltrated YSZ sample, with zero Si content on the surface indicating the CMAS melt has fully penetrated the entire structure. As for the amount of CaO and Al_2O_3 observed, this is averaging similar amount that is analysed in the resultant microstructure.

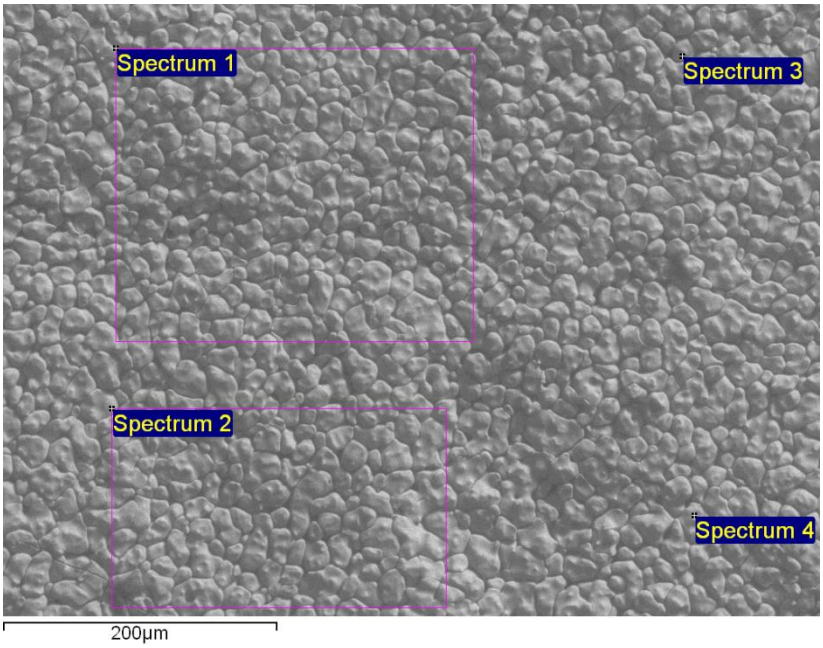

Spectrum	O	Mg	Al	Si	Ca	Y	Zr
Spectrum 1	68.24	0.29	1.99	**0.00**	4.16	0.69	24.62
Spectrum 2	68.22	0.31	1.51	**0.00**	4.04	0.94	24.98
Spectrum 3	66.25	0.39	1.14	**0.00**	3.91	1.25	27.07
Spectrum 4	67.18	0.35	1.03	**0.00**	3.96	1.13	26.35

All results in atomic%

Figure 135: Top analysis of Near Neutral B.I. deposited sample after 4h at 1480 °C heat treatment

8.1 30 Minutes Exposure at 1458 °C

Basicity index determines the aggressivity of the deposits interacting with zirconia-yttria TBCs, hence affecting the severity of the damage caused. So far, it has shown that coating

degradation increases with increasing Basicity Index of the deposits. Therefore, High B.I. deposits infiltrated TBCs were expected to show more aggressive attack than its Low and Near Neutral counterparts. A High B.I. sample was heat treated for 30 minutes at 1458 °C (melting point of deposit + 50 °C fixed ΔT) and the microstructural evolution is shown in Figure 136.

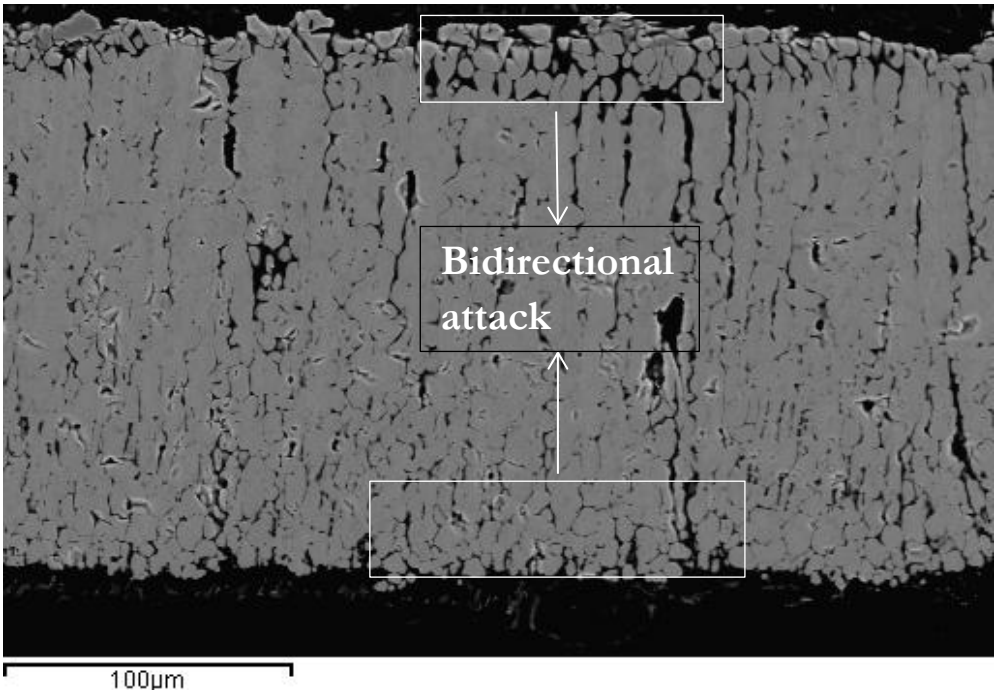

Figure 136: High B.I. attack after 30 minutes at 1458 °C, showing bidirectional attack mechanism.

As expected, High B.I. samples experienced severe microstructural degradation after just 30 minutes, as observed in Figure 136. Unlike its Near Neutral counterpart, here the attack mechanism is bi-directional both from top and bottom of the sample. 30 minutes exposure with High B.I. deposits showed comparable degree of degradation to four hours exposure with Near Neutral deposit. An interesting feature noticed after only 30 minutes exposure was the evolution of calcium zirconate, which can be seen in Figure 137.

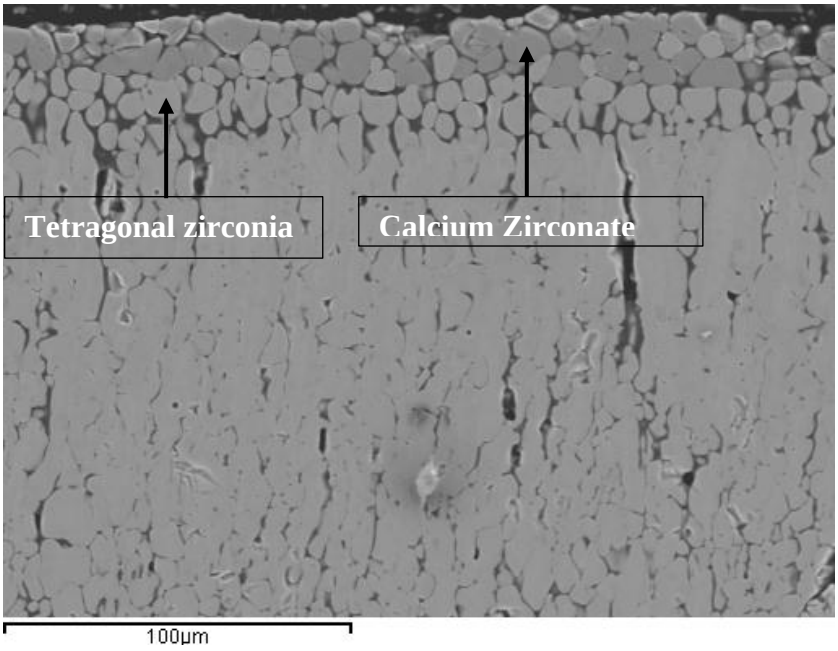

Figure 137: Polycrystalline structure of YSZ TBC infiltrated with High B.I. melt for 30 minutes at 1458 °C.

EDAX elemental mapping was used to study the proportion of calcium zirconate formed within the overall TBC structure. Figure 138 shows that, a significant portion of the upper quarter of the TBC has recrystallized possibly as calcium zirconate. Also, this portion was found to constitute a polycrystalline, fine grains mixture of calcium zirconate and tetragonal zirconia (Figure 139).

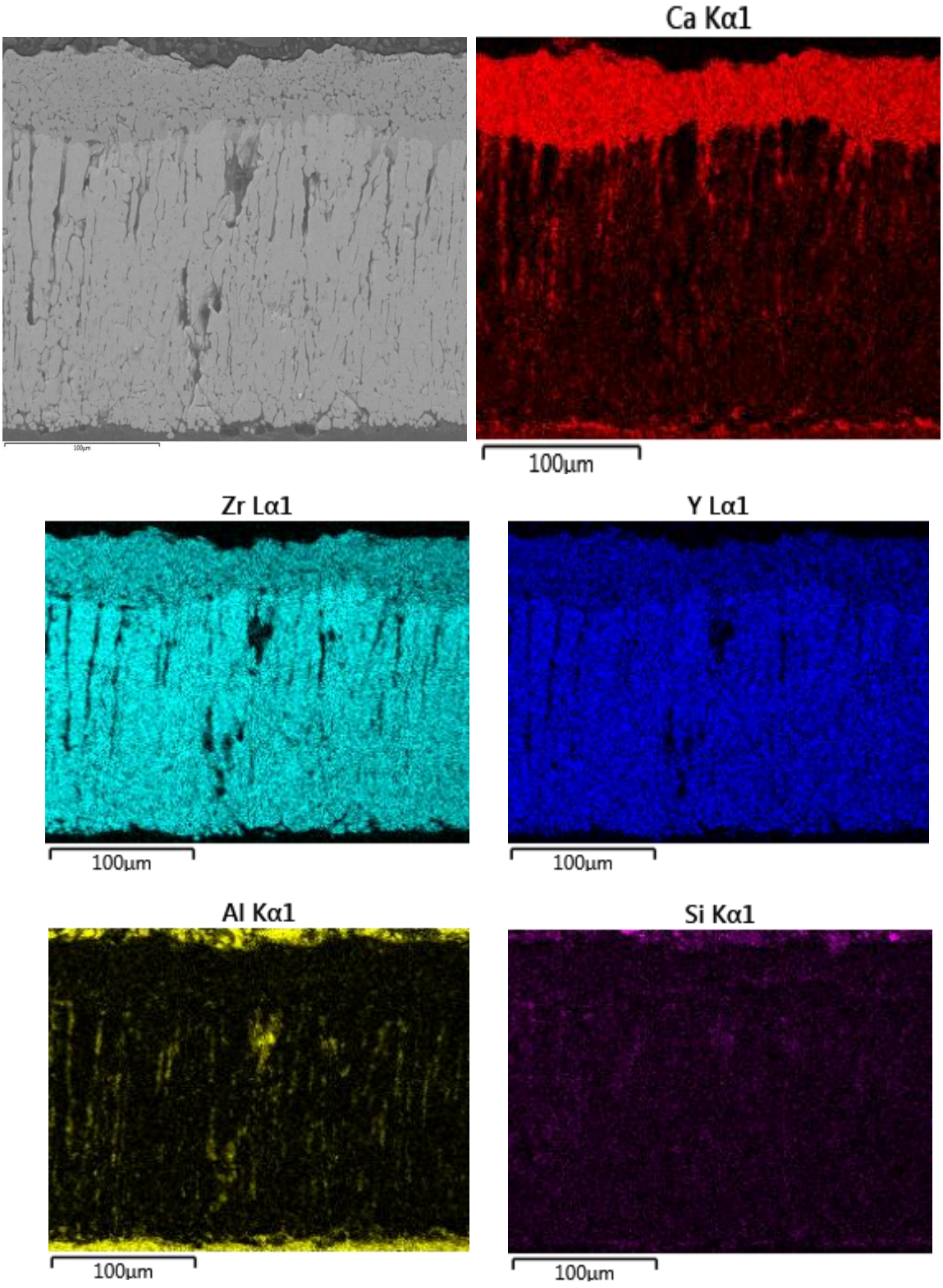

Figure 138: High B.I. EDAX elemental mapping of infiltrated TBC – 30 minutes at 1458 °C.

The elemental mappings on Figure 138 revealed that after only 30 minutes exposure, the top of the coating has undergone a 50 µm transformation zone of fine grains, significantly rich in calcium zirconate. An EDAX layered image of this reaction zone can be seen in Figure 139.

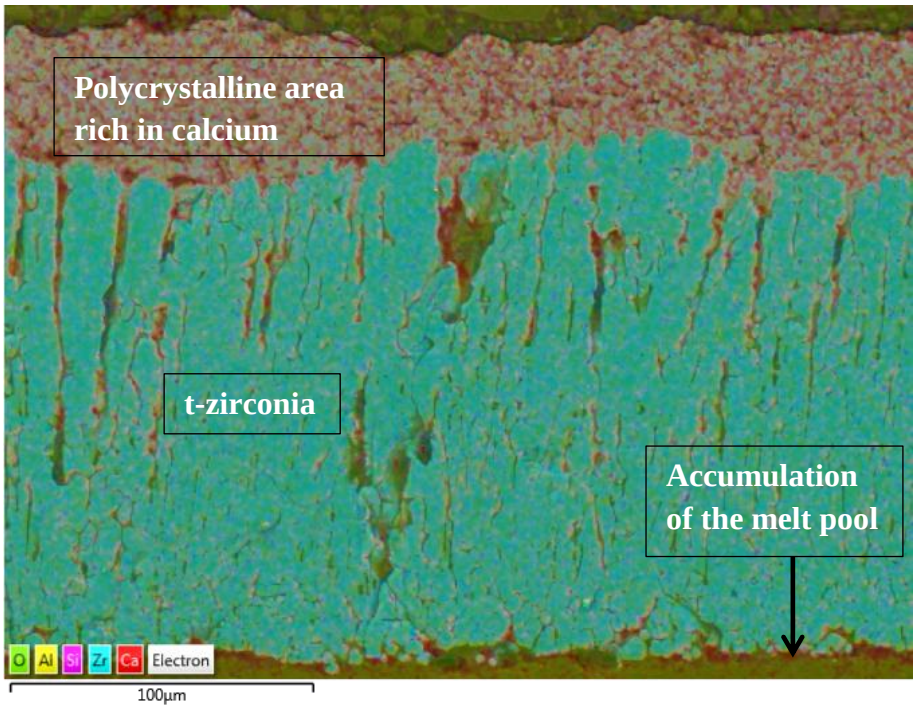

Figure 139: EDAX layered image analysis, High B.I. melt for 30 minutes at 1458 °C, showing calcium zirconate rich zone.

However, no evidence of calcium zirconate was found at the bottom of the coating, in the transformation zone, as shown in Figure 137 and Figure 139. EDAX spot analysis shown on Figure 140 identified a significant amount of CaO (as well as Y_2O_3) in the newly formed grains (spectrums 60 and 61 in Figure 140b). This is indicative that the zirconia has not undergone a monoclinic phase transformation, since CaO and Y_2O_3 stabilise zirconia. The CaO + $YO_{1.5}$ value calculated based on the analysis of the structures in the transformation zone, was found to be ~7 at% after 30 minutes of ageing.

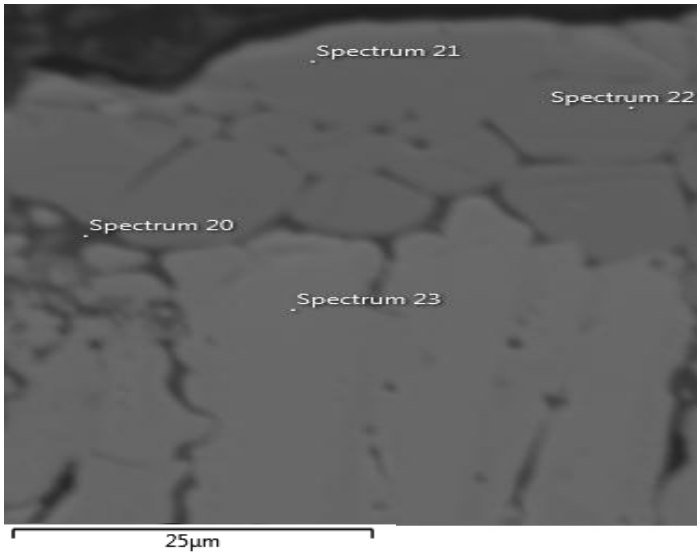

Spectrum	O	Mg	Al	Si	Ca	Y	Zr
Spectrum 20	30.9	0.6	5.9	3.8	24.1	0.8	33.9
Spectrum 21	25.6	0.1	0.4	0.0	22.4	1.2	50.3
Spectrum 22	25.3	0.1	0.4	0.0	22.7	1.1	50.3
Spectrum 23	23.3	0.0	0.2	0.0	0.1	5.6	70.9

(a)

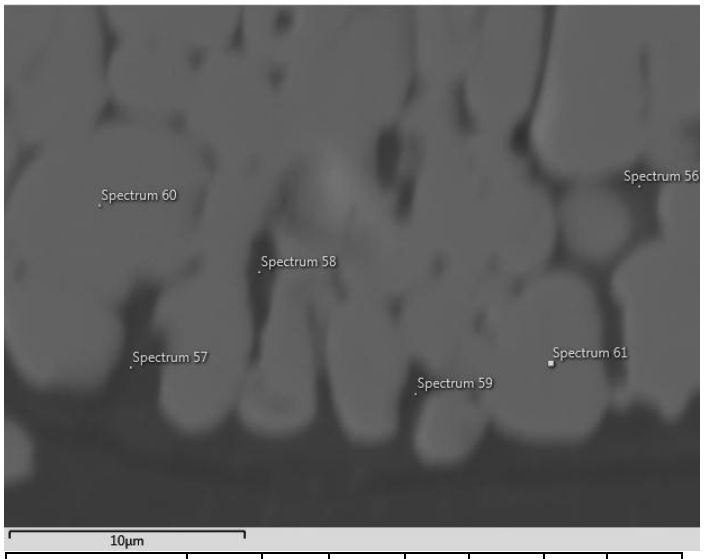

Spectrum	O	Mg	Al	Si	Ca	Y	Zr
Spectrum 56	50.7	0.1	10.8	4.3	15.8	3.6	34.7
Spectrum 57	41.1	8.3	21.4	0.4	3.4	1.7	23.8
Spectrum 58	28.4	6.2	14.8	0.0	2.2	3.1	35.3
Spectrum 59	39.7	6.3	16.0	0.7	4.3	2.6	30.5
Spectrum 60	22.5	0.2	0.2	0.0	3.1	5.9	68.1
Spectrum 61	23.7	0.2	0.4	0.0	2.4	6.5	66.8

All results in atomic%

(b)

Figure 140: EDAX analysis of High B.I. sample after 30 minutes (a) suggesting calcium zirconate at top (spectrums 21 and 22) and zirconia-yttria bulk TBC (spectrum 23), (b) absence of calcium zirconate at bottom, with Ca absorbed in recrystallized grains.

As well as calcium zirconate, another feature identified in this category of degradation mechanism was the formation of a new phase at the interface, between the TBC/substrate and the melt pool/substrate interface. EDAX mapping of this phase was shown to be magnesium and aluminium rich, as can be seen from Figure 141. Further spot analysis revealed the phase to be a spinel phase, probably $MgAl_2O_3$. Figure 141 shows the elements present within this region and Figure 142 confirms the presence of magnesia spinel phase. The trail of this spinel phase revealed substantial deprivation of CaO and SiO_2 from the melt but rich in magnesium and aluminium.

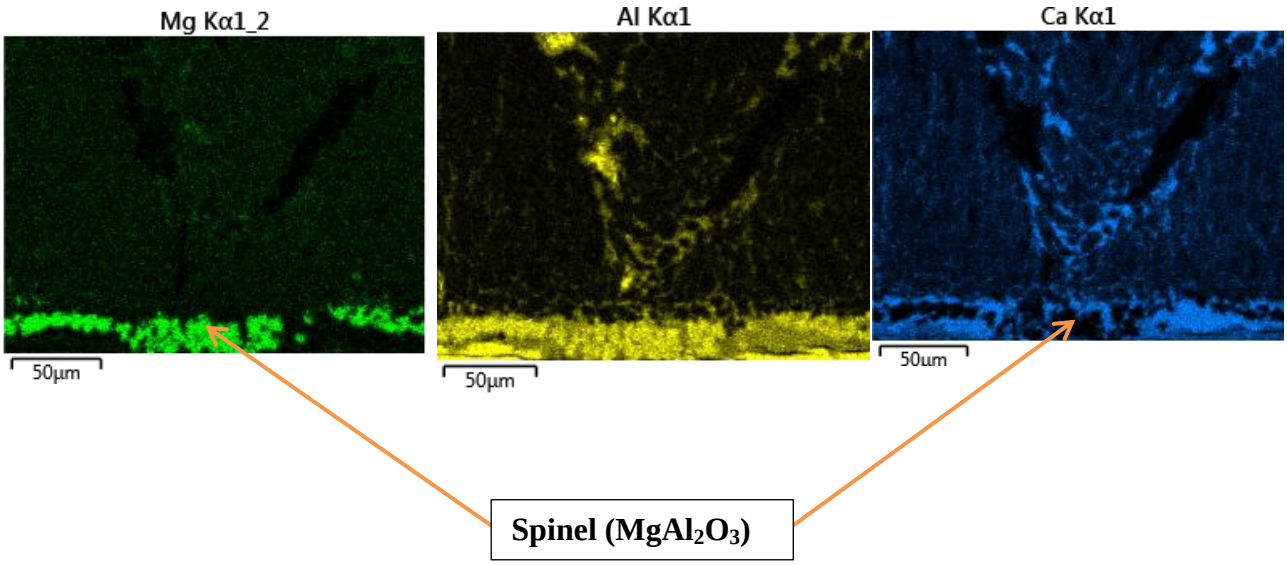

Figure 141: Elemental map identifying the spinel phase after 30 minutes of High B.I. deposit within the melt pool region.

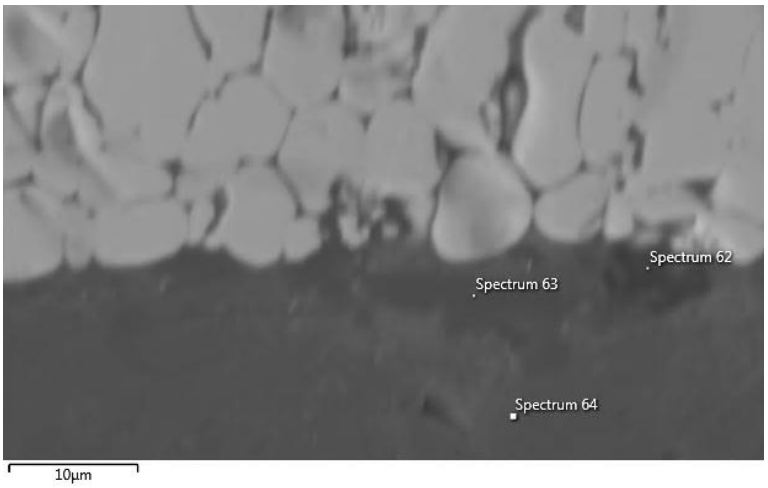

Spectrum	O	Mg	Al	Si	Ca	Y	Zr
Spectrum 62	39.4	5.3	35.5	8.3	7.0	0.0	4.5
Spectrum 63	**42.1**	**16.3**	**40.5**	**0.3**	**0.6**	**0.0**	**0.2**
Spectrum 64	40.6	0.7	44.0	2.0	10.2	0.1	2.5

All results in atomic%

Figure 142: Confirmation of the spinel phase (spectrum 63).

8.2 One Hour Exposure at 1458 °C

An hour exposure with High B.I. deposit showed a level of coating degradation comparable with eight hours exposure using Near Neutral deposits. Severe damage was noticed through the entire TBC structure with the attack being bi-directional. There was total loss of coating integrity and the residual structure showed growth of the transformation zone from both directions. Figure 143 shows a cross sectional micrograph of a High B.I. sample that has been heat treated for one hour at 1458 °C (melting point of High B.I. deposits + 50 °C).

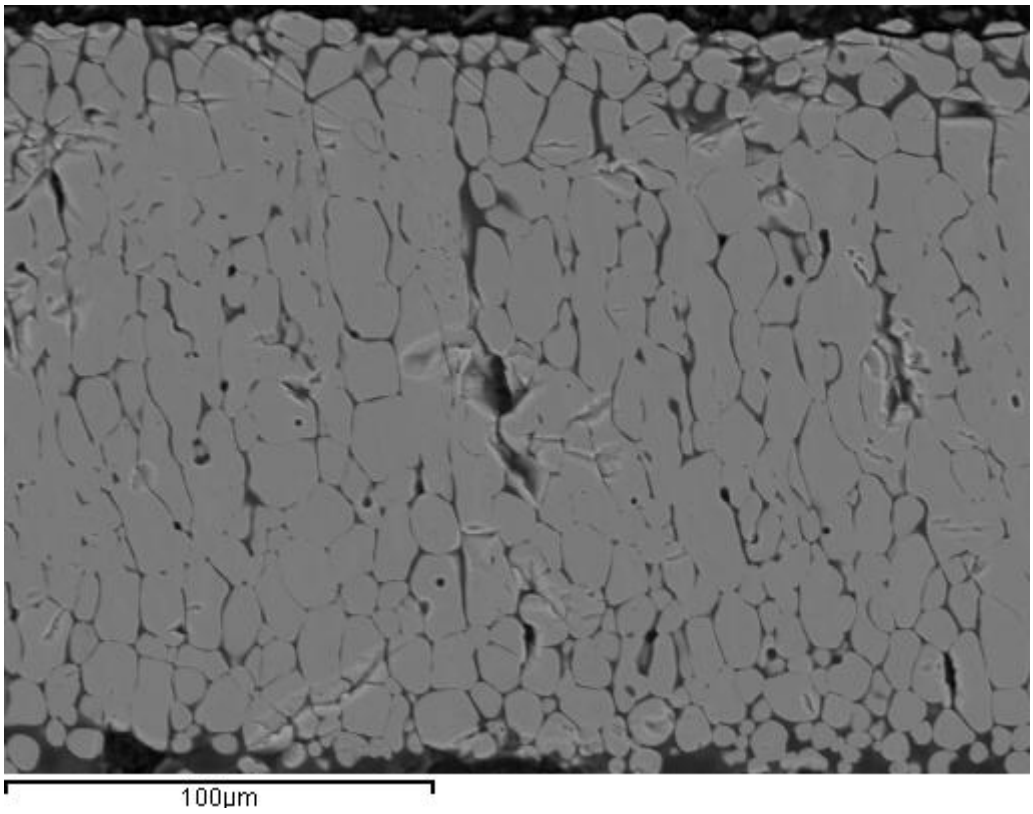

Figure 143: High B.I. sample after one hour heat treatment at 1458 °C, showing all-through structural degradation.

The formation of calcium zirconate at the upper quarter of the coating remains a characteristic with this category of attack, and was observed after both 30 minutes and one hour exposure. However, there was no evidence of calcium zirconate formed at the bottom part of the coating, which was in line with observations made for 30 minutes exposure. Also

noticeable was that the newly recrystallized grains were bigger compared to the structure after 30 minutes heat treatment. Analysis revealed that, about 65 µm of the upper transformation zone contained a mixture of calcium zirconate and tetragonal zirconia, as illustrated in the images on Figure 144.

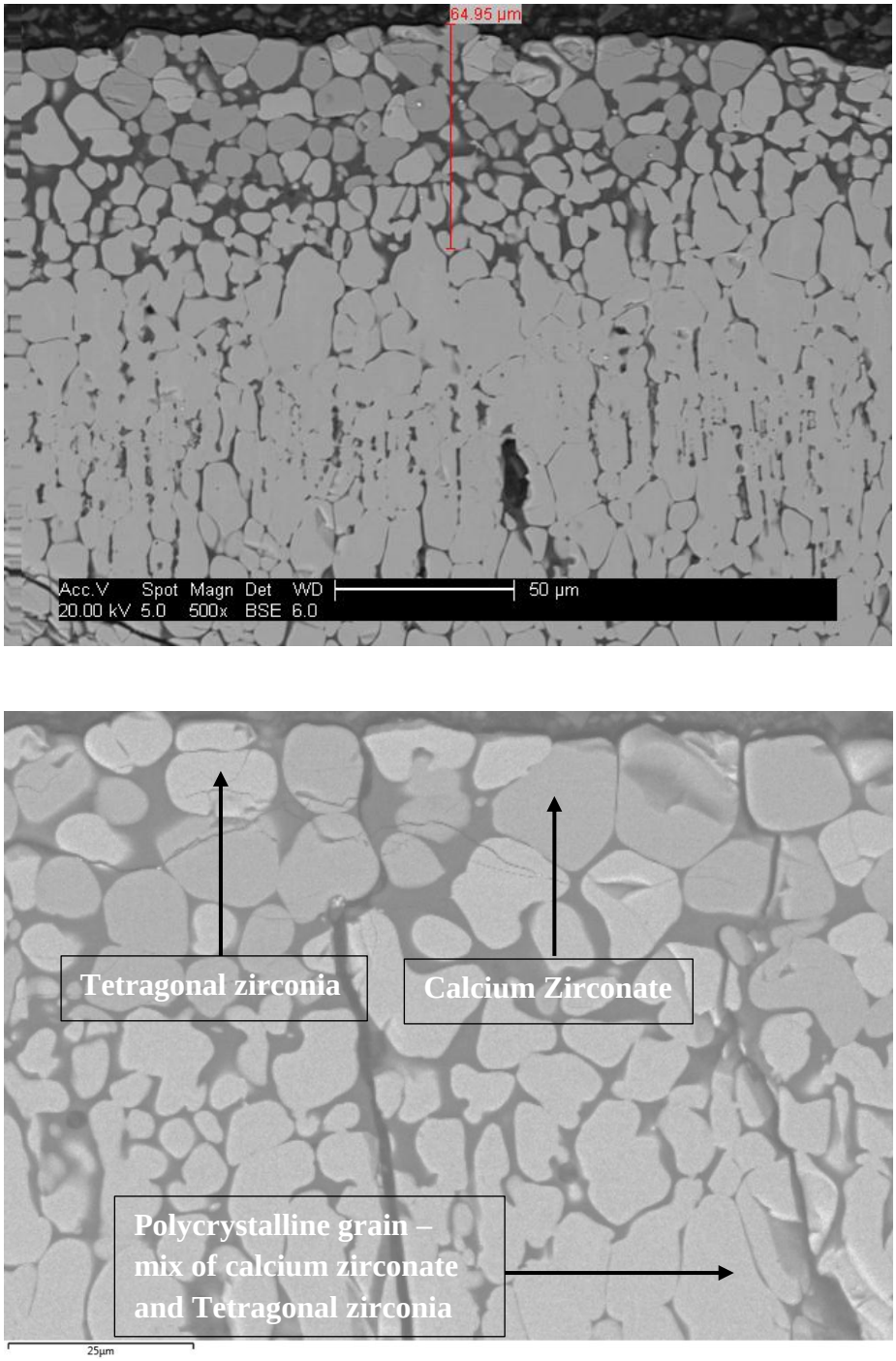

Figure 144: Polycrystalline structure of YSZ TBC infiltrated with High B.I. after 1 hour exposure at 1458 °C.

To further quantify the proportion of calcium zirconate grains formed within the overall TBC structure, EDAX elemental mapping was used. The maps in Figure 145 shows the resulting microstructures formed as a consequence of High B.I. infiltration of the PYSZ TBC.

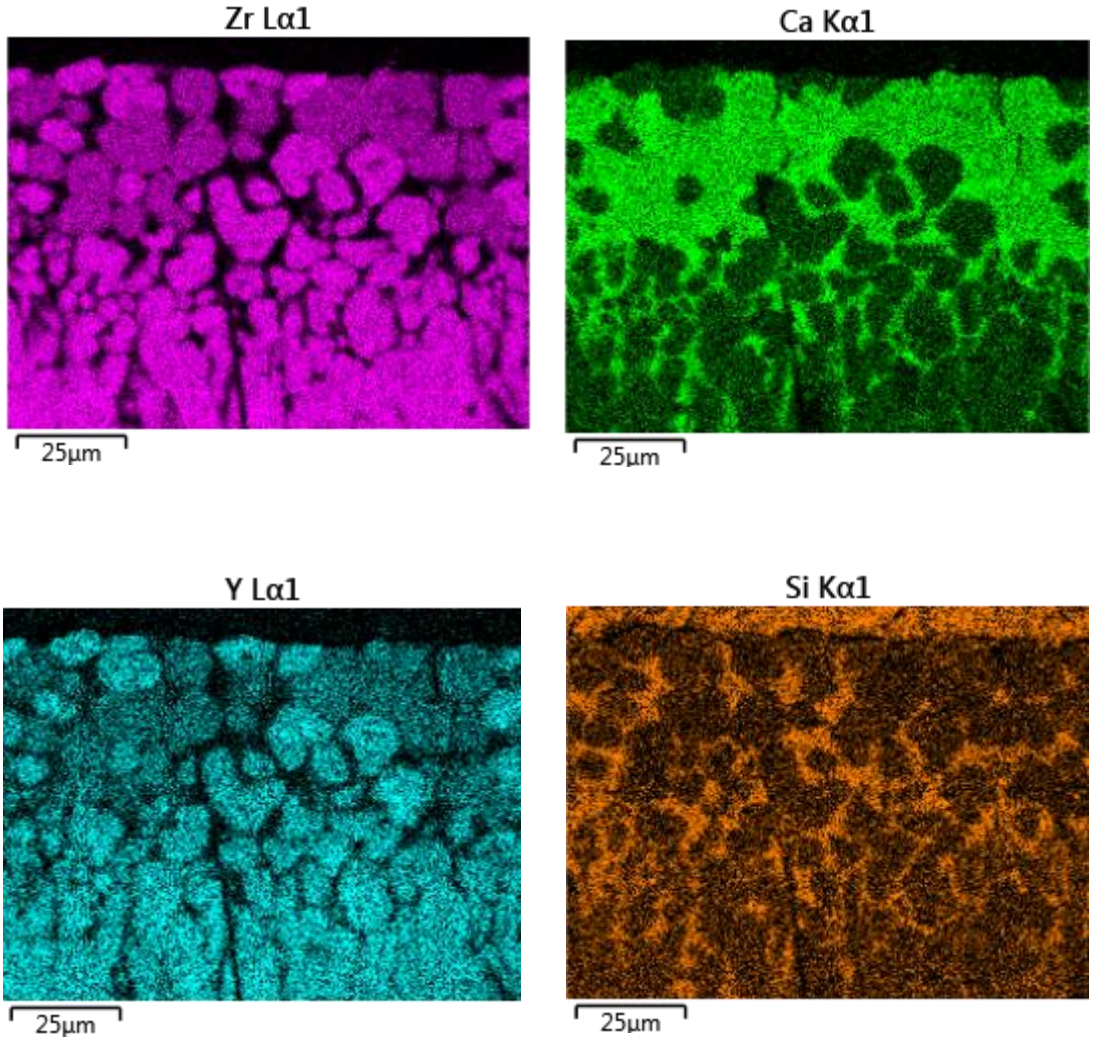

Figure 145: EDAX maps showing the presence of calcium zirconate structures after 1h exposure at 1458 °C.

The following conclusions can be made based on the images in Figure 145;

- Zr map showed three distinct regions; faint coloured zirconia depleted area, corresponding to calcium zirconate phase; very bright zirconia rich cells, indicating

tetragonal zirconia phase; and a mixture of bright and faint cells, suggesting a polycrystalline grain of partly calcium zirconate and partly zirconia.

- Ca map showed calcium to have diffused/penetrated the whole sample, especially in the grain boundaries where it was found to act as a binder for accelerating the sintering and diffusion rate.
- Yttria was shown to be severely depleted at the top of the coating, especially in calcium zirconate grains. However, there was no evidence of excess yttria diffusing into the surrounding melt, instead regions within the coating were found to contain significantly high yttria content (spectrums 17 and 18, Figure 147), ~9 at%, enough to fully stabilise the zirconia.
- Si map shows that Si does not penetrate into the cells of resulting microstructure of High B.I. attack, but is instead locked in the amorphous melt marix.

Calcium zirconate structures were further evident by performing EDAX layered analysis (Figure 146). As expected, the result confirmed the residual structure to be a polycrystalline structure, with detectable calcium zirconate at the upper transformation zone and t-zirconia in the rest of the coating. Unlike Low B.I. degradation, High B.I. does not result to a zirconia phase transformation, because of the cubic recrystallized calcium zirconate and also the fact that Ca is absorbed by the residual zirconia structure which together with Y_2O_3, stabilises the zirconia.

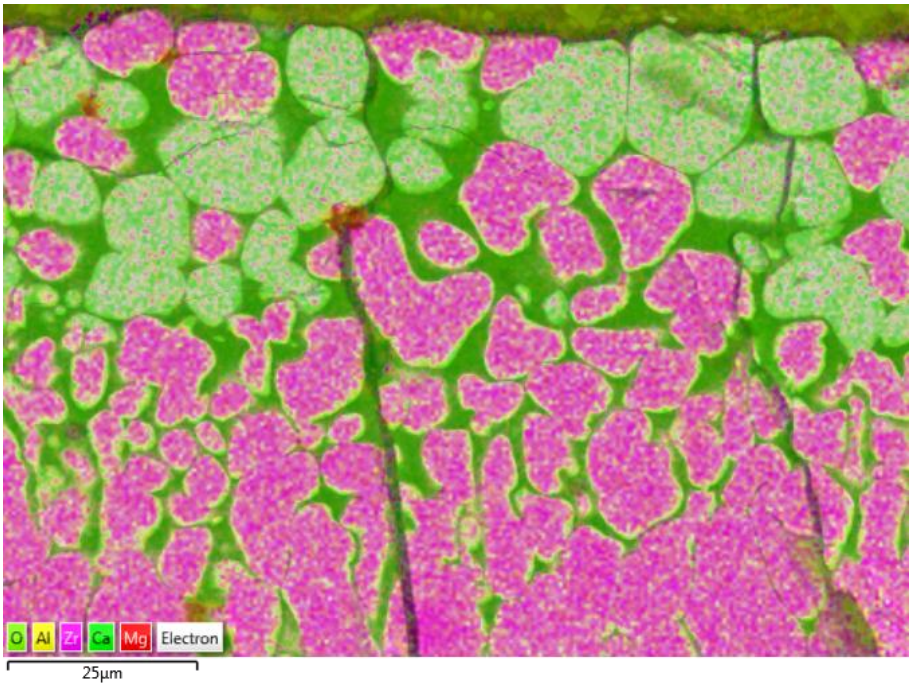

Figure 146: EDAX layered image analysis, showing calcium zirconate rich zone – 1h at 1458 °C

EDAX spot analysis was used to confirm the presence and composition of the various grains present within the structure. Similar to the result obtained after 30 minutes, calcium zirconate was confirmed but with a higher calcium content (spectrums 13-15, Figure 147). Also, it was noticed that the CaO and $YO_{1.5}$ value (~12 at%) was higher under these conditions, compared to 30 minutes analysis. EDAX analysis is shown in Figure 147.

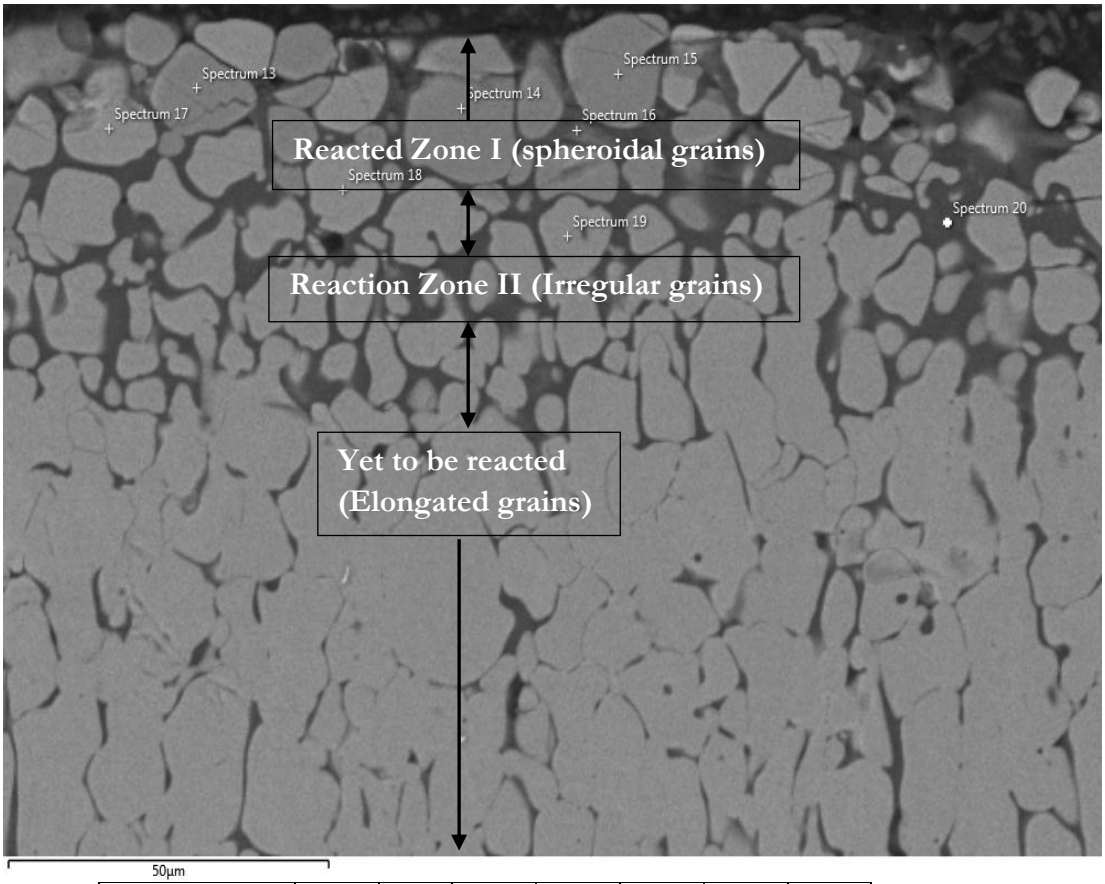

Spectrum	O	Mg	Al	Si	Ca	Y	Zr
Spectrum 13	36.0	0.4	0.3	0.0	32.8	1.6	28.9
Spectrum 14	34.4	0.2	0.5	0.0	32.9	2.7	29.2
Spectrum 15	36.0	0.4	0.3	0.0	31.9	2.7	28.7
Spectrum 16	50.1	1.4	10.0	6.6	16.8	1.2	14.0
Spectrum 17	40.3	0.5	0.6	0.0	8.5	8.5	41.6
Spectrum 18	40.8	0.5	0.6	0.0	8.2	9.0	41.0
Spectrum 19	41.8	0.9	0.2	0.0	9.7	5.2	42.3
Spectrum 20	38.5	0.1	21.7	10.3	26.8	0.5	2.1

All results in atomic%

Figure 147: High B.I. sample after 1h at 1458 °C, showing composition of calcium zirconate and calcium-absorbed YSZ cells.

EDAX analysis of the entire sample was also performed, to evaluate microstructural changes. The results showed that a substantial amount of Ca had been absorbed into the newly formed cells, and also there was absolutely zero Si in the residual cell structures, instead it is trapped

in the melt matrix. As can be seen from the analysis in Figure 145, Figure 147 and Figure 148, SiO_2, MgO and Al_2O_3 do not influence the composition of the residual structure. However, they are locked in phases in the reacted CMAS matrix as well as formed a melt pool at the bottom.

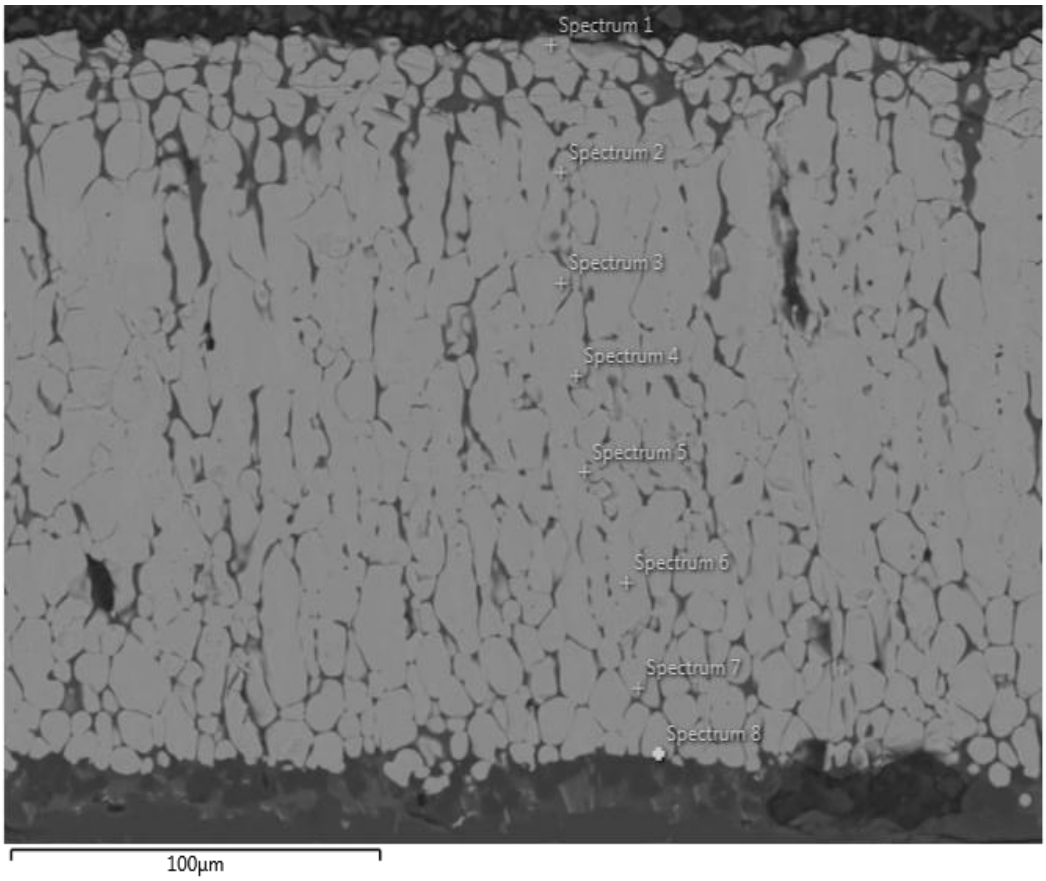

Spectrum	O	Mg	Al	Si	Ca	Y	Zr
Spectrum 1	61.2	0.3	0.5	0.0	6.8	1.6	29.6
Spectrum 2	60.7	0.3	0.3	0.0	5.2	2.4	31.0
Spectrum 3	62.0	0.3	0.8	0.0	4.9	2.3	29.8
Spectrum 4	54.8	0.4	1.4	0.0	5.7	3.1	34.7
Spectrum 5	60.6	0.4	0.5	0.0	4.8	2.9	30.9
Spectrum 6	60.6	0.2	0.5	0.0	4.0	3.0	31.7
Spectrum 7	59.7	0.3	6.1	2.2	8.6	2.2	20.9
Spectrum 8	57.6	0.2	0.5	2.6	4.7	3.1	31.4

All results in atomic%

Figure 148: EDAX analysis of residual structure, 1 hour at 1458 °C

8.3 Two Hours Exposure at 1458 °C

These samples appear to have suffered more severe damage than in previous experiments (30 minutes and 1 hour) in this category. The damage mechanism was similar to those observed in the 30 minutes and one hour experiments, only difference being that the damage severity increases with time, hence samples exposed for two hours were shown to have an increased transformation zone in both directions. Characteristic calcium zirconate and t-zirconia polycrystalline structure was also found. However, a new feature was identified after two hours exposure at this category. Because of the aggressive nature of High B.I. melt, it was noticed that this sample has undergone second stage recrystallization, seen in Figure 149, especially obvious at the bottom of the coating in contact with the melt pool.

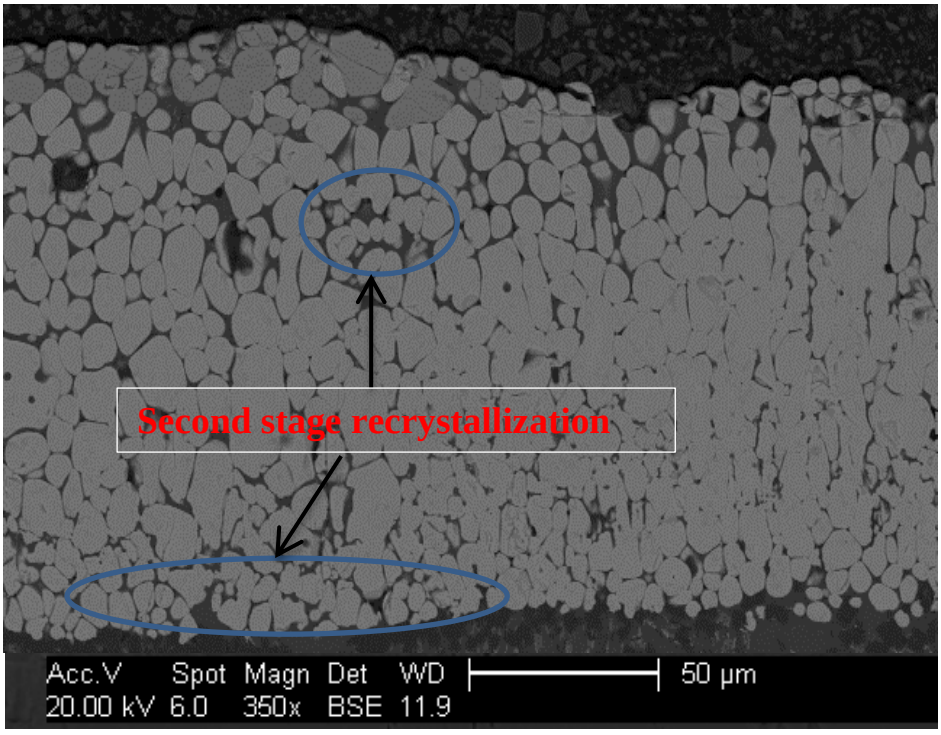

Figure 149: Second stage recrystallization after 2h exposure at 1458 °C with High B.I. melt.

As well as severely degraded the entire TBC, High B.I. deposit showed substantial attack of the alumina substrate after two hours of exposure. This was caused by the aggressive nature of the High B.I. deposit, destabilizing the substrate while aluminium diffused into solution.

The melt then becomes rich in Al forming $CaO\text{-}SiO_2\text{-}Al_2O_3$ rich phases along the grain boundaries and at the bottom of the TBC. Certain features were also identified between the TBC/substrate interface of which the melt pool is sandwiched in between, as demonstrated in Figure 150 shows the features identified in this category of attack.

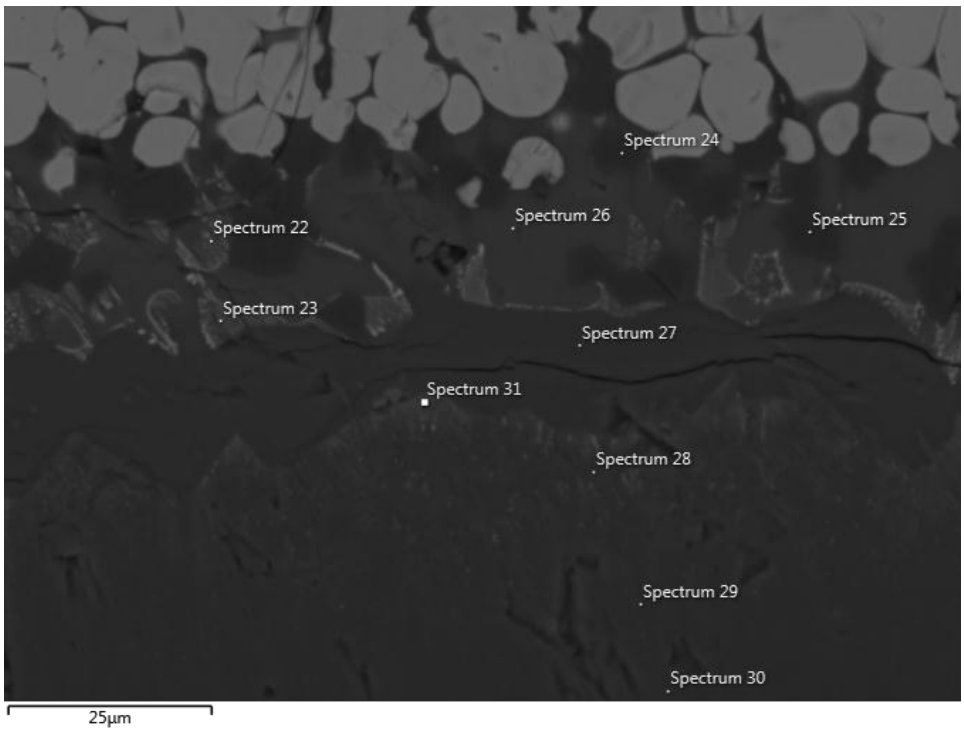

Spectrum	O	Mg	Al	Si	Ca	Y	Zr
Spectrum 22	35.8	0.1	16.2	7.7	25.1	1.2	14.0
Spectrum 23	35.2	0.2	17.5	8.8	28.1	1.2	9.1
Spectrum 24	41.5	16.2	41.9	0.1	0.3	0.0	0.0
Spectrum 25	41.4	16.5	41.4	0.2	0.0	0.0	0.0
Spectrum 26	37.4	0.1	20.4	9.7	30.5	2.0	0.0
Spectrum 27	39.7	0.3	42.3	0.4	17.4	0.0	0.0
Spectrum 28	41.6	1.4	39.1	3.2	10.9	0.2	3.7
Spectrum 29	42.0	0.7	48.1	0.7	7.3	0.0	1.2
Spectrum 30	42.0	0.6	48.5	0.6	7.3	0.0	0.9
Spectrum 31	36.1	0.5	22.7	8.1	25.6	1.0	6.1

All results in atomic%

KEY

YSZ leached in melt pool

Spinel ($MgAl_2O_3$)

Ca, Si YAG

Calcium aluminate layer

Substrate infiltrated by CMAS. Alumina purity increases downward

Figure 150: Features identified for two hours heat treatment at 1458 °C with High B.I. deposits.

These features were further confirmed by performing an EDAX elemental mapping on the sample. The results are shown in Figure 151 where it can be seen from the Zr map that TBC has dissolved and migrated into the melt pool, resulting in CMAS + TBC patches. Also noticed were assorted spinel phases as shown on the Mg map. A band can be seen from Si and Zr maps, showing deficiency of both elements within the band. However, from Ca and Al maps, it can be concluded that this band is a calcium-aluminium rich layer. EDAX spot analysis further confirmed this to possibly be a calcium aluminate.

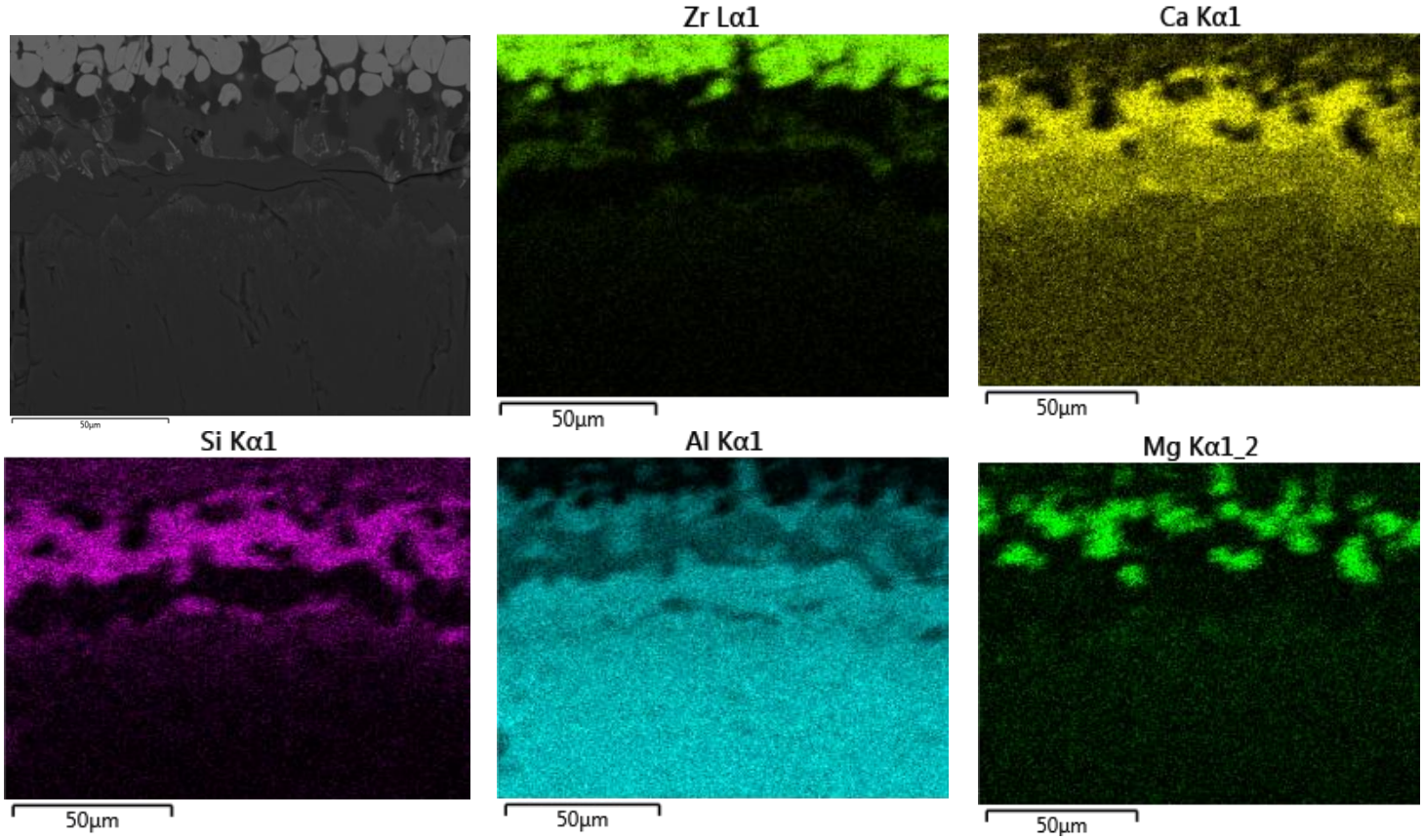

Figure 151: EDAX mapping of High B.I. sample after two hours at 1458 °C, revealing the features formed with this category of attack.

The various features identified can be summarized in the image on Figure 152. The identification of these features is based upon the analytical techniques mentioned (EDAX mapping, spot analysis and EBSD) previously.

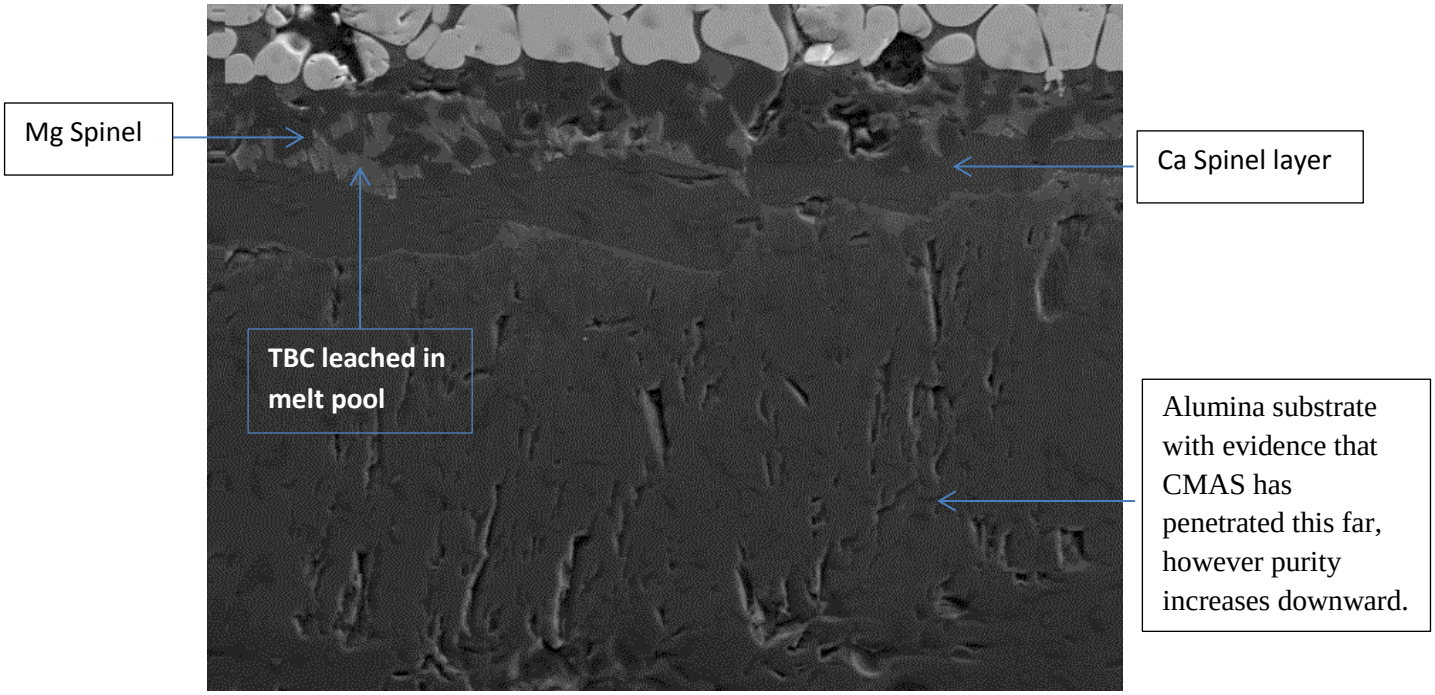

Figure 152: Summary of features identified after two hours heat treatment at 1458 °C with High B.I.

8.4 Four Hours Exposure at 1458 °C

Similar to two hours exposure, evidence of second stage recrystallization was particularly evident for the four hours sample, especially in the upper half of the TBC. There was little evidence of second stage recrystallization at the lower half of the TBC, where the new grains were much larger than that observed after two hours indicating a transition from second stage recrystallization towards grain growth. Also, the entire structure showed thorough all through transformation, as can be seen from Figure 153.

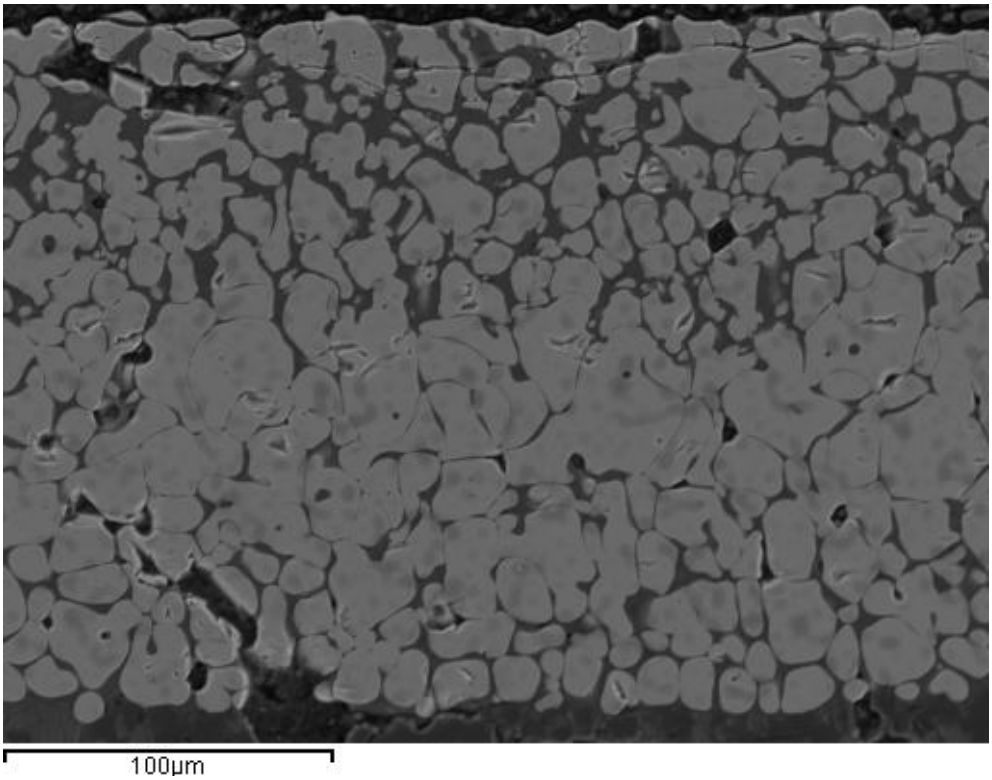

Figure 153: Resulting microstructure of 4h exposure at 1458 °C with High B.I. showing thorough all through transformation.

As was observed during two hours of heat treatment, there were also intense activities at the base of the TBC which resulted in similar features being identified in the two hour experiment. EDAX spot analysis was also used to study the composition of the newly formed grains in this category. A characteristic of Near Neutral and High B.I. degradation mechanism is the customary role of MgO, Al_2O_3 and SiO_2 from the deposit, playing an inert role in the composition of the residual microstructure. As can be seen from the micrograph in Figure 154, the CaO + $YO_{1.5}$ value in this category was ~ 13-14 at%, again preventing a monoclinic phase transformation.

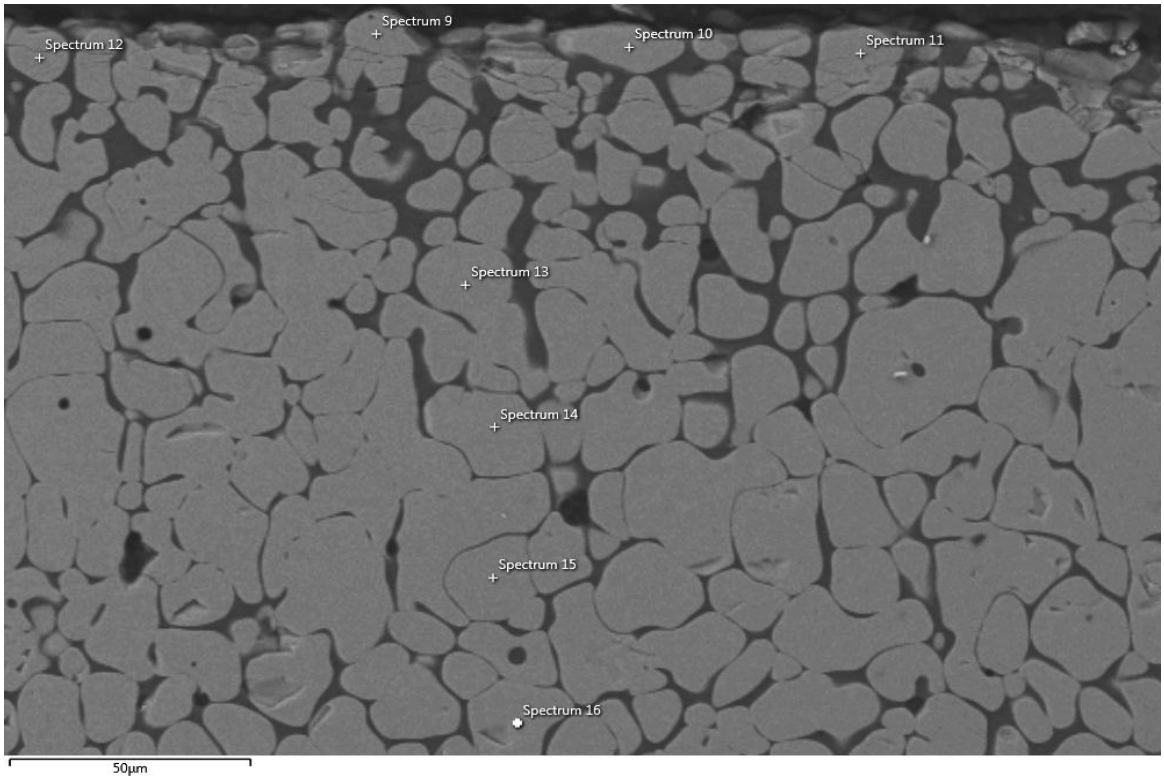

Spectrum	O	Mg	Al	Si	Ca	Y	Zr
Spectrum 9	35.6	0.5	1.1	0.0	10.2	6.3	46.5
Spectrum 10	37.7	0.7	0.4	0.0	8.9	4.3	47.9
Spectrum 11	37.0	0.2	0.4	0.0	8.3	6.3	47.7
Spectrum 12	38.2	0.7	0.6	0.0	8.2	5.7	46.5
Spectrum 13	40.2	0.5	0.6	0.0	8.4	5.8	44.5
Spectrum 14	40.5	0.7	0.6	0.0	7.8	5.7	44.8
Spectrum 15	39.7	0.5	1.0	0.0	7.7	5.2	45.8
Spectrum 16	40.5	0.7	0.8	0.0	7.4	5.7	44.9

All results in atomic%

Figure 154: Composition of residual structure after 4h heat treatment with High B.I. at 1458 °C having highest $CaO + YO_{1.5}$ content.

8.5 Eight Hours Exposure at 1458 °C

The attack morphology is very similar to that observed with the four hours exposure sample. Second stage recrystallization was minimal at the upper half of the coating, with the structure showing mainly a transition to grain growth while the bottom half is comprised of grain transformation zone. Anchored in between the upper and lower parts of the coating are large

irregularly shaped grains which analysis showed to be rich in calcium content. A new feature was identified under these conditions, as shown in Figure 155.

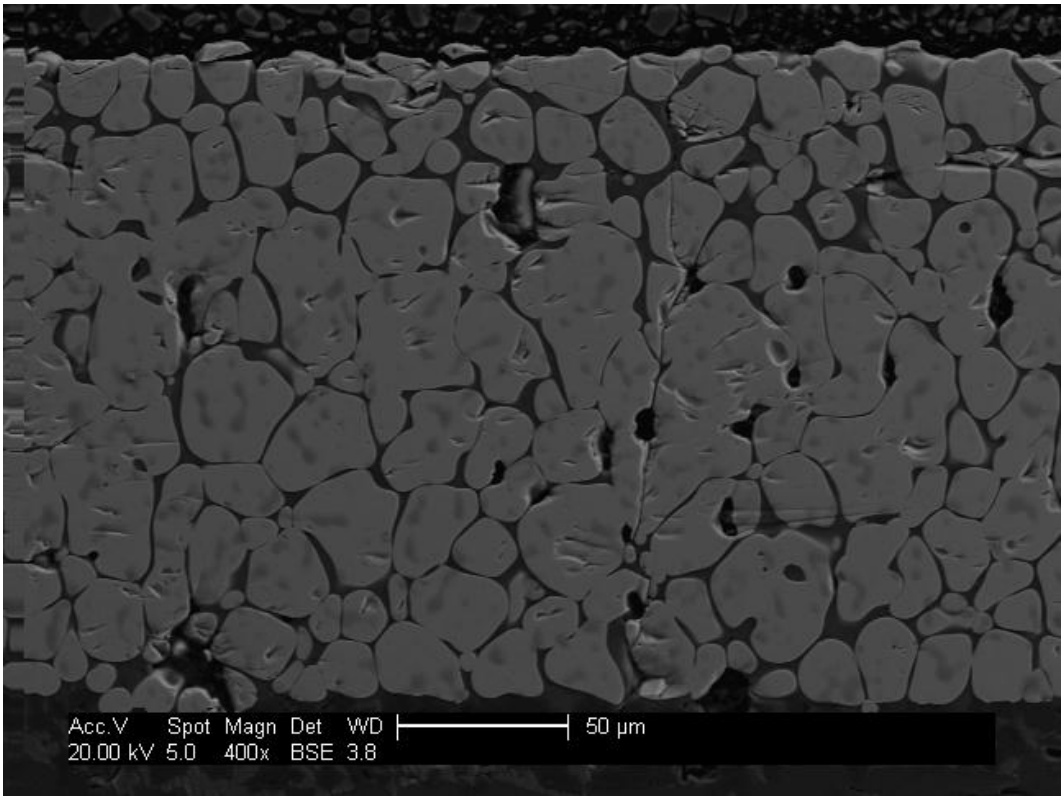

Figure 155: Eight hours exposure with High B.I. showing thorough all through transformation and a solidified new phase at 1458 °C.

As expected with High B.I. attack chemistry, High B.I. interaction showed a very aggressive attack at the TBC/substrate interface and followed through to the substrate. The features identified at the base of the TBC and the substrate can be seen on Figure 156.

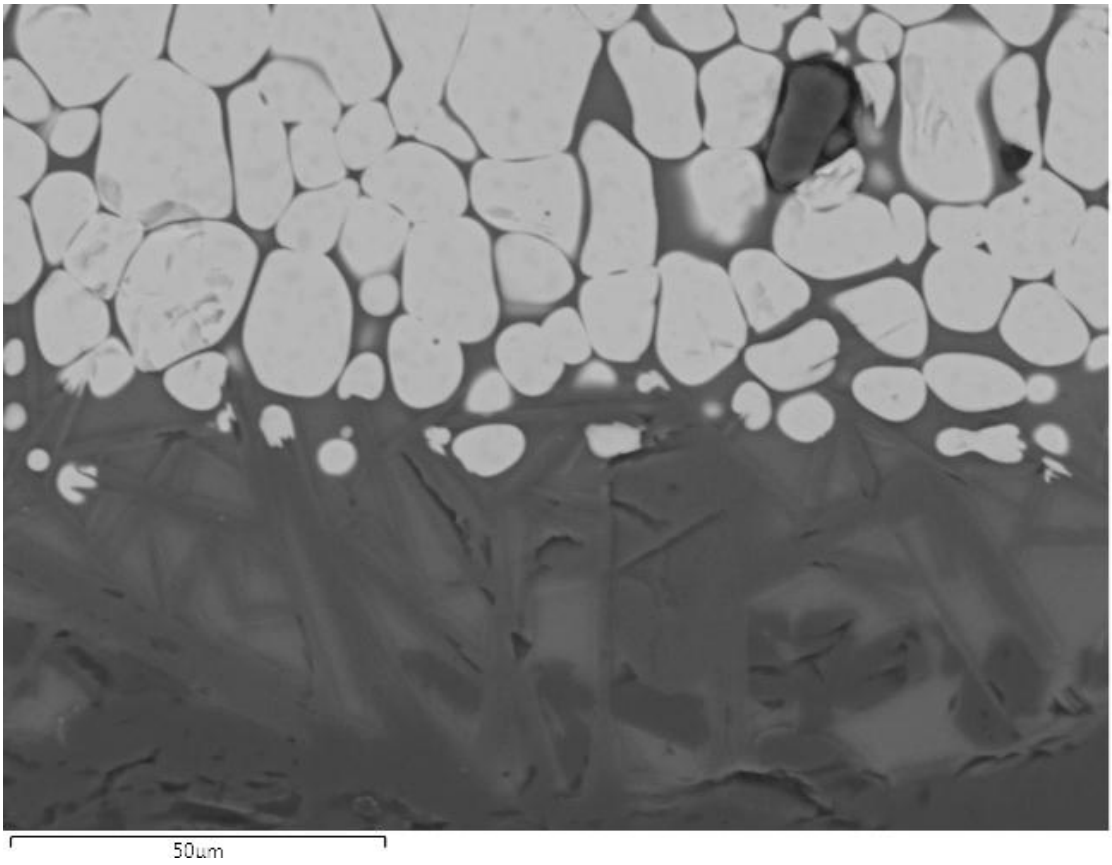

Figure 156: 8h at 1458 °C High B.I. samples showed similar features as identified with 4h sample.

It was also noticed that significant amounts of zirconia were entrapped in the melt in certain regions of the sample, as shown in Figure 157. Elemental analysis revealed this phase to be rich in Ca (16 at%), Zr (27 at%) and Al (9 at%), as well as high Y content (3 at%) in the melt compared to starting composition. This is an indication that, due to the aggressive nature of High B.I. deposits, the TBC is dissolved in the melt and later recrystallizes where it can either form calcium zirconate or Ca doped YSZ, depending on the local melt chemistry. The highlighted spectrum 2 in Figure 157 is an EDAX spot analysis of what was previously a zirconia grain partly dissolved in the local Ca-rich melt that has recrystallized to a calcium zirconate structure.

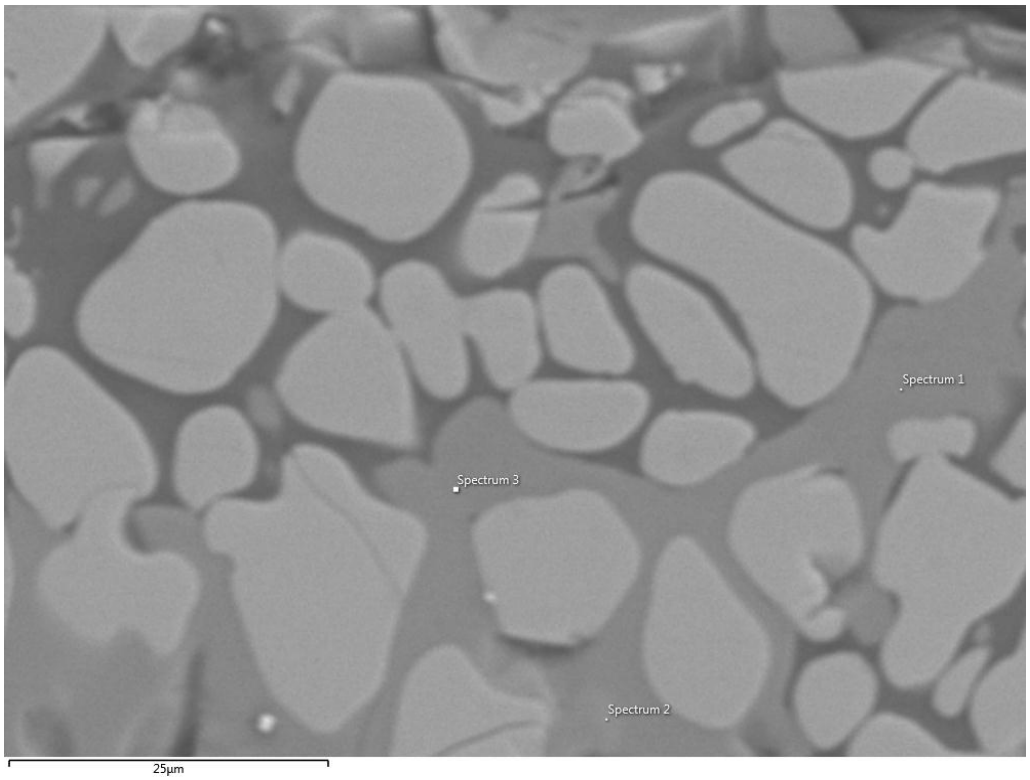

Spectrum	O	Mg	Al	Si	Ca	Y	Zr
Spectrum 1	37.7	0.2	15.9	4.9	24.2	2.3	14.9
Spectrum 2	**42.2**	**0.2**	**9.3**	**1.9**	**16.2**	**3.3**	**27.0**
Spectrum 3	37.1	0.2	15.8	5.0	24.8	2.3	14.8

All results in atomic%

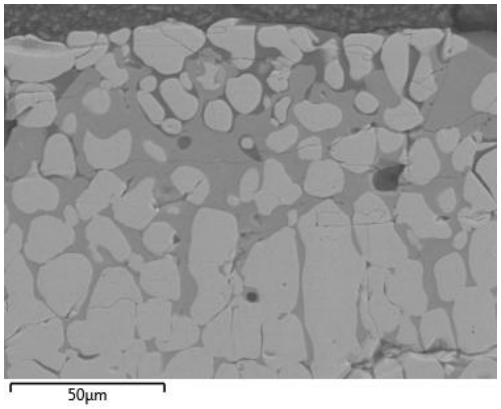

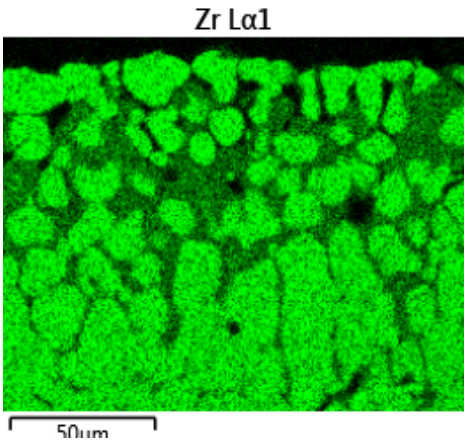

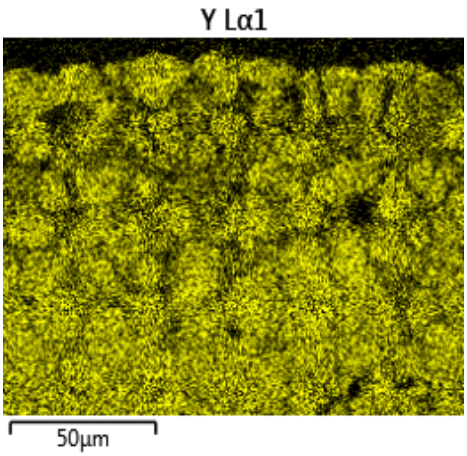

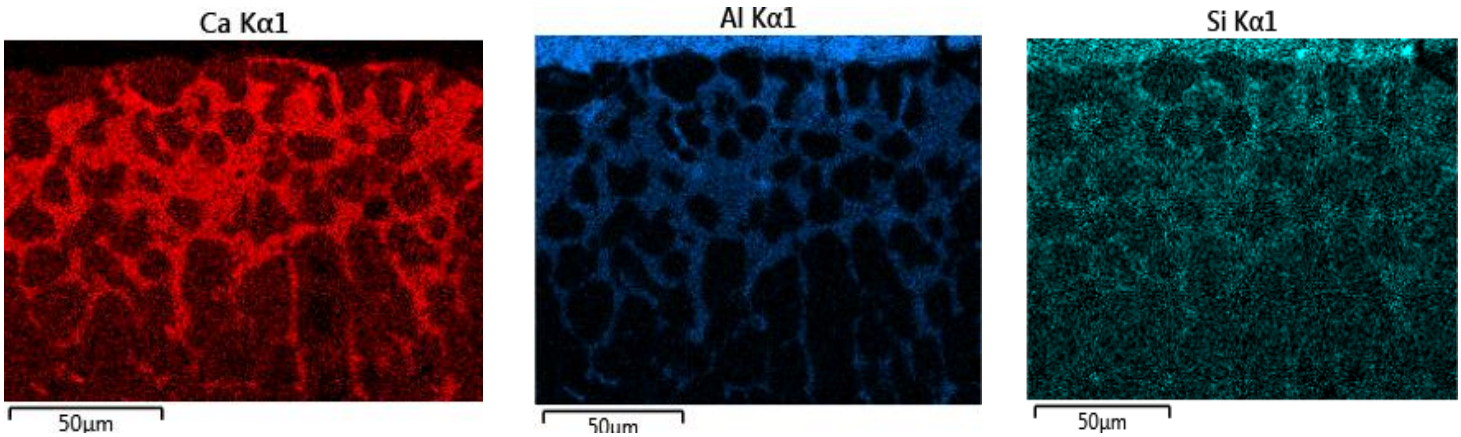

Figure 157: 8h at 1458 °C – evidence of TBC locked in CMAS between grain boundaries.

EDAX spot analysis was also performed on the newly formed grains, on both small and large grains to determine whether or not there is a compositional effect. As has been seen so far herein, MgO, Al_2O_3 and SiO_2 continue to play an inert role in the composition of the resulting structure, as confirmed in the analysis on Figure 158. The Ca content in the smaller grains was found to be less than that in the larger grains.

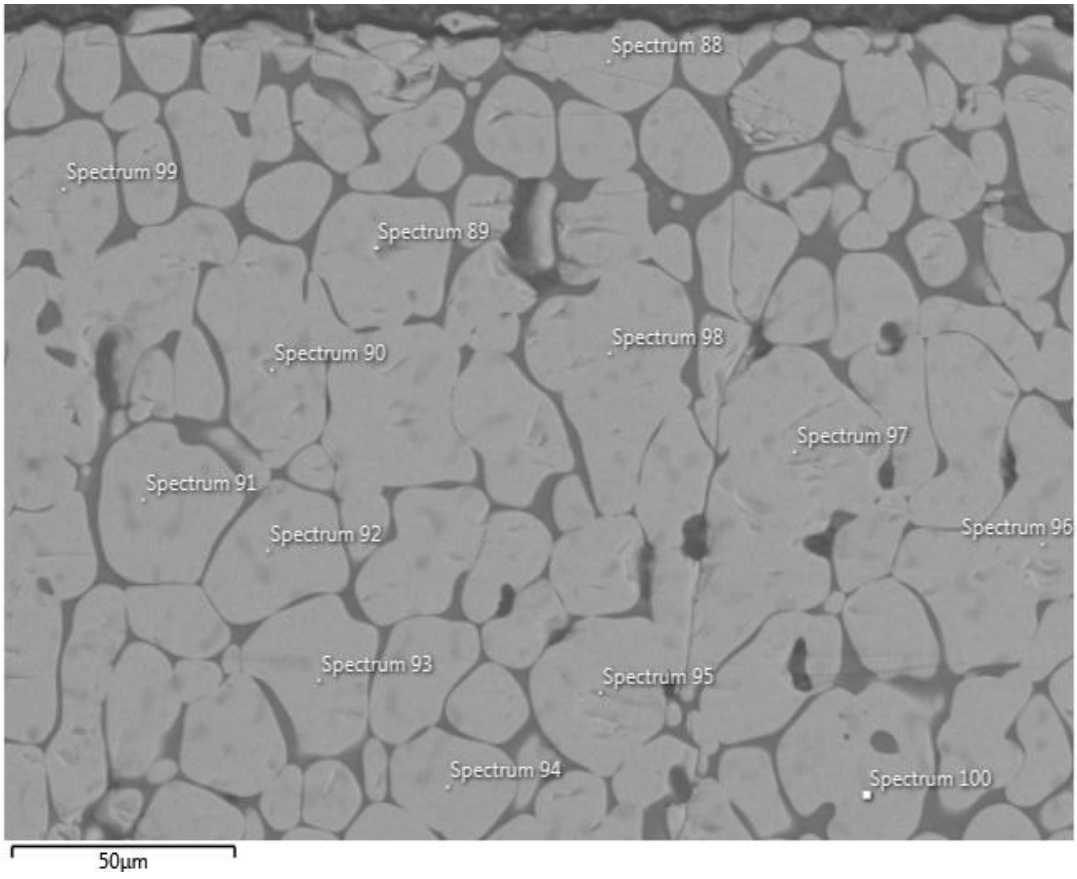

Spectrum	O	Mg	Al	Si	Ca	Y	Zr
Spectrum 88	59.0	0.5	0.6	0.0	5.6	3.6	30.6
Spectrum 89	34.9	0.7	1.3	0.0	9.1	5.8	48.1
Spectrum 90	68.6	0.5	0.4	0.0	4.1	2.8	23.6
Spectrum 91	62.2	0.3	0.5	0.0	4.6	3.5	29.0
Spectrum 92	63.4	0.3	0.6	0.0	4.4	3.3	28.0
Spectrum 93	62.5	0.5	0.5	0.0	4.5	3.6	28.4
Spectrum 94	62.7	0.3	0.2	0.0	4.4	3.5	28.9
Spectrum 95	53.2	0.4	0.7	0.0	6.1	4.3	35.3
Spectrum 96	62.4	0.3	0.3	0.0	4.3	3.5	29.1
Spectrum 97	61.5	0.5	0.3	0.0	4.8	3.4	29.5
Spectrum 98	62.0	0.5	0.3	0.0	4.8	3.5	29.0
Spectrum 99	62.7	0.2	0.5	0.0	4.6	3.3	28.8
Spectrum 100	62.0	0.3	0.3	0.0	4.6	3.8	28.9

(a)

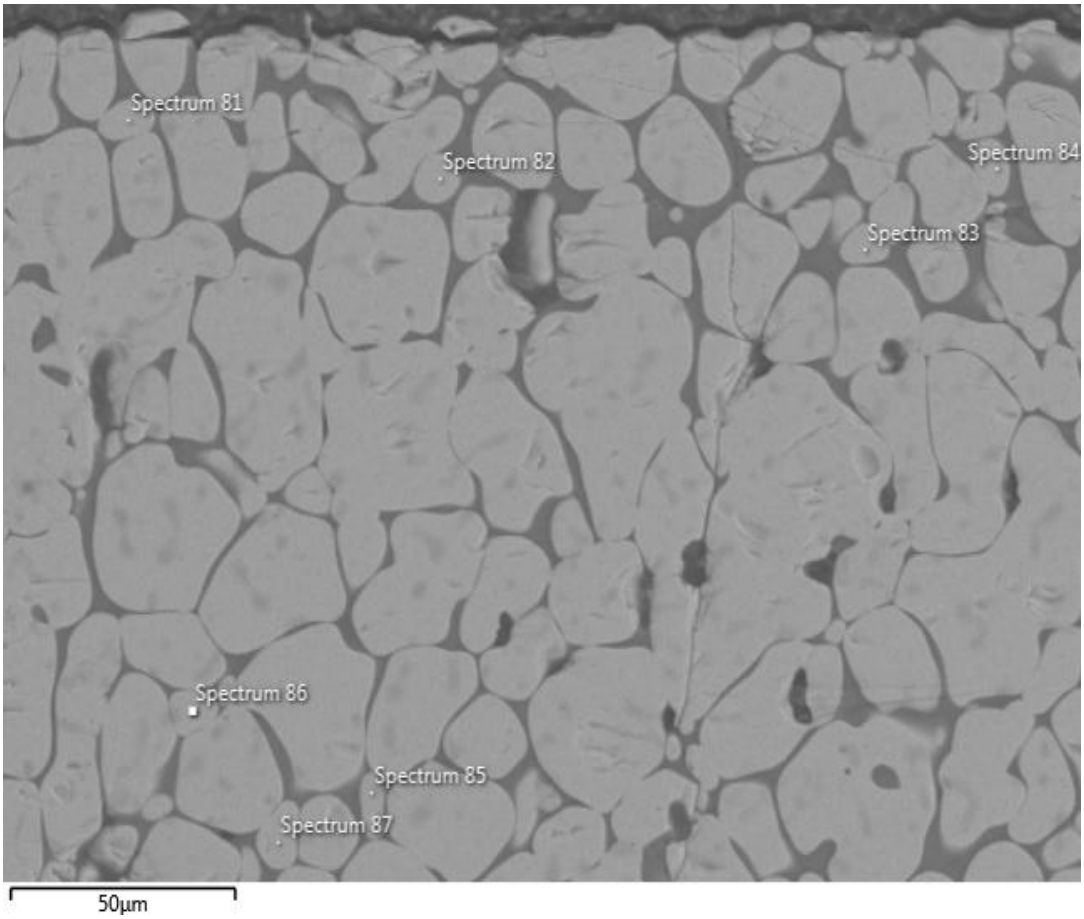

Spectrum	O	Mg	Al	Si	Ca	Y	Zr
Spectrum 81	63.3	0.5	0.6	0.0	3.8	3.5	28.3
Spectrum 82	62.7	0.2	0.5	0.0	4.1	3.6	28.9
Spectrum 83	63.2	0.3	0.3	0.0	4.0	3.1	29.0
Spectrum 84	63.5	0.3	0.5	0.0	4.2	3.3	28.3
Spectrum 85	62.4	0.3	0.8	0.0	4.3	3.2	29.0
Spectrum 86	63.9	0.5	0.3	0.0	4.4	3.0	27.8
Spectrum 87	63.6	0.3	0.5	0.0	4.4	3.1	28.1

All results in atomic%

(b)

Figure 158: High B.I. 8h exposure at 1458 °C analysis on (a) large and (b) small grains.

The melt pool has shown in this category to attack the alumina substrate, due to the aggressive nature of High B.I. deposits and leached out excess aluminium into the melt. It was paramount to investigate this occurrence in order to understand the possible attack mechanism taking place. By increasing the B.I. of the CMAS used to High B.I. regime, penetration of the melt into the substrate was noticed, severely destabilising the alumina

substrate and releasing aluminium into the melt. This indicates that High B.I. could potentially cause problems to the TGO and may interact with the bond coat. Therefore an understanding of the behaviour of High B.I. CMAS with TBC bond coat maybe necessary, although bond coats are not design to operate under such temperature so molten deposits interacting with bond coat may induce a new failure mode.

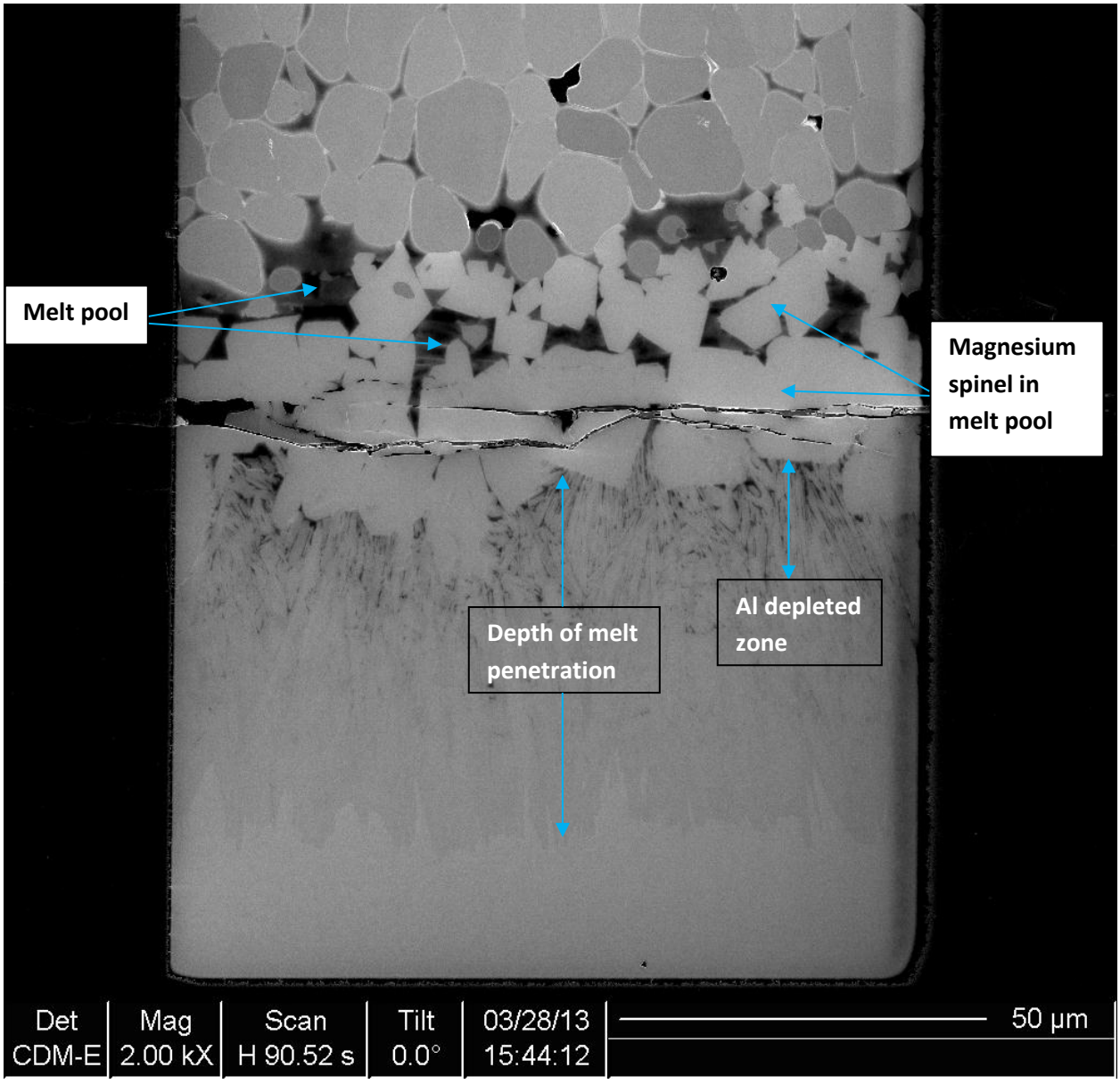

Figure 159: FIB image of High B.I. sample exposed for 1h at 1458 °C, showing penetration of the molten CMAS in the alumina substrate

Figure 159 shows significant penetration of the melt into the alumina substrate after just one hour exposure, in turn destabilising the substrate. It has been shown in this study that the time taken for High B.I. deposits to form a melt pool can be as quick as <30 minutes. It can be inferred from Figure 159 that, once High B.I. melt penetrates to the bottom of TBC due to thermodynamics effect (i.e. viscosity), then almost instantly it starts to attack the alumina substrate, creating an aluminium depleted zone in the substrate. Also noticeable is the magnesium spinel phases formed at the bottom of the coating, sitting on the surface of the substrate. The depth of penetration of the melt was measured at ~50 μm into the substrate, which is significantly greater than the TGO thickness (< 10 μm). This implies High B.I. attack is likely to result in the destruction of the TGO and potentially causing thermal and/or chemical damage to the bond coat.

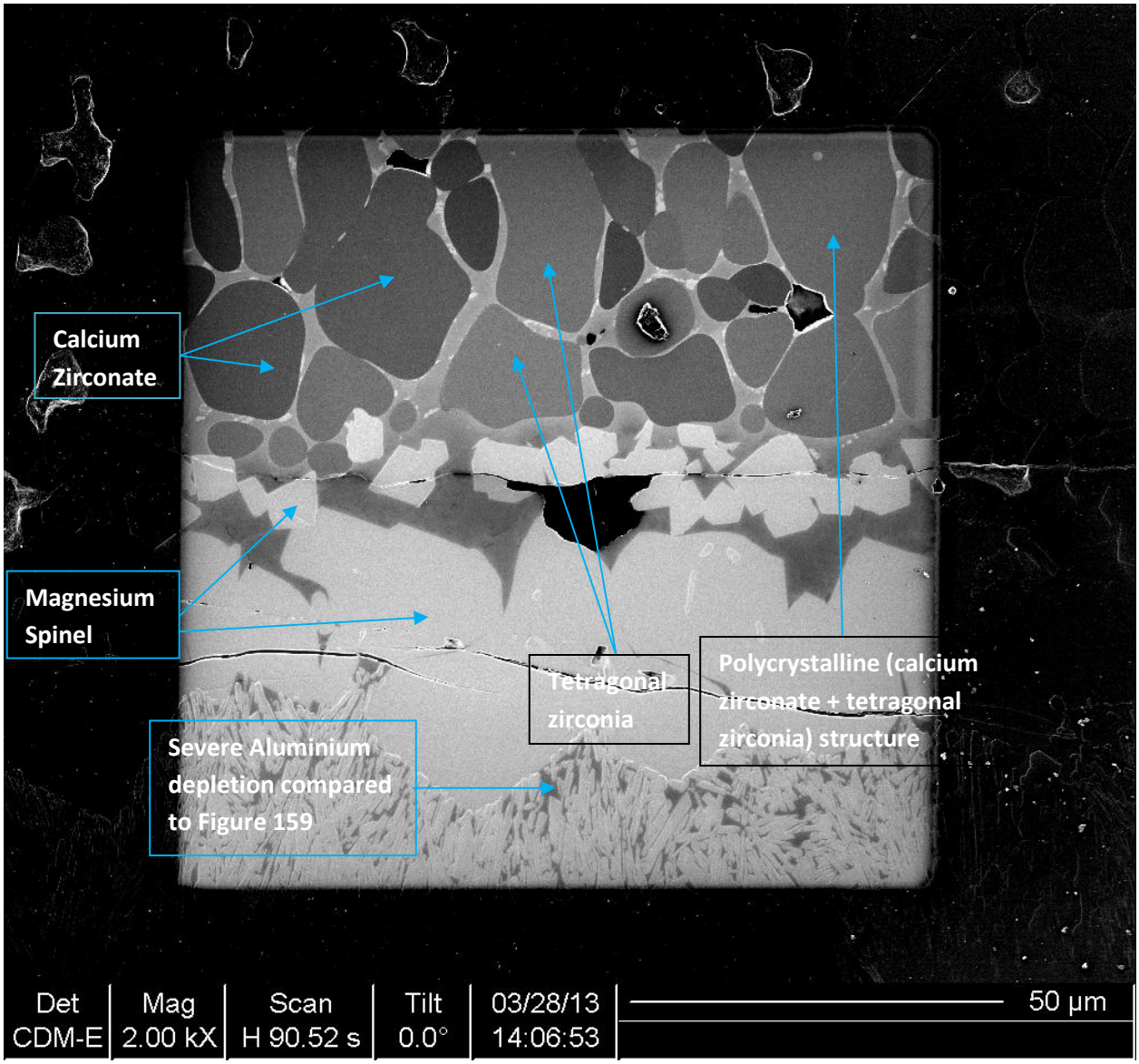

Figure 160: FIB image of High B.I. sample exposed for 4h at 1458 °C, showing higher loss of Al_2O_3

The severity of damage to the substrate was found to increase with increasing the exposure time (Figure 160), with Al diffusing from the Al_2O_3 substrate into the melt pool, creating a gradient within the substrate which is suggestive of a diffusion mechanism. The result of this inter-diffusion is an Al depleted zone formed nearer to the melt pool (labelled in Figure 160). The colour contrast identifies different phases formed as a result of High B.I. attack, as illustrated on the image in Figure 160.

8.6 Free-Standing TBC Eliminating the Effect of Excess Aluminium Leached out from the Substrate

High B.I. degradation of free-standing PYSZ TBC samples showed similar morphology to the High B.I. categories observed earlier in this study. The morphology of attack is characterised by microstructural transformation from columnar to spherical shaped, recrystallized zirconia (Figure 161), rich in calcium content. The microstructural transformation of PYSZ attack by High B.I. deposit showed similar features to Near Nuetral attack, with High B.I. microstructure showing larger, rounded grains with more CaO content compared to Near Neutral sample. This is an indication that, their degradation mechanism maybe similar but with different severity, with High B.I. deposits being more aggressive than its Near Neutral counterpart.

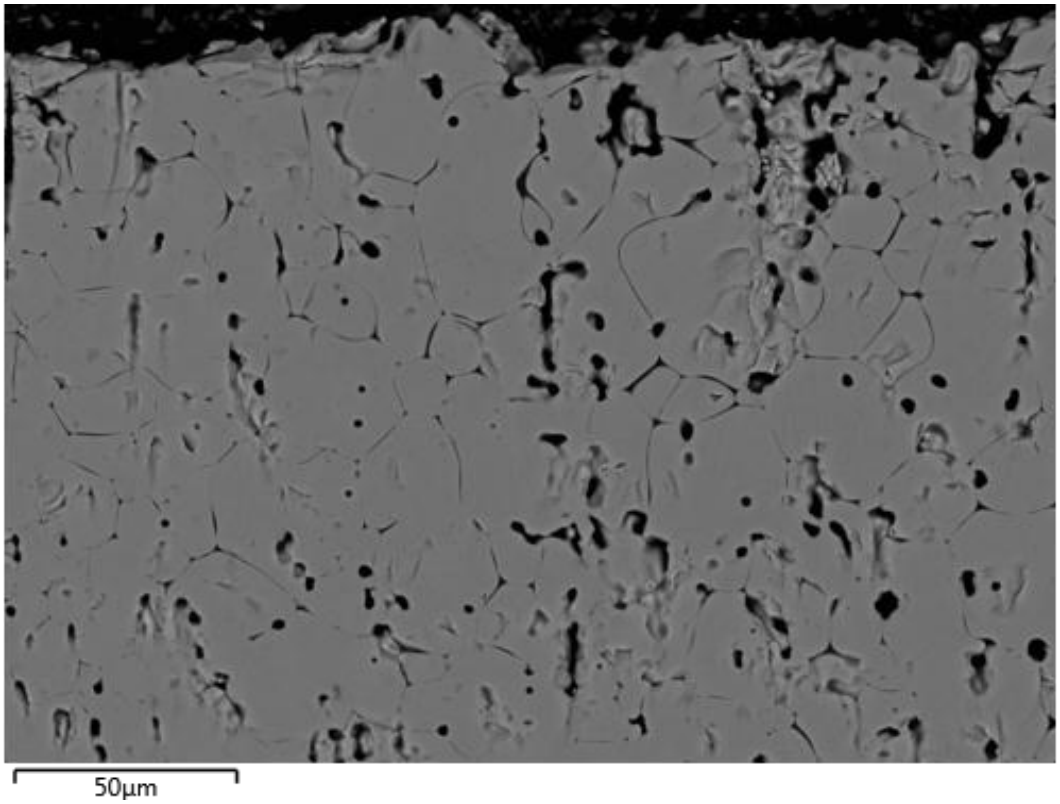

Figure 161: Free-standing TBC samples sprayed High B.I. deposits for 4h, showing rounded grains similar to Near Neutral sample.

EDAX spot analysis of High B.I. free-standing sample showed that the amount of calcium absorbed into the recrystallized grains is higher than for the Near Neutral sample. As it has become accustomed with Near Neutral and High B.I. attack, MgO, Al_2O_3 and SiO_2 played no reactive part in the degradation mechanism and this was further confirmed by the results shown in Figure 162, which is that of using free-standing samples. Again, the ($CaO + YO_{1.5}$) content was found to be higher compared with Near Neutral sample, averaging about 10 at%. This explains why High B.I. samples have bigger fragmented grains than Near Neutral B.I. microstructure, and also the reason there is the lack of monoclinic zirconia in the resultant TBC structure, irrespective of a substrate interface.

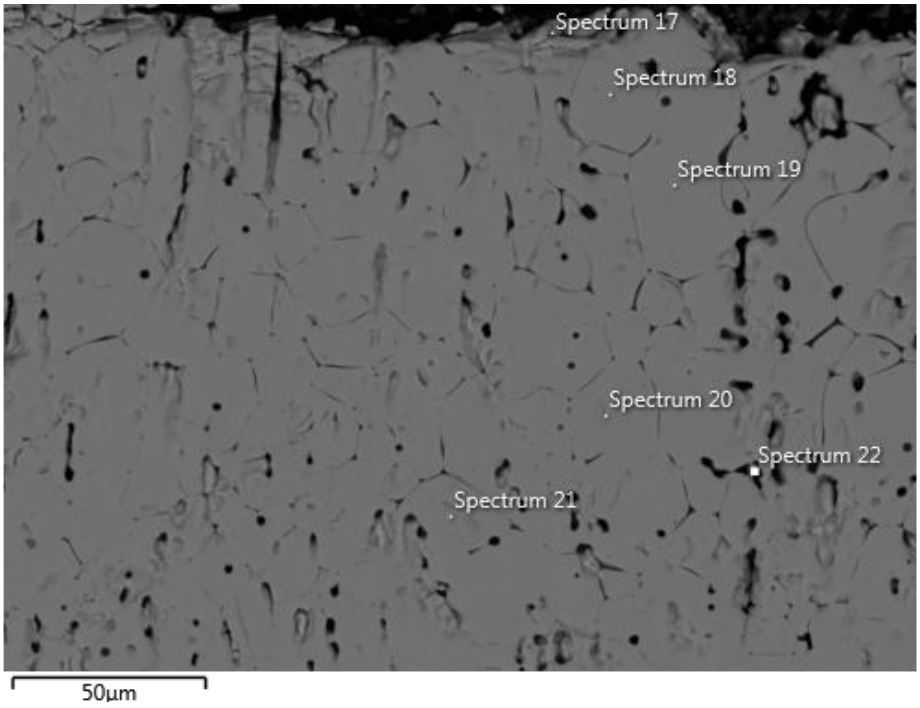

Spectrum	O	Mg	Al	Si	Ca	Y	Zr
Spectrum 17	34.1	0.0	7.0	0.4	6.6	4.6	47.3
Spectrum 18	58.5	0.5	0.2	0.0	5.1	3.2	32.6
Spectrum 19	59.1	0.5	0.0	0.0	5.2	3.2	31.9
Spectrum 20	63.1	0.7	0.2	0.0	4.3	2.4	29.4
Spectrum 21	56.7	0.9	0.0	0.0	3.8	3.0	35.5
Spectrum 22	69.5	0.6	0.3	0.0	3.5	2.3	23.9

All results in atomic%

Figure 162: Analysis of High B.I. free-standing TBC after 4h at 1458 °C, showing high ($CaO + YO_{1.5}$) content.

Another characteristic of High B.I. attack mechanism is the formation of calcium zirconate, which is very much a distinct feature with High B.I. attack as mentioned previously in the High B.I. degradation mechanism. Calcium zirconate was also noticed in the free-standing High B.I. sample after four hours of heat treatment. Spectrums 9-12 shown on Figure 173 confirm the presence of the calcium zirconate phase in High B.I. free-standing category.

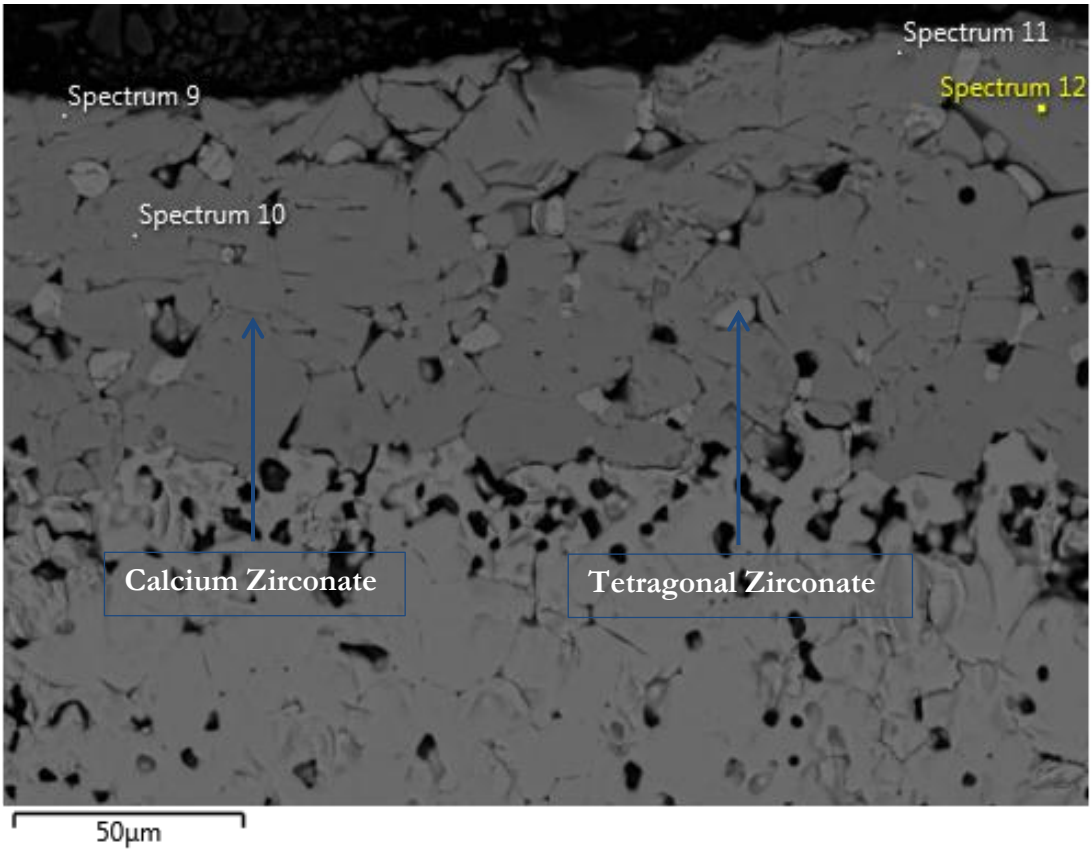

Spectrum	O	Mg	Al	Si	Ca	Y	Zr
Spectrum 9	55.3	0.3	0.3	0.0	21.9	0.4	21.7
Spectrum 10	53.5	0.2	0.3	0.0	22.7	0.7	22.7
Spectrum 11	50.6	0.2	0.3	0.0	24.9	0.3	23.7
Spectrum 12	53.9	0.3	0.0	0.0	23.4	0.0	22.4

All results in atomic%

Figure 163: Free-standing TBC with High B.I. deposit after 4h at 1458 °C confirming calcium zirconate transformation.

8.7 Mechanism of Attack

Due to the aggressive nature of High B.I. deposits, substantial amount of Al_2O_3 was detected in the upper interaction zone of the coating after just 30 minutes of heat treatment, suggesting that the molten deposit had formed a melt pool after only 30 minutes resulting in severe attack of the alumina substrate. The amount of Al_2O_3 detected here was comparable to that found in the melt pool of Near Neutral sample after one hour heat treatment. The amount of

excess Al_2O_3 is expected to be greater in the melt pool than anywhere else in the coating. Figure 164 shows very high Al_2O_3 content in the reaction product in the upper region of the TBC. This composition was consistent throughout the upper interaction zone of the coating, within the melt matrix.

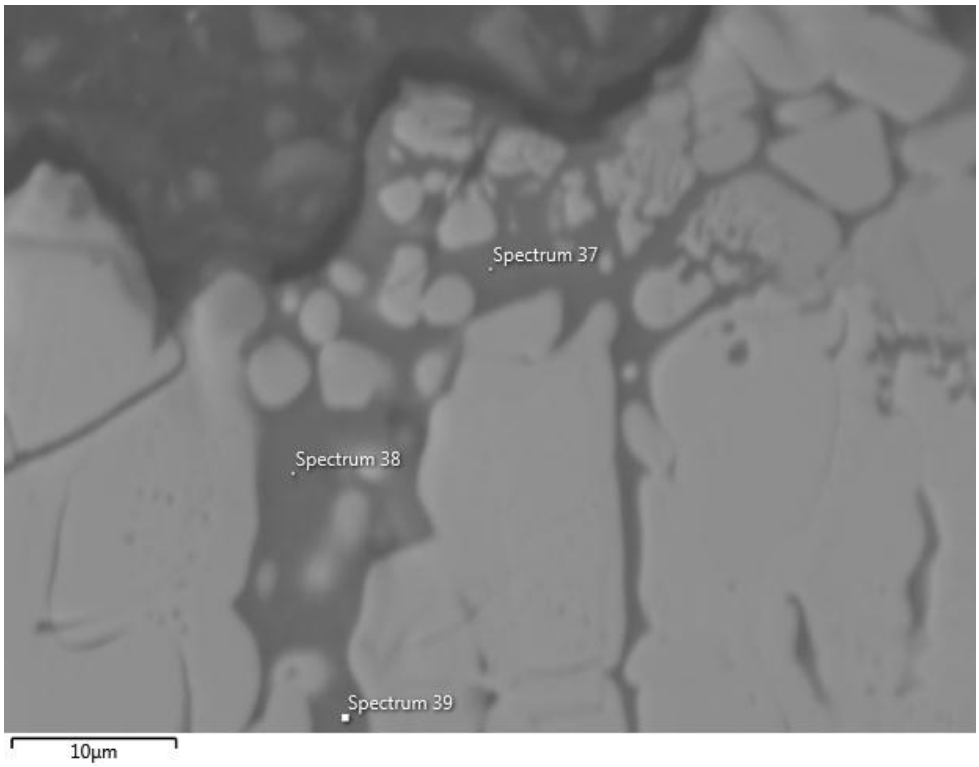

Spectrum	O	Mg	Al	Si	Ca	Y	Zr
Spectrum 37	57.0	0.1	15.9	7.4	16.1	0.5	3.1
Spectrum 38	53.7	0.2	17.7	8.4	18.9	0.4	0.7
Spectrum 39	55.5	1.5	22.6	7.1	9.3	0.3	3.8

All results in atomic%

Figure 164: 30 minutes exposure with High B.I. deposit showing significant Al_2O_3 content in the upper part of the TBC.

High B.I. attack mechanism was found to be bi-directional as opposed to Near Neutral mechanism where the attack was initiated from the bottom, the composition of the reaction products within the grain boundaries were almost similar throughout the entire coating. In High B.I. samples, transformation zones can be seen from the top and bottom of the sample

after just 30 minutes exposure and for this reason, the composition of the phases formed within the boundaries are very similar, except for regions that have undergone second stage recrystallization, where CaO was found to be less than overall, as can be seen in Figure 165.

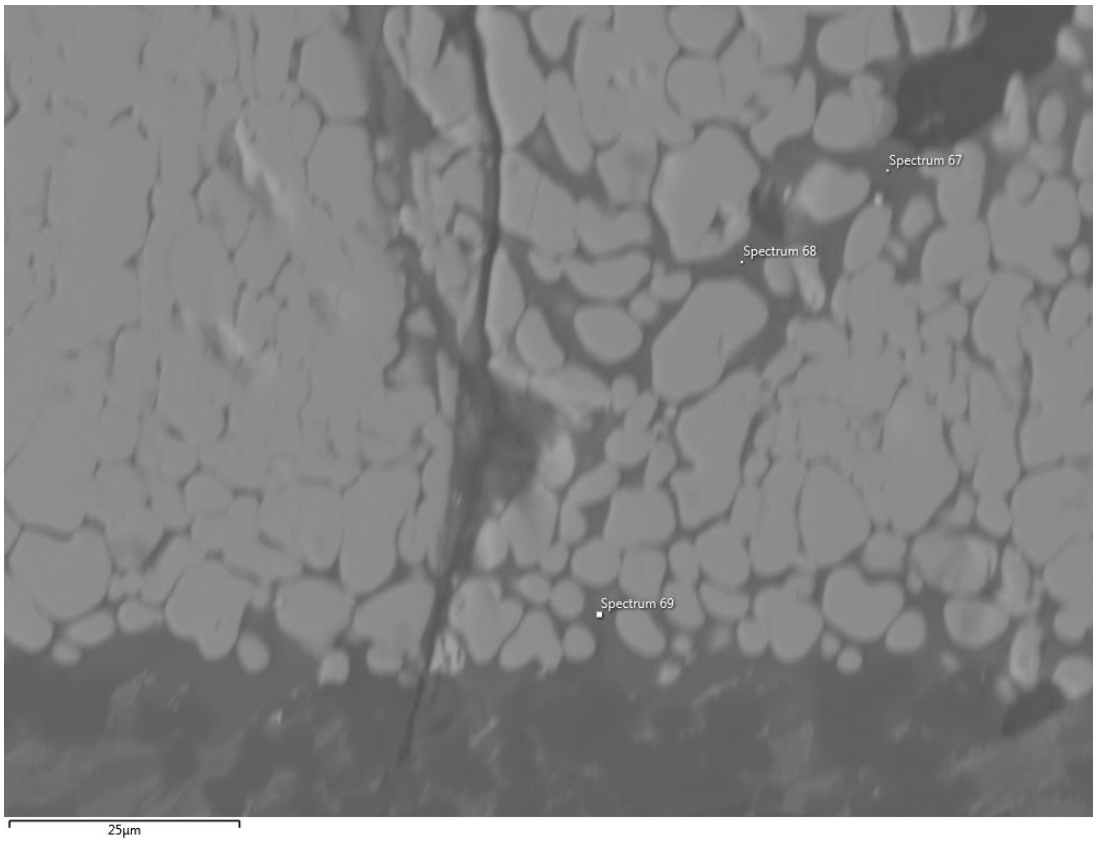

Spectrum	O	Mg	Al	Si	Ca	Y	Zr
Spectrum 67	55.8	1.0	15.5	9.5	18.1	0.2	0.0
Spectrum 68	56.4	1.8	13.2	10.0	17.8	0.1	0.7
Spectrum 69	58.3	0.3	15.8	6.7	13.7	0.5	5.0

All results in atomic%

Figure 165: 30 minutes High B.I. sample with composition of reaction products across TBC.

Similar to the pattern observed with Near Neutral samples, the amount of CaO in the reaction phases in the grain boundaries of High B.I. samples decreased with increasing exposure time, as can be seen in Figure 166. Depending on the local melt chemistry, the TBC will completely dissolve in the aggressive High B.I. melt and recrystallized either as calcium zirconate or Ca-doped YSZ. The amount of CaO content in the newly crystallised grains

increases with longer exposure time, as the mechanism is known to be a diffusion controlled process.

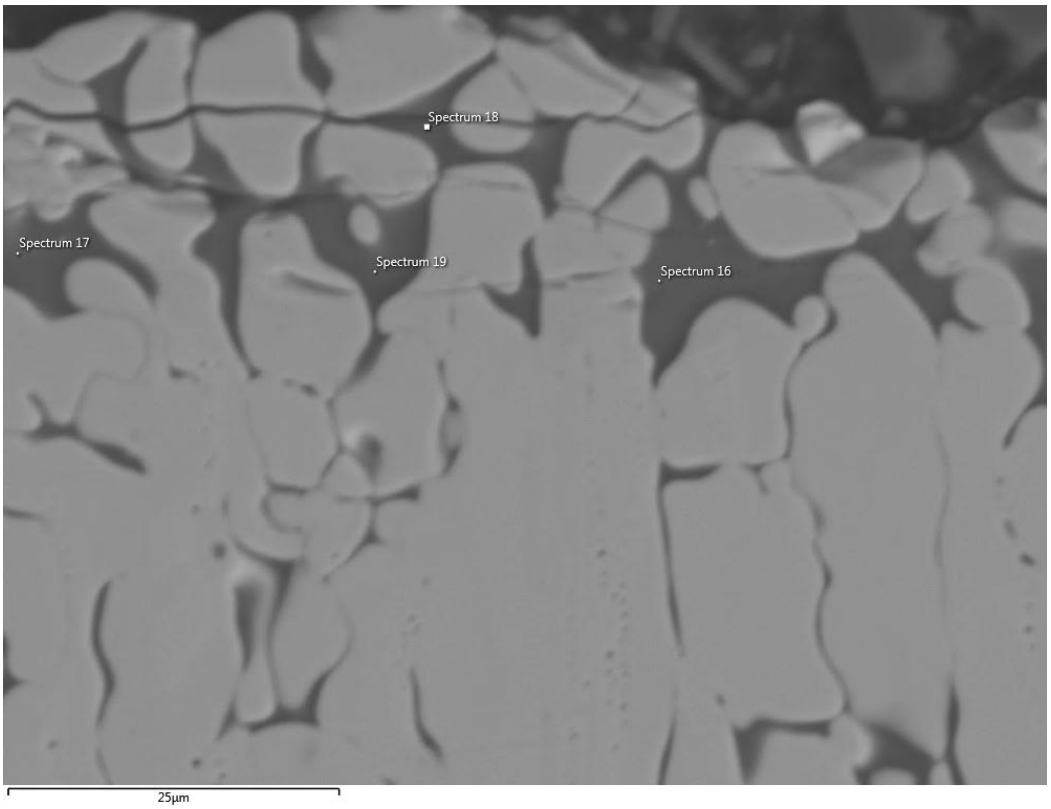

Spectrum	O	Mg	Al	Si	Ca	Y	Zr
Spectrum 16	55.8	0.5	16.7	8.2	17.5	0.3	1.0
Spectrum 17	56.1	0.8	16.0	8.3	15.0	0.4	3.5
Spectrum 18	56.7	0.8	14.5	7.4	15.1	0.6	4.9
Spectrum 19	60.1	3.1	15.8	9.2	8.1	0.3	3.4

All results in atomic%

Figure 166: Upper part analysis of the reaction product of one hour High B.I. sample

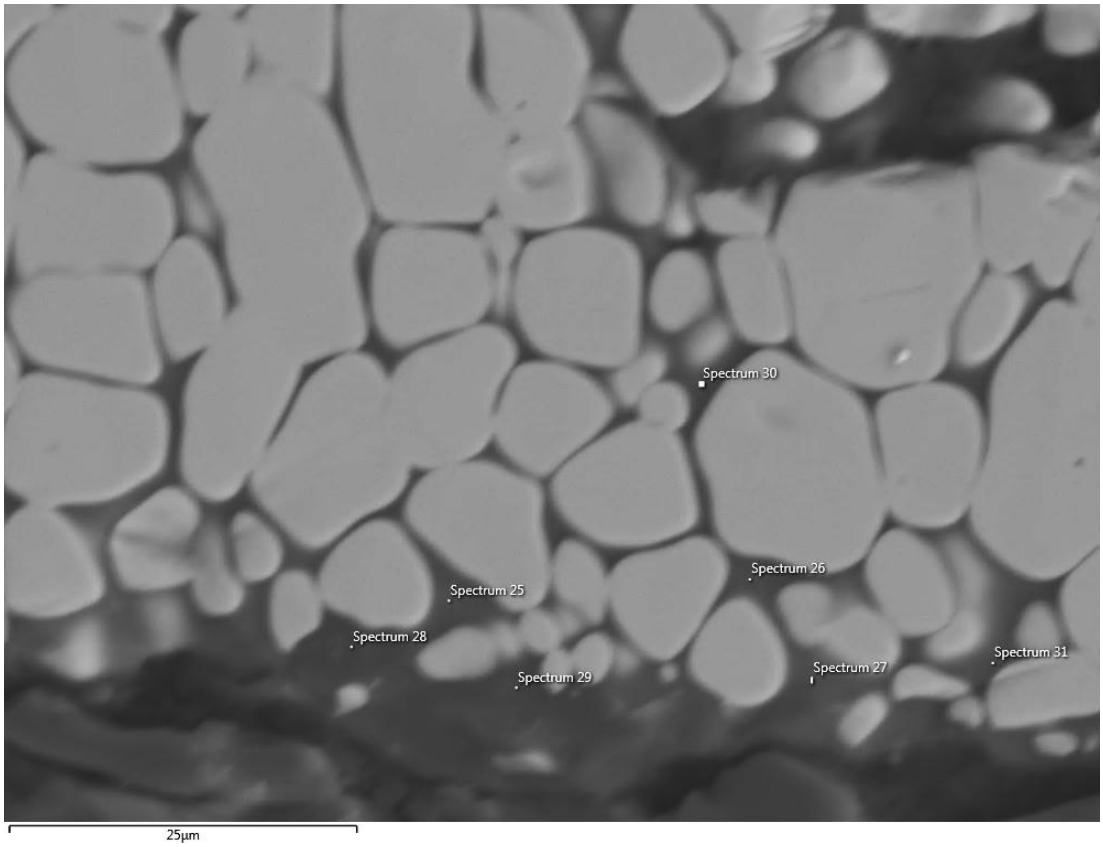

Spectrum	O	Mg	Al	Si	Ca	Y	Zr
Spectrum 25	59.6	1.0	19.0	7.4	11.2	0.2	1.6
Spectrum 26	57.8	1.7	21.7	7.5	8.7	0.3	2.3
Spectrum 27	60	0.8	17.0	6.3	11.0	0.4	4.4

All results in atomic%

Figure 167: Bottom analysis of the reaction products of High B.I. sample after one hour heat treatment

However, Figure 167 showed that the composition of the phases locked between grain boundaries is different at the bottom to that at the top of the TBC. While Al_2O_3 content increases as expected, the amount of CaO also varied between the upper and lower interaction zone of the TBC, indicating that more Ca from the melt was absorbed by the newly formed grains in the lower interaction zone. High B.I. sample is known by [65] to form a polycrystalline structure consisting of calcium zirconate and tetragonal zirconia, depending on the composition of the local melt, which eventually determines the composition of the recrystallized grains, as shown in Figure 168.

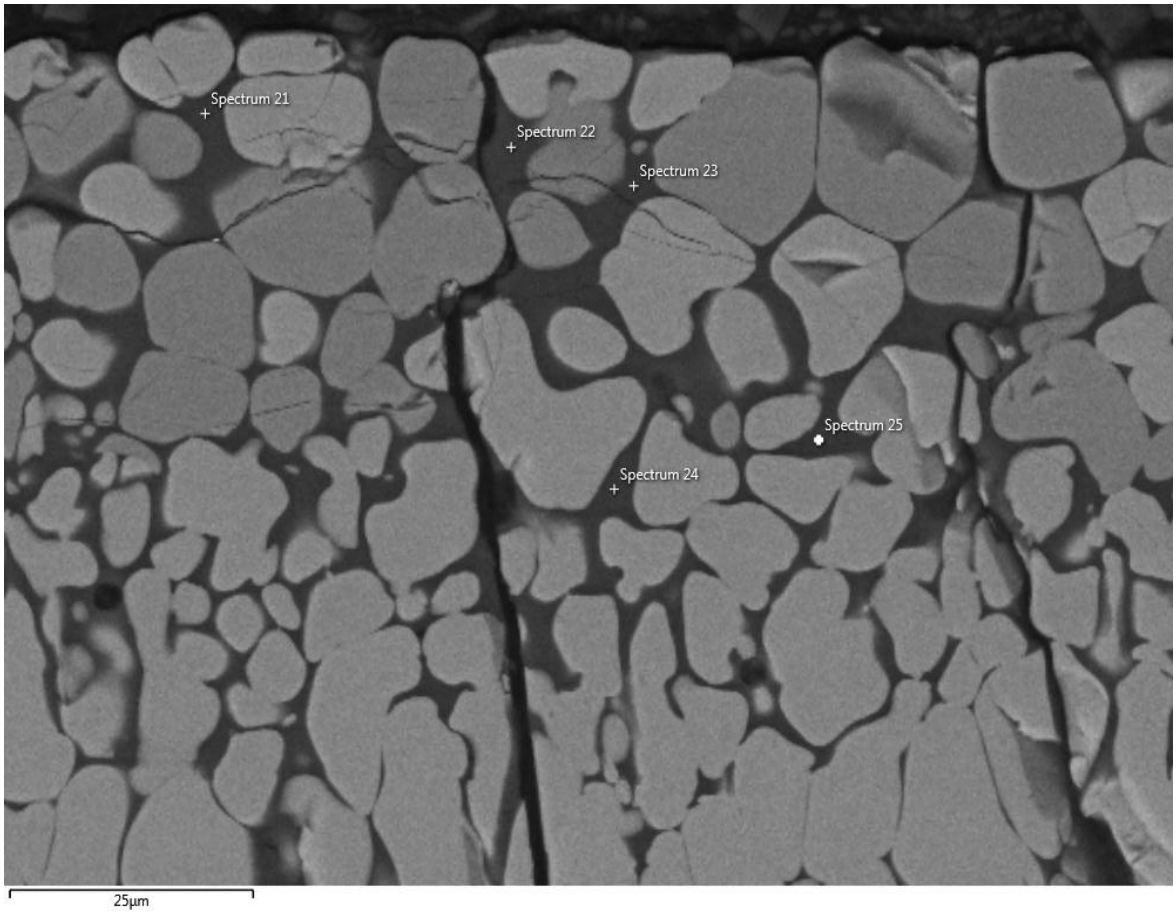

Spectrum	O	Mg	Al	Si	Ca	Y	Zr
Spectrum 21	39.4	0.9	19.5	10.7	27.4	0.1	1.9
Spectrum 22	39.3	0.5	20.7	10.3	27.0	0.3	1.9
Spectrum 23	40.0	0.5	19.9	11.4	26.5	0.4	1.4
Spectrum 24	38.9	0.3	21.9	10.8	26.9	0.5	0.7
Spectrum 25	39.8	0.5	19.0	10.1	25.4	0.8	4.5

All results in atomic%

Figure 168: Formation of calcium zirconate depending on local melt chemistry. 4h at 1458 °C

One of the phases formed in the melt matrix at the bottom of a High B.I. sample was identified as magnesium spinel, as illustrated on spectrums 37-39 in Figure 169. The excess Al from the substrate is arrested by magnesia from the deposit and because of their high affinity for each other, they react to form a magnesium spinel phase.

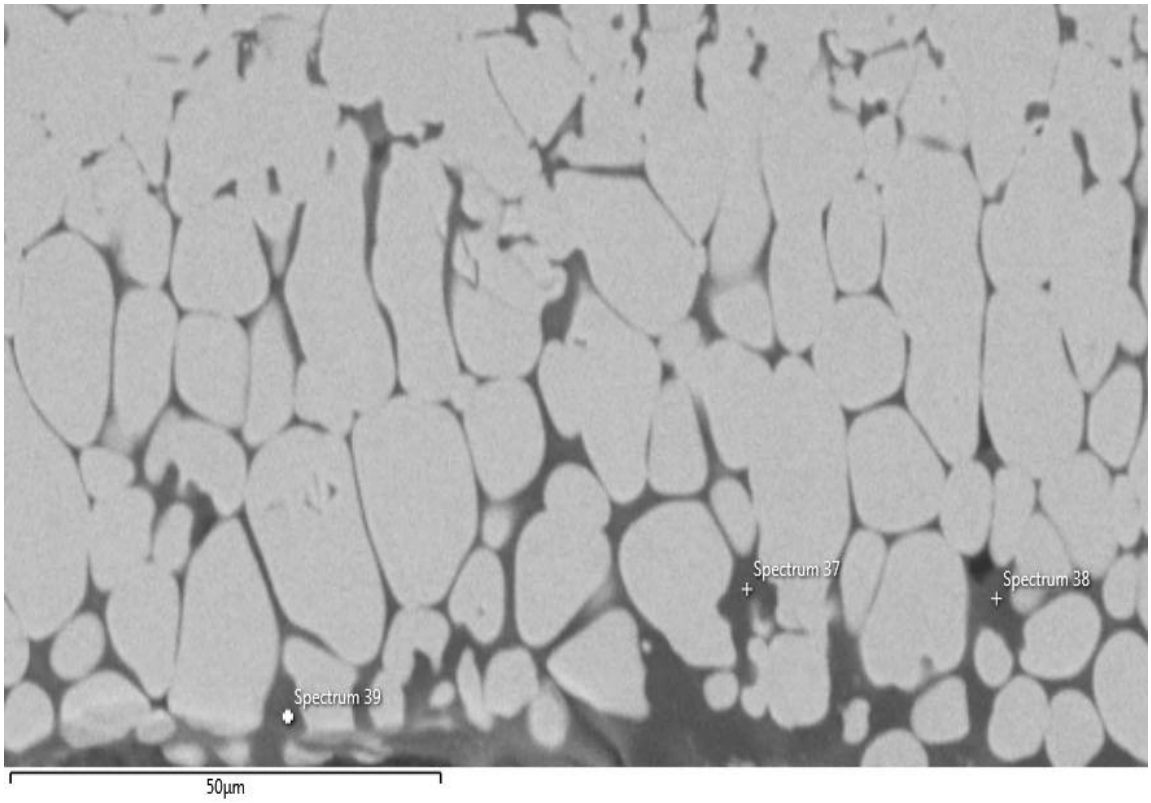

Spectrum	O	Mg	Al	Si	Ca	Y	Zr
Spectrum 37	47.5	14.7	34.0	0.6	2.3	0.1	0.9
Spectrum 38	47.3	15.0	35.0	0.3	0.9	0.1	1.1
Spectrum 39	48.4	15.0	34.6	0.5	0.8	0.1	0.7

All results in atomic%

Figure 169: Identification of spinel phase

Spectrums 28-30 on Figure 170 show the melt composition prior to crystallisation into calcium zirconate grains. It was noted that substantial amount of zirconia from the dissolved TBC was entrapped in the local melt, containing significant amount of CaO. Previously in this chapter, it has been reported that MgO, Al_2O_3 and SiO_2 play no major role in the composition of the resulting microstructure, which is further confirmed by examining the initial composition of the calcium zirconate melt (Figure 170), rich in Al_2O_3 and SiO_2 with that of the resulting microstructure.

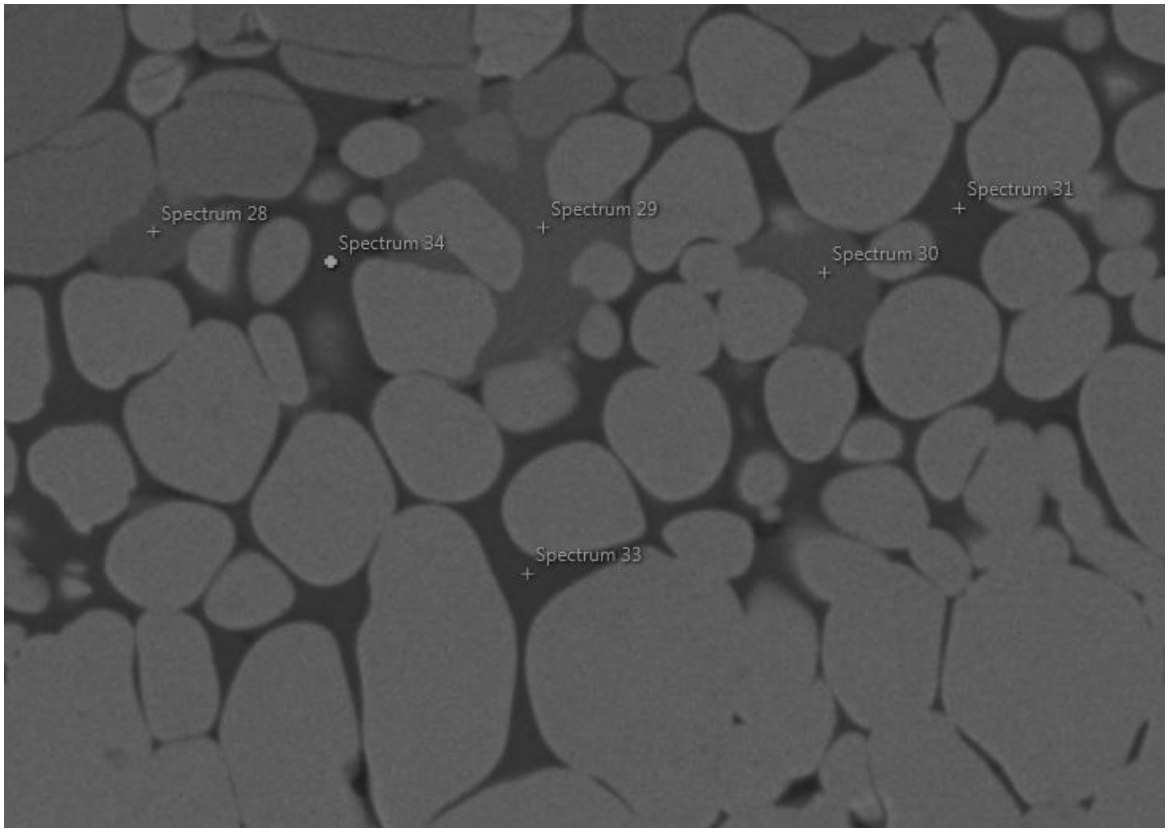

Spectrum	O	Mg	Al	Si	Ca	Y	Zr
Spectrum 28	38.6	0.1	16.0	4.3	23.6	2.5	14.8
Spectrum 29	40.0	0.2	15.8	4.4	23.4	2.5	14.7
Spectrum 30	38.4	0.2	16.2	4.4	23.6	2.4	14.8

All results in atomic%

Figure 170: Melt chemistry prior to the formation of calcium zirconate

8.8 Summary – High Basicity Index (Basic deposit): B.I. = 2.2 or above

High B.I. in this study refers to Basicity Index with ratios greater than 2.2. In this test, the CMAS composition used was $C_{73}M_9A_7S_{11}$ in mole% (B.I. = 4.68). High B.I. melt was shown to be less viscous than Near Neutral melt which in turns was less viscous than Low B.I. melt. Stott et al. investigated the interactions between TBCs and several Middle East sand compositions and their results are published [65]. It can be inferred from the calculation of the B.I. of these samples, based on their characterisation that they belong in the High B.I. category. While it is acknowledged that Middle Eastern sand compositions fall in the High

B.I. category, the attack mechanism found in this study agrees well with that published by Stott et al. [65].

Due to the aggressiveness of High B.I. melt, the alumina substrate was severely attacked by the melt, destabilising and releasing excess Al into the melt pool. Figure 160 reveals the features identified at the bottom of the sample, showing that High B.I. melt significantly infiltrates the substrate, altering the composition of the substrate and creating an Al depleted zone within the substrate. With High B.I. attack, there is certainly a possibility of thermal and/or chemical damage to the TGO, potentially extending to the bond coat in engine conditions. The most common rate-controlling factors for a reaction between the slag and the TBC are the diffusion of the reacting species in the slag and the transfer of the species across the slag-TBC interface, so the viscosity and surface tension of the slag are also of considerable importance [65].

Due to the possibility of High B.I. melt infiltrating and destabilising the substrate material thereby leaching Al_2O_3 into the melt, free-standing coatings were used in order to understand the degradation effect of excess Al_2O_3 in the melt matrix. Whilst this was the case, it does not however influence the degradation mechanism and severity of attack. The degradation mechanism and morphology of attack in PYSZ with substrate and free standing TBC without substrate were similar, both forming a polycrystalline microstructure consisting of calcium zirconate and high Ca-stabilised tetragonal zirconia, preventing a monoclinic phase transformation.

Also, the attack mode of High B.I. deposits is bi-directional. High B.I. samples showed complete failure in coating integrity after as little as 30 minutes exposure. The degradation mechanism by High B.I. melt is characterised by complete dissolution of the TBC into the

melt pool and recrystallization, to form a completely new polycrystalline microstructure of calcium zirconate and Ca doped PYSZ.

The degradation mechanism of Near Neutral and High B.I. CMAS attack are very similar, with varying degree of severity. High B.I. attack is more severe than Near Neutral melts, due to the aggressiveness of High B.I. deposits. The mechanism of attack can be summarised as;

1. Agressivity of CMAS deposits increases with increasing Basicity Index. A high B.I. deposit is experimentally proven to be the most aggressive CMAS category. Viscosity is a function of B.I. and showed inverse proportionality relationship, meaning that High B.I. deposit is less viscous and Low B.I. compositions more viscous.

2. The high CaO content in the melt acts as a sintering aid in the melt matrix, accelerating the sintering of TBC columns. The accelerated sintering rate combined with the columnar, porous microstructure of EB-PVD coatings enable the melt to penetrate to the bottom of the coating. High B.I. and Near Neutral compositions form a melt pool at the TBC interface. The ability of CMAS to form a melt pool is a direct consequence of the B.I. (therefore viscosity) of the melt. The rate of penetration (hence formation of melt pool) increases with increasing B.I., with Low B.I. incapable of forming a melt pool. Melt pool was formed after 30 minutes and one hour for High and Near Neutral B.I. respectively.

3. Near Neutral and High B.I. attack penetrates to the substrate/coating interface, where severe destabilisation of the substrate material was observed thereby releasing excess Al_2O_3 into the melt. High B.I. melt showed severe Al_2O_3 depletion zone, similar to TGO attack in real life situation. De-bonding of the TBC was also noticed as a result of the melt pool and spinel layer formed at the base.

4. The destabilisation of the substrate and subsequent diffusion of excess Al_2O_3 into the melt results in three scenarios; (1) Excess Al_2O_3 in the melt reduces the melting temperature of the melt pool, thereby creating a thermal gradient between the melt matrix at the top of the coating and in the melt pool. (2) An Al_2O_3 diffusion gradient is created, with Al diffusing along this gradient. (3) Excess Al_2O_3 in the melt pool attracts magnesium from the melt and combines to form a magnesium spinel layer that sits on the surface of the substrate, leading to de-bonding of the TBC. Due to the presence of low melting, super-saturated phases formed at the bottom (melt pool), Near Neutral and High B. I. molten deposits attack is initiated at the bottom of the coating.

5. Complete dissolution of the TBC in the melt followed by recrystallization into a polycrystalline structure of calcium zirconate or Ca-doped PYSZ, depending on the B.I. of the surrounding melt matrix. Since zirconia is partly ionic and partly covalent (hence amphoteric), its behaviour in a Near Neutral and High B.I. environment is more covalent, abide with the ΔG of CaO, form a more stable compound, calcium zirconate. Also, the diffusion of calcium into the grains helps to stabilise the tetragonal phase, hence preventing the detrimental monoclinic phase transformation characteristic with Low B.I. attack mechanism.

The covalent character of zirconium is attributed to zirconium having a very small ionic radii (86 pm) and being highly charged (+4), thus causing polarisation of the anion. In the case of zirconium silicate, the silicate ion is held very tightly by the zirconia ion, as the cation has a greater charge and is smaller, therefore the charge density is greater. The charge density (charge/ionic radius) influences the establishment of covalent character in ionic compounds. The higher the charge density, the easier an anion is polarised and covalent character is shown. Zirconium has a high “charge-to-ionic radius” ratio which makes it highly polarising.

6. Near Neutral attack initiates from the bottom of the coating. However, due to the aggressiveness of High B.I. melt, the attack was found to be bi-directional, both resulted in grain fragmentation (round grains). The ceramic TBC is dissolved in the melt and depending on the local melt chemistry, recrystallizes either as tetragonal zirconia or calcium zirconate. The rounded grain morphology that results can be attributed to wetting characteristics and the minimisation of surface energy (interfacial tension) between the calcium zirconate and residual molten slag compositions.

7. MgO, Al_2O_3 and SiO_2 don't play a role in the degradation morphology of this category of attack, as they were found not to penetrate the grains of the newly formed structures. However, the excess Al in the melt pool depresses the melting temperature by forming low melting eutectics.

8. There's the potential of High B.I. attack certainly spreading to the substrate, not only resulting in chemical attack/failure but also thermo-mechanical susceptibility and leading to spallation of the dense, brittle calcium zirconate TBC and subsequent failure.

A pictorial summary of the microstructural evolution of High B.I. infiltrated sample is shown in Figure 171.

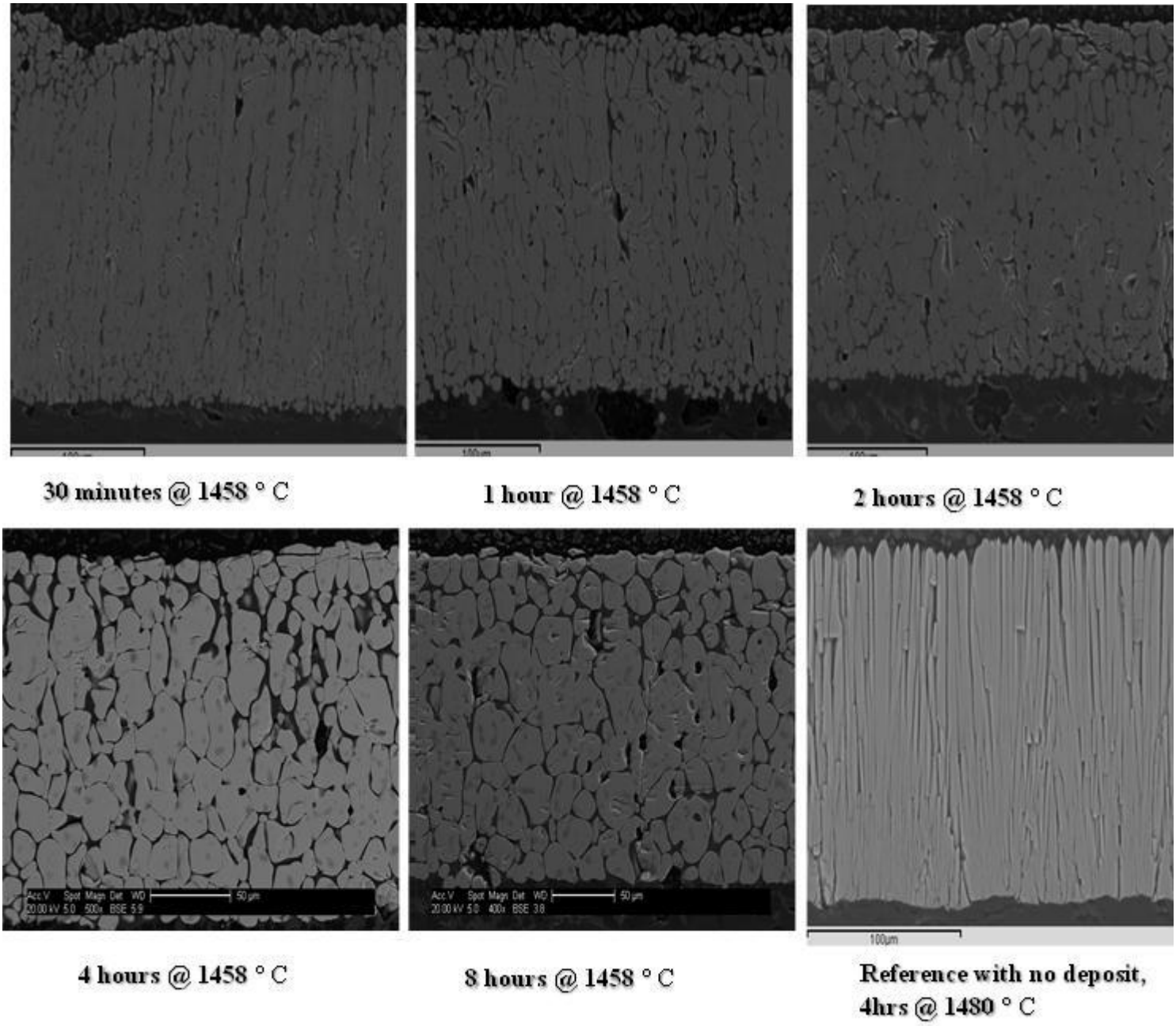

Figure 171: Summary - High Basicity Index (Basic deposits); B.I. = 2.2 or above

Basicity Index and Viscosity influence the penetrating prowess of molten deposits. Low B.I. deposits formed a glaze on the surface of the coating, meanwhile Near Neutral sample showed a shallow melt on the surface, with grains visibly sticking out while majority of melt is penetrated all through to the bottom. High B.I. melt on the other hand penetrated straight through to the bottom of the sample, forming a melt pool. In this case, the "dried up" grains of the High B.I. sample can be seen (Figure 172), with no indication of a melt visible on the surface.

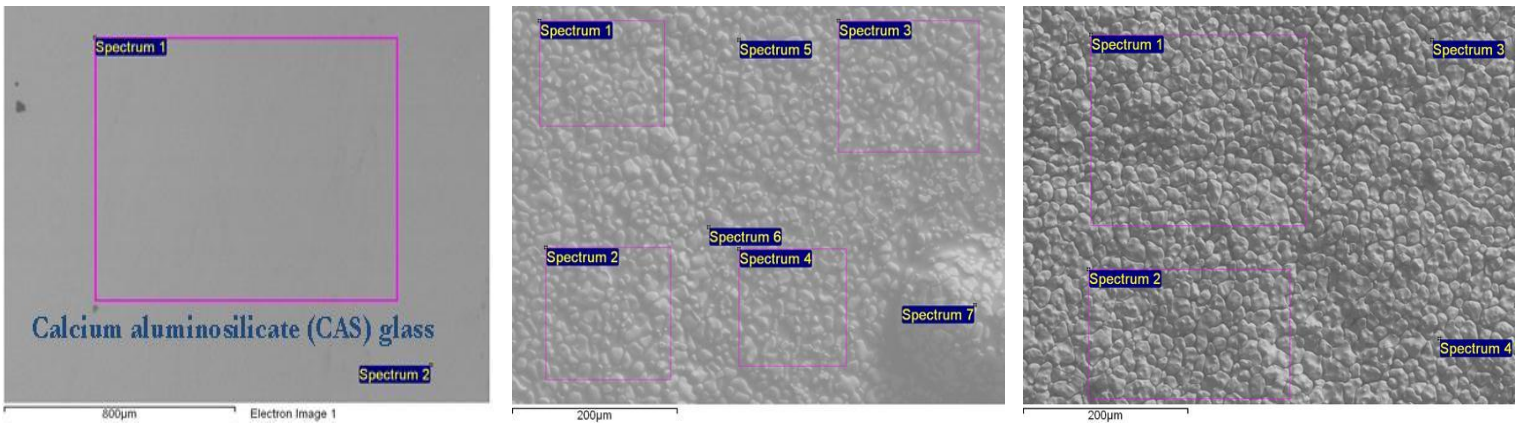

Figure 172: Viscosity and melt penetration – (a) Low B.I. melt formed a glassy layer, low penetrating power. (b) Shallow melt by Near Neutral deposits (c) Dry cells, very quick penetration rate of High B.I. melts.

The experiments to study the effect of Basicity Index of slag and TBC degradation were carried out at 50 °C above the melting point of the individual deposit. For this reason, the tests were performed at a range of different temperatures and because CMAS and CMAS-type attack has been reported by various authors to be temperature dependent, there was a possibility that the microstructural evolution observed in the Basicity Index study may be linked to temperature effect.

It may be argued that the difference in attack mechanisms shown previously within this study is a function of temperature where the temperatures range from 1298 °C to 1480 °C and 1458 °C for low, mid and high B.I. CMAS compositions respectively. In order to isolate the effect

of temperature, Low, Near Neutral and High B.I. samples were heat treated the same time in a box furnace for four hours at a constant temperature, the highest experimental temperature in this set of experiments, which happened to be the temperature of the Near Neutral test category (1430 °C + 50 °C). Low, Mid-range and High B. I. deposits were found not to be proportional to melting temperatures. In other words, increasing Basicity Index is not attributed to increasing melting temperature, although Low B. I. deposits had the lowest melting temperature, the highest melting point deposits were found to be Near Neutral deposits as opposed to High B.I. deposits, indicating that increasing melting temperature is not a direct consequence of increasing B.I. The effects of testing with variations of B. I. revealed that CMAS degradation is purely down to the chemical reaction between the CMAS and TBC and once melting has occur the degradation mechanism is dependent on basicity (Figure 173).

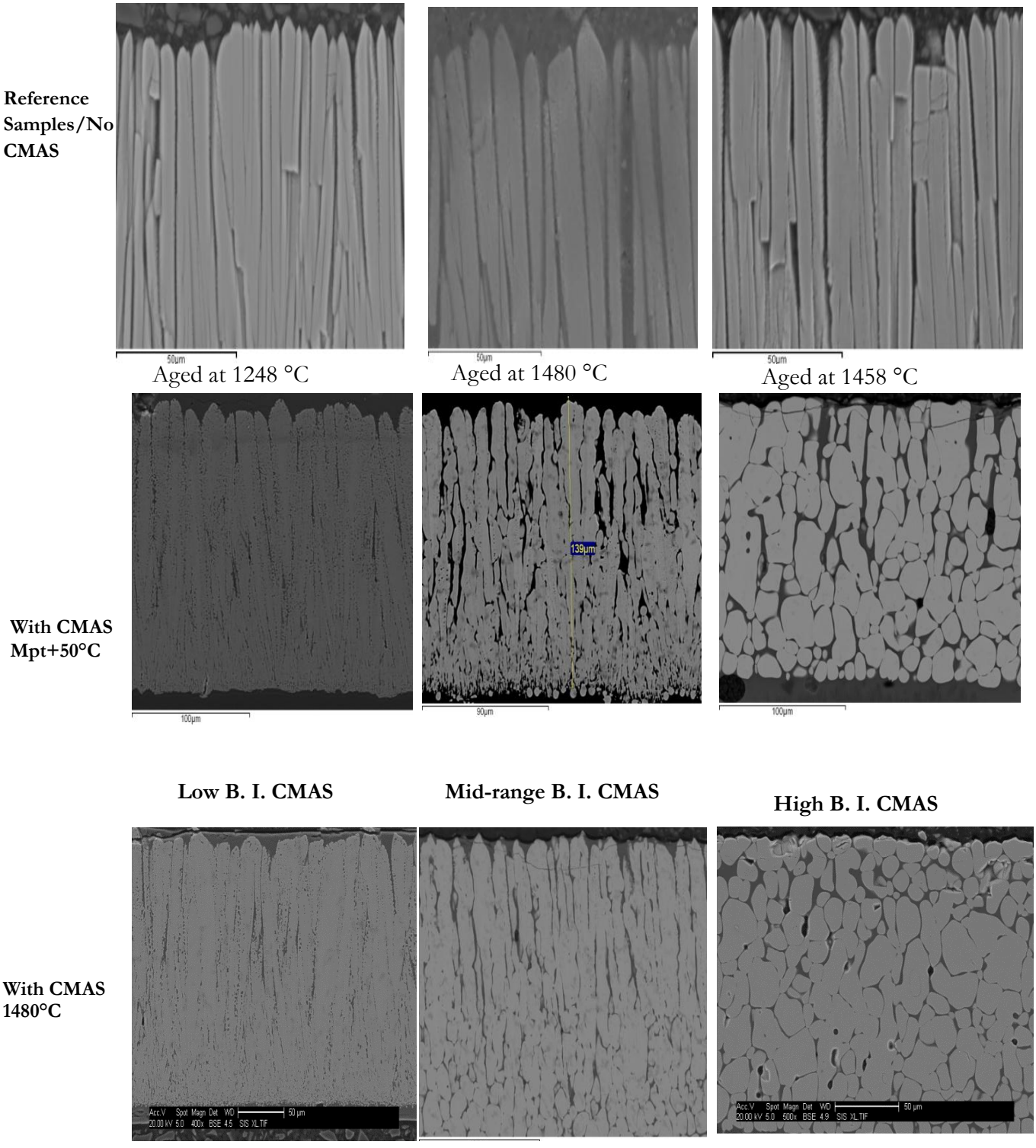

Figure 173: Comparison of the morphologies of degraded EB-PVD TBCs for different CMAS at composition over temperatures from 1248 ºC -1480 ºC

9 The Effect of Basicity on Novel TBCs (Gadolinium Zirconate)

Gadolinium zirconate ($Gd_2Zr_2O_7$) is widely accepted in literature to mitigate the effect of CMAS damage [104] [71] [69; 82] – [7; 160; 161]. Levi et al. investigated the thermochemical interaction between GZO and CMAS and reported that the $Gd_2Zr_2O_7$ + CMAS reaction zone consisted of a dense, fine-grained layer, about 6 μm thick. It was also reported that the melt infiltration into the inter-columnar grain boundaries was largely suppressed, with penetration rarely exceeding ~30 μm below the original surface. The microstructural evidence obtained by Levi et al. [162] suggests that the degradation mechanism is influenced by the dissolution of the GZO into the melt followed by the arrest of CMAS infiltration by rapid filling of the gaps with solid crystalline phases. The extent of CMAS degradation to the column tips and the penetration depth was measured to be in the top 20 μm of the coating, forming a stable refractory compound of a fluorite and hexagonal apatite phase based on $Ca_2Gd_8(SiO_4)_6O_2$. Based on these findings, it is generally accepted that $Gd_2Zr_2O_7$ has a far superior CMAS resistance compared to 7YSZ.

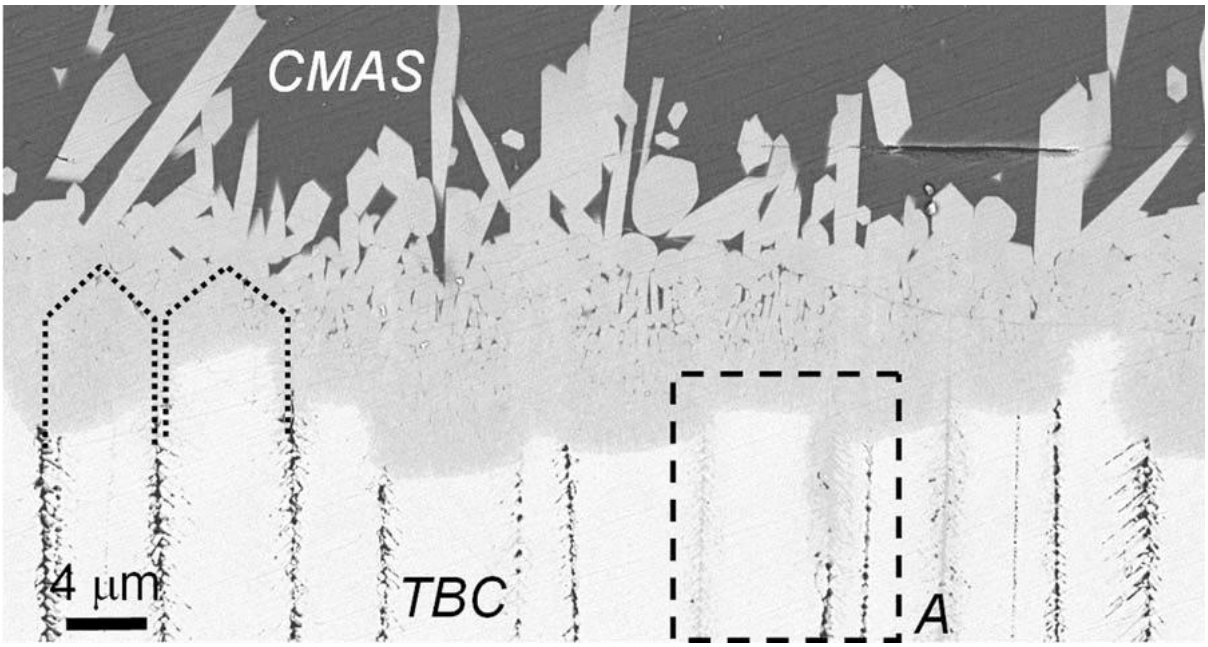

Figure 174: Reaction zone between Low CMAS and a columnar Gadolinium zirconate TBC [69].

In order to validate the concept that the severity of molten deposit attack varies with the Basicity Index of the slag, GZO samples were manufactured at Cranfield University and tested against the three categories of deposits (Low, Near Neutral and High B.I.). As can be seen in Figure 174, GZO was shown to mitigate standard or Low B.I. CMAS attack. For the purpose of comparison, gadolinium zirconate was deposited on a number of 99.99% pure alumina coupons by electron beam physical vapour deposition at Cranfield University. But because of the poor adhesion of GZO and the alumina interface, direct deposition of the GZO onto the alumina coupons proved difficult and for this reason, a layer of YSZ was deposited onto the substrate before the GZO could be deposited, as illustrated in Figure 175.

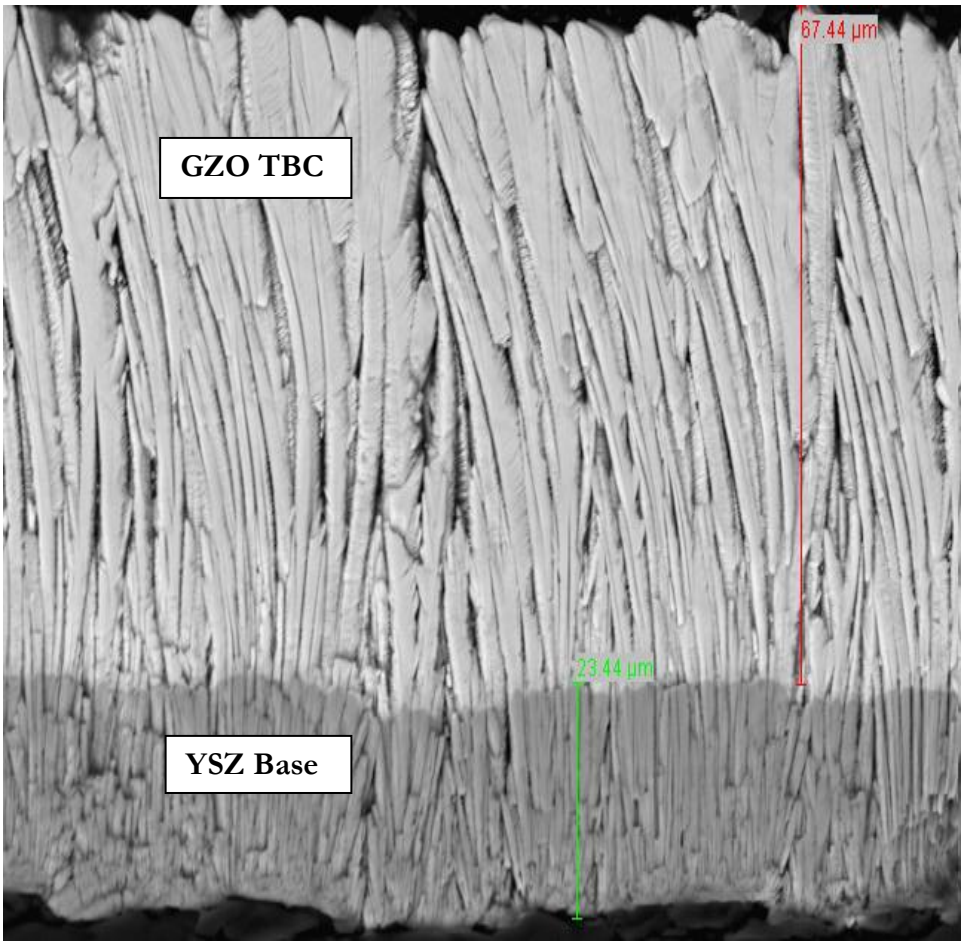

Figure 175: Reference – as deposited GZO coating

As part of these set of tests, a reference sample without CMAS was also heat treated for four hours at 1430 °C, the result is presented in Figure 176. Apart from a small amount of sintering which is associated with this level of heat treatment, the coating remained in good condition.

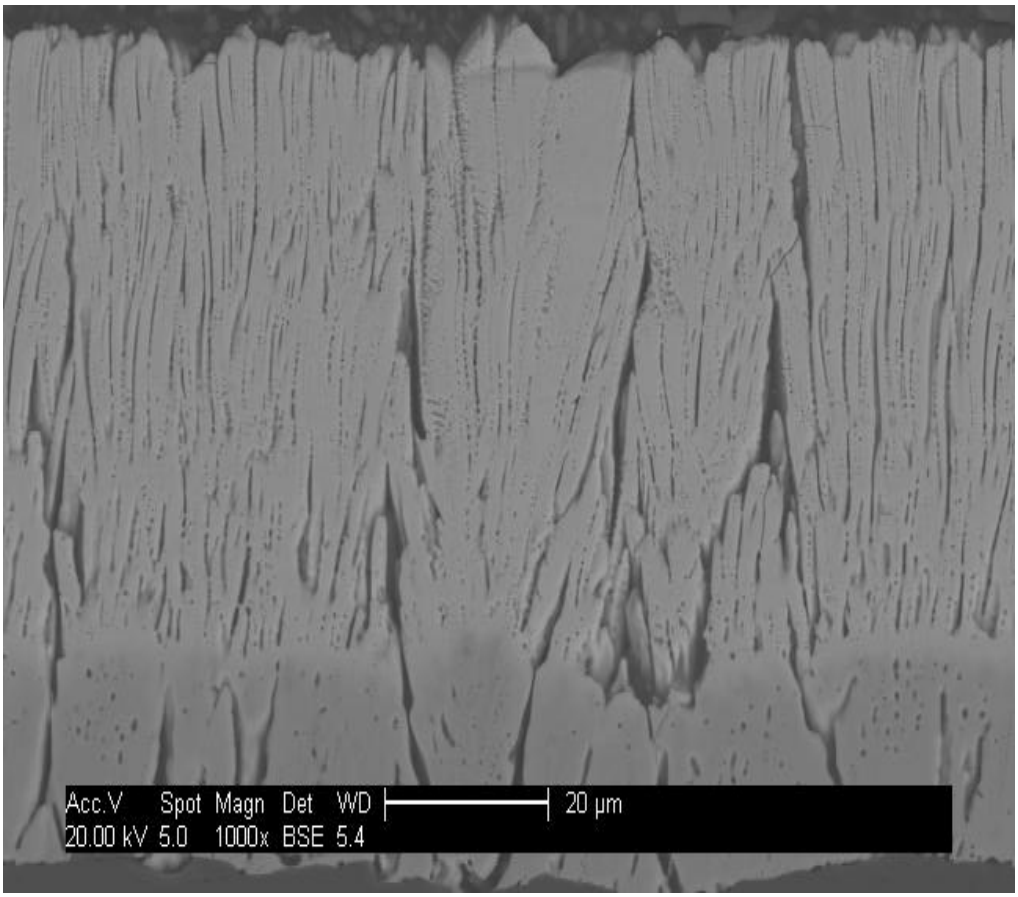

Figure 176: Reference – Aged at 1430 °C for 4h. No CMAS deposits

9.1 Low B.I. Deposit

Samples were sprayed with Low B.I. deposit and heat treated for four and eight hours at 1250 °C and showed similar attack morphology to that observed by Levi et al. [69], consisting of a fairly shallow interaction zone and the reaction products crystallised within about 10 µm, sealing the inter-columnar grain boundaries and preventing further likely attack. The observed characteristics of the Low B.I. attack agreed well with that made by Levi et al. [69], as can be seen in Figure 177. Levi et al. [69] explained that this retardation mechanism was due to the consequences of the system forming an apatite phase which crystallises and prevents absorption of the molten deposit by the coating.

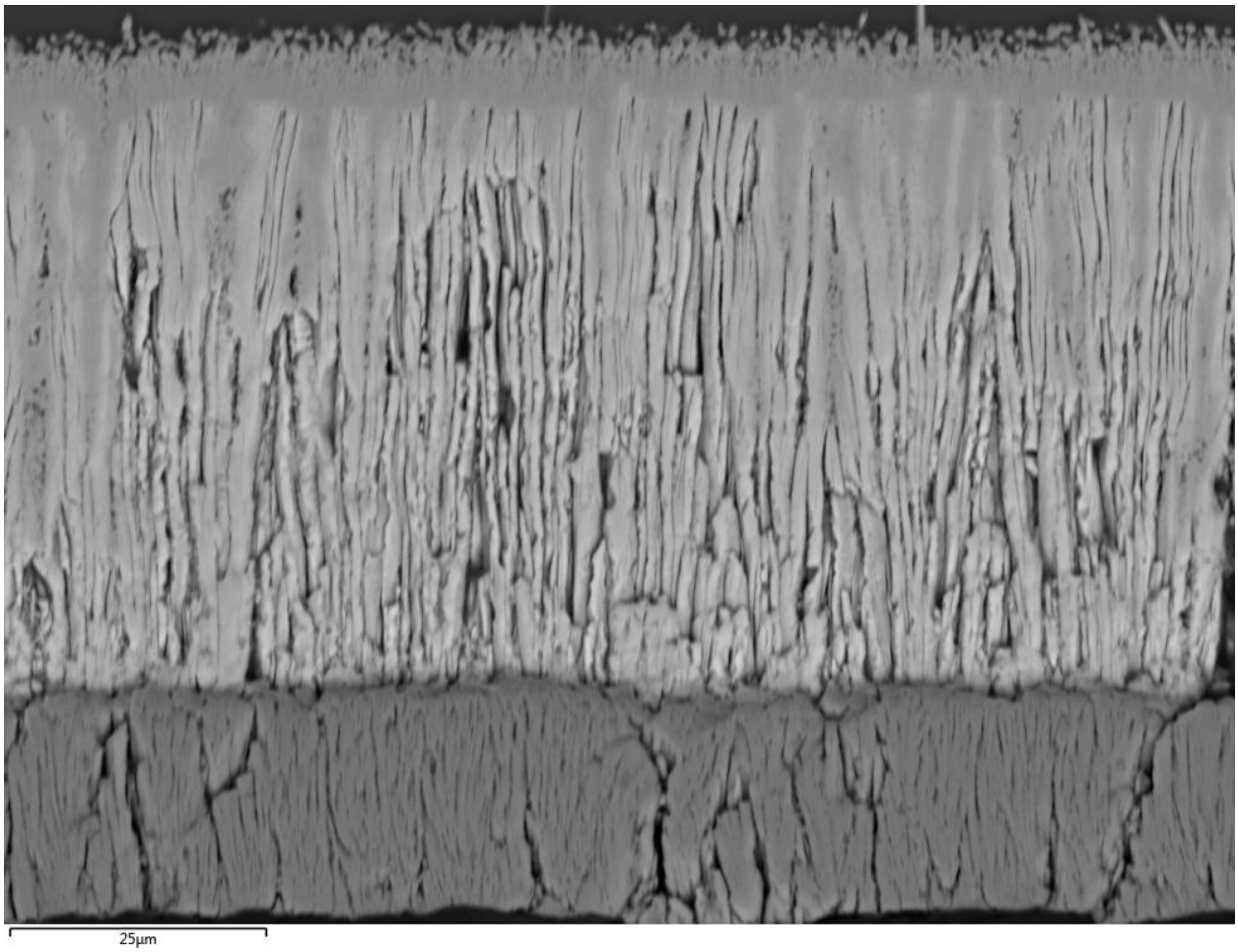

Figure 177: Low B.I. 4h at 1250 °C with GZO coating.

EDAX spot and elemental analyses were used to study the phases and composition of the reaction products formed in the interaction zone. Whilst three regions of interest are evident from Figure 177 (light and grey regions and also the dark area at the bottom of the coating structure), EDAX elemental mapping (Figure 178) identified the grey regions to be a crystallised phase rich in reaction products whilst the light areas were shown to be TBC rich. Also, the reacted phase is seen to have sealed the inter-grain boundaries hence minimising further penetration through the TBC structure. The characteristic porous dark globules associated with standard CMAS attack of YSZ was shown to have been eradicated (or minimised).

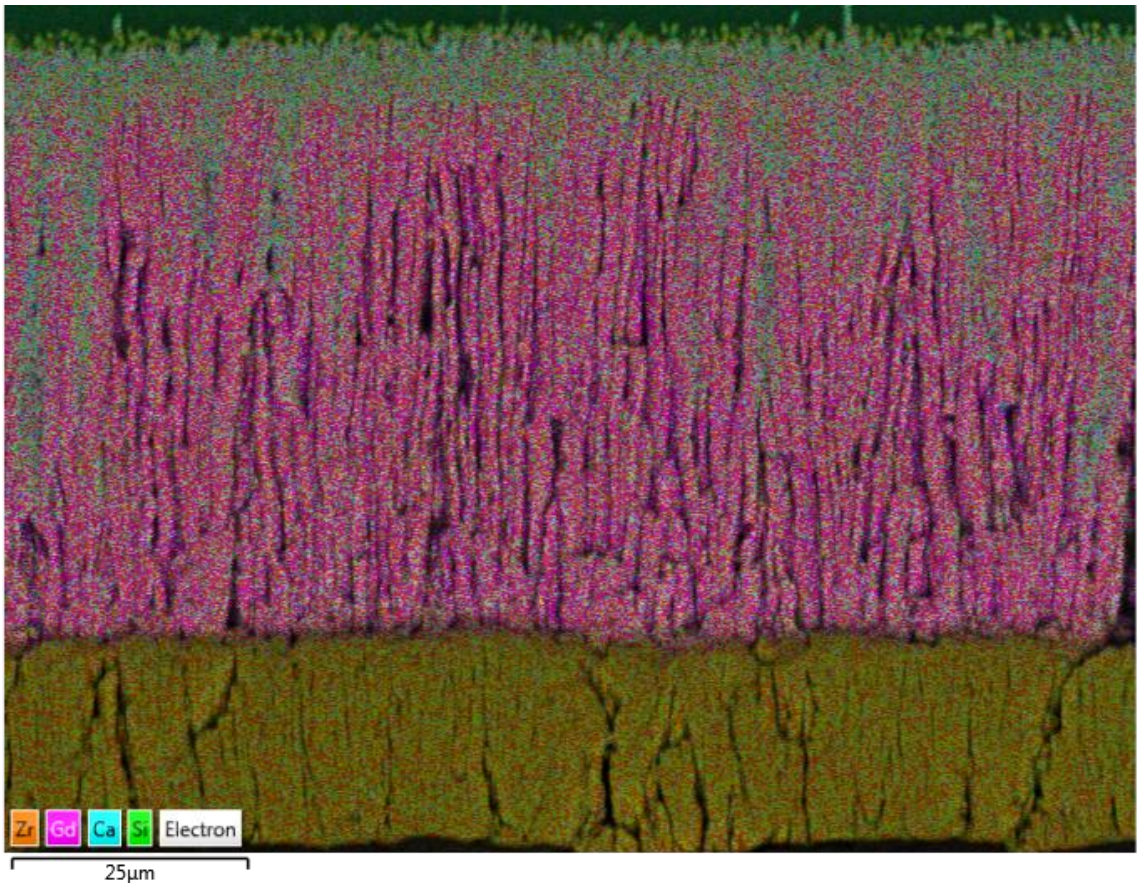

Figure 178: EDAX elemental mapping of Low B.I. sample with GZO – 4h at 1250 °C.

EDAX spot analysis was then used to determine the chemistry and possible phases formed in the interaction zone. The top 3 µm of the coating consisted of a fine-grained layer showing complete degradation of the column tips, this was followed by a dense region, ~8 µm thick, where the reaction products were arrested and by so doing, restrained any further damage. EDAX analysis in Figure 179 showed that the composition of the reacted product matches that reported in literature which was identified to be a stable apatite phase containing Ca and Zr.

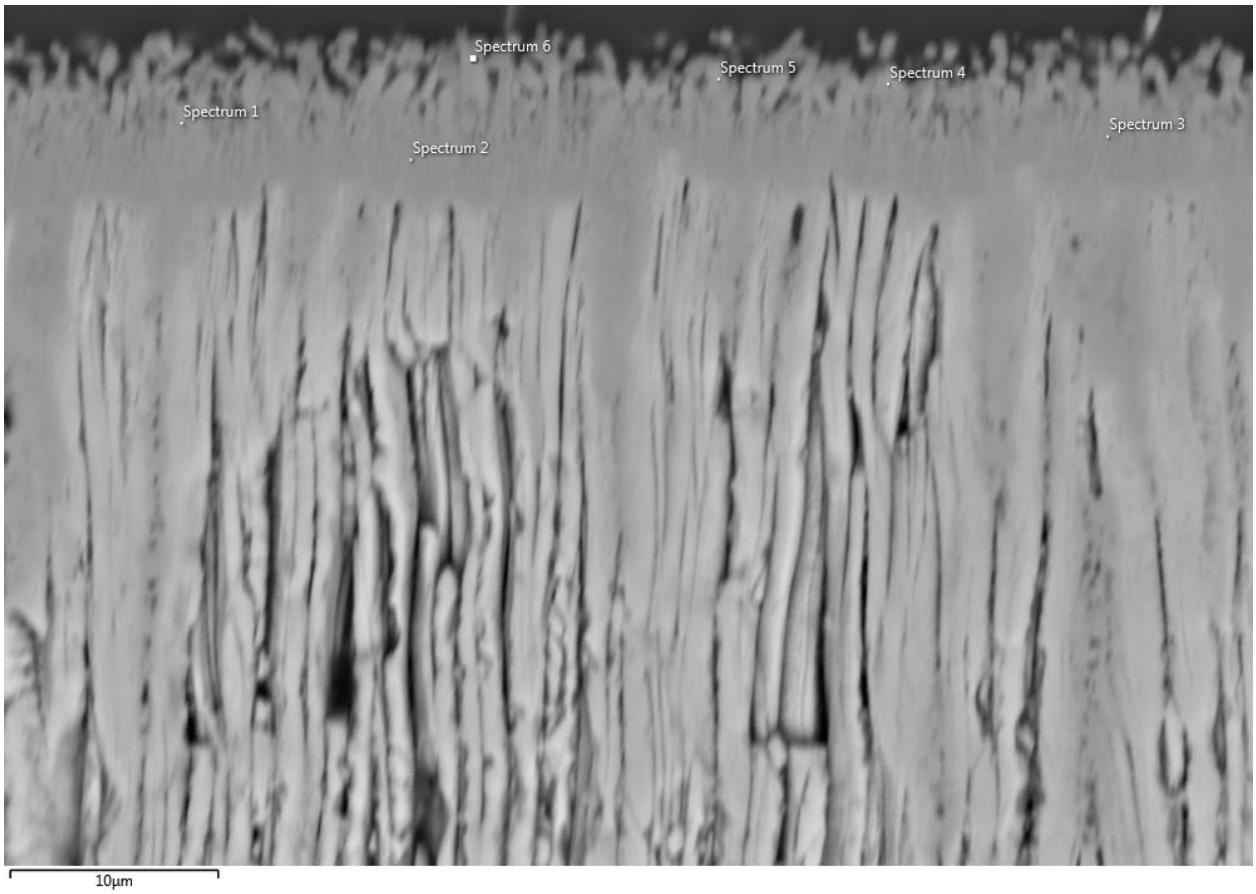

Spectrum	O	Mg	Al	Si	Ca	Y	Zr	Gd
Spectrum 1	46.8	0.0	0.6	14.8	7.2	0.1	6.3	24.3
Spectrum 2	44.9	0.0	0.3	11.1	5.5	0.6	17.2	20.5
Spectrum 3	45.6	0.0	0.3	11.8	5.5	0.5	15.9	20.4
Spectrum 4	46.8	0.6	1.0	16.0	6.7	0.0	8.2	20.7
Spectrum 5	47.9	0.5	1.3	15.6	6.2	0.4	9.4	18.7
Spectrum 6	45.5	0.8	1.7	13.1	5.2	0.9	20.2	12.5

All results in atomic%

Figure 179: ~8 µm thick crystallised phase, arresting further attack.

Separate analyses of the two distinct regions formed within the GZO are shown in Figure 180, confirming the grey region to be reaction product and the white areas to be the core TBC with very little interaction with the molten deposits. It can be inferred from Figure 180 that GZO alters the degradation mechanism compared to 7YSZ by preventing the formation of

porous dark globules and arresting the GZO/CMAS reaction, limiting penetration to a few µm into the coating.

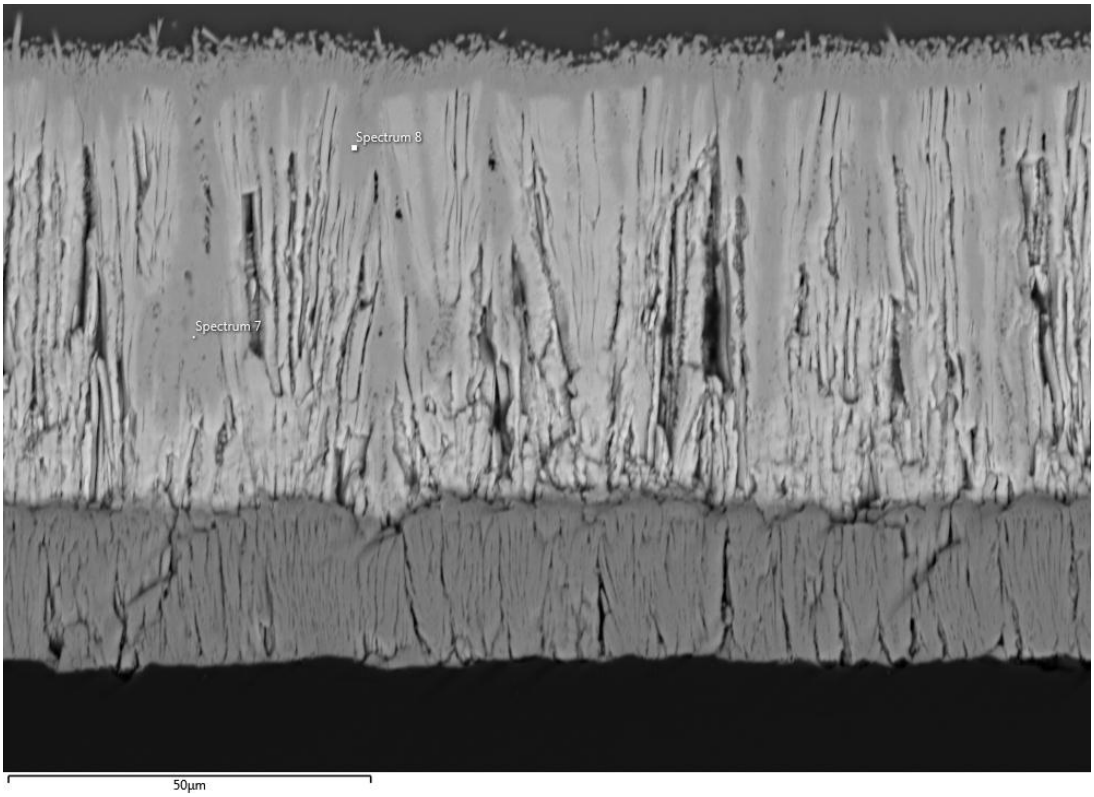

Spectrum	O	Mg	Al	Si	Ca	Y	Zr	Gd
Spectrum 7	44.6	0.0	0.2	11.1	5.4	0.2	12.8	25.7
Spectrum 8	43.3	0.0	0.7	11.6	5.5	0.2	11.6	27.1

(a)

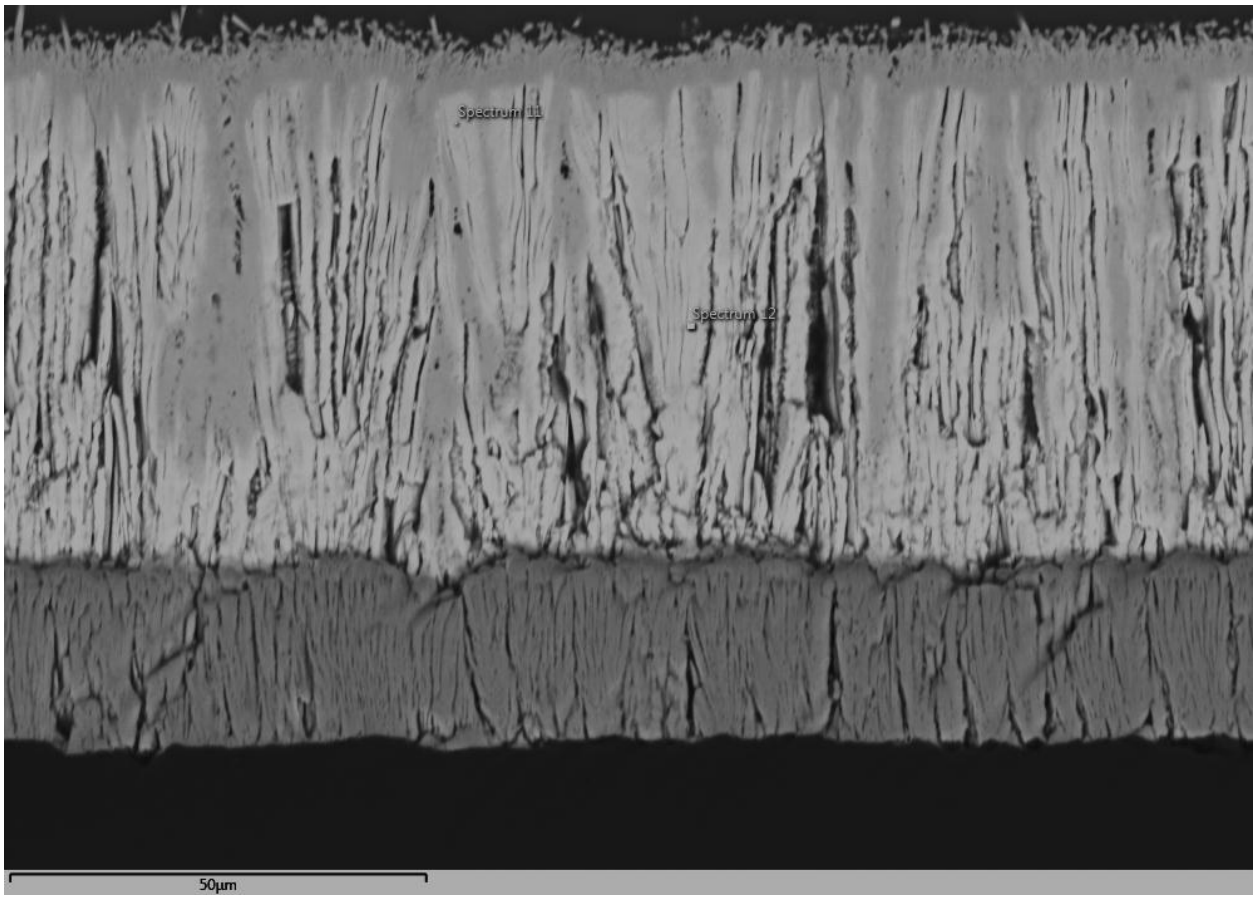

Spectrum	O	Mg	Al	Si	Ca	Y	Zr	Gd
Spectrum 11	42.6	0.0	0.5	0.0	0.3	0.6	22.2	33.9
Spectrum 12	45.8	0.0	1.0	0.0	0.3	0.9	19.9	32.2

(b)

All results in atomic%

Figure 180: Analysis of (a) Grey crystallised phase arresting further attack, (b) Light GZO TBC

Another typical characteristic of Low B.I. attack with zirconia based TBC is the formation of zirconium silicate. Zirconium is said to be amphoteric and depending on the Basicity of the melt, a zirconium-based TBC will either behave as a glass former with a coordination number of 6 or as a modifier, with coordination number 8. The formation of zirconium silicate

indicates that zirconium was behaving in an ionic manner. Confirmation of the zirconium silicate phase is shown in Figure 181.

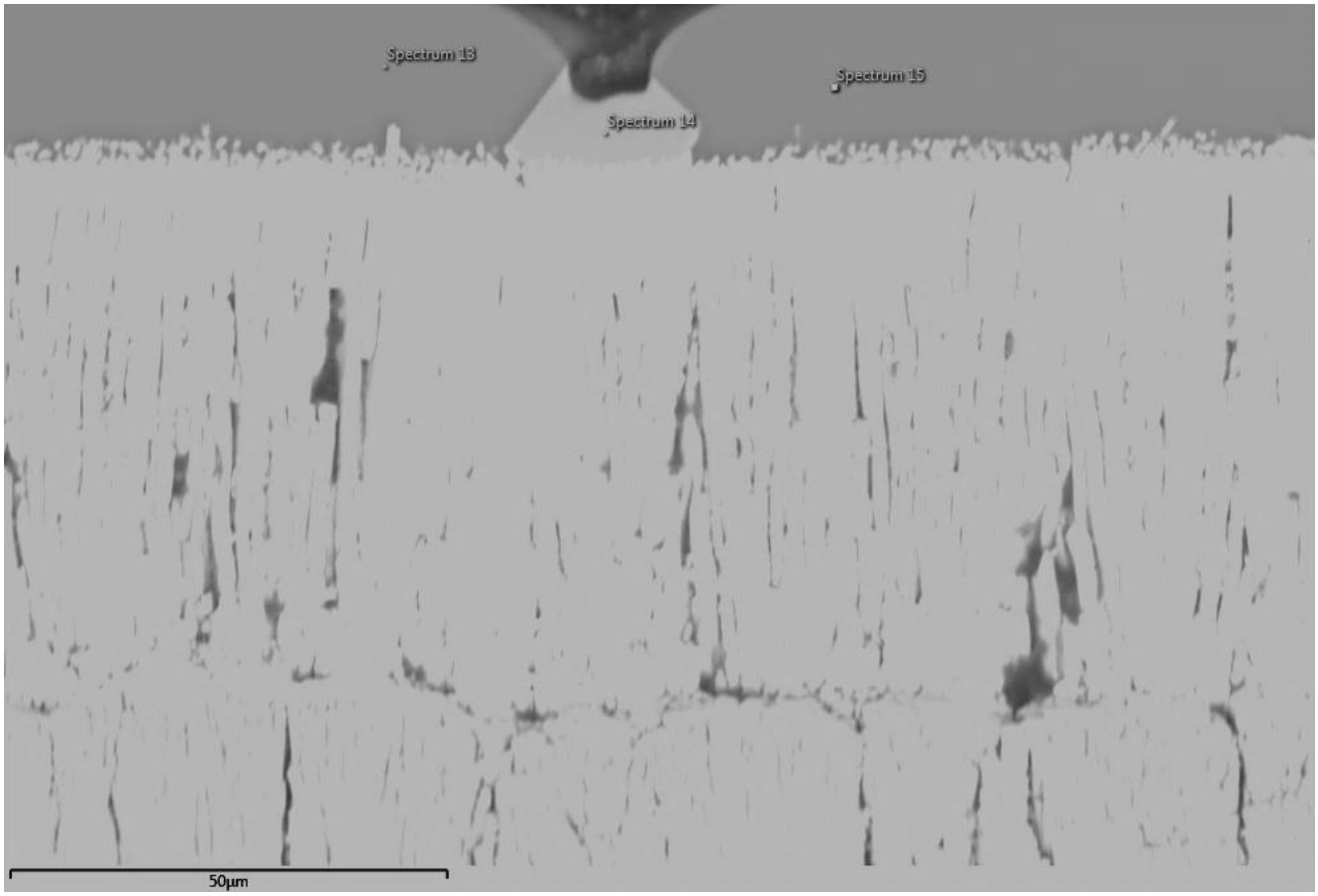

Spectrum	O	Mg	Al	Si	Ca	Y	Zr	Gd
Spectrum 14	46.2	0.0	0.1	26.3	0.1	1.2	24.6	1.6

All results in atomic%

Figure 181: Zirconium silicate, suggesting that zirconium was behaving in an ionic manner.

The composition of CMAS used in the study by Levi et al. [69] had a Basicity Index of 1.08 and sits in the Low B.I. end of the scale. It can hence be inferred that, Low B.I. deposits of varying compositions are expected to show similar (if not identical) attack mechanism and morphology. This is further confirmed by the image in Figure 177 of a molten deposit attack with B.I. of 0.7 showing similar degradation morphology to Figure 174 (B.I. = 1.08).

However, if the concept of Basicity is to be validated, then a different severity of attack is expected with Near Neutral and High B.I. deposits. Gadolinium zirconate as a CMAS resistance TBC has never been tested across the board with different compositions of CMAS from various part of the world. This section of the project examines GZO interactions with Near Neutral and High B.I. deposits.

9.2 Near Neutral B.I. Deposit

For GZO to be considered a suitable CMAS resistant TBC, then it should be able to resist against molten deposit attacks from different sand contents around the world. Near Neutral and High B.I. represent sand/soil contents across the Middle East and North Africa. It has been deduced as part of this project that the current state-of –the –art TBC system (7YSZ) is susceptible to all categories of molten deposit attacks. However, GZO has shown to be resistant to Low B.I. molten deposit attack, but the results with Near Neutral and High B.I. showed significant weakness to this attack mode. Figure 182 shows a sample of GZO infiltrated with Near Neutral deposit and heat treated at 1430 °C for four and eight hours respectively.

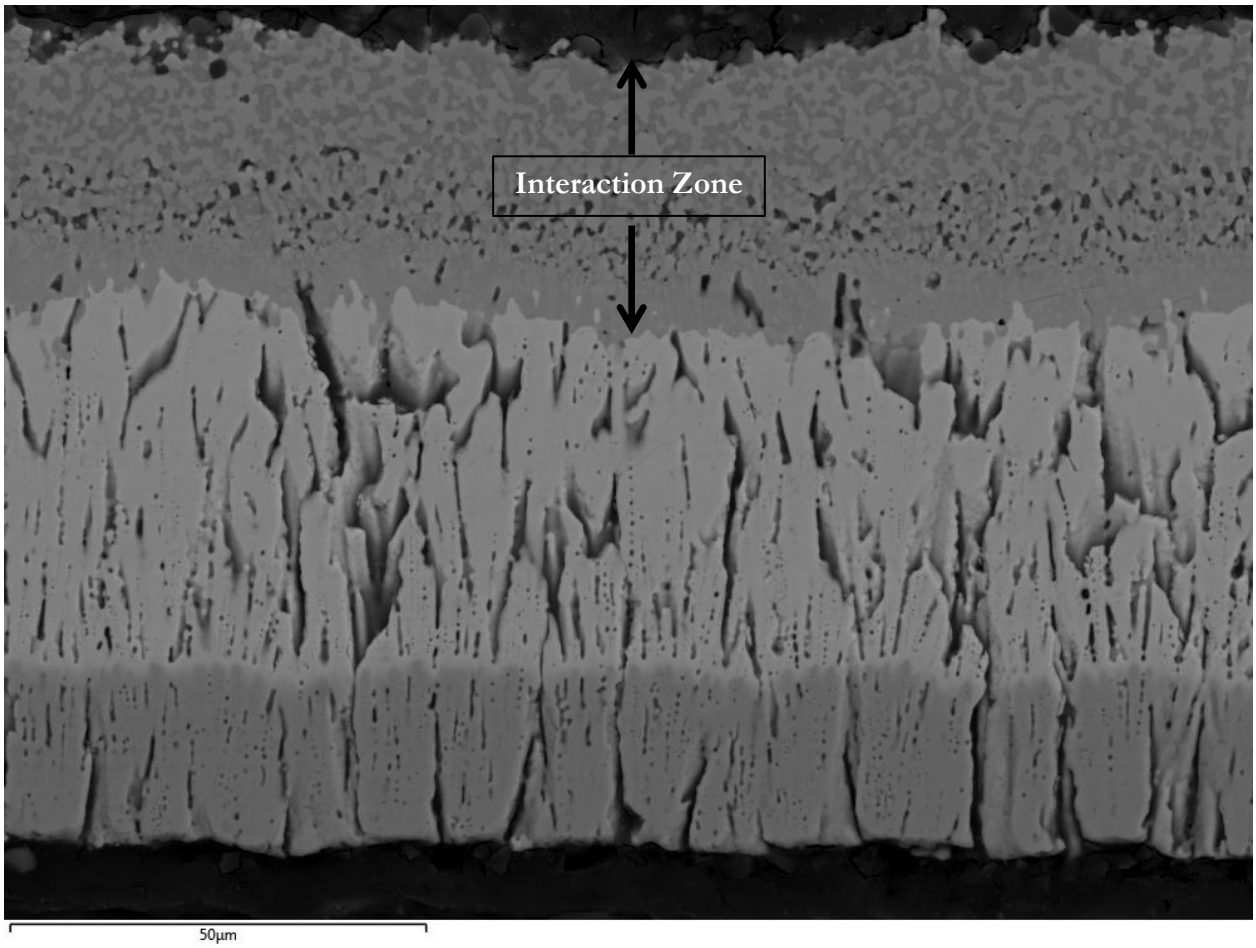

a

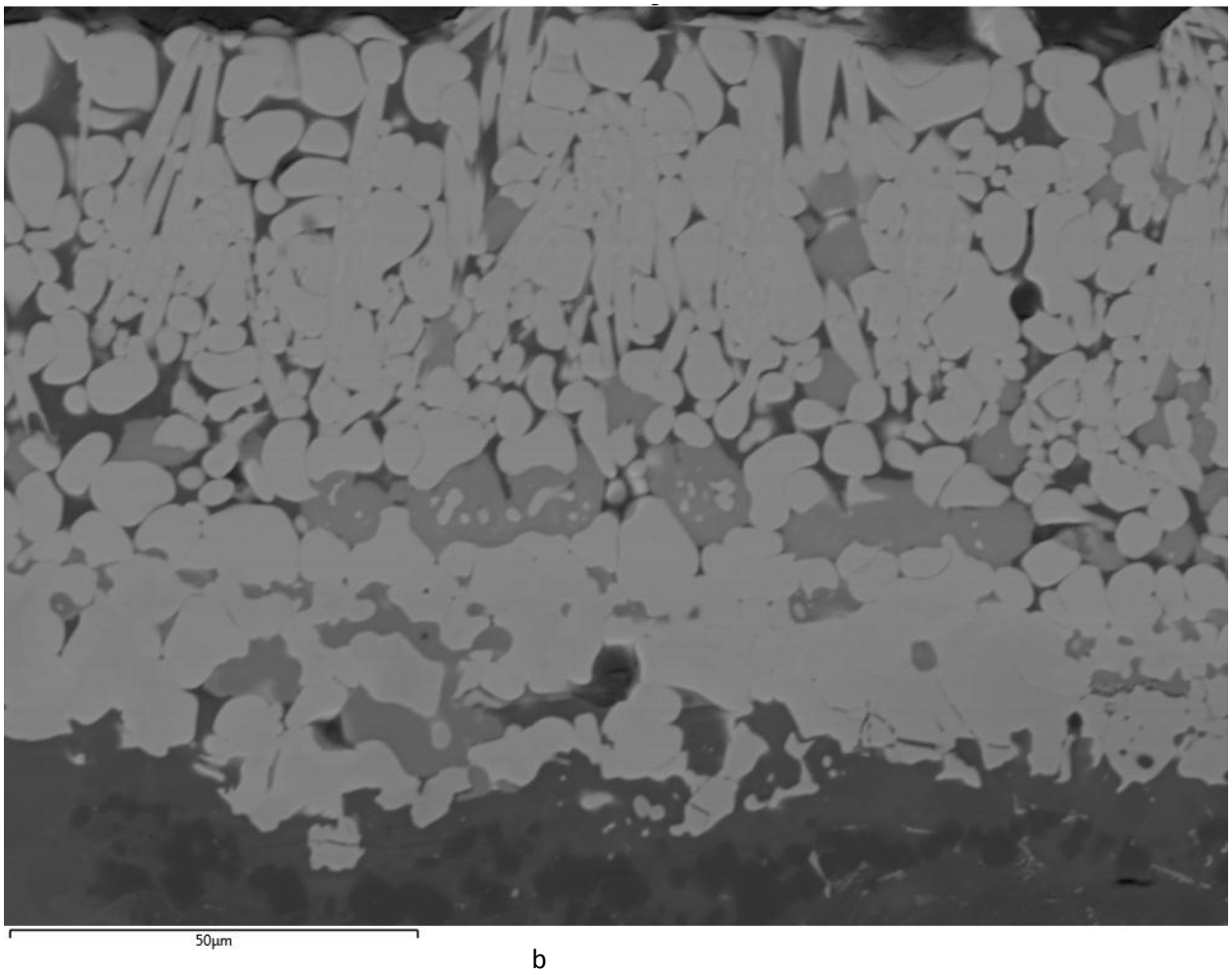

Figure 182: Near Neutral deposit on PYSZ TBC, heat treated at 1430 °C for (a) 4h and (b) 8h

GZO resistance to CMAS attack was tested against Near Neutral deposit and from the results illustrated in Figure 182 it can be inferred that GZO provide limited resistance to this category of attack (Figure 182a) for short exposure time (four hours), showing an increased interaction zone of ~30 µm and a more severe attack. However, the eight hours sample showed adverse degradation through the entire TBC, with complete loss of coating integrity. The coating morphology observed after eight hours exposure indicates that GZO does not mitigate CMAS attack against Near Neutral deposits, as was the case with Low B.I. interaction. Figure 182b shows complete degradation within the GZO part of the coating,

resulting in a binary matrix of round and needle shaped grains. The compositions of the resultant structures were studied and the results are presented in Figure 183.

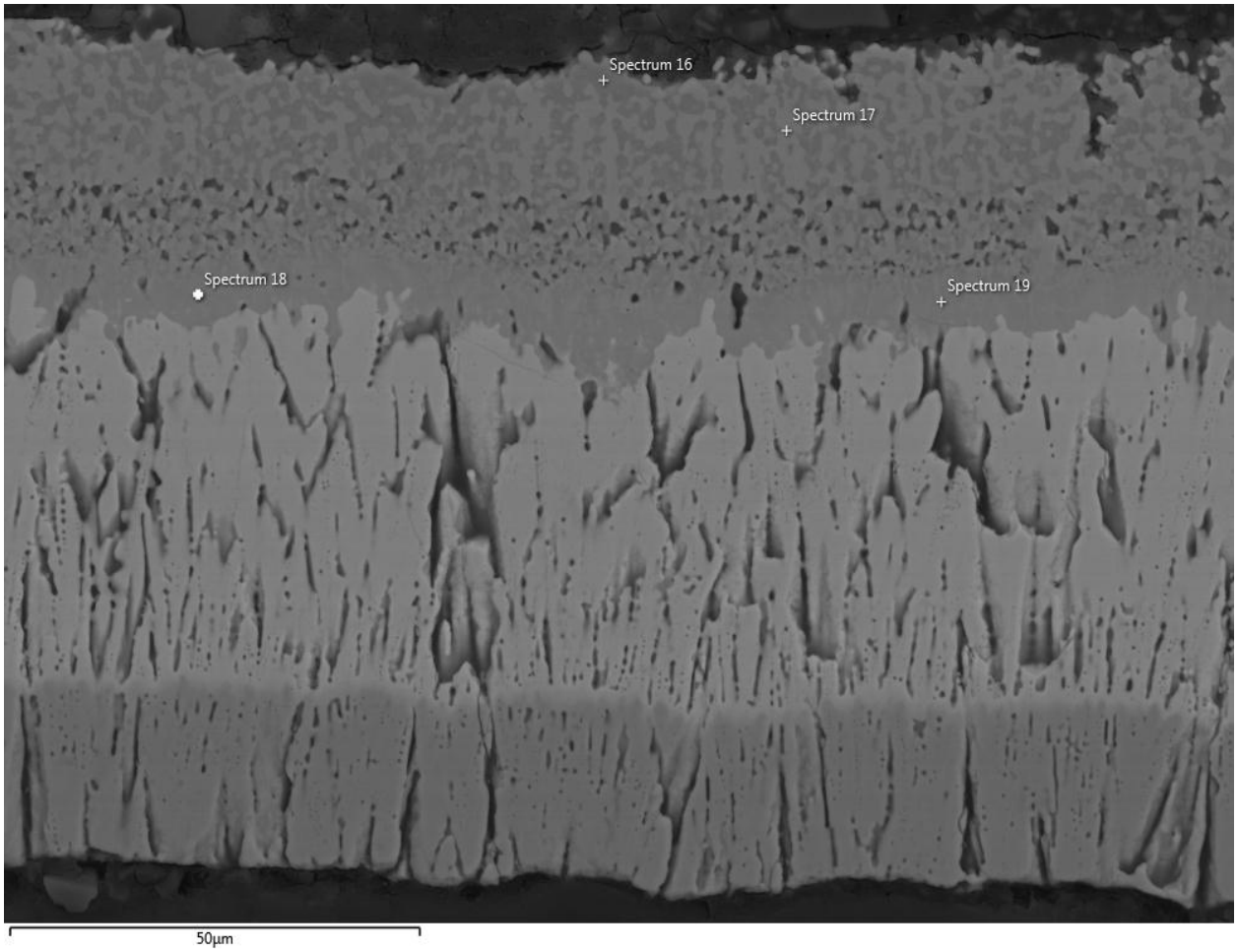

Spectrum	O	Mg	Al	Si	Ca	Y	Zr	Gd
Spectrum 16	32.1	0.9	1.0	0.0	31.4	1.6	26.7	6.0
Spectrum 17	30.9	0.4	8.1	0.0	28.5	1.0	15.4	15.8
Spectrum 18	32.0	0.6	3.2	0.0	25.2	0.4	19.8	18.7
Spectrum 19	33.0	1.6	0.9	0.0	23.5	0.5	22.6	17.9

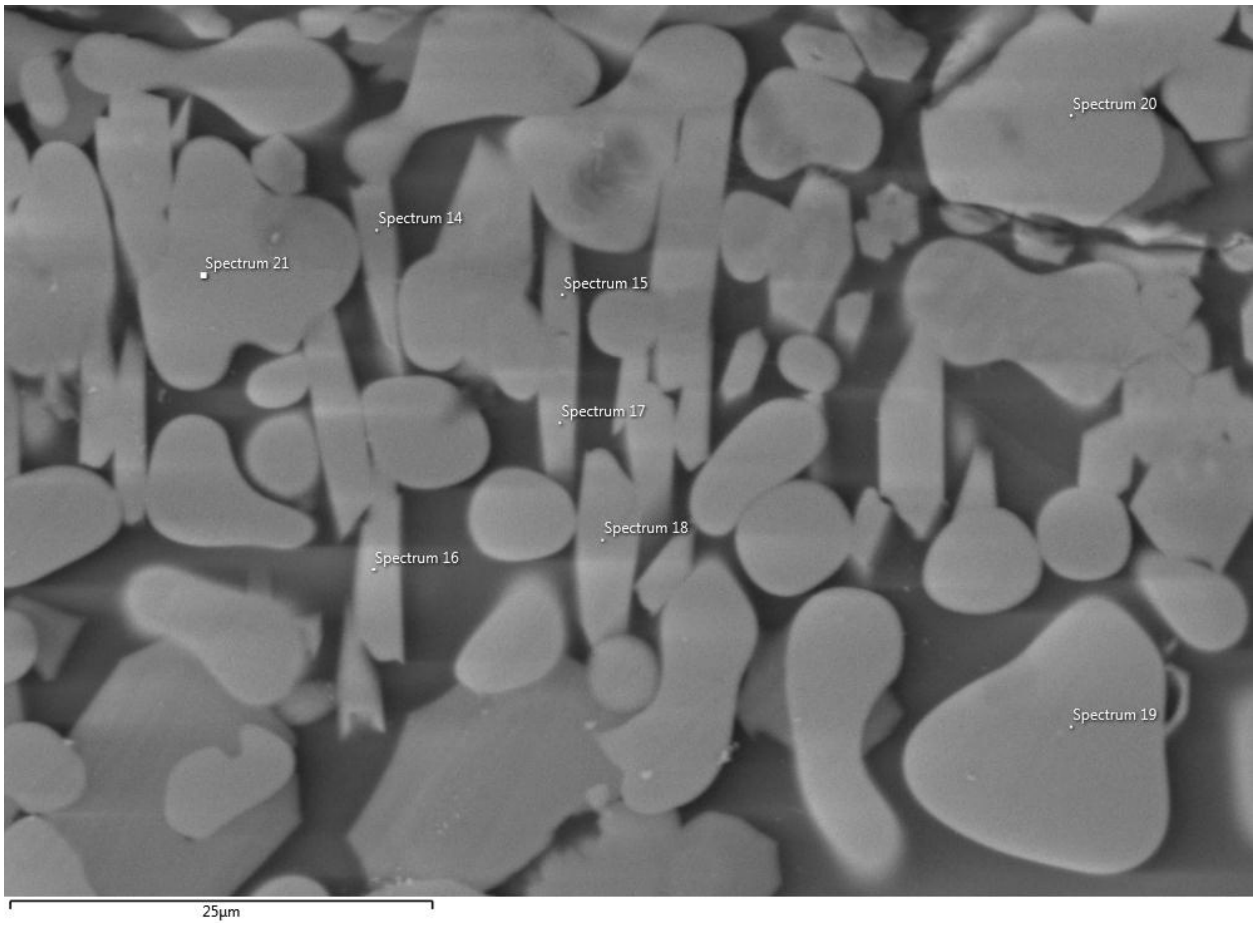

Spectrum	O	Mg	Al	Si	Ca	Y	Zr	Gd
Spectrum 16	59.0	0.0	2.5	14.6	5.7	0.0	0.0	18.0
Spectrum 17	58.9	0.0	1.7	15.4	5.6	0.0	0.4	18.1
Spectrum 18	60.3	0.0	0.9	13.9	5.3	0.4	0.3	19.0
Spectrum 19	60.1	0.0	0.5	0.0	0.8	0.4	25.8	11.9
Spectrum 20	63.0	0.0	0.4	0.0	0.9	0.6	24.1	11.1
Spectrum 21	60.9	0.0	0.2	0.0	0.9	0.7	25.7	11.6

All results in atomic%

Figure 183: 4h and 8h analysis respectively

Based on the results of the chemical analyses of GZO TBC samples infiltrated with Near Neutral deposit, as presented in Figure 183, it was noticed that the reaction product formed was different to that observed for the Low B.I. samples (apatite - $Ca_2Gd_8(SiO_4)_6O_2$).

Although Figure 182a shows a similar mitigation mechanism to Low B.I. samples, the phase formed however was different, a more corrosive flux with significant amount of CaO and a complete lack of Si was found. EDAX elemental analysis (Figure 182b) was used to identify the resulting bi-shaped round and needle structures formed due to complete delamination of the GZO indicating an incapacity to mitigate Near Neutral attack especially at exposure times >4h. The rounded grains were identified as recrystallized GZO while the needle shaped structures were found to be a mullite, as opposed to the apatite phase mentioned by Levi et al. [69] with respect to Low B.I. category.

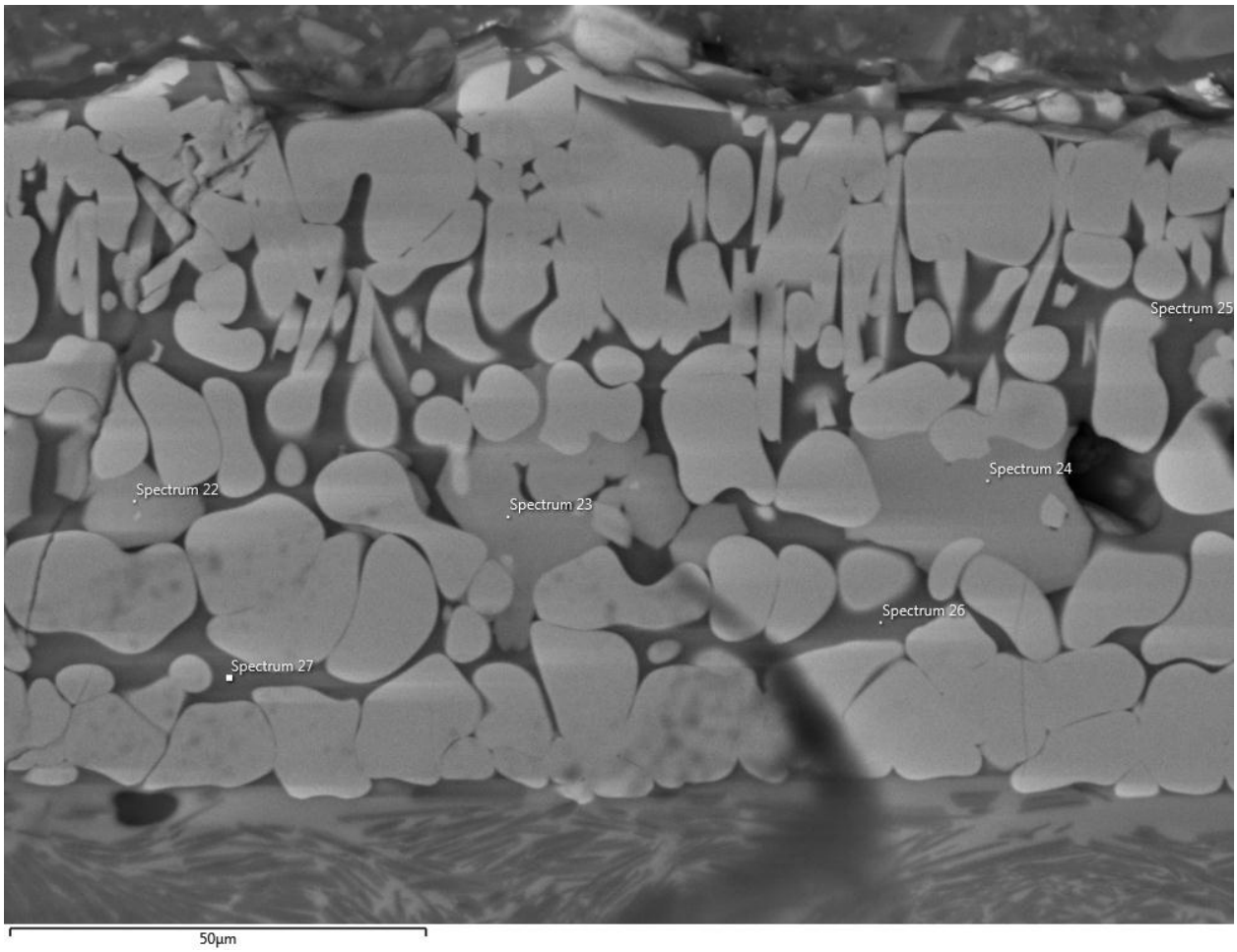

Spectrum	O	Mg	Al	Si	Ca	Y	Zr	Gd
Spectrum 22	56.1	0.0	23.0	2.5	3.8	0.8	1.7	12.2
Spectrum 23	55.5	0.4	23.0	2.8	4.3	0.4	1.9	11.8
Spectrum 24	56.1	0.2	23.2	2.3	4.1	0.6	1.9	11.8
Spectrum 25	57.2	1.3	17.6	11.3	9.4	0.0	0.7	2.5
Spectrum 26	58.2	1.0	16.6	10.6	8.7	0.1	0.9	4.0
Spectrum 27	57.4	1.3	16.2	9.6	8.3	0.0	2.4	4.8

All results in atomic%

Figure 184: Composition of melt matrix of Near Neutral deposit after 8h exposure.

The phase compositions formed in the inter-grain boundaries were studied for the eight hours sample, Figure 184. Two distinctive phases were identified, as illustrated in the tabulated results section by two different highlighted colours. Spectrums 22-24 correspond to the

gadolinium aluminium garnet phase while spectrums 25-27 were identified to fall in the apatite phase. These findings can be summarised as shown in Figure 185 below.

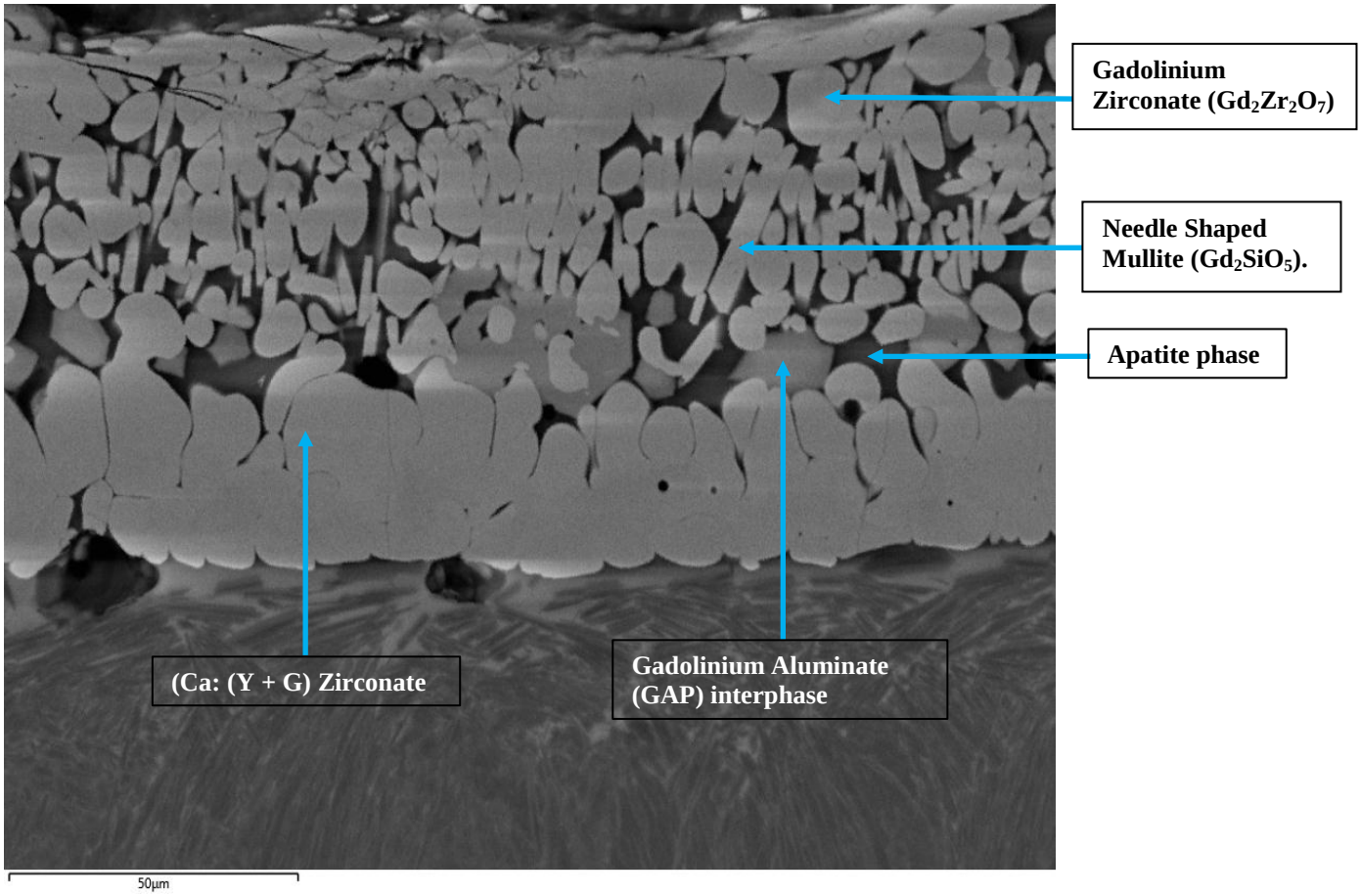

Figure 185: Features identified after 8h exposure at 4h at 1430 °C with Near Neutral B.I.

9.3 High B.I. Deposits

It has been shown so far that GZO provides resistance to Low B.I. degradation but is susceptible to Near Neutral attack mechanism. In order to determine whether GZO will be resistant to High B.I. attack, samples were sprayed with High B.I. deposits and heat treated at 1430 °C for four and eight hours. High B.I. deposit is known to be more aggressive and during testing with 7YSZ, a more severe degradation was observed. Figure 186 are SEM images of two GZO samples infiltrated with High B.I. deposit and aged for four and eight

hours respectively. The morphology of Figure 186a is similar to Figure 182b which is a GZO/Near Neutral sample aged for eight hours. From the findings in this project, High B.I. was shown to be the most aggressive CMAS composition with 7YSZ TBC after very short exposure time, completely disintegrating the entire coating thickness. Although GZO has been shown to mitigate Low B.I. (standard CMAS) attack, it showed very high susceptibility to High B.I. attack similar to YSZ but with different residual features.

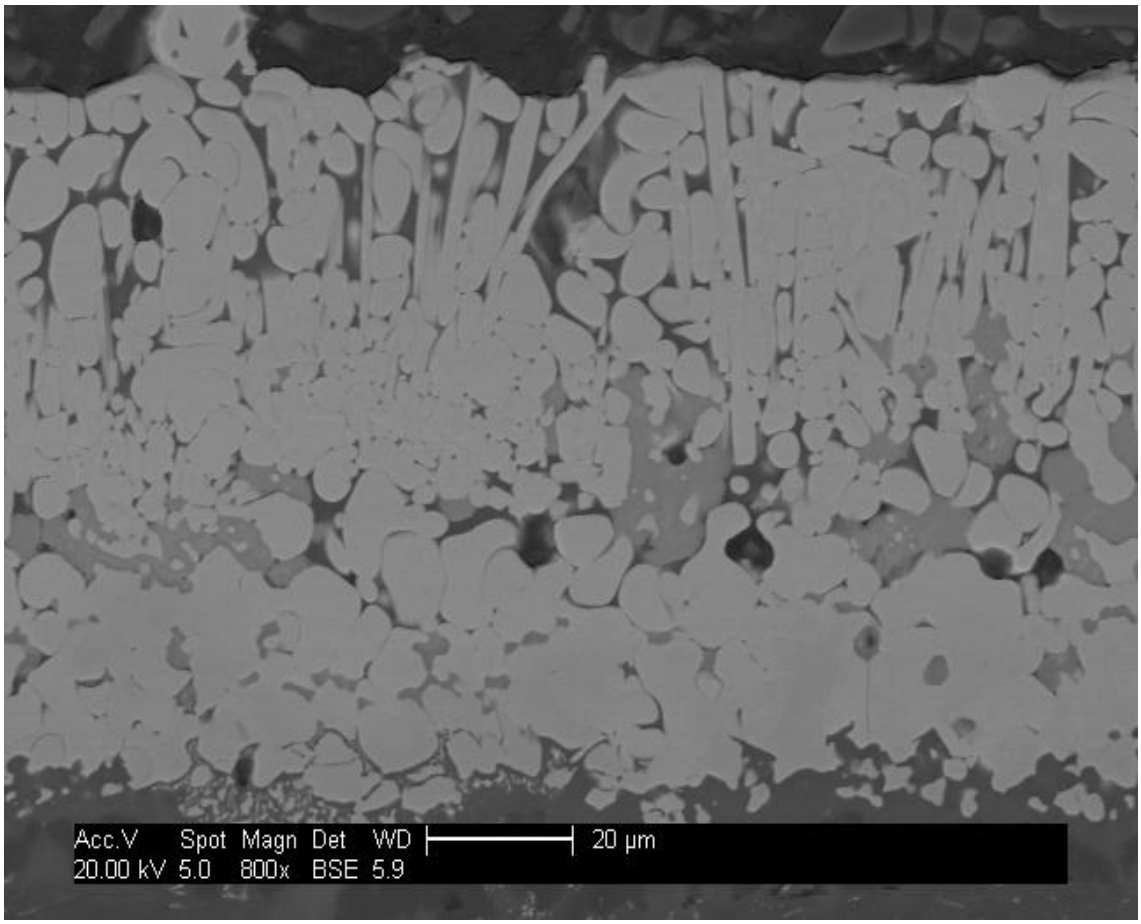

(a)

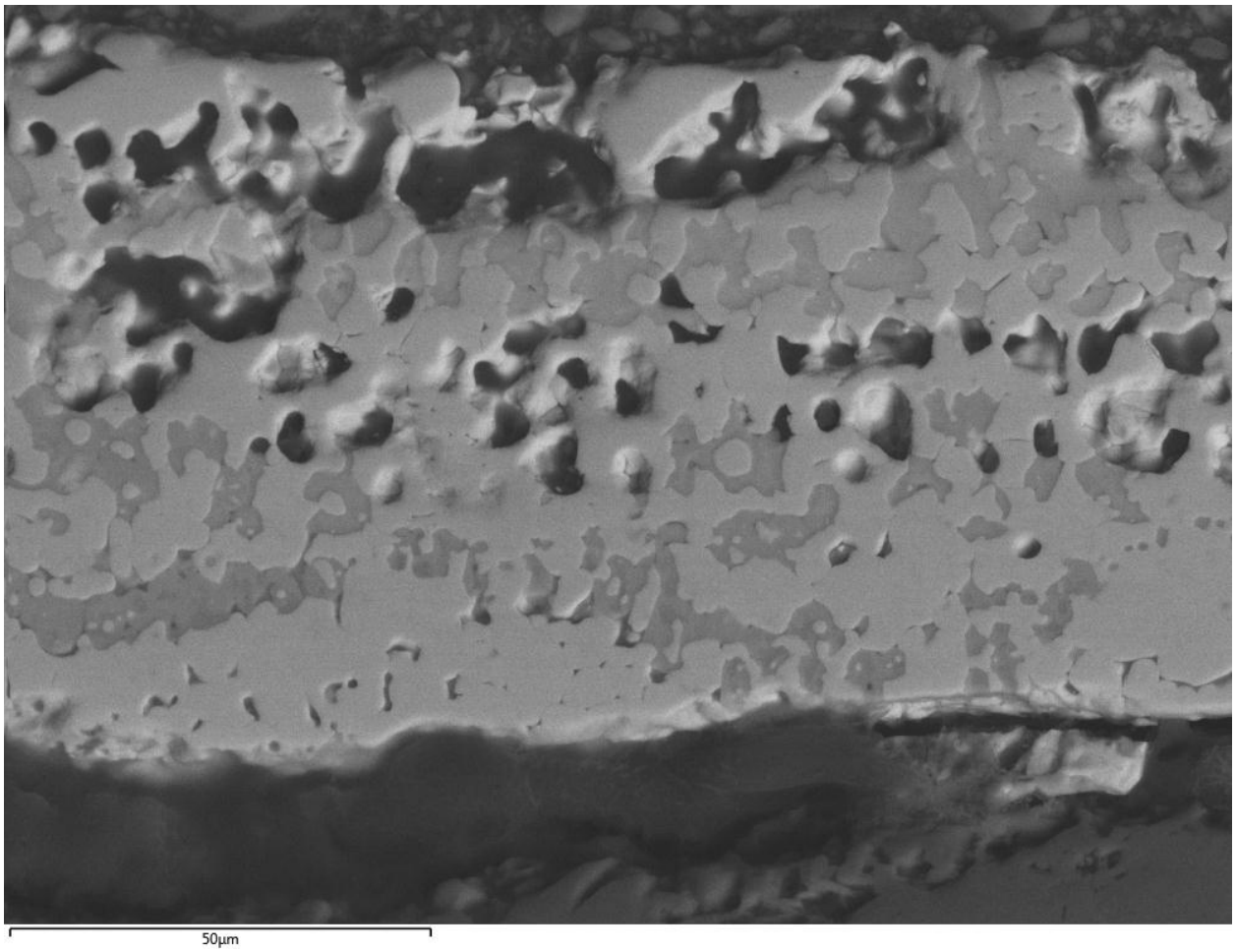

(b)

Figure 186: High B.I. deposit, heat treated at 1430 °C for (a) 4h and (b) 8h

Four hours exposure of GZO with High B.I. deposit revealed a similar morphology to that seen at eight hours with Near Neutral deposit. Figure 186b showed an unprecedented degree of damage, with complete failure of the coating integrity. Once more GZO has failed to provide any resistance to this category of attack, instead showing more severe coating degradation compared to 7YSZ samples under similar conditions.

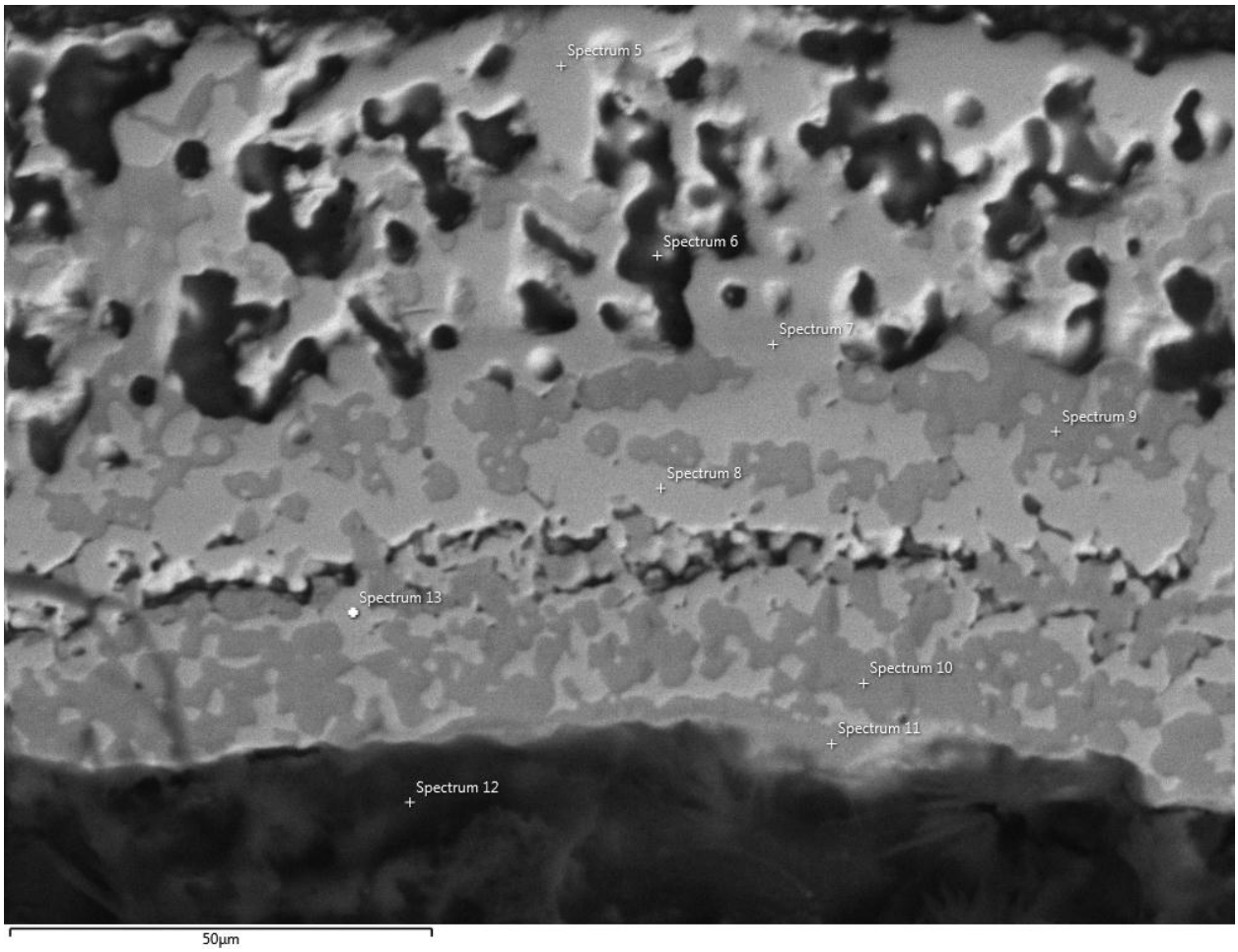

Spectrum	O	Mg	Al	Si	Ca	Y	Zr	Gd
Spectrum 5	38.6	0.0	0.1	0.0	4.1	1.4	28.9	27.1
Spectrum 6	33.9	0.0	0.9	0.2	4.0	1.6	30.6	28.8
Spectrum 7	36.3	0.0	0.0	0.0	3.2	3.0	29.8	27.8
Spectrum 8	43.2	0.4	0.4	0.0	2.9	1.9	30.0	21.1
Spectrum 9	32.9	2.4	7.9	0.7	20.6	1.4	19.4	14.8
Spectrum 10	34.7	0.0	6.1	0.3	28.0	1.3	24.5	5.0
Spectrum 11	42.7	1.3	16.8	1.7	16.2	1.3	13.0	7.0
Spectrum 12	73.4	0.4	4.6	9.8	10.2	0.0	1.3	0.3
Spectrum 13	41.0	0.0	0.9	0.0	5.8	2.1	31.5	18.7

All results in atomic%

Figure 187: Analysis of High B.I. sample exposed for 8h.

GZO was found to dissociate in High B.I. melt with gadolinia appearing to indicate a very high solubility in High B.I. Significant amounts of gadolinia were noticed to have dissolved in the melt, increasing the aggressiveness (Basicity Index) of the melt and exposing the residual zirconia to the harsh composition of the local melt.

It can be concluded from this study that, GZO negates Low B.I. attack by forming a crystallised apatite phase which was seen to arrest the reaction and by so doing, preventing the reaction product from being absorbed by the coating. However, this was inverted with Near Neutral and High B.I. attacks, with GZO providing little or no protection with a detrimental outcome. GZO readily dissociates in High B.I. melt, with a significant amount of gadolinium retained in the melt. The aggressivity of the melt then increases, as shown herein, zirconia is severely vulnerable to attack by basic deposits and a similar trend was observed for GZO, with the column morphology completely deteriorated. From the results obtained, it can be inferred that more understanding is required in order to develop thermal barrier coatings that are resistance to all categories of CMAS attack. There is a tendency that, a TBC that resists Low B.I. attack in a certain part of the world will become susceptible if exposed to Near Neutral or High B.I. type deposits in other regions of the world, which can result to loss of performance and increased thermal conductivity. Also, the resultant structure is very brittle and the fracture toughness is severely reduced, resulting in the coating spalling.

The adopted concept of Basicity Index have been shown in this study to be a tool capable of predicting the mechanism and severity of CMAS attack, in terms of microstructural degradation. High B.I. CMAS deposit was found to be the most aggressive deposit hence resulting to the most severe TBC degradation whereas Low B.I. was the least damaging CMAS composition and showed the least microstructural damage. The hypothesis that the severity of CMAS damage is dependent on Slag Basicity is thereby supported.

Results Summary

- Three Low B.I. deposits with different Basicity were studied in this project. Similarly, most CMAS compositions in open literature fall into this B.I. category. In all cases, the attack mechanism was very similar, all displaying “classic” CMAS attack characteristics.
- The aggressiveness of Low, Near Neutral and High B.I. deposits has been shown to increase with increasing Basicity Index of the deposits.
- Near Neutral and High B.I. both showed a different degradation mechanism to Low B.I. attack
- Degradation of zirconia based TBC’s by Near Neutral and High B.I. molten deposits showed similar attack mechanism but with different degree of severity.
- Free-standing TBC with no substrate was used to investigate whether or not the alumina substrate had an effect on the degradation mechanism. The results were identical to the TBC with substrate samples, suggesting that the substrate did not influence the degradation mechanism although Near Neutral and High B.I. deposits both attacked the substrate and released excess Al into the melt, which forms a low melting eutectic hence lowering the temperature at which degradation attack initiates.
- GZO was found to alleviate Low B.I. attack. However, this was inverted with Near Neutral and High B.I. attacks, with GZO providing little or no protection with a detrimental outcome. GZO readily dissociates in High B.I. melt, with a significant amount of gadolinium retained in the melt and the aggressiveness of the melt increases.
- It has also been shown in this study that small amounts of CMAS infiltration significantly increases the erosion rate of EB-PVD TBCs due to the deterioration of columnar identity as a result of CMAS degradation, which also reduces the strain compliance of the coating.

10 Conclusion

A novel technique of assessing the mechanism and severity of damage is introduced, by adopting the concept of Basicity Index (B.I.). Here, Basicity Index has successfully been applied to ceramic chemistry in understanding molten deposits degradation of ceramic coatings. From the results obtained in this project, it can be concluded that the Basicity Index (B.I.) of CMAS is an important parameter that will influence the mechanism of molten deposit attack of TBC's. The Basicity Index of the melt will determine the attack mechanism and severity of damage, influencing both the degraded coating morphology and depth of penetration. Three categories of Basicity Index of CMAS were proposed and corroborated in this project, based on soil composition across the world.

CMAS as well as volcanic ash compositions that are likely to be ingested by an aircraft engine will either be a Low, Near Neutral or High basicity deposit. Hence by understanding the behaviour of the individual categories, a degradation map can be developed as an aid to predict the likely degradation morphology of zirconia based TBC's from various parts of the world. The following conclusions have been drawn from this study;

- Three Low B.I. deposits (Eyjafjallajokull volcanic ash, $C_{24}M_{10}A_7S_{59}$ and $C_{35}M_{10}A_7S_{48}$) with different Basicity Indexes (0.46, 0.69 and 1.08 respectively) were studied in this project. Similarly, most CMAS compositions in open literature fall into this B.I. category. In all cases, the attack mechanism was very similar. Low B.I. mechanism comprises of silica in the melt reacting with the TBC, leading to complete dissolution of the column tips and attack along the TBC columnar boundaries, leaching Y_2O_3 from the ZrO_2 grains. The depletion of yttria destabilises the TBC and instigates a zirconia phase transformation from metastable tetragonal phase (t') to monoclinic phase (m) (t' → m + F), but in different proportions at different depths into the TBC columnar structure. This is true for

all Low B.I. deposits, regardless of the CMAS chemistry. This can be thought of as "classic" CMAS attack.

- The aggressiveness of Low, Near Neutral and High B.I. deposits has been shown to increase with increasing Basicity Index of the deposits. Basicity – Viscosity model (Figure 31) predicts High B. I. melt to be less viscous than Low B. I., which was found to be the case in this study, with Low B.I. deposits forming a viscous glass at the surface of the sample (Figure 86) while High B.I. melt quickly formed a melt pool at the bottom of the coating. The driving force behind Near Neutral and High B.I. degradation mechanism is viscosity.
- Degradation of zirconia based TBC's by Near Neutral and High B.I. molten deposits showed similar attack mechanism but with different degree of severity because the High B.I. deposits are more aggressive than Near Neutral deposits, resulting in more severe degradation. Near Neutral and High B.I. deposits both formed a melt pool at the TBC/substrate interface (at different rate; High B.I. ≤30 minutes, Near Neutral B.I. ≥2h) which destabilises the alumina substrate, releasing excess Al into the melt. Excess Al creates low melting eutectic and a "melting point" gradient is established between the melts on the surface of the sample and the melt pool. Attack is initiated at the bottom of the coating, in the low melting, super-saturated melt pool. However, due to the aggressiveness of High B.I. melts, the Al substrate is severely attacked, creating an Al-depleted zone in the substrate. Free-standing TBC with no substrate material was used to investigate the effect of the excess Al on the degradation mechanism. However, the results were identical to the TBC with substrate samples, suggesting that excess Al in the melt does not influence the degradation mechanism although it lowers the degradation temperature at which attack initiates.

- Due to the aggressiveness of the melt, High B.I. attack mode was shown to be bi-directional. High B.I. attack was noted to be ~x2 more severe than Near Neutral attack. For example the degradation morphology after 4h exposure with High B.I. deposit was comparable to 8h exposure with Near Neutral deposit.
- The high content of CaO in Near Neutral and High B.I. melts acts as a "sintering aid", which helps to bind the columns together. This mechanism of attack is characterised by complete dissolution of the TBC into the melt matrix and recrystallization, to form a completely new microstructure of calcium zirconate or Ca-doped PYSZ, depending on the composition of the surrounding melt. The rounded grain morphology that results can be attributed to the wetting characteristics and the minimisation of surface energy (interfacial tension) between the newly formed grains and residual molten slag compositions.
- Near Neutral and High B.I. attack does not result in a monoclinic phase transformation observed in Low B.I. attack. This is partly due to Ca in the melt being absorbed by the PYSZ, which further stabilises the tetragonal phase, as well as the amphoteric behaviour of zirconia (zirconia is partly covalent and partly ionic). In an acidic (Low B.I.) melt, zirconia assumes an ionic role with a coordination number of 8. This is further confirmed by the characteristic formation of a zirconium silicate phase in Low B.I. degradation. However, in a more basic (High B.I.) melt, zirconia acts as a glass former (in a covalent manner), with a cation coordination number of 6. Confirmation of this characteristic was seen in the formation of calcium zirconate in High B.I. attack mode.
- Due to Al affinity for Mg, a magnesia spinel layer is formed in Near Neutral and High B.I. attacks, possibly introducing a dual failure mode of coating degradation and spallation due to attack at the interface. The very aggressive High B.I. melt significantly infiltrates the substrate, altering the composition of the substrate, creating an Al depleted

zone within the Al_2O_3 substrate. With High B.I. attack, there is certainly a possibility of thermal and/or chemical damage to the TGO, potentially extending to the bond coat in engine conditions. Sufficient adhesion between the TBC/substrate interfaces is critical for the functionality of coated part.

- By using free-standing samples, the effect of B.I. variations was isolated to the CMAS/TBC interaction, with respect to time and temperature and the potential influence of the substrate was negated. It can be inferred from this study that, GZO alleviates Low B.I. attack by forming a crystallised apatite phase which was seen to arrest the reaction, by so doing preventing the reaction product from being absorbed by the coating. However, this was inverted with Near Neutral and High B.I. attacks, with GZO providing little or no protection with a detrimental outcome. GZO readily dissociates in High B.I. melt, with a significant amount of gadolinium retained in the melt and the aggressiveness of the melt increases. It has been shown that zirconia is vulnerable to attack by basic deposits and a similar trend was observed for GZO, with complete deterioration of the columnar identity.

Basicity Index model is a great tool in the fight against CMAS infiltration of TBCs due to the apparent need to increase the turbine entry temperature, especially with recent developments in producing low thermal conductive (low k) TBCs. CMAS attack remains an obstacle in the need to increase the operating temperature of next generation aero engines and realising the benefits it brings (SFC and greenhouse emission). Mitigating solutions to TBC microstructural degradation caused by CMAS have so far been reactive, rather than incorporating molten degradation problems during the design stage. Engine manufacturers have been clever in the past and customise engine hardware depending on part of the world the aircraft is operating, to mitigate against erosion damage. In order to make the transition from mainly reactive as it has been in the past, towards predictive with proactive solutions for

CMAS problems, the concept of Basicity Index may be used to predict the severity of TBC damage expected in various regions of the world based on the aggressiveness of the respective sand chemistry and a mitigating solution incorporated during design. From the results obtained in this study, the morphology of attack of an EB-PVD TBC, as expected from various regions in the world, is mapped in terms of the Basicity scale, Figure 188.

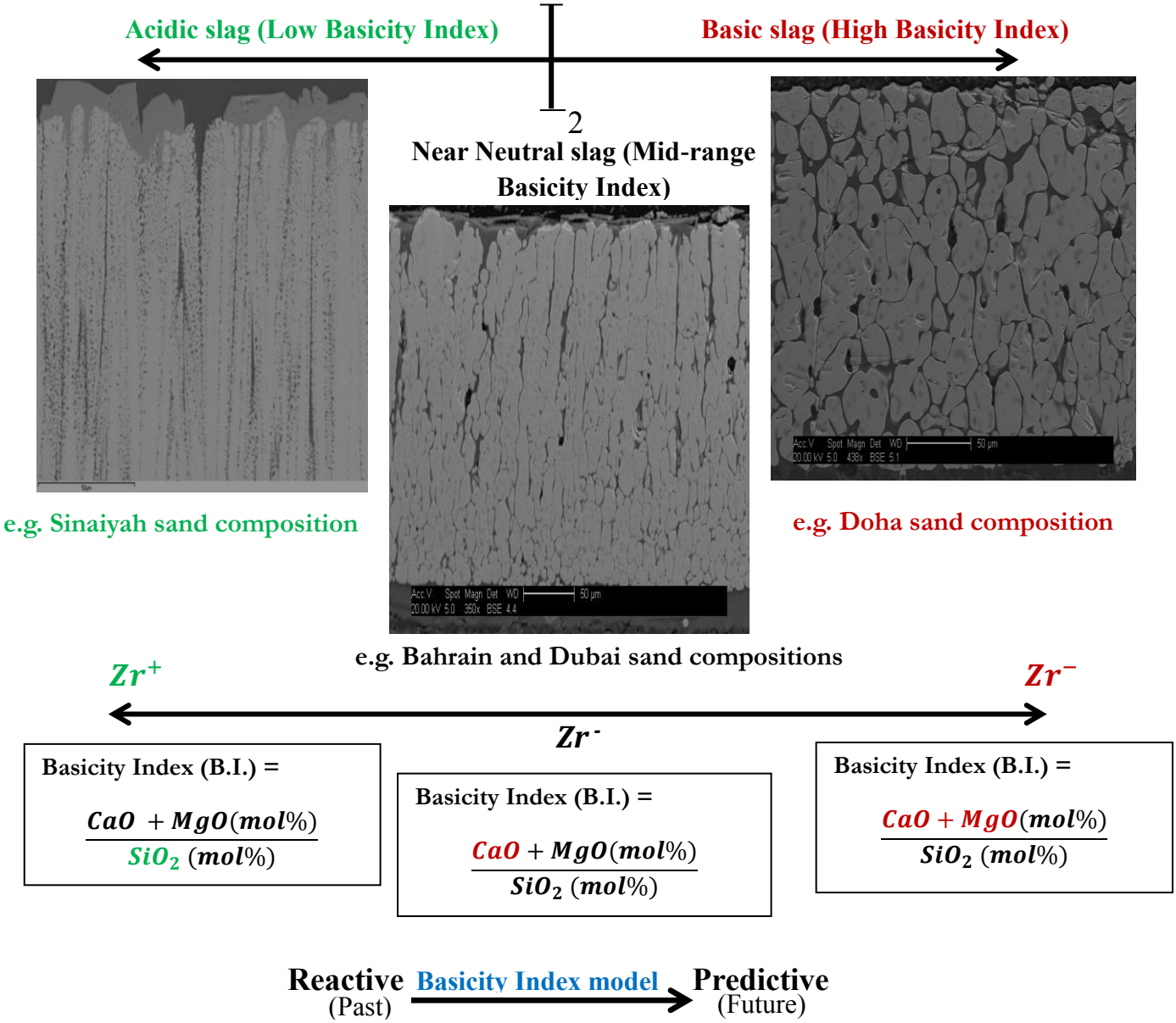

Figure 188: A Reactive – Predictive model illustrating different mechanisms of CMAS attack on EB-PVD TBC based on sand/B.I. chemistry from across the world.

Chapter 10: Conclusion

A series of erosion tests with volcanic ash and similar sized MIL spec silica sand have been undertaken on two compressor materials; Ti64 and IN718. It has been shown that:

- The erosion behaviour of volcanic ash was not strongly dependent on particle size. Three size fractions were evaluated; 0-53 µm, 53-106 µm and 106-212 µm. Over this range of sizes the erosion rate differed by less than 20%. The erosive response of volcanic ash behaved in a very similar manner to fine silica sand, which had a particle size between 0-150 µm. Coarser silica sand particles, behaved differently with increased erosion at 90°, compared to the fine silica sand. Fine silica sand was marginally more erosive than the volcanic ash particles at 30°, 45° and 90°, the impact angles studied in this project.
- The impact angle dependence for both Ti64 and IN718, when impacted with volcanic ash was that expected for ductile erosion, with a peak in erosion rate at 30°, irrespective of particle size, when accelerated in a gas stream at 250 m/s.
- With volcanic ash behaving similar to fine silica sand and peak erosion rates at 30° impact (ductile erosion) the effect of increased gas velocity was studied under these conditions. These results show a close similarity in erosion response between volcanic ash and fine silica sand at all gas velocities studied. Erosion performance differed by typically 20% between these two types of particle when tested at similar particle size. The only noticeable difference was that at 250 m/s fine silica was more erosive than similar sized volcanic ash, whereas at gas velocities of 210 m/s and below volcanic ash was marginally more erosive than fine silica sand.
- At 450 °C, under the same gas pressure within the erosion rig, volcanic ash was more erosive than at room temperature. The erosion rate was increased by approximately a factor of x2 for ductile erosion at 30° impact. At 90° impact the erosion rate changed little between the room temperature test and the test at 450 °C. These results are

consistent with volcanic ash behaving like fine silica sand both at room temperature and 450 °C. The measured erosion rates are consistent with a ductile erosion mechanism with peak rates of material loss for impact angles close to 30°. The results, both at room temperature and 450 °C, would appear to fit classic ductile erosion models where the material loss on particle velocity follows a power with an exponent close to 2. For volcanic ash the exponent was calculated to be 1.7-1.8, whereas, for fine silica sand it was calculated to be 2.3-2.4.

- It has also been shown in this study that small amounts of CMAS infiltration significantly increases the erosion rate of EB-PVD TBCs due to the deterioration of columnar identity as a result of CMAS degradation, which also reduces the strain compliance of the coating.

11 Future Work

- Further exploit the thermodynamic effect; viscosity and wettability, as contributory parameters in CMAS attack mechanisms. It has been established that viscosity affects the melt's penetrating ability and wettability will determine the tendency of the melt to stick and infiltrate by capillary action. However, their interacting effect is not fully understood hence further work is required to understand the effect of that different CMAS viscosity and wettability has on the reactivity.
- Thermal gradient CMAS test: in this current study, all tests were done under isothermal heat treatment condition. However, in order to replicate engine conditions, CMAS testing should be aimed under a thermal gradient. Hence it is suggested that, more work be carried out to determine the practical depth of CMAS penetration under a thermal gradient, as it is the case in service, as well as whether the detrimental melt pool will form at the bottom of the coating interface.
- Basicity and melting point relationship: the High B.I. CMAS compositions studied in this project have shown very high melting points. However in reality, environmental dust ingested by the engine will contain significant amount of iron oxides as well as alkali-metal oxides, both of which lower the melting point of the deposit. Stott et al. [69] study noted variation in composition and melting temperatures of Middle Eastern sand chemistry (all belonging in the High B.I. category), with some melting as low as in the 1200 °C. So it is suggested as a future work to understand the effect adding melting point depressors elements such as Fe, Na and K has on the mechanism and severity of CMAS attack on EB-PVD TBCs.
- Study novel TBCs resistivity on Near Neutral and High B.I. attack. It is shown in this study that CMAS resistant TBC that mitigates one category of attack can remain susceptible to different categories of CMAS attack. This was shown to be the case with

gadolinium zirconate (GZO) which provided some degree of CMAS resistance to Low B.I. attack, by arresting the CMAS reaction to a short interaction zone. However, very little or no protection was provided with Mid B.I. CMAS and was completely disintegrated by High B.I. It is proposed here that, novel CMAS resistant TBC compositions should be tested against all categories of CMAS and reference provided accordingly. In this case, GZO in can rightly be termed Low B.I. resistant TBC. Low, Mid and High B.I. CMAS compositions should be tested against novel TBC composition in an effort to better understand the reaction kinetics and help towards the development of an all-round CMAS resistant TBC.

- Develop the concept of 2, 3, 4 TBCs for low k and CMAS resilience. The concept of 2, 3, 4 has been proposed as possible composition for a CMAS resistant TBC. Zirconia is the current preferred TBC main element. However, zirconia based TBC was found in this study to be amphoteric which makes it susceptible to both Low B.I. (acidic) and High B.I. (basic) CMAS composition. By employing the 2, 3, 4 dopant, it is suggested that 2^{+} will stabilise zirconia in a basic (High B.I.) melt and 3^{+} will stabilise zirconia in a Low B.I. (acidic) melt. More work is needed to exploit this theory.

Appendix A

Basicity Index Calculation

Table **A1**: B.I. Calculation Based on CMAS Composition Shown Below

Content	**CaO**	**MgO**	**Al_2O_3**	**SiO_2**
Composition (mol.%)	35.0	10.0	7.0	48.0
Oxide type	Basic	Basic	Amphoteric	Acidic

$$\text{Basicity index (B.I.)} = \frac{\sum Basic\ oxides\ (mol\%)}{\sum Acidic\ oxides\ (mol\%)} \qquad \text{Equation A1}$$

In this study, Basicity is modified to acknowledge that amphoteric oxides may exhibit either acidic or basic roles.

- In a binary CaO – SiO_2 slag system, neutral slag corresponds to the formation of $2CaO.SiO_2$, making the B.I. for a neutral slag to be equal to 2.
    - Hence CaO/SiO_2 ratio < 2, amphoteric oxides behaves in a basic manner while for a CaO/SiO_2 ratio > 2, amphoteric oxides will be treated as an acidic oxide.
- The implication of this is that amphoteric oxides provide a buffer such that a neutral slag may exist over a range of compositions. In this study, the range is taken as 1.8 to 2.2, a ±10% variation on the neutral composition known as the Near Neutral B.I. value.

Based on the modified definition of B.I. in this study, the B.I. calculation from the composition shown in Table A1 is given below;

$$\frac{CaO\ mol.\%}{SiO_2 mol.\%} = \frac{35}{48} < 2;\ \rightarrow Amphoteric\ oxide\ (Al_2O_3) \equiv Basic\ oxide.$$

$$\text{Basicity index (B.I.)} = \frac{\sum Basic\ oxides\ (mol\%)}{\sum Acidic\ oxides\ (mol\%)} = \frac{CaO+MgO+Al_2O_3}{SiO_2} = \frac{35+10+7}{48}$$

B.I. = 1.08, belonging in the Low Basicity Index category on the B.I. scale shown below.

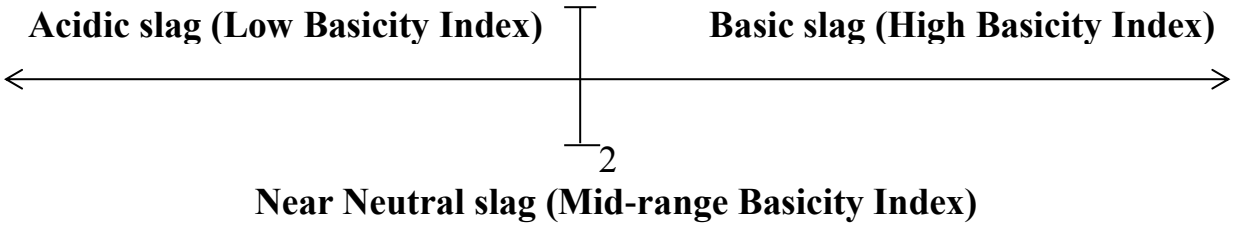

Near Neutral slag (Mid-range Basicity Index)

Figure A1: The Basicity Index Scale

Appendix B

The Viscosity Model

Giordano et. al. [163] developed a comprehensive viscosity model for the measuring the viscosity of silicate-rich melts (SiO_2, CaO, Al_2O_3, MgO, TiO_2, FeO_x, MnO, Na_2O, K_2O). The model predicts the non-Arrhenian Newtonian viscosity of silicate melts as a function of temperature and melt composition. The Giordano et. al. model is based on the measurements of over 1770 viscosity of multicomponent silicate-rich melts [163]. The viscosity model can also be used to predict the glass transition temperatures (T_g) and melt fragility [163]; for example predicting the effect of an individual oxide composition on melting temperatures and viscosity. T_g is the temperature separating the liquid (relaxed) from the glassy (unrelaxed) state. The non-Arrhenian temperature dependence of viscosity was accounted for by the Equation A2;

$$\log \eta = \frac{A + B}{T - C}$$ Equation A2

Where A is a constant independent of composition and B and C are adjustable parameters and T is temperature in degree K. Compositional dependence is attributed to B and C as linear combinations of oxide components (mol%) and several multiplicative oxide cross-terms as can be seen from Equation A3:

$$B = \sum_{i=1}^{7} [b_i M_i] + \sum_{j=1}^{3} \left[b_{1j}\left(M1_{1j} \,.\, M2_{1j}\right)\right]$$ Equation A3

$$C = \sum_{i=1}^{6} [c_i N_i] + \sum_{j=1}^{3} [c_{11}(N1_{11} \,.\, N2_{11})]$$

Where the M's and N's are combinations of mol % oxides

T_g is calculated from the Equation A4:

$$T_g = C + \frac{B}{12 - A}$$ Equation A4

Melt fragility is a measure of the sensitivity of liquid structure and flow properties to changes in temperature and it distinguishes two extreme behaviours of glass forming liquids: strong vs. fragile. "Strong" liquids show near-Arrhenian temperature dependence and show a firm resistance to structural change, even over large temperature variations. Conversely, "fragile" liquids show non-Arrhenian temperature dependence indicating that thermal perturbations are accommodated by continuous changes in melt structure. The "steepness index" (m), is a common measure of melt fragility used to track departures from Arrhenian behaviour and to distinguish strong and fragile melts. Essentially, it is the slope of the viscosity trace taken at Tg and can be calculated from Equation A5:

$$m = \left.\frac{d\,(log_{10}\,\eta)}{d\left(\frac{T_g}{T}\right)}\right|_{T = T_g} = \frac{B}{T_g\left(1 - \frac{C}{T_g}\right)^2}$$ Equation A5

Low values of m correspond to strong (Arrhenian-like) melts and higher values of m indicate increasing fragility (non-Arrhenian).

How to Use the Model

Giordano et. al. [100] also created an excel calculator version of this model, which works by inputting the composition (in weight percent) of the system and an output of viscosity (as a function of temperature in °C) is displayed. Hence by varying the oxide contents, the effect on viscosity and temperature can be predicted. This was how the data plotted in Figure 33 and Figure 34 were calculated. Two viscosity values were calculated; one at the melting temperature and the other at 50 °C above melting temperature because CMAS infiltration study was done at 50 °C above the melting temperature of the CMAS composition used, in

order to ensure that melting of the deposit occurred. A screen shot of the excel version is shown in Figure A1.

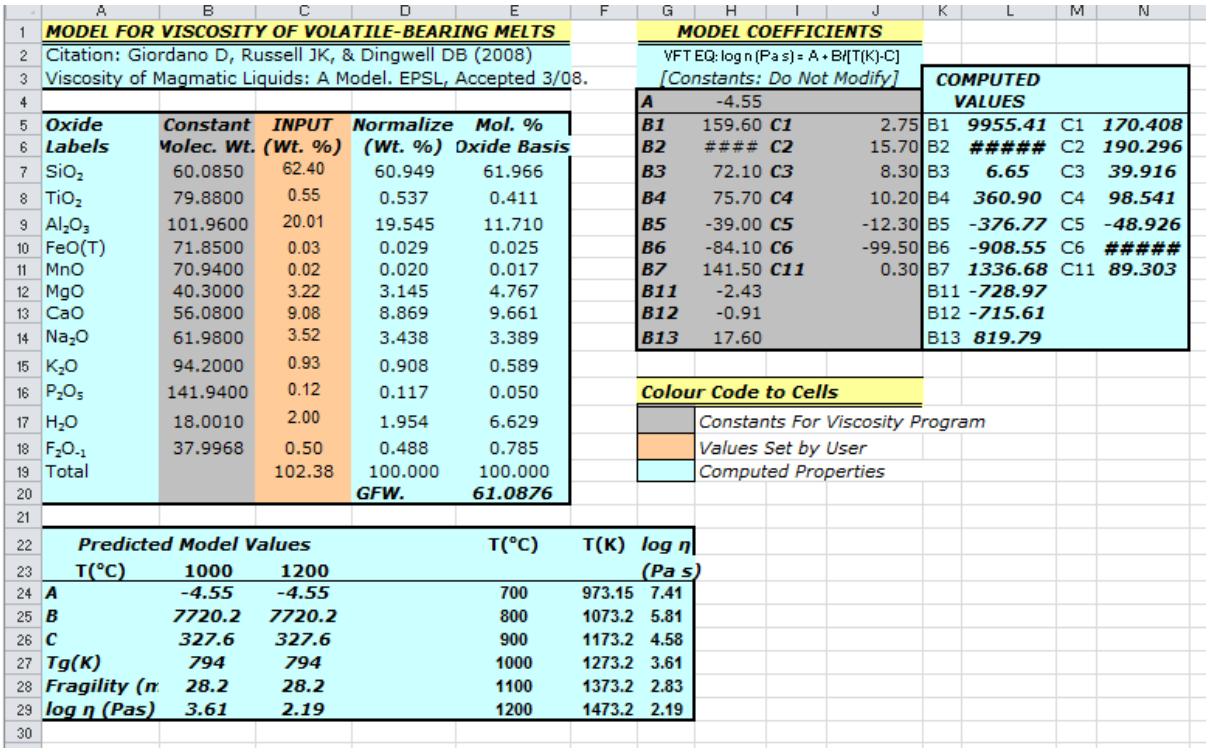

MODEL FOR VISCOSITY OF VOLATILE-BEARING MELTS

Citation: Giordano D, Russell JK, & Dingwell DB (2008)
Viscosity of Magmatic Liquids: A Model. EPSL, Accepted 3/08.

Oxide Labels	Constant Molec. Wt.	INPUT (Wt. %)	Normalize (Wt. %)	Mol. % Oxide Basis
SiO_2	60.0850	62.40	60.949	61.966
TiO_2	79.8800	0.55	0.537	0.411
Al_2O_3	101.9600	20.01	19.545	11.710
FeO(T)	71.8500	0.03	0.029	0.025
MnO	70.9400	0.02	0.020	0.017
MgO	40.3000	3.22	3.145	4.767
CaO	56.0800	9.08	8.869	9.661
Na_2O	61.9800	3.52	3.438	3.389
K_2O	94.2000	0.93	0.908	0.589
P_2O_5	141.9400	0.12	0.117	0.050
H_2O	18.0010	2.00	1.954	6.629
F_2O_{-1}	37.9968	0.50	0.488	0.785
Total		102.38	100.000	100.000
			GFW.	61.0876

MODEL COEFFICIENTS

VFT EQ: log n (Pa s) = A + B/[T(K)-C]
[Constants: Do Not Modify]

					COMPUTED VALUES		
A	-4.55						
B1	159.60	C1	2.75	B1	9955.41	C1	170.408
B2	####	C2	15.70	B2	#####	C2	190.296
B3	72.10	C3	8.30	B3	6.65	C3	39.916
B4	75.70	C4	10.20	B4	360.90	C4	98.541
B5	-39.00	C5	-12.30	B5	-376.77	C5	-48.926
B6	-84.10	C6	-99.50	B6	-908.55	C6	#####
B7	141.50	C11	0.30	B7	1336.68	C11	89.303
B11	-2.43			B11	-728.97		
B12	-0.91			B12	-715.61		
B13	17.60			B13	819.79		

Colour Code to Cells

- Constants For Viscosity Program
- Values Set by User
- Computed Properties

Predicted Model Values T(°C)	1000	1200
A	-4.55	-4.55
B	7720.2	7720.2
C	327.6	327.6
Tg(K)	794	794
Fragility (n	28.2	28.2
log η (Pas)	3.61	2.19

T(°C)	T(K)	log η (Pa s)
700	973.15	7.41
800	1073.2	5.81
900	1173.2	4.58
1000	1273.2	3.61
1100	1373.2	2.83
1200	1473.2	2.19

Figure A2: Excel version of Giordano et. al., viscosity model [100].

12 References

[1] Boyce, M. P. (1995), "Condition monitoring of turbomachinery: more than just good vibrations", *Electrotechnology*, vol. 6, no. 1, pp. 10-11.

[2] *The jet engine / Rolls-Royce plc*, (2005), London : Rolls-Royce, 2005; 'Latest ed.'.

[3] Costa, M. F. M., Batista, C., Portinha, A., Teixeira, V., Oliveira, C. R. and Ribeiro, R. M. (2008), "Microtopographic inspection of laser-glazed thermal barrier coatings", *Optical Engineering*, vol. 47, no. 6.

[4] Han, J. -. (2001), "Gas Turbine Heat Transfer and Cooling Technology", Vol. 2, pp. 1943.

[5] Johnson, M. and Spurlock, M. (2009), "Strategic oil analysis: Selecting alarms, setting limits", *Tribology and Lubrication Technology*, vol. 65, no. 11, pp. 18-20+22-23+26.

[6] Wellman, R. G. and Nicholls, J. R. (2007), "A review of the erosion of thermal barrier coatings", *Journal of Physics D: Applied Physics*, vol. 40, no. 16, pp. R293-R305.

[7] Drexler, J. M., Aygun, A., Li, D., Vaßen, R., Steinke, T. and Padture, N. P. (2010), "Thermal-gradient testing of thermal barrier coatings under simultaneous attack by molten glassy deposits and its mitigation", *Surface and Coatings Technology*, vol. 204, no. 16-17, pp. 2683-2688.

[8] Li, L., Hitchman, N. and Knapp, J. (2010), "Failure of thermal barrier coatings subjected to CMAS attack", *Journal of Thermal Spray Technology*, vol. 19, no. 1-2, pp. 148-155.

[9] Mohan, P., Patterson, T., Yao, B. and Sohn, Y. (2010), "Degradation of thermal barrier coatings by fuel impurities and CMAS: Thermochemical interactions and mitigation approaches", *Journal of Thermal Spray Technology*, vol. 19, no. 1-2, pp. 156-167.

[10] Krämer, S., Yang, J. and Levi, C. G. (2008), "Infiltration-inhibiting reaction of gadolinium zirconate thermal barrier coatings with CMAS melts", *Journal of the American Ceramic Society*, vol. 91, no. 2, pp. 576-583.

[11] Krämer, S., Yang, J., Levi, C. G. and Johnson, C. A. (2006), "Thermochemical interaction of thermal barrier coatings with molten CaO-MgO-Al2O3-SiO2 (CMAS) deposits", *Journal of the American Ceramic Society*, vol. 89, no. 10, pp. 3167-3175.

[12] Rai, A. K., Bhattacharya, R. S., Wolfe, D. E. and Eden, T. J. (2010), "CMAS-resistant thermal barrier coatings (TBC)", *International Journal of Applied Ceramic Technology*, vol. 7, no. 5, pp. 662-674.

[13] Wellman, R., Whitman, G. and Nicholls, J. R. (2010), "CMAS corrosion of EB PVD TBCs: Identifying the minimum level to initiate damage", *International Journal of Refractory Metals and Hard Materials*, vol. 28, no. 1, pp. 124-132.

[14] Meetham, G. W. (1988), "Requirements for and factors affecting high temperature capability. Part A of 'The Requirements for the Limitations of Materials at High Temperatures'", *Materials and Design*, vol. 9, no. 5, pp. 244-252.

[15] Mason, M. , *Materials Used in Aircraft Engines*, available at: http://www.ehow.com/list_7628069_materials-used-aircraft-engines.html (accessed 03/04/2013).

[16] Hass, D. D., Parrish, P. A. and Wadley, H. N. G. (1998), "Electron beam directed vapor deposition of thermal barrier coatings", *Journal of Vacuum Science and Technology A: Vacuum, Surfaces and Films*, vol. 16, no. 6, pp. 3396-3401.

[17] Moskal, G., Iwaniak, A. and Witala, B., (2011), *Characterization of microstructure and properties of plasma sprayed ceramic coatings on az91 magnesium alloy*.

[18] R. Darolia (2013), "
Thermal barrier coatings technology: critical
review, progress update, remaining
challenges and prospects ", *International Materials Reviews*, .

[19] Zhu, D. and Miller, R. A. (2004), "Thermal and environmental barrier coatings for advanced propulsion engine systems", Vol. 1, pp. 703.

[20] Bose, S. and DeMasi-Marcin, J. (1997), "Thermal barrier coating experience in gas turbine engines at Pratt & Whitney", *Journal of Thermal Spray Technology*, vol. 6, no. 1, pp. 99-104.

[21] Richer, P., Yandouzi, M., Beauvais, L. and Jodoin, B. (2010), "Oxidation behaviour of CoNiCrAlY bond coats produced by plasma, HVOF and cold gas dynamic spraying", *Surface and Coatings Technology*, vol. 204, no. 24, pp. 3962-3974.

[22] Levi, C. G. (2004), "Emerging materials and processes for thermal barrier systems", *Current Opinion in Solid State and Materials Science*, vol. 8, no. 1, pp. 77-91.

[23] Kim, D. -., Shin, I. -., Koo, J. -., Seok, C. -. and Lee, T. -. "Failure mechanisms of coin-type plasma-sprayed thermal barrier coatings with thermal fatigue", *Surface and Coatings Technology*, .

[24] Batista, C., Portinha, A., Ribeiro, R. M., Teixeira, V. and Oliveira, C. R. (2006), "Evaluation of laser-glazed plasma-sprayed thermal barrier coatings under high temperature exposure to molten salts", *Surface and Coatings Technology*, vol. 200, no. 24, pp. 6783-6791.

[25] Aygun, A., Vasiliev, A. L., Padture, N. P. and Ma, X. (2007), "Novel thermal barrier coatings that are resistant to high-temperature attack by glassy deposits", *Acta Materialia*, vol. 55, no. 20, pp. 6734-6745.

[26] Goteng, G., Tiwari, A. and Roy, R. (2010), "Grid services for multi-objective design optimisation", *CIRP Journal of Manufacturing Science and Technology*, vol. 3, no. 4, pp. 249-261.

[27] Postolenko, V., Prof. Schneider, J. M. and Prof. Singheiser, L. (2008), *Failure Mechanisms of Thermal Barrier Coatings for High Temperature Gas Turbine Components under Cyclic Thermal Loading* (PhD thesis), RWTH Aachen University, Germany.

[28] Key to Metals. (2012), ***Nickel-Based Superalloys: Part One***, available at: http://www.keytometals.com/page.aspx?ID=CheckArticle&LN=EN&site=KTN&NM=234 (accessed November 21).

[29] Moskal, G., (2011), *Microstructure characterization of TBC layers of Gd2Zr 2O7 type*.

[30] Guo, H., Li, D., Peng, H., Cui, Y. and Gong, S. (2011), "High-temperature oxidation and hot-corrosion behaviour of EB-PVD β-NiAlDy coatings", *Corrosion Science*, vol. 53, no. 3, pp. 1050-1059.

[31] Atkinson, A., Clarke, D. R. and Webb, S. J. (1998), "Mapping residual stress using optical microprobe in alumina films formed by thermal oxidation of NiAl", *Materials Science and Technology*, vol. 14, no. 6, pp. 531-534.

[32] Evans, A. G., Mumm, D. R., Hutchinson, J. W., Meier, G. H. and Pettit, F. S. (2001), "Mechanisms controlling the durability of thermal barrier coatings", *Progress in Materials Science*, vol. 46, no. 5, pp. 505-553.

[33] Toscano, J., Vaßen, R., Gil, A., Subanovic, M., Naumenko, D., Singheiser, L. and Quadakkers, W. J. (2006), "Parameters affecting TGO growth and adherence on MCrAlY-bond coats for TBC's", *Surface and Coatings Technology*, vol. 201, no. 7 SPEC. ISS., pp. 3906-3910.

[34] Padture, N. P., Gell, M. and Jordan, E. H. (2002), "Thermal barrier coatings for gas-turbine engine applications", *Science*, vol. 296, no. 5566, pp. 280-284.

[35] Mechnich, P., Braue, W. and Schulz, U. (2011), "High-temperature corrosion of EB-PVD yttria partially stabilized zirconia thermal barrier coatings with an artificial volcanic ash overlay", *Journal of the American Ceramic Society*, vol. 94, no. 3, pp. 925-931.

[36] Fray, D. (1992), "Solid electrolytes and the analysis of molten metals", *Chemistry and Industry (London)*, , no. 12, pp. 445-448.

[37] Mohan, P., Yao, B., Patterson, T. and Sohn, Y. H. (2009), "Electrophoretically deposited alumina as protective overlay for thermal barrier coatings against CMAS degradation", *Surface and Coatings Technology*, vol. 204, no. 6-7, pp. 797-801.

[38] Miller, R. A. (1997), "Thermal barrier coatings for aircraft engines: History and directions", *Journal of Thermal Spray Technology*, vol. 6, no. 1, pp. 35-42.

[39] Rhys-Jones, T. N. (1989), "Coatings for blade and vane applications in gas turbines", *Corrosion Science*, vol. 29, no. 6, pp. 623-646.

[40] Hongyu, Q., Xiaoguang, Y. and Yamei, W. (2009), "Interfacial fracture toughness of APS bond coat/substrate under high temperature", *International Journal of Fracture*, vol. 157, no. 1-2, pp. 71-80.

[41] Giolli, C., Scrivani, A., Rizzi, G., Borgioli, F., Bolelli, G. and Lusvarghi, L. (2009), "Failure mechanism for thermal fatigue of thermal barrier coating systems", *Journal of Thermal Spray Technology*, vol. 18, no. 2, pp. 223-230.

[42] Taylor, M. P., Pragnell, W. M. and Evans, H. E. (2008), "The influence of bond coat surface roughness on chemical failure and delamination in TBC systems", *Materials and Corrosion*, vol. 59, no. 6, pp. 508-513.

[43] Padture, N. P., Gell, M. and Jordan, E. H. (2002), "Thermal barrier coatings for gas-turbine engine applications", *Science*, vol. 296, no. 5566, pp. 280-284.

[44] Miller, R. A. (1987), "Current status of thermal barrier coatings - An overview", *Surface and Coatings Technology*, vol. 30, no. 1, pp. 1-11.

[45] Wolfe, D. E. and Singh, J. (2002), "Synthesis and characterization of TiBCN coatings deposited by ion beam assisted, co-evaporation electron beam-physical vapor deposition (EB-PVD)", *Journal of Materials Science*, vol. 37, no. 17, pp. 3777-3787.

[46] White, B. D., Kesler, O. and Rose, L. (2008), "Air plasma spray processing and electrochemical characterization of SOFC composite cathodes", *Journal of Power Sources*, vol. 178, no. 1, pp. 334-343.

[47] Beele, W., Marijnissen, G. and Van Lieshout, A. (1999), "The evolution of thermal barrier coatings - Status and upcoming solutions for today's key issues", *Surface and Coatings Technology*, vol. 120-121, pp. 61-67.

[48] Sampath, S. (2009), "Thermal sprayed ceramic coatings: fundamental issues and application considerations", *International Journal of Materials and Product Technology*, vol. 35, no. 3-4, pp. 425-448.

[49] Hass, D. D., Slifka, A. J. and Wadley, H. N. G. (2001), "Low thermal conductivity vapor deposited zirconia microstructures", *Acta Materialia*, vol. 49, no. 6, pp. 973-983.

[50] Hass, D. D. (2000), ***Directed Vapor Deposition of Thermal Barrier Coatings*** (Ph.D thesis), University of Virginia, Virginia, USA.

[51] Nicholls, J. R., Lawson, K. J., Johnstone, A. and Rickerby, D. S. (2002), "Methods to reduce the thermal conductivity of EB-PVD TBCs", *Surface and Coatings Technology*, vol. 151-152, pp. 383-391.

[52] Evans, A. G., Clarke, D. R. and Levi, C. G. (2008), "The influence of oxides on the performance of advanced gas turbines", *Journal of the European Ceramic Society*, vol. 28, no. 7, pp. 1405-1419.

[53] Haynes, J. A., Ferber, M. K. and Porter, W. D. (2000), "Thermal cycling behavior of plasma-sprayed thermal barrier coatings with various MCrAIX bond coats", *Journal of Thermal Spray Technology*, vol. 9, no. 1, pp. 38-48.

[54] Fossati, A., Di Ferdinando, M., Lavacchi, A., Bardi, U., Giolli, C. and Scrivani, A. (2010), "Improvement of the isothermal oxidation resistance of CoNiCrAlY coating sprayed by High Velocity Oxygen Fuel", *Surface and Coatings Technology*, vol. 204, no. 21-22, pp. 3723-3728.

[55] Naumenko, D., Shemet, V., Singheiser, L. and Quadakkers, W. J. (2009), "Failure mechanisms of thermal barrier coatings on MCrAlY-type bondcoats associated with the formation of the thermally grown oxide", *Journal of Materials Science*, vol. 44, no. 7, pp. 1687-1703.

[56] Clarke, D.R. and Levi, C.G., (2003), *Materials design for the next generation thermal barrier coatings*.

[57] Locci, I. E., Dickerson, R., Bowman, R. R., Whittenberger, J. D., Nathal, M. V. and Darolia, R. (1993), "Microstructure and mechanical properties of cast, homogenized and aged NiAl single crystal containing Hf", *Materials Research Society Symposium - Proceedings*, Vol. 288, pp. 685.

[58] Walston, W. S., Field, R. D., Dobbs, J. R., Lahrman, D. F. and Darolia, R. (1993), "Microstructure and high temperature strength of NiAl alloys", pp. 523.

[59] Cambridge University (2013), *Creep mechanisms*, available at: http://www.doitpoms.ac.uk/tlplib/creep/mechanisms.php (accessed June 2013).

[60] Odegard, B. C. and Thompson, A. W. (1974), "LOW TEMPERATURE CREEP OF Ti-6 Al-4 V.", *Metall Trans*, vol. 5, no. 5, pp. 1207-1213.

[61] Thompson, A. W. and Odegard, B. C. (1973), "The influence of microstructure on low temperature creep of ti-5 al-2.5 sn", *Metallurgical Transactions*, vol. 4, no. 4, pp. 899-908.

[62] Tsui, Y. C., Thompson, J. A. and Clyne, T. W. (1998), "The effect of bond coat creep on residual stresses and debonding in plasma sprayed thermal barrier systems", *Proceedings of the International Thermal Spray Conference*, Vol. 2, pp. 1565.

[63] Hutchinson, J. W. and Evans, A. G. (2002), "On the delamination of thermal barrier coatings in a thermal gradient", *Surface and Coatings Technology*, vol. 149, no. 2-3, pp. 179-184.

[64] Cawley, J. D. (1984), "OVERVIEW OF ZIRCONIA WITH RESPECT TO GAS TURBINE APPLICATIONS.", *NASA Technical Paper*, .

[65] Stott, F. H., de Wet, D. J. and Taylor, R. (1994), "Degradation of thermal-barrier coatings at very high temperatures", *MRS Bulletin*, vol. 19, no. 10, pp. 46-49.

[66] Mercer, C., Faulhaber, S., Evans, A. G. and Darolia, R. (2005), "A delamination mechanism for thermal barrier coatings subject to calcium-magnesium-alumino-silicate (CMAS) infiltration", *Acta Materialia*, vol. 53, no. 4, pp. 1029-1039.

[67] Steinke, T., Sebold, D., Mack, D. E., Vaßen, R. and Stöver, D. "A novel test approach for plasma-sprayed coatings tested simultaneously under CMAS and thermal gradient cycling conditions", *Surface and Coatings Technology*, .

[68] Grant, K. M., Krämer, S., Seward, G. G. E. and Levi, C. G. (2010), "Calcium-magnesium alumino-silicate interaction with yttrium monosilicate environmental barrier coatings", *Journal of the American Ceramic Society*, vol. 93, no. 10, pp. 3504-3511.

[69] Krämer, S., Yang, J. and Levi, C. G. (2008), "Infiltration-inhibiting reaction of gadolinium zirconate thermal barrier coatings with CMAS melts", *Journal of the American Ceramic Society*, vol. 91, no. 2, pp. 576-583.

[70] Borom, M. P., Johnson, C. A. and Peluso, L. A. (1996), "Role of environmental deposits and operating surface temperature in spallation of air plasma sprayed thermal barrier coatings", *Surface and Coatings Technology*, vol. 86-87, no. PART 1, pp. 116-126.

[71] Levi, C. G., Hutchinson, J. W., Vidal-Sétif, M. and Johnson, C. A. (2012), "Environmental degradation of thermal-barrier coatings by molten deposits", *MRS Bulletin*, .

[72] Smialek, J. L., Archer, F. A. and Garlick, R. G. (1992), "Chemistry of Saudi Arabian sand: a deposition problem on helicopter turbine airfoils", *International SAMPE Metals and Metals Processing Conference*, Vol. 3, pp. 63.

[73] Aygun, A., Vasiliev, A. L., Padture, N. P. and Ma, X. (2007), "Novel thermal barrier coatings that are resistant to high-temperature attack by glassy deposits", *Acta Materialia*, vol. 55, no. 20, pp. 6734-6745.

[74] Peng, H., Wang, L., Guo, L., Miao, W., Guo, H. and Gong, S. (2012), "Degradation of EB-PVD thermal barrier coatings caused by CMAS deposits", *Progress in Natural Science: Materials International*, .

[75] Braue, W. (2009), "Environmental stability of the YSZ layer and the YSZ/TGO interface of an in-service EB-PVD coated high-pressure turbine blade", *Journal of Materials Science*, vol. 44, no. 7, pp. 1664-1675.

[76] Krogstad, J. A., Krämer, S., Lipkin, D. M., Johnson, C. A., Mitchell, D. R. G., Cairney, J. M. and Levi, C. G. (2011), "Phase stability of t′-zirconia-based thermal barrier coatings: Mechanistic insights", *Journal of the American Ceramic Society*, vol. 94, no. SUPPL. 1, pp. S168-S177.

[77] Stiger, M. J., Yanar, N. M., Jackson, R. W., Laney, S. J., Pettit, F. S., Meier, G. H., Gandhi, A. S. and Levi, C. G. (2007), "Development of intermixed zones of alumina/zirconia in thermal barrier coating systems", *Metallurgical and Materials Transactions A: Physical Metallurgy and Materials Science*, vol. 38, no. 4, pp. 848-857.

[78] Braue, W. (2009), "Environmental stability of the YSZ layer and the YSZ/TGO interface of an in-service EB-PVD coated high-pressure turbine blade", *Journal of Materials Science*, vol. 44, no. 7, pp. 1664-1675.

[79] Bacos, M. P., Dorvaux, J. M., Lavigne, O., Mévrel, R., Poulain, M., Rio, C., & Vidal-Setif, M. H. (2011), "Performance and Degradation Mechanisms of Thermal Barrier Coatings for Turbine Blades: a Review of Onera Activities.", *Aerospace Lab: The ONERA Journal.*, .

[80] Borom, M. P., Johnson, C. A. and Peluso, L. A. (1996), "Role of environmental deposits and operating surface temperature in spallation of air plasma sprayed thermal barrier coatings", *Surface and Coatings Technology*, vol. 86-87, no. PART 1, pp. 116-126.

[81] Nicholls, J. R., Deakin, M. J. and Rickerby, D. S. (1999), "A comparison between the erosion behaviour of thermal spray and electron beam physical vapour deposition thermal barrier coatings", *Wear*, vol. 233-235, pp. 352-361.

[82] Steenbakker, R. J. L., Wellman, R. G. and Nicholls, J. R. (2006), "Erosion of gadolinia doped EB-PVD TBCs", *Surface and Coatings Technology*, vol. 201, no. 6, pp. 2140-2146.

[83] Evans, A. G., Fleck, N. A., Faulhaber, S., Vermaak, N., Maloney, M. and Darolia, R. (2006), "Scaling laws governing the erosion and impact resistance of thermal barrier coatings", *Wear*, vol. 260, no. 7-8, pp. 886-894.

[84] Chen, X., He, M. Y., Spitsberg, I., Fleck, N. A., Hutchinson, J. W. and Evans, A. G. (2004), "Mechanisms governing the high temperature erosion of thermal barrier coatings", *Wear*, vol. 256, no. 7-8, pp. 735-746.

[85] Cao, X. (2007), "Application of rare earths in thermal barrier coating materials", *Journal of Materials Science and Technology*, vol. 23, no. 1, pp. 15-35.

[86] Cao, X. (2007), "Application of rare earths in thermal barrier coating materials", *Journal of Materials Science and Technology*, vol. 23, no. 1, pp. 15-35.

[87] Lee, K. N. (2000), "Current status of environmental barrier coatings for Si-based ceramics", *Surface and Coatings Technology*, vol. 133-134, pp. 1-7.

[88] Clarke, D. R. and Phillpot, S. R. (2005), "Thermal barrier coating materials", *Materials Today*, vol. 8, no. 6, pp. 22-29.

[89] Cao, X. Q., Vassen, R. and Stoever, D. (2004), "Ceramic materials for thermal barrier coatings", *Journal of the European Ceramic Society*, vol. 24, no. 1, pp. 1-10.

[90] Bull, S. J., Kingswell, R. and Scott, K. T. (1996), "The sliding wear of plasma sprayed alumina", *Surface and Coatings Technology*, vol. 82, no. 3, pp. 218-225.

[91] Lawn, B. R. and Swain, M. V. (1975), "Microfracture beneath point indentations in brittle solids", *Journal of Materials Science*, vol. 10, no. 1, pp. 113-122.

[92] Lawn, B. R. and Marshall, D. B. (1984), "INDENTATION FRACTOGRAPHY: A MEASURE OF BRITTLENESS.", *Journal of Research of the National Bureau of Standards (United States)*, vol. 89, no. 6, pp. 435-451.

[93] Lawn, B. and Wilshaw, R. (1975), "Indentation fracture: principles and applications", *Journal of Materials Science*, vol. 10, no. 6, pp. 1049-1081.

[94] Krishnamurthy, N., Murali, M. S., Venkataraman, B. and Mukunda, P. G. (2012), "Characterization and solid particle erosion behavior of plasma sprayed alumina and calcia-stabilized zirconia coatings on Al-6061 substrate", *Wear*, vol. 274-275, pp. 15-27.

[95] Ramaswamy, P., Seetharamu, S., Varma, K. B. R. and Rao, K. J. (1997), "Al2O3-ZrO2 composite coatings for thermal-barrier applications", *Composites Science and Technology*, vol. 57, no. 1, pp. 81-89.

[96] Widjaja, S., Limarga, A. M. and Yip, T. H. (2003), "Modeling of residual stresses in a plasma-sprayed zirconia/alumina functionally graded-thermal barrier coating", *Thin Solid Films*, vol. 434, no. 1-2, pp. 216-227.

[97] Limarga, A. M., Widjaja, S. and Yip, T. H. (2005), "Mechanical properties and oxidation resistance of plasma-sprayed multilayered Al2O3/ZrO2 thermal barrier coatings", *Surface and Coatings Technology*, vol. 197, no. 1, pp. 93-102.

[98] Djurado, E., Bouvier, P. and Lucazeau, G. (2000), "Crystallite size effect on the tetragonal-monoclinic transition of undoped nanocrystalline zirconia studied by XRD and Raman spectrometry", *Journal of Solid State Chemistry*, vol. 149, no. 2, pp. 399-407.

[99] Ghosh, D., Krishnamurthy, V. A. and Sankaranarayanan, S. R. (2010), "Application of optical basicity to viscosity of high alumina blast furnace slags", *Journal of Mining and Metallurgy, Section B: Metallurgy*, vol. 46, no. 1, pp. 41-49.

[100] Giordano, D., Russell, J. K. and Dingwell, D. B. (2008), "Viscosity of magmatic liquids: A model", *Earth and Planetary Science Letters*, vol. 271, no. 1-4, pp. 123-134.

[101] Ozerov, A. Y. (2009), "Experimental modeling of the explosion mechanism of basaltic magmas", *Petrology*, vol. 17, no. 7, pp. 653-668.

[102] Mechnich, P., Braue, W. and Schulz, U. (2011), "High-temperature corrosion of EB-PVD yttria partially stabilized zirconia thermal barrier coatings with an artificial volcanic ash overlay", *Journal of the American Ceramic Society*, vol. 94, no. 3, pp. 925-931.

[103] Svancarek, P., Galusek, D., Calvert, C., Loughran, F., Brown, A., Brydson, R. and Riley, F. (2004), "A comparison of the microstructure and mechanical properties of two liquid phase sintered aluminas containing different molar ratios of calcia-silica sintering additives", *Journal of the European Ceramic Society*, vol. 24, no. 12, pp. 3453-3463.

[104] Bodsworth, C. and Bell, H. B. (1972), *Physical chemistry of iron and steel manufacture*, Second ed, LONGMAN, London.

[105] Holappa, L., Forsbacka, L. and Han, Z. (2006), "Measuring and modeling of viscosity and surface properties in high temperature systems", *ISIJ International*, vol. 46, no. 3, pp. 394-399.

[106] Jia, D., Hamilton, J., Zaman, L. M. and Goonewardene, A. (2007), "The time, size, viscosity, and temperature dependence of the Brownian motion of polystyrene microspheres", *American Journal of Physics*, vol. 75, no. 2, pp. 111-115.

[107] Kondratiev, A. and Jak, E. (2000), "Viscosity model in the Al2O3-CaO-'FeO'-SiO2 system", *Australasian Institute of Mining and Metallurgy Publication Series*, pp. 445.

[108] Kondratiev, A. and Jak, E. (2001), "Predicting coal ash slag flow characteristics (viscosity model for the Al2O3-CaO-'FeO'-SiO2 system)", *Fuel*, vol. 80, no. 14, pp. 1989-2000.

[109] Nakashima, K., Saito, N., Shinozaki, S., Tanaka, R., Maeda, T., Shimizu, M. and Mori, K. (2004), "Wetting and penetration behavior of calcium ferrite melts to sintered hematite", *ISIJ International*, vol. 44, no. 12, pp. 2052-2056.

[110] Seok, S. -., Jung, S. -., Lee, Y. -. and Min, D. -. (2007), "Viscosity of highly basic slags", *ISIJ International*, vol. 47, no. 8, pp. 1090-1096.

[111] NCERT (2011), *Chemical Bonding And Molecular Structure*, available at: http://textbook.s-anand.net/ncert/class-11/chemistry/4-chemical-bonding-and-molecular-structure (accessed June 2013).

[112] Liang, X., Jin, Y. and Wang, Y. (2011), "Effect of additives on melting point and viscosity of RH refining slag", *Open Materials Science Journal*, vol. 5, pp. 9-14.

[113] Polity, A., Meyer, B. K., Kramer, T., Wang, C., Haboeck, U. and Hoffmann, A. (2006), "ZnO based ternary transparent conductors", *Physica Status Solidi (A) Applications and Materials*, vol. 203, no. 11, pp. 2867-2872.

[114] Swanson, S. E. and Beget, J. E. (1994), "Melting properties of volcanic ash", *US Geological Survey Bulletin*, vol. 2047, pp. 87-92.

[115] Kurz R., B. K. (2001), "Degradation in gas turbine systems", *Journal of Engineering for Gas Turbines and Power*, vol. 123, no. 1, pp. 70-77.

[116] Shinozaki, M., Roberts, K. A., Van De Goor, B. and William Clyne, T. (2013), "Deposition of ingested volcanic ash on surfaces in the turbine of a small jet engine", *Advanced Engineering Materials*, vol. 15, no. 10, pp. 986-994.

[117] Wellman, R.G. and Nicholls, J.R., (2001), *A mechanism for the erosion of EB PVD TBCS*.

[118] MDS Coating Technologies Corporation (MCT) (15 August 2012), *Erosion-resistant nanocoating for turbine blades saves fuel, lowers costs*, available at: http://www.greencarcongress.com/2012/08/mct-20120815.html (accessed May 2013).

[119] Krestnikov, I. L., Heitz, R., Ledentsov, N. N., Hoffmann, A., Kosel, T. H., Merz, J. L. and Mintairov, A. M. (2003), "
Inherent nature of localized states in highly planar monolayer InAs/GaAsN pseudo-alloys", *Applied Physics Letters,* vol. 83, no. 18.

[120] Kosel, T. H. (1992), "
Solid particle erosion. ", *ASM Handbook on Friction, Lubrication and Wear Technology.*, vol. 18, pp. 199.

[121] Hussein, M. F. and Tabakoff, W. (1973), " Dynamic Behavior of Solid Particles Suspended by Polluted Flow in a Turbine Stage ", *Journal of Aircraft,* vol. 10, no. 7, pp. 434-434-440.

[122] Hamed, A., Tabakoff, W. and Singh, D. (1998), "Modeling of compressor performance deterioration due to erosion", *International Journal of Rotating Machinery,* vol. 4, no. 4, pp. 243-248.

[123] Tabakoff, W., Hamed, A. and Beacher, B. (1983), "Investigation of gas particle flow in an erosion wind tunnel", *Wear,* vol. 86, no. 1, pp. 73-88.

[124] Gunes, D. and Menguturk, M. (1983), "IMPROVED PARTICLE TRAJECTORY CALCULATION AROUND BLADE LEADING EDGE.", pp. 52. 1.

[125] Nelson, W. A. and Orenstein, R. M. (1997), "TBC experience in land-based gas turbines", *Journal of Thermal Spray Technology,* vol. 6, no. 2, pp. 176-180.

[126] Finnie, I. and McFadden, D. H. (1978), "On the velocity dependence of the erosion of ductile metals by solid particles at low angles of incidence", *Wear,* vol. 48, no. 1, pp. 181-190.

[127] Flores, J. F., Neville, A., Kapur, N. and Gnanavelu, A. (2009), "An experimental study of the erosion-corrosion behavior of plasma transferred arc MMCs", *Wear,* vol. 267, no. 1-4, pp. 213-222.

[128] Wensink, H. and Elwenspoek, M. C. (2002), "A closer look at the ductile-brittle transition in solid particle erosion", *Wear,* vol. 253, no. 9-10, pp. 1035-1043.

[129] Tilly, G. P. and Sage, W. (1970), "The interaction of particle and material behaviour in erosion processes", *Wear,* vol. 16, no. 6, pp. 447-465.

[130] Conway, G. (2007), "At one with the land", *New Scientist,* vol. 194, no. 2609, pp. 47.

[131] Lawn, B. and Wilshaw, R. (1975), "Indentation fracture: principles and applications", *Journal of Materials Science,* vol. 10, no. 6, pp. 1049-1081.

[132] Hutchings, I. M. (1992), "Ductile-brittle transitions and wear maps for the erosion and abrasion of brittle materials", *Journal of Physics D: Applied Physics,* vol. 25, no. 1 A, pp. A212-A221.

[133] Evans, A. G., Gulden, M. E. and Rosenblatt, M. (1978), "IMPACT DAMAGE IN BRITTLE MATERIALS IN THE ELASTIC-PLASTIC RESPONSE REGIME.", *Proc R Soc London Ser A*, vol. 361, no. 1706, pp. 343-365.

[134] Rothwell, J. (2007), "An 18th century temperature series for the East Midlands 1748-1784", *International Journal of Meteorology*, vol. 32, no. 323, pp. 303-316.

[135] Mévrel, R. (1989), "State of the art on high-temperature corrosion-resistant coatings", *Materials Science and Engineering A*, vol. 120-121, no. PART 1, pp. 13-24.

[136] Evans, A. G. and Wilshaw, T. R. (1977), "Dynamic solid particle damage in brittle materials: an appraisal", *Journal of Materials Science*, vol. 12, no. 1, pp. 97-116.

[137] Wang, M., Fleck, N. A. and Evans, A. G. (2011), "Elastodynamic erosion of thermal barrier coatings", *Journal of the American Ceramic Society*, vol. 94, no. SUPPL. 1, pp. S160-S167.

[138] Nicholls, J. R. and Wellman, R. G. (2004), "Erosion and Foreign Object Damage of Thermal Barrier Coatings", *The Control and Reduction of Wear in Military Platforms*, 7-9 June 2003, Williamsburg, USA., .

[139] Zhu, D., Miller, R. A. and Kuczmarski, M. A. (2009), "Development and life prediction of erosion resistant turbine low conductivity thermal barrier coatings", *Annual Forum Proceedings - AHS International*, Vol. 2, pp. 1088.

[140] Nicholls, J.R., Jaslier, Y. and Rickerby, D.S., (1997), *Erosion and foreign object damage of thermal barrier coatings*.

[141] Oxford Instruments (2013), *Introduction to EBSD*, available at: http://www.ebsd.com/index.php/ebsd-explained/introduction-to-ebsd (accessed August 2013).

[142] Sitzman, S. D. (2004), "Introduction to EBSD analysis of micro- to nanoscale microstructures in metals and ceramics", *Proceedings of SPIE - The International Society for Optical Engineering*, Vol. 5392, pp. 78.

[143] Elliot, A. J., Singh, N., Loveridge, P., Harcourt, S., Smith, S., Pnaiser, R., Kavanagh, K., Robertson, C., Ramsay, C. N., McMenamin, J., Kibble, A., Murray, V., Ibbotson, S., Catchpole, M., McCloskey, B. and Smith, G. E. (2010), "Syndromic surveillance to assess the potential public health impact of the Icelandic volcanic ash plume across the United Kingdom, April 2010", *Eurosurveillance*, vol. 15, no. 23.

[144] Tarefder, R. A. and Faisal, H. (2012), " Effects of Dwell Time and Loading Rate on the Nanoindentation Behavior of Asphaltic Materials ", *Journal of Nanomechanics and Micromechanics*, vol. 3, no. 2, pp. 17-17-23.

[145] Bhushan, B. and Li, X. (2003), "Nanomechanical characterisation of solid surfaces and thin films", *International Materials Reviews*, vol. 48, no. 3, pp. 125-164.

[146] Bayhurst, G. K., Wohletz, K. H. and Mason, A. S. (1994), "A method for characterizing volcanic ash from the December 15, 1989, eruption of Redoubt Volcano, Alaska", *US Geological Survey Bulletin*, vol. 2047, pp. 13-17.

[147] Thomas, H. E. and Watson, I. M. (2010), "Observations of volcanic emissions from space: Current and future perspectives", *Natural Hazards*, vol. 54, no. 2, pp. 323-354.

[148] Yu, J., Meixner, F. X., Sun, W., Mamtimin, B., Xia, C. and Xie, W. (2010), "Biogenic nitric oxide emission of mountain soils sampled from different vertical landscape zones in the changbai mountains, Northeastern China", *Environmental Science and Technology*, vol. 44, no. 11, pp. 4122-4128.

[149] Lee, W. E. and Zhang, S. (1999), "Melt corrosion of oxide and oxide-carbon refractories", *International Materials Reviews*, vol. 44, no. 3, pp. 77-104.

[150] Ndamka, N. L., Wellman, R. G. and Nicholls, J. R. (2011), "Comparison of CMAS and Volcanic Ash Interaction with EB-PVD TBCs", *Thermal Barrier Coatings III*, August 2011, Kloster Irsee, Germany, .

[151] Prof. Koria, S. C. (2012), *Physico-chemical properties of slag*, available at: http://nptel.iitm.ac.in/courses/113104059/5 (accessed September 15).

[152] Seyfarth, A. and Pecard, D. (2008), "Slag analysis by a dedicated energy dispersive X-ray fluorescence spectrometry", *Steel Times International*, vol. 32, no. 5, pp. 22-24.

[153] Sandvik Materials Technology , *Welding flux basicity index*, available at: http://www.smt.sandvik.com/en/products/welding-products/welding-flux/basicity/ (accessed April 2014).

[154] Boles, M. A. and Yunus, A. C. (2006), *Thermodynamics : An Engineering Approach IN SI UNITS*, 5th ed, Tata McGraw-Hill.

[155] Wellman, R. G. and Nicholls, J. R. (2008), "Erosion, corrosion and erosion-corrosion of EB PVD thermal barrier coatings", *Tribology International*, vol. 41, no. 7, pp. 657-662.

[156] Cernuschi, F., Guardamagna, C., Lorenzoni, L., Capelli, S., Bossi, F., Vaßen, R. and Von Niessen, K. (2013), "Solid particle erosion of thermal spray and physical vapour deposition thermal barrier coatings", *Ceramic Engineering and Science Proceedings*, Vol. 33, pp. 37.

[157] Cernuschi, F., Lorenzoni, L., Capelli, S., Guardamagna, C., Karger, M., Vaßen, R., von Niessen, K., Markocsan, N., Menuey, J. and Giolli, C. (2011), "Solid particle erosion of thermal spray and physical vapour deposition thermal barrier coatings", *Wear*, vol. 271, no. 11-12, pp. 2909-2918.

[158] Wellman, R. G., Nicholls, J. R. and Murphy, K. (2009), "Effect of microstructure and temperature on the erosion rates and mechanisms of modified EB PVD TBCs", *Wear*, vol. 267, no. 11, pp. 1927-1934.

[159] Wellman, R. G., Deakin, M. J. and Nicholls, J. R. (2005), "The effect of TBC morphology and aging on the erosion rate of EB-PVD TBCs", *Tribology International*, vol. 38, no. 9 SPEC. ISS., pp. 798-804.

[160] Drexler, J. M., Gledhill, A. D., Shinoda, K., Vasiliev, A. L., Reddy, K. M., Sampath, S. and Padture, N. P. (2011), "Jet engine coatings for resisting volcanic ash damage", *Advanced Materials*, vol. 23, no. 21, pp. 2419-2424.

[161] Gledhill, A. D., Reddy, K. M., Drexler, J. M., Shinoda, K., Sampath, S. and Padture, N. P. (2011), "Mitigation of damage from molten fly ash to air-plasma-sprayed thermal barrier coatings", *Materials Science and Engineering A*, .

[162] Zaleski, E. M. Ensslen, C. Levi, C. G. (2012), "Thermochemical Interactions of Rare Earth Based TBCs with Molten CMAS Deposits", *The Electrochemical Society*, vol. 2334.

[163] Giordano, D., Russell, J. K., Dingwell, D. B. (2008) "Viscosity of magmatic liquids: A model", Earth and Planetary Science, Letter 271, pp. 123-134.